UNIVERSITÀ DEGLI STUDI DI TORINO

DIPARTIMENTO DI SCIENZE DELLA TERRA

UNIVERSITÀ
DI TORINO

Scuola di Dottorato in Scienza della Natura e Tecnologie Innovative

Ph.D. PROGRAMME IN EARTH SCIENCES

Cycle XXXIV

Ph.D. Thesis

Rock magnetism of shear zones in sedimentary rocks: study of exhumed analogues to understand modern convergent margins

THESIS' AUTHOR/CANDIDATE: **Claudio Robustelli Test**

Supervisor: Elena Zanella

Co-Tutor: Andrea Festa

Ph.D. Programme Co-ordinator: Francesco Dela Pierre

Academic years of enrolment: 2018/2019 – 2019/2020 – 2020/2021

CODE OF SCIENTIFIC DISCIPLINE: GEO/10 – SOLID EARTH GEOPHYSICS

ABSTRACT

Active convergent margins shear zones are heterogeneous and highly deformed zones that exhibit structures from both distributed and localized deformation. The presence of heterogeneous material with contrasting competence (e.g., broken formations and mélanges) and the complex structural architectures (superposition of different tectonic units) of shear zones are inferred to affect the frictional properties, the slip weakening mechanisms, and variation in slip behaviours. Deciphering the stress and strain distribution across convergent margin shear zones is critical to understanding the physical processes involved in the nucleation of convergent margin shear zones and its behaviour.

Magnetic properties of fault rocks (i.e., mineral assemblages, concentration, granulometry and preferred orientation of grains) are known to be sensitive to chemical and physical changes related to the faulting processes. Magnetic mineralogy is lithology-dependent, with a variety of subpopulations of grains (different mineralogy and grain-size) that can form and alter at distinct diagenetic and deformation stages. In particular, magnetic fabric analysis has proven to be a reliable petrofabric tool for examining subtle changes in the stress regime, providing insight into the relationships between petrofabric and deformation intensity associated with faulting.

In modern subduction contexts, the internal architecture of the plate interface is difficult to observe seismically. In contrast, studies of exhumed analogues offer an invaluable opportunity to directly investigate the characteristics of the internal structures of convergent margins shear zones and to constrain changes in magnetic properties with respect to their geodynamic evolution. This thesis reports a detailed investigation of the magnetic fabric of three exhumed analogues of convergent margin shear zones involving different lithological units (e.g., carbonate- or clay-rich sediments). Here, specific meso-structural fabrics are associated with lithology-dependent deformation mechanisms, providing an opportunity to probe the influence of lithological variations/heterogeneities in the recording of multiple deformation events by the magnetic fabric.

The protocol applied for AMS analysis (combination of density diagrams and cluster analysis at site level) shows a great potential for isolating the contribution of coexisting sedimentary and/or tectonic petrofabrics and assess their statistical significance and relative distribution within convergent margin shear zones. Geometrical relationships between magnetic and structural fabric have been investigated using specially designed ternary diagrams, allowing semi-quantitative interpretations of the different subfabrics in terms of prevailing deformation processes.

The main results provide valuable evidence of localized deformation that are difficult to observe both in actual convergent margins and in laboratory experiments. Distinct subfabrics showed reasonably straightforward correlations with structural data, the intensity of the tectonic shear-related reworking, and the structural position within the shear zone (i.e., the proximity to the main thrust faults).

Close to the main thrusts, the occurrence of shear-related fabric indicates a high degree of non-coaxial strain and strain localization along the main fault planes. As the distance increases, the degree of anisotropy and the ellipsoids' oblateness gradually decrease. Thus, the presence of subfabrics related to less intense deformation (e.g., S-C intersection fabric) and previous tectonic events become dominant, revealing minor to absent evidence of shearing. Discrimination of subfabrics also allowed unveiling the presence of minor thrust plane and a qualitative assessment of the heterogeneous registration of strain (i.e., distributed versus localized deformation).

Since each mineral may respond independently to deformation mechanisms, separating the preferred orientation of different magnetic subfabrics may help to discern multiple deformation events, providing insights into faulting processes and strain partitioning. The orientation of remanence-bearing grains was isolated performing separate anisotropy of magnetic remanence experiments, obtaining significant information on the variable response of different subpopulations of ferromagnetic minerals to shearing. In addition, the paramagnetic and ferromagnetic subfabrics were derived by high-field torque magnetometry to evaluate their different contribution to the total AMS and to the recording of strain.

Different sensitivity of para- and ferro-magnetic grains to deformation is observed depending on the lithology and the dominant deformation mechanism affecting the matrix. Carbonate-rich sediments, which are strongly influenced by pressure-solution, reveal a slight variation in the orientation of para- and ferro-magnetic subfabrics, which suggests similar registration of strain by different subpopulation of grains.

In contrast, in clay-rich sediments, which deformed mainly by progressive rotation and micro-folding of phyllosilicates, ferromagnetic grains display variable behaviour. The ferromagnetic subfabrics show orientations that can be consistent with or independent of those of the paramagnetic matrix, depending on the intensity of deformation and the different lithification state prior to the shear related deformation.

In conclusion, results presented in this thesis allow to distinguish the superposition of deformation events, unravelling the strain partitioning/concentration and the links between magnetic subfabrics and rheological behaviour of the matrix, providing a better comprehension of the heterogeneous magnetic signature observed in actual convergent margin shear zones and their geodynamic evolution.

CONTENTS

ABSTRACT ii

CONTENTS iv

GLOSSARY vi

LIST OF FIGURES x

1. INTRODUCTION 1

1.1 Thesis Rationale 1

1.2 Thesis Objectives 2

1.3 Thesis Outlines 4

2. MAGNETIC FABRIC & ROCK MAGNETISM IN SHEAR ZONES: A brief overview 6

3. METHODOLOGY 20

3.1 Sampling strategy 20

3.2 Magnetic mineralogy investigation 21

3.2.1 Low- and high-temperature experiments and SEM-EDS analysis (Case study from the SVU – Chapter 5) 22

3.3 AMS data and statistical treatments 23

3.4 ApARM, AARM, AIRM and High-field AMS 26

3.5 Ternary Diagrams and comparison with mesoscale structural fabric 27

4. FIRST CASE STUDY: The OAS thrust 30

4.1 Geological setting 30

4.2 Structural data 33

4.2.1 Shear zones along frontal thrust ramps 33

4.2.2 Shear zones along oblique thrust ramps 34

4.3 Results 35

4.3.1 Magnetic Mineralogy 35

4.3.2. AMS 39

4.3.3 AARM, AIRM and HF-AMS 45

4.4 Discussion & comparison with structural data 47

4.5 Conclusions 54

5. SECOND CASE STUDY: The SVU 56

5.1 Geological setting 56

5.1.1 The Gova Tectonic Window 57

5.1.2 The Vidiciatico sector 58

5.2 Results 61

5.2.1 Magnetic Mineralogy ... 61
5.2.2 AMS ... 72
5.2.3 AARM, AIRM and HF-AMS ... 83
5.2.4 Ternary ... 88
5.3 Discussion ... 93
5.3.1 Local heterogeneities in strain recorded by AMS ... 93
5.3.2 Ferromagnetic fabric insight into the deformation history of a shear zone ... 96
5.3.3 Magnetic signature of fluid-rock interaction ... 98
5.4 Conclusions ... 101
6. THIRD CASE STUDY: The ELAW ... 102
6.1 Geological setting ... 102
6.2 Meso-Structural Fabrics of Chaotic Rock Units ... 104
6.2.1 The Broken Formation ... 105
6.2.2 The Tectonic Mélange ... 107
6.2.3 The Sedimentary Mélange ... 107
6.2.4 The Polygenetic Mélange ... 109
6.3 Results ... 110
6.3.1 Magnetic Mineralogy ... 110
6.3.2 AMS ... 113
6.3.3 AARM, AIRM and HF-AMS ... 118
6.4 Discussion & correlation of the magnetic fabric with mélange forming processes ... 122
6.4.1 The Broken Formation ... 122
6.4.2 The Tectonic Mélange ... 123
6.4.3 The Sedimentary Mélange ... 125
6.4.4 The Polygenetic Mélange ... 127
6.5 Concluding Remarks ... 128
7. SUMMARY & CONCLUDING REMARKS ... 130
7.1 Summary of main findings & comparison with modern equivalent ... 130
7.2 Lithological control on magnetic fabric record of strain & outlook ... 141
APPENDIX ... 146
I. Rock magnetic parameters ... 146
II. Supplementary figures & tables ... 147
ACKNOWLEDGMENTS ... 164
REFERENCES ... 165

GLOSSARY

Rock magnetism and anisotropy terminology

(see APPENDIX for parameters equations and references)

AMS or **LF-AMS**	low-field anisotropy of magnetic susceptibility
ApARM	anisotropy of partial anhysteretic remanent magnetization:
ApARM$_{100-40}$	ApARM in the coercivity window of 100 to 40 mT
ApARM$_{40-0}$	ApARM in the coercivity window of 40 to 0 mT
AARM	anisotropy of anhysteretic remanent magnetization – In this work we referred to the coercivity window of 100 to 0 mT
ARM	anisotropy of magnetic remanence or anhysteretic remanent magnetization
HF-AMS	high-field AMS
HF-AMS$_{para}$	high-field AMS paramagnetic subfabric
HF-AMS$_{ferro}$	high-field AMS ferromagnetic subfabric
LT-AMS	low temperature AMS
AIRM	anisotropy of isothermal remanent magnetization
blended or mixed AMS fabric	AMS fabric resulting from the combination of incompatible subfabrics (e.g., normal and inverse subfabrics - Borradaile & Jackson, 2004; 2010).
non-orthorhombic fabric	fabric showing confidence regions inclined to the planes of symmetry (Borradaile, 2001)
k_m	mean magnetic susceptibility [SI]
χ_m	mass magnetic susceptibility [m^3/Kg]
k_1, k_2 and k_3	minimum, intermediate and maximum magnetic susceptibility axes, respectively
Pj	corrected anisotropy degree
k'	mean deviatoric susceptibility – anisotropy factor [m^3/Kg]
T	shape parameter
U	difference shape factor
L	magnetic lineation
F	magnetic foliation
χ–T	thermomagnetic susceptibility curves – mass susceptibility versus temperature
$\chi_{fd\%}$	frequency-dependent magnetic susceptibility [%]
χ_{lf}	low-frequency magnetic susceptibility [m^3/Kg]
χ_{hf}	high-frequency magnetic susceptibility [m^3/Kg]

χ_a	ARM susceptibility (ARM normalized by acquisition bias field)
SP	superparamagnetic particles
SD	single domain
PSD	single vortex or pseudo single domain state
MD	multidomain
RM	remanent magnetization [A/m or Am^2/Kg]
NRM	natural remanent magnetization [A/m or Am^2/Kg]
IRM	isothermal remanent magnetization [A/m or Am^2/Kg]
B_{cr} or H_{cr}	coercivity of remanence [mT]
B_c or H_c	Coercivity [mT]
M_s	saturation magnetization [A/m or Am^2/Kg]
M_{rs}	saturation remanent magnetization [A/m or Am^2/Kg]
Bh	mean remanence coercivity [mT or $\log_{10}$ units]
σ_{hyst}	hysteresis loop shape parameter
DP	dispersion parameter
MDF	median destructive field [mT]
AF	alternating field
AC	alternating current
DC	direct current
FC	field cooled
ZFC	zero-field cooled
LT-SIRM	low temperature SIRM – In this work we referred to a SIRM imparted at 10 K
RT-SIRM	room temperature SIRM
T_V	Verwey transition
T_M	Morin transition
T_B	Besnus transition
δ_{FC} and δ_{ZFC}	remanence loss proxies
δ_{FC}/δ_{ZFC}	delta-delta ratio
G%	goethite proxy

Structural terminology

SSEs	slow slip events
LFEs	low-frequency earthquakes
GEQs	great thrust earthquakes
EQs	earthquakes
LPS	layer-parallel shortening
FTR	frontal thrust ramp
OTR	oblique thrust ramp
C	shear planes
S	cleavage planes
T	thrust plane
E, E'	extensional planes
R	Riedel planes
OCT	ocean-continental transition
MTDs	mass-transport deposits

Regional/Local geological terminology

SVU	Sestola-Vidiciatico Tectonic Unit
OAS	Olevano-Antrodoco-Sibillini
ELAW	External Ligurian accretionary wedge

Samples names rationale

Olevano-Antrodoco-Sibillini (OAS) thrust – Chapter 4

*Sample names includes information on **Locality**, **Lithology** and **Site number***

*(e.g., **MSC1** = **Monastero** - **Scaglia Cinerea** - **Site 1**)*

Locality	**S**	Sassotetto
	I	Infernaccio
	M	Monastero
	B	Mt. Boragine
	V	Vallescura
Lithology	**SR**	Scaglia Rossa Fm.
	SC	Scaglia Cinerea Fm.
	MC	Marne con Cerrogna Fm.
Site number	**n**	progressive numbers with increasing distance from the thrust plane

Sestola-Vidiciatico Tectonic Unit (SVU) - Chapter 5

*Sample names includes **Transect number**, **Structural position or types of tectonic units** and **Site number***

*(e.g., **T1S1** = **Transect 1** – **Sheared sandstones**- **Site 1**)*

Transect number	**T1**, **T2** or **T3**	Transect 1, 2 or 3
Structural position or types of tectonic units	**U**	Underthrusting sediments
	S	Sheared sandstones
	B	plate Boundary shear zone
	AR	Broken Formation - Argille a Palombini or varicolored shales
	SM	Sedimentary mélanges
Site number	**n**	progressive distance from the main thrust plane

External Ligurian accretionary wedge (ELAW) - Chapter 6

*Sample names includes information on **types of chaotic rock units** and **site number***

*(e.g., **TMé1** = **Tectonic mélange** - **Site 1**)*

Type of chaotic rock unit	**TMé**	Tectonic mélanges
	BrFm	Broken formations
	SMé	Sedimentary mélanges
	PMé	Polygenetic mélanges

LIST OF FIGURES

Figure 1.1. Location and structural position of the studied convergent margin shear zones 5

Figure 2.1. Early studies on anisotropy in deformed rocks 8
Figure 2.2. Representative examples of composite fabric 9
Figure 2.3. Changes in magnetic fabric during early stages of LPS 11
Figure 2.4. Representative magnetic fabrics related to different structural positions 12
Figure 2.5. Examples of magnetic fabric in shear zones, in both exhumed and actual contexts 13
Figure 2.6. Main variations in shear-related magnetic fabric configuration. 14
Figure 2.7. Magnetic fabric in analogue models 15
Figure 2.8. Representative relationships between AMS and AARM in deformed rocks 16
Figure 2.9. Examples of different relationships between AMS and AARM in deformed rocks 17
Figure 2.10. Rock magnetism revealing fault-related processes 19

Figure 3.1. Example of subfabric unmixing 25
Figure 3.2. Histogram and density distribution of angles among cluster means 26
Figure 3.3. Procedure for plotting ternary diagrams 29

Figure 4.1. Schematic geological map of the OAS 31
Figure 4.2. Detail view of the shear zones along the OAS. 33
Figure 4.3. Summary of the structural data (OAS) 34
Figure 4.4. Thermomagnetic susceptibility curves and IRM acquisition and backfield curves (OAS) 35
Figure 4.5. IRM unmixing and thermal demagnetization of three-component IRMs (OAS) 37
Figure 4.6. Field and frequency variations and Hysteresis loop results (OAS) 38
Figure 4.7. Variations in anisotropy of magnetic susceptibility parameters at OAS 39
Figure 4.8. Pj vs. χ_m and T vs. Pj for the various localities at OAS 40
Figure 4.9. Magnetic fabric from the frontal thrust ramp at Sassotetto, Monastero and Infernaccio 41
Figure 4.10. Magnetic fabric from the oblique thrust ramp at Boragine 43
Figure 4.11. Magnetic fabric from the oblique thrust ramp at Vallescura 44
Figure 4.12. Anisotropy of magnetic remanence (ARM) experiments (OAS) 46
Figure 4.13. Para- and ferro-magnetic subfabrics for representative samples, classified after stages (OAS) 48
Figure 4.14. Summary of magnetic fabric stages and comparison with structural data (OAS) 50
Figure 4.15. Ternary diagrams relating structural and AMS data at OAS 51
Figure 4.16. Ternary diagrams relating structural and anisotropy of magnetic remanence data at OAS 54

Figure 5.1. Structural sketch map of the Northern Apennines (SVU sector) 57
Figure 5.2. Structural data and sites position at Gova 59
Figure 5.3. Structural data and sites position at Vidiciato sector 60
Figure 5.4. Thermomagnetic susceptibility curves and IRM acquisition and backfield curves (SVU – Gova) 61
Figure 5.5. IRM acquisition and backfield curves (SVU – Vidiciatico) 62

Figure 5.6. IRM unmixing and thermal demagnetization of three-component IRMs at Gova 63
Figure 5.7. IRM unmixing and thermal demagnetization of three-component IRMs at Vidiciatico 64
Figure 5.8. Field and frequency variations and Hysteresis loop results (SVU) 65
Figure 5.9. Representatives low-temperature experiments from the Gova Sector 67
Figure 5.10. Representatives low-temperature experiments from the Vidiciatico Sector 68
Figure 5.11. Stepwise thermomagnetic susceptibility curves from the Gova Sector 69
Figure 5.12. Stepwise thermomagnetic susceptibility curves from the Vidiciatico Sector 70
Figure 5.13. Hysterisis loops after stepwise thermal treatment 71
Figure 5.14. SEM-EDS analysis 73
Figure 5.15. Variations in anisotropy of magnetic susceptibility parameters from the Gova Tectonic window 74
Figure 5.16. Variations in anisotropy of magnetic susceptibility parameters from Vidiciatico 75
Figure 5.17. Magnetic fabric from the footwall and Transect 1, Gova Tectonic window 77
Figure 5.18. Magnetic fabric from Transect 2 and 3, Gova tectonic window 78
Figure 5.19. Distribution of the AMS patterns from the Gova Tectonic window 80
Figure 5.20. Magnetic fabric from Transect 1 and 2, Vidiciatico sector 81
Figure 5.21. Magnetic fabric from Transect 3, Vidiciatico sector 82
Figure 5.22. Distribution of the AMS subfabrics from the Vidiciatico sector 84
Figure 5.23. Anisotropy of magnetic remanence (ARM) experiments at Gova 86
Figure 5.24. Anisotropy of magnetic remanence (ARM) experiments at Vidiciatico 87
Figure 5.25. Para- and ferro-magnetic subfabrics for representative samples, classified after patterns (SVU) 89
Figure 5.26. Ternary diagrams relating structural and magnetic fabrics (AMS and AARM) at Gova 91
Figure 5.27. Ternary diagrams relating structural and magnetic fabrics (AMS and AARM) at Vidiciatico 92

Figure 6.1. Structural sketch map and geological cross section across the Northern Apennines 103
Figure 6.2. Simplified geological-structural map (ELAW) 104
Figure 6.3. Close up view of the structures of the different chaotic rock units 106
Figure 6.4. Summary of the structural data (ELAW). 108
Figure 6.5. Thermomagnetic susceptibility curves and IRM acquisition and backfield curves (ELAW) 110
Figure 6.6. IRM unmixing and thermal demagnetization of three-component IRMs (ELAW) 111
Figure 6.7. Field and frequency variations and Hysteresis loop results (ELAW) 112
Figure 6.8. Variations in anisotropy of magnetic susceptibility parameters at ELAW 113
Figure 6.9. Plots of K_m, Pj, and T versus distance from the main thrust faults 114
Figure 6.10. Magnetic fabric of broken formation and tectonic mélange 115
Figure 6.11. Tectonic fabric of tectonic mélange 117
Figure 6.12. Magnetic fabric of sedimentary (SMé1) and polygenetic (PMé1) mélange 119
Figure 6.13. Anisotropy of magnetic remanence (ARM) experiments (ELAW) 120
Figure 6.14. Para- and ferro-magnetic subfabrics for representative samples, classified after stages (ELAW) 121
Figure 6.15. Conceptual 3D stratigraphic column and summary of magnetic fabric at ELAW (Part I) 124
Figure 6.16. Conceptual 3D stratigraphic column and summary of magnetic fabric at ELAW (Part II) 126
Figure 6.17. Ternary diagrams relating structural and magnetic fabrics (AMS and AARM) at ELAW 127

Figure 7.1. Summary of the main AMS findings..... 132
Figure 7.2. AMS results across the Japan Trench and Nankai Trough (Muroto and Ashizuri transect) 134
Figure 7.3. AMS results across the Kumano transect, Nankai Trough**.**..... 136
Figure 7.4. Magnetic fabric results observed across the Hikurangi subduction margin 137
Figure 7.5. AMS results at the Central America Trench/Costa Rica subduction margin 138
Figure 7.6. Distribution of magnetic fabric in analogue model of fold-and-thrust belt and thrust imbricate 140
Figure 7.7. Para- and ferro-magnetic subfabrics for representative S-C intersection and shear-related fabrics... 142
Figure 7.8. Comparison of magnetic mineralogy between study areas and different lithological units 144

APPENDIX **- Supplementary Figures**

Figure 4.S 1. Pj variation among AMS and ARM experiments, at OAS..... 149
Figure 4.S 2. T variation among AMS and ARM experiments, at OAS..... 149

Figure 5.S 1. Distribution of the magnetic mineral assemblages at SVU – Gova Tectonic window..... 150
Figure 5.S 2. Distribution of the magnetic mineral assemblages at SVU – Vidiciatico sector 151
Figure 5.S 3. Hysterisis loops (raw data) after stepwise thermal treatment at progressive increased T_{max}..... 152
Figure 5.S 4. Pj variation among AMS and ARM experiments at SVU – Gova Tectonic window. 157
Figure 5.S 5. T variation among AMS and ARM experiments at SVU – Gova Tectonic window. 158
Figure 5.S 6. Pj variation among AMS and ARM experiments at SVU – Vidiciatico sector..... 159
Figure 5.S 7. T variation among AMS and ARM experiments at SVU – Vidiciatico sector. 160

Figure 6.S 1. Pj variation among AMS and ARM experiments at ELAW 163
Figure 6.S 2. T variation among AMS and ARM experiments at ELAW. 163

Chapter 1

INTRODUCTION

This chapter addresses the main research questions explored in this thesis. The rationale behind and the structure of the thesis is also given. This thesis summarises my original work and include previously published materials. The performed work and the outcomes are reported in the following chapters.

1.1 Thesis Rationale

In active convergent margins, intraplate shear zones at shallow depth, including megathrusts, are known to display a variety of fault slip behaviours (Peng & Gomberg, 2010; Fagereng et al., 2014; Saffer & Wallace, 2015). The continuous spectrum of slip styles spans from great thrust earthquakes (GEQs) and stable sliding (i.e., aseismic creep), including slow slip events (SSEs), low-frequency earthquakes (LFEs), and tremors (Dragert et al., 2001; Obara, 2002; Ide et al., 2007; Obara & Kato, 2016; Araki et al., 2017). The seismogenic zone typically extends from 3-4 km to 15-20 km depth depending on the thermal gradient (Hyndman, 1997; Scholz et al., 2019). Thermal modelling of modern seismogenic megathrusts suggests the location of the seismogenic zone in a temperature range between 100-150 °C and 350-450 °C (Hyndman et al., 1997; Oleskevich et al., 1999; Moore & Saffer, 2001; Moore et al., 2007).

Over the past decades, geodetic and seismic monitoring, and scientific ocean drilling (i.e., Ocean Drilling Program, ODP; International Ocean Discovery Program, IODP) along modern convergent margins have extensively investigated the conditions and physical processes influencing the slip events in the seismogenic zone at shallow depth (Sagiya, 2004; Okada et al., 2004; Saffer & Tobin, 2011; Chester et al., 2013; Fagereng et al., 2019).

Plate boundaries are complex and highly deformed zones showing structures from both distributed and localized deformation (Collot et al., 2011; Sibson, 2013). Depending on the heterogeneity of the rock assemblage (i.e., competent vs. incompetent materials and/or clay contents) within the shear zone and the strain rates, shearing can be localized along discrete faults during seismic slip, whereas aseismic slip produces a scaly fabric associated with distributed deformation (Fagereng & Sibson, 2010; Kirkpatrick et al., 2015; Meneghini et al., 2020). Lithological heterogeneities have proven to strongly influence frictional properties, degree of shear localization and slip weakening mechanisms, controlling the seismic behaviour (Rice & Coco, 2007; Bullock et al., 2014; Kirkpatrick et al., 2015). Indeed, siliciclastic and clay-rich sediments deform by cataclasis, whereas carbonate-rich sediments undergo pressure-solution (e.g., stylolitization) (Leoni et al., 2007; Leah et al., 2020). Differences in the deformation mechanism have

significant implications for the rheological behaviour, resulting in variations of slip behaviour along shallow convergent margin subduction shear zones (Leah et al., 2020).

However, in modern convergent margin settings, the internal architecture of shear zones is difficult to observe. Seismic reflection surveys have a low spatial resolution, which is not sufficient to detect the structural features (size of meters to tens of meters) within the fault zones. Moreover, scientific ocean drilling is challenging in this context and core data are punctual, lacking the 3D control essential to constrain the structural heterogeneities of convergent margin shear zones.

Several meso-to-map scale structural studies have successfully investigated exhumed intraplate shear zones on-land, documenting spatial heterogeneities in the material inputs and cyclical variation of tectonic stresses and fluid pressure (Cowan, 1985; Leoni et al., 2007; Meneghini et al., 2007, 2020; Vannucchi et al., 2008; Festa et al., 2012, 2022; Kimura et al., 2012; Fagereng et al., 2014; Dielforder et al., 2015; Mittempergher et al., 2018; Ogawa, 2019; Cerchiari et al., 2020). Studies of exhumed analogue have the opportunity to directly investigate the 3D characteristics of convergent margin shear zones, providing key insights into mechanisms of deformation of convergent margins in the P-T conditions where modern EQs occur.

The research and application of analytical methods, which can be applied to both modern and ancient fault zones, is of primary importance for understanding the physical processes involved in the nucleation and behaviour of megathrust faults and constraining models built from modern convergent margins.

As magnetic minerals are sensitive to stress regime and fluid-rock interactions, the investigation of the magnetic properties of rocks can be an effective tool in studying faulting processes at intraplate shear zones (Yang et al., 2020). Particularly, the magnetic fabric of deformed rocks has been widely used to describe progressive deformation in different tectonic regimes, both experimentally and theoretically (e.g., Graham, 1966; Borradaile & Henry, 1997; Hrouda & Ježek, 1999; Borradaile & Hamilton, 2004; Weil & Yonkee, 2009; Ferré et al., 2014; Parés, 2015; Almqvist & Koyi, 2018; Hrouda & Chadima, 2020; Schöfish et al., 2021). Indeed, in both modern and exhumed subduction thrust faults, rock magnetic studies have successfully provided important information on kinematics, fluid circulation and strain distribution. So far, relatively few studies have targeted brittle shear zones in the shallow portion of convergent margins and the relationships between heterogeneous materials and the magnetic signature still needed an explanation.

1.2 Thesis Objectives

The main purpose of this thesis is to gain a wider understanding of how the rock magnetic signature reflects faulting processes in convergent margin shear zones developed at shallow depth, where brittle deformation is dominant.

To achieve this goal, I here focus on three exhumed analogues of present-day convergent margin shear zones located in the Northern Apennine (Italy) (**Figure 1.1a**), where the internal structural architecture is well known at multiscale through field data (geological map and structural and stratigraphic analyses): (i) The

Sestola-Vidiciatico Tectonic Unit (SVU), interpreted as the basal décollement of an exhumed analogue of actual intraplate brittle shear zones at shallow depths (Remitti et al., 2007; Vannucchi et al., 2008); (ii) The Olevano-Antrodoco-Sibillini (OAS) thrust, which represents an exhumed out-of-sequence thrust system (Cipollari & Cosentino, 1995; Ghisetti & Vezzani, 1997); (iii) The out-of-sequence thrust system of the exhumed outer part of the External Ligurian accretionary wedge (ELAW) (Codegone et al., 2012; Festa et al., 2020). The selected case studies show specific structural position within the accretionary complex (**Figure 1.1b**). Different inputs materials (e.g., clay- and/or carbonate-rich sediments) are involved, allowing the investigation of possible causal relationship between lithological variation and strain partitioning/localization.

Key objective is to investigate the correlation between magnetic fabric and both structural heterogeneities and strain distribution (i.e., localized vs. distributed deformation). Here, to improve the understanding of spatial and temporal variation of the strain, I have explored the significance of magnetic fabric (low-field anisotropy of magnetic susceptibility - AMS) by making comparisons with the mesoscale structural fabric associated with the dominant deformation mechanisms that occur during faulting.

In this framework, I further investigate the statistical processing of AMS data which is essential to define the statistical significance of data when deformation is heterogeneous. Statistical treatment may be useful to enquire about the presence of subfabric related to different tectonic events. This is of particular importance for discern the origins (i.e., sedimentary, tectonic and/or polygenetic) of highly heterogeneous materials, as mélanges and broken formations, which commonly occur along convergent margin shear zones. Here, as a secondary outcome, the discrimination of representative magnetic fabrics can help to refine analytical criteria to be combined with well constrained meso-structural characterization, improving the recognition of chaotic rock units where deformation is not clearly visible.

Another significant objective is to outline the variations in the magnetic fabric depending on the different lithology involved in the subduction or thrusting stage. Thus, I have investigated the preferred orientation of paramagnetic minerals and iron oxides, which can unravel multiple deformation events. This approach may help in testing the different sensitivity of subpopulations of grains (e.g., different mineralogy and grain size) in recording the deformation mechanisms that operate during faulting.

An important aspect is also the variations in magnetic mineralogy across shear zones in order to consider possible spatial and temporal changes in physicochemical conditions during faulting. Variations in magnetic mineral assemblages may provide insights into the complex evolution of megathrust faults, from the partial preservation of the diagenetic signature to the fluid-related processes (e.g., alteration, leaching and neoformation of minerals) during seismic cycles. The characterization of the magnetic mineralogy is also essential to understand the source of the magnetic fabric.

Lastly, to better constraints models built from modern convergent margins, a comparison with data from active megathrust shear zones was also investigated. This may support the modelling of the internal architecture of modern subduction settings, and the related control on seismic behaviour and natural hazards.

1.3 Thesis Outlines

This thesis is divided into seven chapters. After this short introduction, Chapter 2 synthesizes the relevant pervious knowledge on magnetic properties of fault rocks. The chapter begins with early studies of magnetic fabric in deformed rocks and then moves on to recent advances and applications to active convergent margins, as well as numerical and analogue modelling.

Chapter 3 gives a general description of the applied methodology. Details are provided on magnetic sub-fabric separations, statistical analysis of AMS data and magnetic mineralogy experiments performed to characterize the magnetic signature of fault rocks. This chapter also describes the approaches used to compare magnetic and mesoscale structural fabric.

In the next three chapters, I reported my findings from the different convergent margin shear zones. Each case study is reported in separate chapters based on differences in sediment composition, maximum temperature, prevailing deformation mechanism and related variations in the meso-structural fabric (**Figure 1.1**):

Chapter 4 reports my results from the OAS thrust. Here, I investigated the magnetic properties of carbonate-rich sediments showing brittle to ductile deformation with solution and diffusion-dominated processes. Particular emphasis was given to characterize the magnetic fabric in tectonites showing different facies associated with variable degree of simple to pure shear (**Figure 1.1c**).

Chapter 5 explores heterogeneities in magnetic properties and their anisotropy across an exhumed intraplate shear zone (the SVU - **Figure 1.1d**). This chapter addresses the changes in the magnetic fabric of deformed marls and clay-rich units as deformation evolves from diffuse soft-sediment deformation to discontinuous brittle deformation. Evidence of the circulation of different fluids during the seismic cycle has been reported from the SVU (Cerchiari et al., 2020). Hence, further characterization of the magnetic signature to investigate fluid-rock interaction is included in this chapter.

Chapter 6 reports the results obtained from the out-of-sequence thrust system of the exhumed outer part of ELAW, which involve different type of chaotic rock units (i.e., mélanges and broken formations - **Figure 1.1e**). This chapter deals with the comparison between magnetic fabric and mesoscale structural investigations of non-metamorphic tectonic, sedimentary, and polygenetic mélanges. Here, I evaluate the use of rock magnetic studies as a diagnostic tool suitable to analytically distinguish the contribution of different mélange forming-processes and their mutual superposition.

Finally, Chapter 7 discusses the main findings in the broader contexts of exhumed and modern convergent margins. Results are compared with pre-existing data from present-day equivalents (IODP data) to outline and explain similarities and differences. Then, a summary and discussion of the results in a broader context of brittle shear-zones is provided, with particular focus on the influence of lithological heterogeneities on the magnetic fabric record of faulting processes. Suggestions for future research are also outlined.

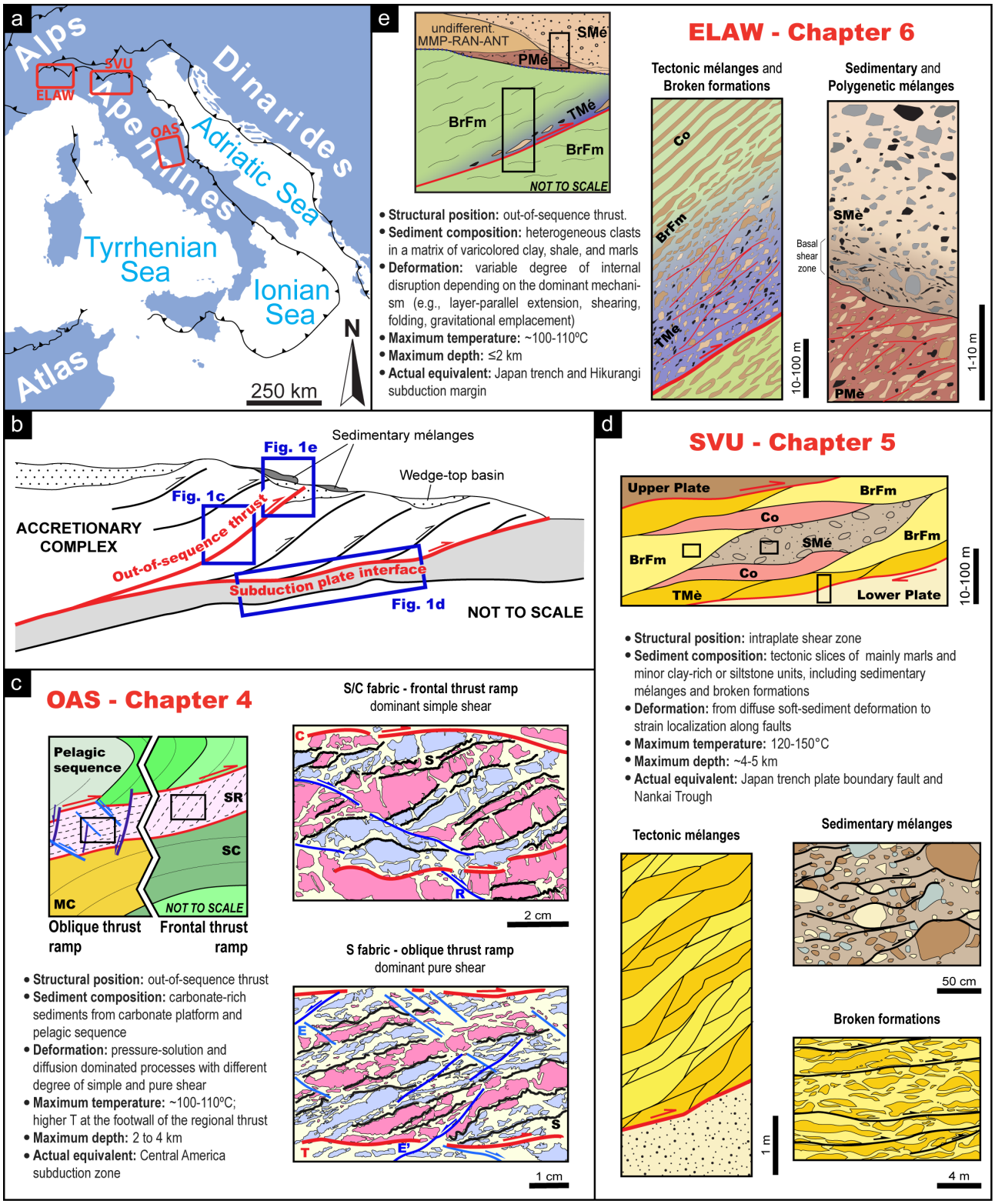

Figure 1.1. (**a**) Location of the case studies in Northern Apennines, Italy. (**b**) Structural position of the studied convergent margin shear zones within an accretionary complex (modified from Robustelli Test et al., 2019). Sketch of the different mesoscale structural fabrics and summary of lithological variations and deformation condition are reported for: (**c**) the OAS (see Chapter 4 for details) (modified from Calamita et al., 2012); (**d**) the SVU (Chapter 5) (modified from Pini, 1999; Festa et al., 2022).; (e) the ELAW (Chapter 6) (modified from Robustelli Test et al., 2019).

Chapter 2

MAGNETIC FABRIC & ROCK MAGNETISM IN SHEAR ZONES: A brief overview

Magnetic properties of rocks have been widely used to provide insights into the kinematics, strain distribution, and physicochemical processes occurring in fault zones in compressional regimes. This chapter is aimed at providing a summary of advances in magnetic studies of shear zones. The focus is on magnetic fabric and properties of deformed sedimentary materials, which are the main input of intraplate convergent margin shear zones and megathrusts at shallow depth.

Magnetic properties of shear zones are related to changes in regional to local strain and faulting-related processes (e.g., fluid-rock interactions and/or frictional heating). Rock magnetic techniques allow to unravel transformations of magnetic properties induced by faulting processes such as variations in magnetic mineral grain-size due to grain fining and changes in mineral concentration related to neoformation or dissolution of specific phases driven by fluid circulation (Yang et al., 2020 and references therein). Major changes are associated to strain effects that can induce reorientation of magnetic minerals and changes in remanence or bulk susceptibility intensities (Jackson et al., 1993). Therefore, the application of rock magnetic and, in particular, magnetic fabric studies are documented to be a very powerful tool to unravel essential aspects of the complex and heterogeneous evolution of convergent margin shear zones. Nowadays, in fact, the anisotropy of magnetic susceptibility (AMS) is a routine measurement used as a petrofabric indicator to assess subtle variations in the preferred orientation of mineral grains in rock samples and provide insights into the origin or history of progressive deformation of rocks.

The possibility to use the AMS as a petrofabric tool was first proposed by Graham (1954). The advent of this application emerged after Graham's (1966) masterpiece that related changes in the orientation of the principal magnetic susceptibility axes to increasing compressive deformation in sedimentary rocks of the Appalachian Mountains (**Figure 2.1a**). Indeed, he observed that the initial flat-lying sedimentary fabric progressively evolved toward a final deformational stage in which the minimum (k_{min} or k_3) and maximum (k_{max} or k_1) axes of the magnetic anisotropy become parallel to the directions of compression and extension, respectively (**Figure 2.1a**). He also observed changes in the shape of the magnetic ellipsoid, from initially oblate to triaxial at an intermediate state, and finally oblate again at the last deformation stage. Changes were interpreted in term of reorientation of ferromagnetic grains under plastic condition during the early stages of layer-parallel shortening (LPS), when the sediments were still unlithified. Attempting to understand

anomalous natural remanent magnetization (NRM) in pyrrhotite-dominated Welsh slates, Fuller (1960, 1963) observed similar relationships between principal susceptibility axes and macroscopic cleavage (**Figure 2.1b**).

Subsequently, several researchers explored the possibility of using AMS measurements to estimate the finite strain on a local and/or regional scale. Empirical studies investigated the existing relationships between AMS and finite strain in terms of both axis orientation and magnitude on low-grade metamorphic mudstones, slates (e.g., Kneen, 1976; Wood et al., 1976; Hrouda, 1976, 1979; Kligfield et al., 1981, 1983; Borradaile & Tarling, 1981; Rathore & Henry, 1982; Rochette & Vialon, 1984; Parés et al., 1999), sandstones (Kligfield et al., 1977; Clendenen et al., 1988; Hirt et al., 1988), and limestones (Kligfield et al, 1982), comparing AMS with tectonic structures and finite strain inferred from field or microstructural elements. AMS-strain correlations have also been studied through mathematical modelling (e.g., Hrouda, 1987, 1993; Benn, 1994; Hrouda & Ježek, 1999; Ježek & Hrouda, 2000, 2002; Humber et al., 2014) and experimental deformation of analogues in laboratory (e.g., Borradaile & Alford, 1987, 1988; Borradaile & Puumala, 1989; Almqvist & Koyi, 2018; Till et al., 2012; Schöfisch et al., 2021, 2022). Overall, good agreement between principal magnetic susceptibility axes and structural elements has been observed in nature, with k_{min} typically subparallel with the pole of the cleavage and k_{max} either parallel to mineral lineation and stretched objects (e.g., consistent with the maximum extension direction - **Figure 2.1c, e**; Rathore, 1979; Kligfield et al., 1977, 1982; Rathore & Henry, 1982) or to the bedding-cleavage intersection (**Figure 2.1e-g**; Hrouda, 1976; Borradaile & Tarling, 1981; Rochette & Vialon, 1984). Locally, a quantitative correlation between AMS and strain has been established (**Figure 2.1c-d**; Kligfield et al., 1982; Clendenen et al., 1988; Hirt et al., 1988). Nevertheless, quantitative relationships are complicated by magnetic mineralogy, mechanical behaviour, non-coaxial deformation history and partial preservation of primary fabric (Borradaile, 1987; Housen et al., 1993; Borradaile & Henry, 1997; Larrasoaña et al., 1997; Borradaile & Jackson, 2004). No universal law can be extrapolated due to the presence of subfabric related to different stage of deformation, subpopulation of minerals and/or grain-size that can interfere with each other generating complex and heterogeneous composite fabrics (Rochette & Vialon, 1984; Hounslow, 1985; Lüneburg et al., 1999; Borradaile & Jackson, 2004, 2010). For example, the bedding-cleavage intersection fabric (**Figure 2.1 e-g**), which is one of the most frequent fabric in compressional settings, represents the superposition of two orthogonal subfabrics such as depositional plane and stylolite cleavage for pressure dissolution (Borradaile & Tarling, 1981; Rochette & Vialon, 1984; Borradaile, 1988). The resulting composite fabric leads to a k_{max} subparallel to meso- to micro-scale folds axes (Hrouda, 1976; Borradaile & Brown, 1987; Mattei et al., 1995) which does not represent the maximum extensional axis, but remarks the internal petrofabric (**Figure 2.1 g**; Rochette & Vialon, 1984; Lüneburg et al., 1999; Borradaile & Henry, 1997; Borradaile & Jackson, 2004, 2010). In deformed mudrocks, pencil structure reveals a composite fabric that can influence the interpretation of the AMS in terms of strain. In fact, the k_{max} remarks the long axis of the structural elements while the pole of the magnetic foliation still preserves the original bedding orientation (**Figure 2.2a**; Parés & van der Pluijm, 2003).

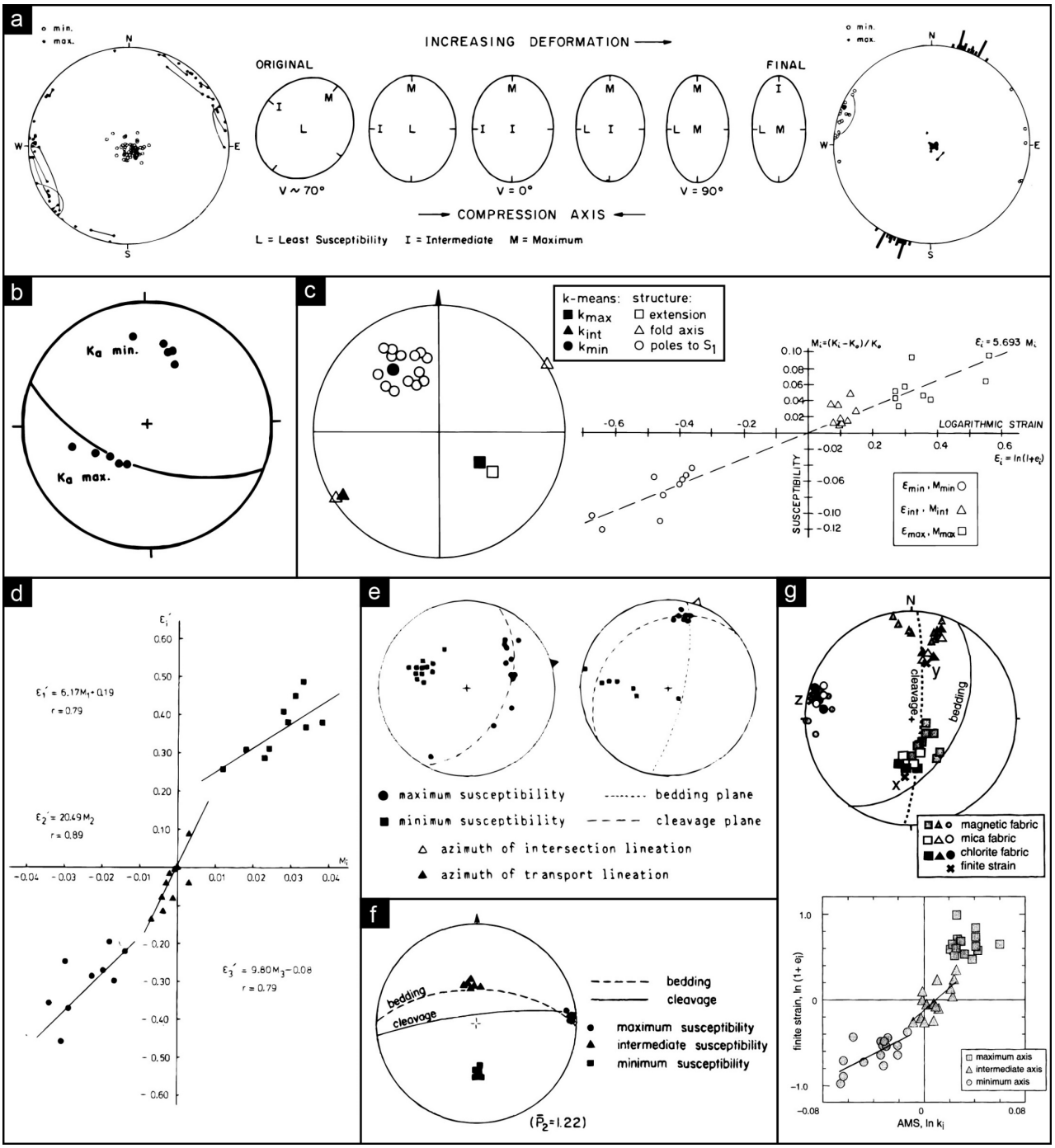

Figure 2.1. (**a**) Main observations and interpretation provided by Graham (1966). Changes in anisotropy of magnetic susceptibility (AMS) axes orientation and shape from a flat-lying undeformed sedimentary fabric (on the left) to a greater deformed fabric (on the right). Flattened and prolate ellipsoids show a V angle equal to 90° and 0°, respectively. (**b**) Direction of the principal susceptibility axes of pyrrhotite-dominated Welsh slates (Fuller, 1963). The magnetic foliation is sub-parallel to the cleavage plane. (**c**) Comparison between the principal AMS directions and the structural elements. Linear correlation between normalized principal magnetic susceptibilities M_i, and logarithmic principal strain ε_i inferred from mesoscopic strain elements (modified from Kligfield et al., 1982). (**d**) Correlation of finite strain derived from the microstructure with each AMS axes separately (Hirt et al., 1988). (**e**) Comparison between AMS and structural elements for tectonic and intersection lineation fabrics (Rochette & Vialon, 1984). (**f**) Bedding-cleavage intersection fabric (Borradaile & Tarling, 1981); (**g**) Comparison of principal direction of mica, chlorite, and magnetic fabric with the finite strain. Correlation between finite strain and AMS ellipsoids are reported as linear regressions between set of axes. K_{max} does not show significant correlation with finite strain (Lüneburg et al., 1999).

Composite fabric showing magnetic lineation (k_{max}) perpendicular to the shortening direction can be observed in normal faults reactivated in compressional regimes (Oliva-Urcia et al., 2013; Izquierdo-Llavall et al., 2013; García-Lasanta et al., 2018). The magnetic foliation can show different orientation between bedding and cleavage depending on structural position (i.e., proximity to the basal thrust), deformation intensity, and relative orientation of the extension and compression stages (Oliva-Urcia et al., 2013; Izquierdo-Llavall et al., 2013). The occurrence of composite fabric and mostly the reorientation of the magnetic lineation in deformed rocks result in a delicate balance between magnitude and orientation of the primary or previous fabrics and the applied strain (Housen et al., 1993; Parés & van der Pluijm, 2002). When shortening is < 20-30%, the initial fabric is still preserved and a direct correlation between AMS and strain cannot be established (Borradaile, 1991; Borradaile & Henry, 1997). In addition, for shortening > 75%, the maximum anisotropy related to the intrinsic properties of the minerals is reached, and again no quantitative correlation can be made (Borradaile & Tarling, 1981; Borradaile & Henry, 1997). In the intermediate window we can expect good correlation, but we must always consider the influence of lithology, mineralogy, and deformation mechanisms (Borradaile & Tarling, 1981; Mattei et al., 1995). However, AMS measurements reflect the arrangement of minerals and thus its use as a petrofabric and kinematic indicator is powerful, but the identification of composite fabrics is essential to have reliable semi-quantitatively structural interpretations (Housen et al., 1993).

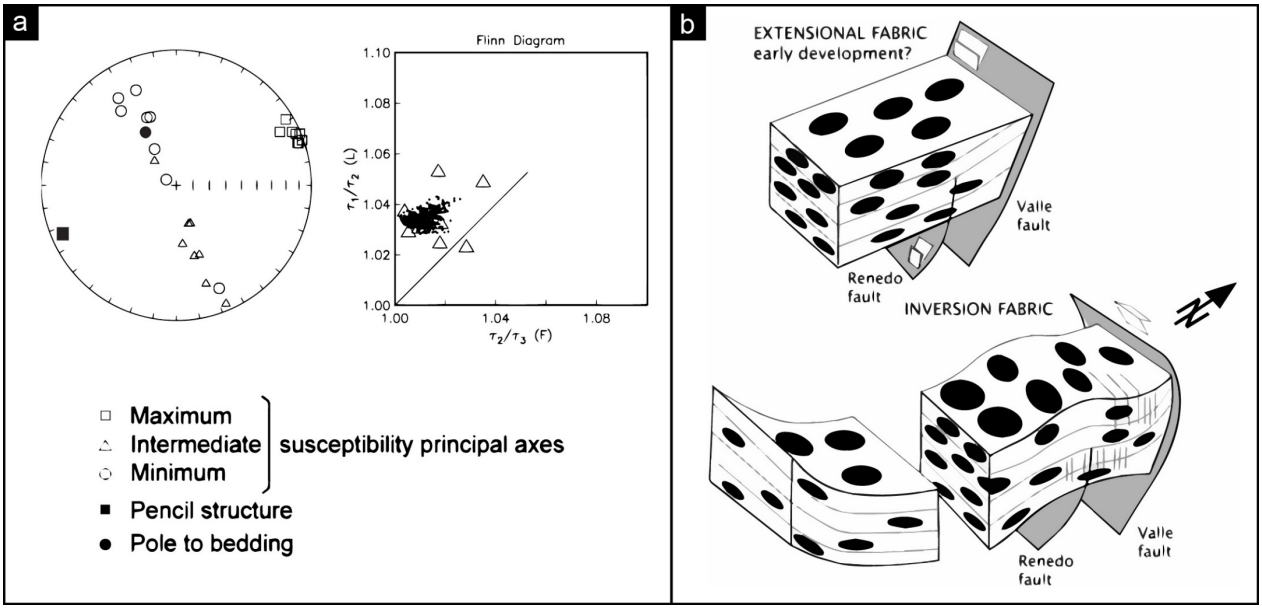

Figure 2.2. Representative examples of composite fabrics in (**a**) mudrocks showing pencil structures (Parès & van der Pluijm, 2003) and (**b**) inversion tectonic of previous sedimentary or extensional fabric (Oliva-Urcia et al., 2013).

Therefore, it is essential to know the potential initial sedimentary fabric and its progressive evolution prior to involvement in convergent margin shear zones. At the front of accretionary prisms and in foreland basins, sediments can undergo initial LPS with progressive modification of the bedding-parallel sedimentary magnetic fabric (Kissel et al. 1986; Averbuch et al. 1992; Sagnotti & Speranza 1993; Mattei et al. 1995; Parés & van der Pluijm, 2004). As deformation increases, a series of composite fabrics form depending on the relative contribution of sedimentary and tectonic petrofabric (**Figure 2.3a-b, d**; Parés et al. 1999; Cifelli

et al., 2009, 2015; Weil & Yonkee, 2009, 2012). Diffuse deformation can be recorded after deposition, even when sediments appear homogeneous and undeformed at outcrop scale (Sagnotti & Speranza, 1993; Cifelli et al., 2005, 2009). The k_{max} clusters in the bedding plane parallel to the intersection between bedding and an incipient LPS fabric (i.e., perpendicular to the shortening direction; **Figure 2.3b**) due to pore space closure through progressive rotation, micro-folding, intergranular slip and intragranular kinking of phyllosilicates (Mattei et al., 1995, 1997; Housen et al., 1993; Parés et al, 1999; Cifelli et al., 2004, 2005; Larrasoaña et al., 2004). These processes are significantly powerful in poorly consolidated sediments due to fluid expulsion and anisotropic volume loss during compaction (Borradaile & Jackson, 2004). The different degree of k_{max} clustering depend on possible attenuation of the compressional stress due to rock hardening and compaction (Mattei et al., 1995; Sagnotti et al., 1999). Increasing ductile deformation disrupt the original sedimentary fabric with the development of a second mechanical weakness and progressive rotation of k_{min} toward the pole of the cleavage and/or to the local shortening direction, while the magnetic lineation remains parallel to the bedding-cleavage intersection (**Figure 2.3b**; Parés et al, 1999; Hirt et al., 2004; Weil & Yonkee, 2009, 2012). At that stage, the AMS principal axes become consistent with structural elements associated with the compressional regime (e.g., cleavage, folds axis, thrust fronts), allowing for distinction from an original sedimentary fabric (Kissel et al., 1986; Mattei et al., 1997). Changes in AMS axes orientations are associated with an initial decrease in anisotropy degree together with a change of the AMS ellipsoids into prolate shape (**Figure 2.3c**). Then, when the sediments undergo ductile deformation with cleavage development, the magnetic lineation locally reorients parallel to the stretching direction in the foliation plane, the anisotropy degree steadily increases and the ellipsoid becomes oblate again (**Figure 2.3c, d**; Parés et al., 1999; Parés & van der Pluijm, 2004; Weil & Yonkee, 2009; Cifelli et al., 2015; Hrouda & Chadima, 2020). The described trend is the most frequent observed in fold-and-thrust belts throughout the world, but local variations in disagreement with this evolution has been observed and associated with variations in lithology, and in the mechanisms and intensity of deformation (Larrasoaña et al., 2004).

Within accretionary prisms, the orientation of AMS axes commonly reflects the LPS related to regional stress, with trench-parallel magnetic lineation and minimum axes of susceptibility consistent with the shortening direction (**Figure 2.4a**; e.g., Housen & Kanamatsu, 2003; Kitamura et al., 2010; Yang et al., 2013). The amount of fabric reorientation associated with regional non-coaxial strain depends on the intensity of the primary fabric and its progressive deformation. According to the entity of the horizontal shortening, the magnetic foliation increases in dip angle (Humbert et al., 2014; Kanamatsu et al., 2012). In fact, the k_{min} axes show a fan-like distribution that reflects the progressive reorientation of grains occurred during offscraping, frontal accretion and partial underplating (Chadima et al., 2006; Yamamoto, 2006; Hrouda et al., 2009). Those variations can be associated to advanced exposure to tectonic stresses as strain localization close to thrust and megasplay fault zones (~15-25% of shortening; Humbert et al., 2014). Competition between LPS and thrusting-related shear fabrics typically occur in fold-thrust structure with well-developed shear fabric localized only along the thrust plane (**Figure 2.4b**; Averbuch et al., 1992).

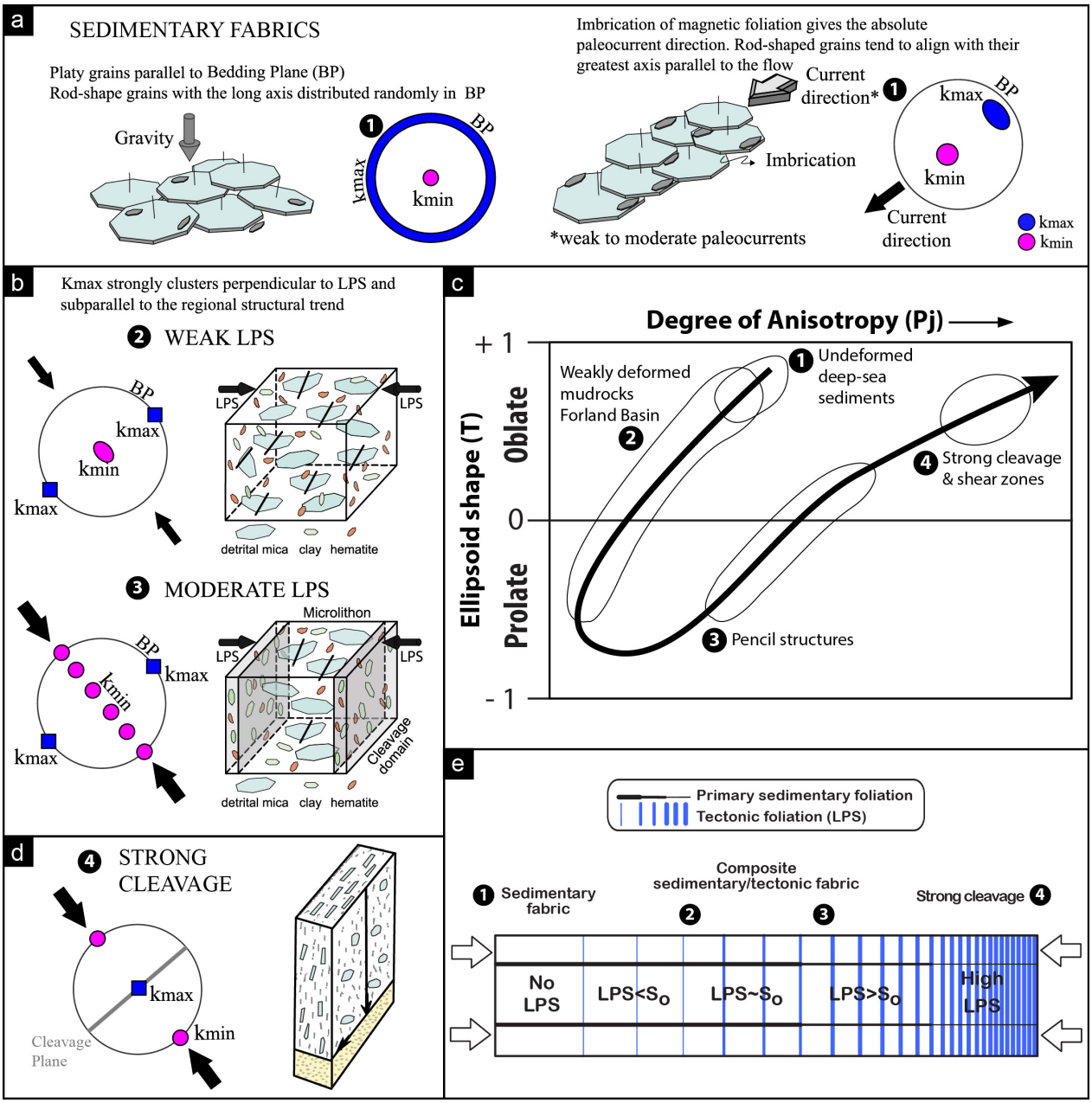

Figure 2.3. (**a**) Distribution of grains and AMS fabric in undeformed sediments (Cifelli et al., 2015). Deposition related to gravity-driven processes (on the left) and under weak currents (on the right). (**b**) Composite magnetic fabrics and block diagrams showing the petrofabric developed during early stages of LPS (modified from Ciffelli et al., 2015; Weil & Yonkee, 2012). (**c**) Changes of magnetic fabric scalar parameters (T and Pj) with increasing strain in mudrocks (Parés & van der Pluijm, 2004). (**d**) Magnetic fabric and petrofabric of strongly deformed sediments (Hrouda & Chadima, 2020). (**e**) Sketch showing the relative proportion of sedimentary versus tectonic foliation depending on the progressive increase of LPS (Weil & Yonkee, 2009).

In contrast, the strain state in the footwall is mostly dominated by vertical loading/compaction (e.g., Owens, 1993; Housen & Kanamatsu, 2003; Yang et al., 2013). Initial underplating can also induce changes in magnetic fabric in the uppermost portion of the underplating sediments (tens to hundreds of meters close to the décollement) due to diffuse or heterogeneous shearing, producing partial clustering of k_{max} in the direction of the plate convergence (**Figure 2.4c**; Ujiie et al., 2000; Housen & Kanamatsu, 2003). Abrupt changes in the magnetic fabric across fault zones indicate strain decoupling between hanging wall and footwall, mainly associated with mechanical decoupling due to fluid overpressure in the décollement zone

(**Figure 2.4a**; Housen et al., 1996; Ujiie et al., 2003; Yang et al., 2013; Greve et al., 2020). In contrast, more gradual changes in the fabric occur when the décollement zone is stronger than surrounding sediments (Housen & Kanamatsu, 2003).

Approaching the fault planes and damage zones, the pre-faulting magnetic fabric is gradually obliterated producing changes in AMS shape and axis orientation. The latter deviates from the regional strain field toward directions consistent with the local strain acquired during the past earthquakes (Levi et al., 2014; Braun et al., 2015). In this case, the AMS fabric tracks the local inhomogeneity of inelastic strain at the meters scale around the fault plane, helping to define shape and extent of the damage zone (**Figure 2.4c**; Levi et al., 2014). Moreover, a progressive deflection of the magnetic foliation approaching the fault planes can provide good approximation of the sense of shear (Borradaile et al., 1989; Rathore & Becke, 1980).

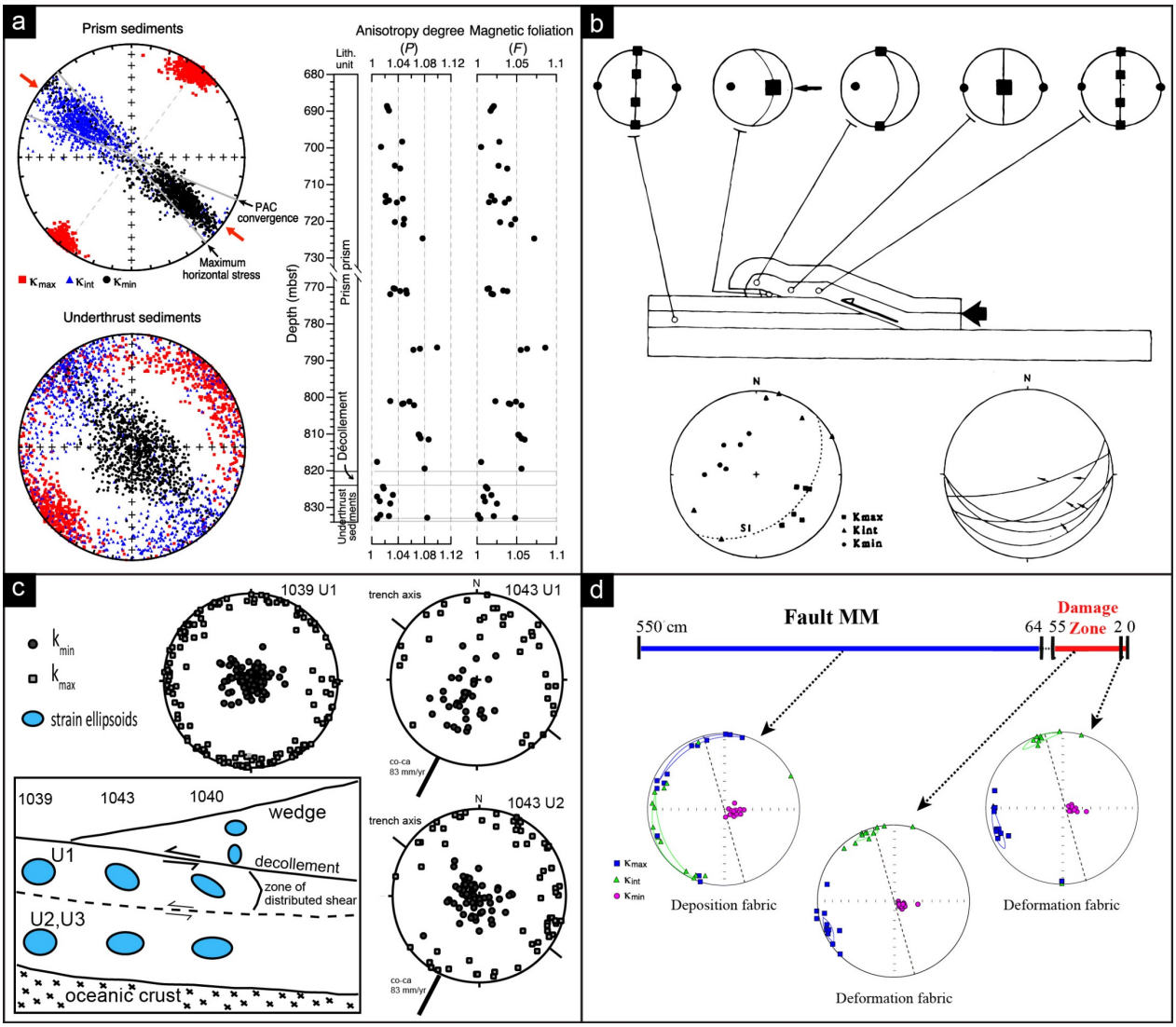

Figure 2.4. (**a**) Magnetic fabric from prism and underthrust sediments in the Japan Trench along with down-core anisotropy degree (P) and magnetic foliation (F) (Yang et al., 2013; 2020). (**b**) Synthetic evolution of the magnetic fabric in thrust-sheets. Representative magnetic fabric and fault measurements close to the basal décollement are also reported (Averbuch et al., 1992). (**c**) Cartoon showing changes in deformation recorded in the Costa Rica subduction margin along with the magnetic fabric from the underthrust sequence (Housen & Kanamatsu, 2003). (**d**) Magnetic fabric variations at progressively shorter distances from a fault plane (Levi et al., 2014).

Within convergent margin shear zones, heterogeneity in the magnetic fabric is often observed. For example, a random orientation of AMS axes is found when shearing is not transmitted inside the brecciated fragments (**Figure 2.5a**; Ujiie et al., 2003). The magnetic fabric of less pervasively deformed portions may be consistent with the sedimentary or transitional fabric of the underthrusting sediments (**Figure 2.5b**; Greve et al., 2020). In case of low degree of deformation, the magnetic foliation can be parallel to the mesoscopic foliation (S plane) and at a high angle to the shear plane (C plane; **Figure 2.5c**; Casas-Sainz et al., 2017; Román-Berdiel et al., 2019) or at an intermediate position (**Figure 2.5d**; Aranguren et al., 1996). The magnetic lineation tends to be orthogonal to the transport direction, revealing local preservation of previous fabrics (Marcén et al., 2018). The magnetic lineation can also show an oblique orientation that can represent either a combination of fabric (e.g., LPS and simple shear) or complex strain related to the occurrence of a lateral slip component (Chou et al., 2020).

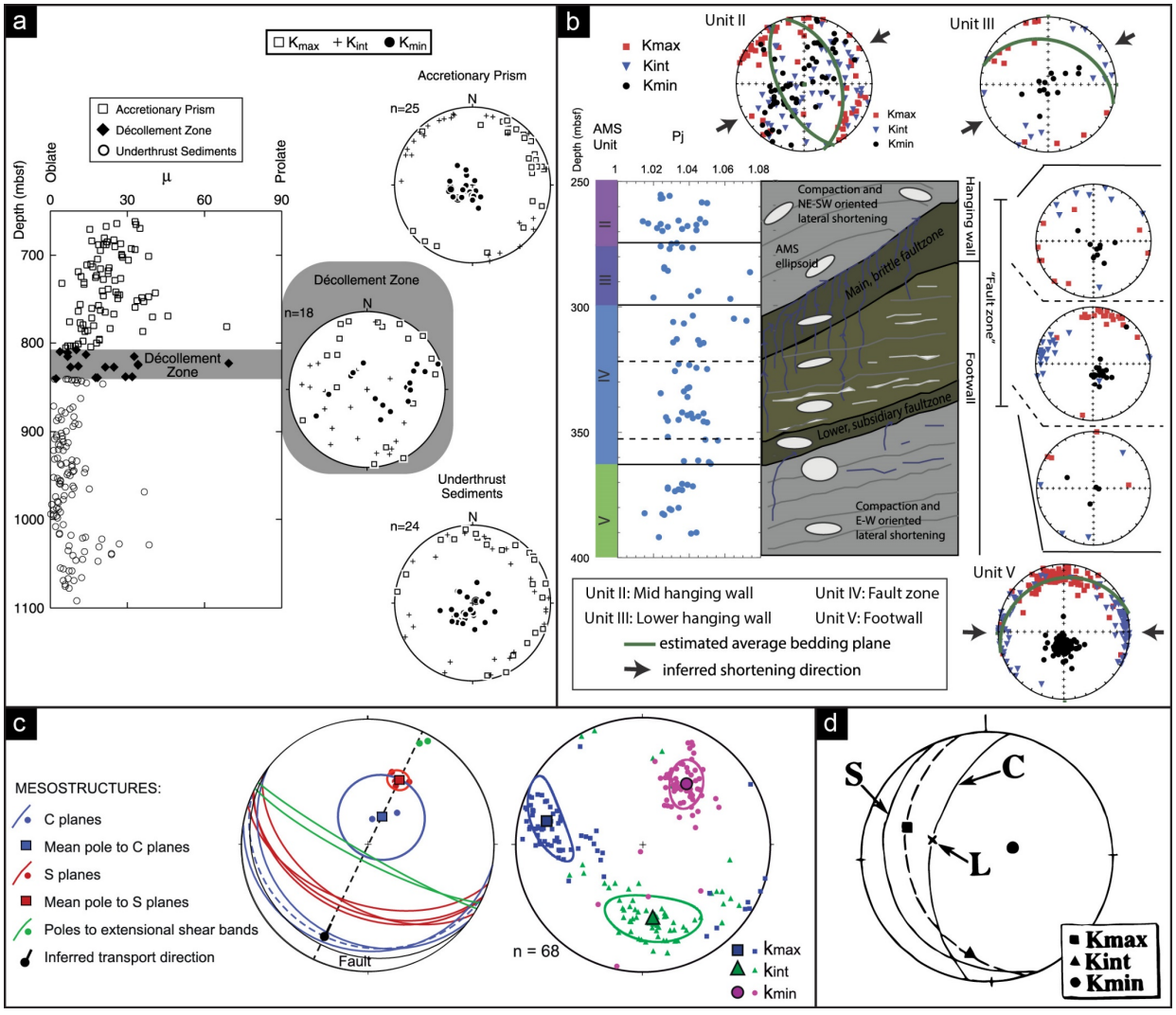

Figure 2.5. (**a**) Changes in shape parameter and AMS fabric of the lower Shikoku Basin (Ujiie et al., 2003). The décollement zone shows random orientation of AMS axes. (**b**) Variations in anisotropy degree and magnetic fabric across a subduction thrust fault (Greve et al., 2020). Same fabric as in the footwall is locally preserved within the fault zone. (**c**) Comparison between structural and magnetic fabrics in an intraplate fault zone. Note the good agreement between magnetic foliation and S planes, while k_{max} is orthogonal to the transport direction (Casas-Sainz et al., 2018). (**d**) Magnetic fabric of S-C mylonites showing magnetic foliation at an intermediate position between S and C planes (Aranguren et al., 1996).

Indeed, laboratory analogues reveal that pre-deformation fabrics are difficult to overprint and strongly influence the development of a shear related fabric, giving sometimes unreliable kinematic indicator (Borradaile, 1988; Borradaile & Alford, 1988). At least 20% of shortening is necessary to rotate the AMS axes to be consistent with those of the non-coaxial strain (Borradaile & Alford, 1987). In well-developed shear-fabric, the magnetic foliation tends to align with the shear plane, and k_{max} can be either parallel or perpendicular to the transport direction (**Figure 2.6a**; Casas-Sainz et al., 2017, 2018; Román-Berdiel et al., 2019; Satolli et al., 2020; Ujiie et al., 2000). Different orientations of magnetic lineation were also observed in mélanges due to changes in the stress conditions with increasing depth along the subduction plate boundary (**Figure 2.6b**; Ujiie et al., 2000; Kitamura & Kimura, 2012). At shallower depths, the magnetic lineation orthogonal to the shear direction has been associated with a dominant pure shear component compared to the simple shear (Ujiie et al., 2000; Kitamura & Kimura, 2012; Yamamoto et al., 2012). This stress component is almost overcome with depth, where a shear-parallel fabric dominates, suggesting a higher degree of simple shear (Ujiie et al., 2000; Kitamura et al., 2005; Kitamura & Kimura, 2012). In fact, at high degree of non-coaxial strain, as in regional scale shear zones and mylonites, magnetic lineation commonly agrees with the stretching direction (**Figure 2.6c**; Goldstein, 1980; Rathore & Becke, 1980; Housen et al., 1995). A similar evolution of fabrics has been observed in laboratory experiments simulating progressive shear as occurring in the margins of accretionary prisms and thrust sheets. The experiments reveal the progressive rotation of grains (and k_{max}) to aligns toward the shear direction and the parallelism between magnetic foliation and shear plane (**Figure 2.6d**; Borradaile & Puumala, 1989; Till et al., 2012).

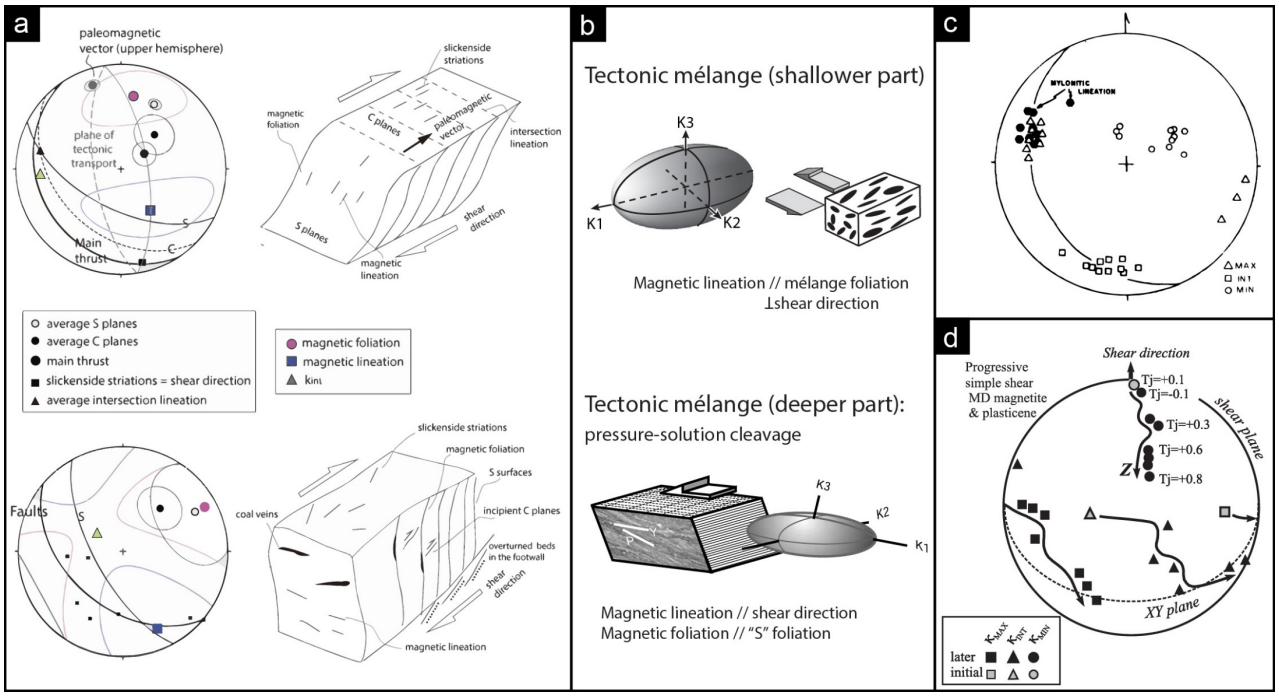

Figure 2.6. (**a**) Structural and AMS data of shear-related magnetic fabric showing a double tendency of the magnetic lineation to be parallel or orthogonal to the transport direction (Casas-Sainz et al., 2017). Conceptual sketches show the orientation of the kinematic indicators. (**b**) Geometric relationships between AMS axes and structural elements in tectonic mélanges at different depths (Kitamura et al., 2005; Yamamoto et al., 2012). (**c**) Magnetic fabric of mylonite characterized by k_{max} parallel to the structural lineation (Goldstein, 1980). (**d**) Evolution of the magnetic fabric during an incremental simple shear deformation experiment (Borradaile & Puumala, 1989; Borradaile & Jackson, 2010).

Variations in fabric are commonly associated with changes in anisotropy degree (Pj) and shape parameter (T). Commonly, Pj increases within a shear zone or with increasing strain by approaching a shear plane (**Figure 2.5a-b**; e.g., Borradaile et al., 1989; Levi & Weinberger, 2011; Marcén et al., 2018; Kusbach et al., 2019). Experiments of simple shear deformation show a rapid increase in the anisotropy degree associated with oblate magnetic fabric during the development of a shear-related fabrics (**Figure 2.7a**; Till et al., 2012). In contrast, when deformation is predominantly accommodated by brittle structures, Pj can also decrease within the damage zone due to a minor ductile reorientation of minerals (Housen & Kanamatsu, 2003; Averbuch et al., 1992). In fact, a dominant brittle deformation is associated to high-fluid pressure coupled with unlithified sediments which can retard the propagation of the ductile strain, producing lower Pj (Housen et al., 1996). The shape of the AMS ellipsoid can become more oblate (Kusbach et al., 2019) or prolate (Braun et al., 2015) depending on the deformation mechanism and lithological control.

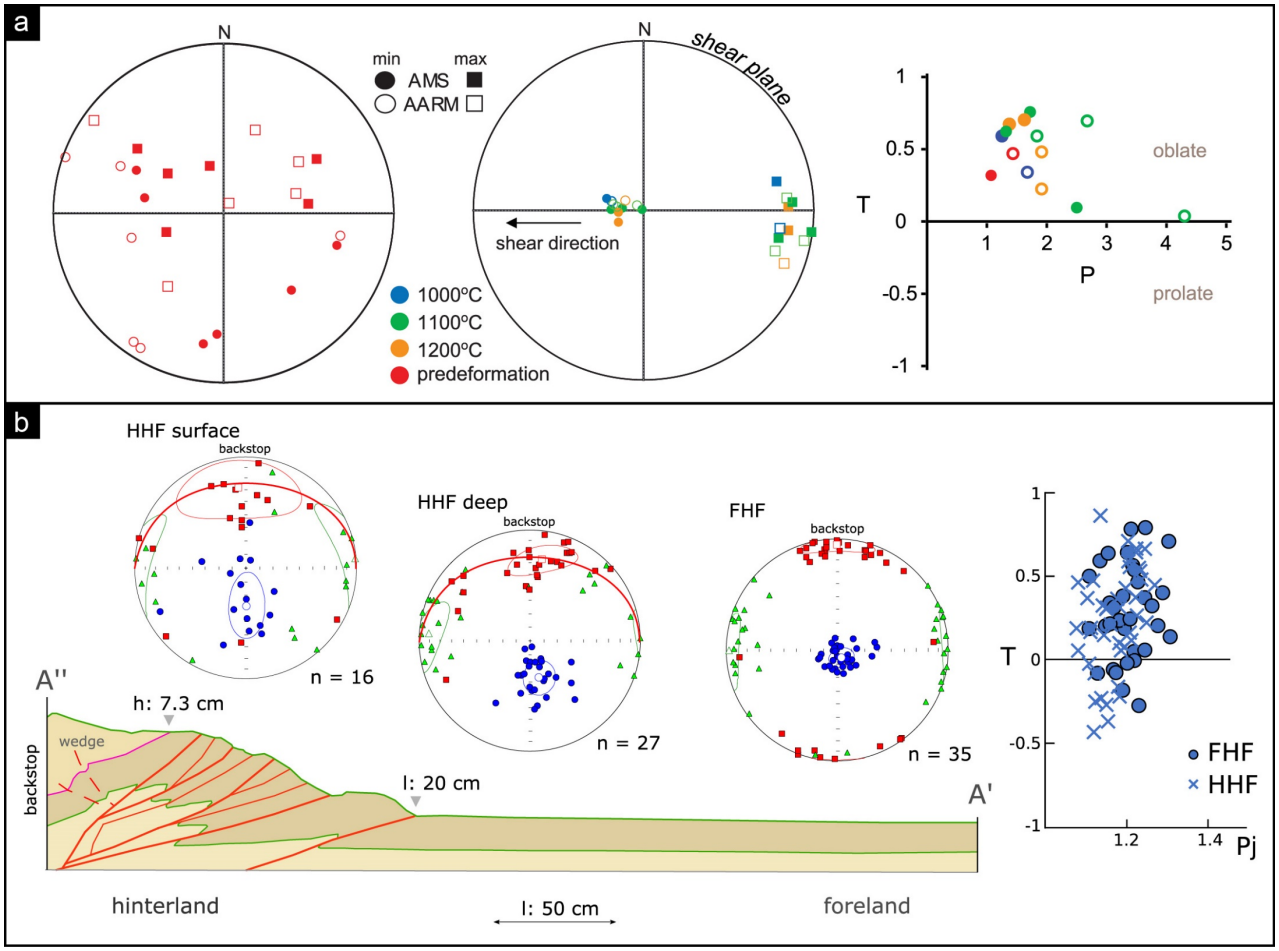

Figure 2.7. (**a**) Evolution of the magnetic fabric and relative scalar parameter in an experimental shear zone (Till et al., 2012). (**b**) Distribution of the magnetic fabric along the different portion of a modelled fold-and-thrust belt resulting from a high friction experiment (Schöfisch et al., 2021). The shortening direction is N-S oriented. Variation of Pj and T are also reported.

The heterogeneous evolution of the magnetic fabric during the development of imbricated thrust structures has been tentatively modelled in laboratory experiments simulating different friction rates along the décollement (Schöfisch et al., 2021, 2022). Only at high-friction rate the magnetic fabric records dominant simple shear with a k_{max} rotating toward the direction of shear and the magnetic foliation parallel to the thrust

surface (**Figure 2.7b**). In contrast, in experiments at low-friction rate, the magnetic fabric is more heterogeneous, showing both intersection lineation and cleavage-related fabrics in different proportions depending on deformation intensity, strain localization and proximity to the thrust surface (Schöfisch et al., 2021, 2022).

Moreover, heterogeneous magnetic fabrics can result from the coexistence of magnetic subfabrics associated with different modal mineral composition, grain-size, deformation intensity, and strain partitioning (Borradaile, 1988; Evans et al., 2003; Pueyo Anchuela et al., 2010, 2012; Kusbach et al., 2019; Román-Berdiel et al., 2019). In fact, the mineralogical carriers of the AMS, both paramagnetic and ferromagnetic minerals, may form at different deformation stages and respond differently to the deformation mechanisms (e.g., Borradaile & Alford, 1988; Ferré et al., 2004; Martín-Hernández & Ferré, 2007). Therefore, along and across faults and shear zones, paramagnetic and ferromagnetic minerals can show similar or different evolution. If ferromagnetic minerals are detrital in origin, they may rotate rigidly during repeated slip events, simultaneously with the matrix, leading to the same tectonic information of the AMS and remarking the local strain field (**Figure 2.8a**; Sagnotti et al., 1998; Braun et al., 2015; Casas-Sainz et al., 2017). In other cases, the ferromagnetic minerals of detrital origin can preserve the original sedimentary fabric (**Figure 2.8b**; Levi et al., 2014). By contrast, other authors observed magnetic lineation consistent with the transport direction for ferromagnetic subfabric, while the paramagnetic subfabric shows a k_{max} perpendicular to the shear direction or compressional strain placed parallel to the bedding cleavage intersection (**Figure 2.8c**; Aubourg et al., 1995; Sagnotti et al., 1998; Oliva-Urcia et al., 2009; Román-Berdiel et al., 2019).

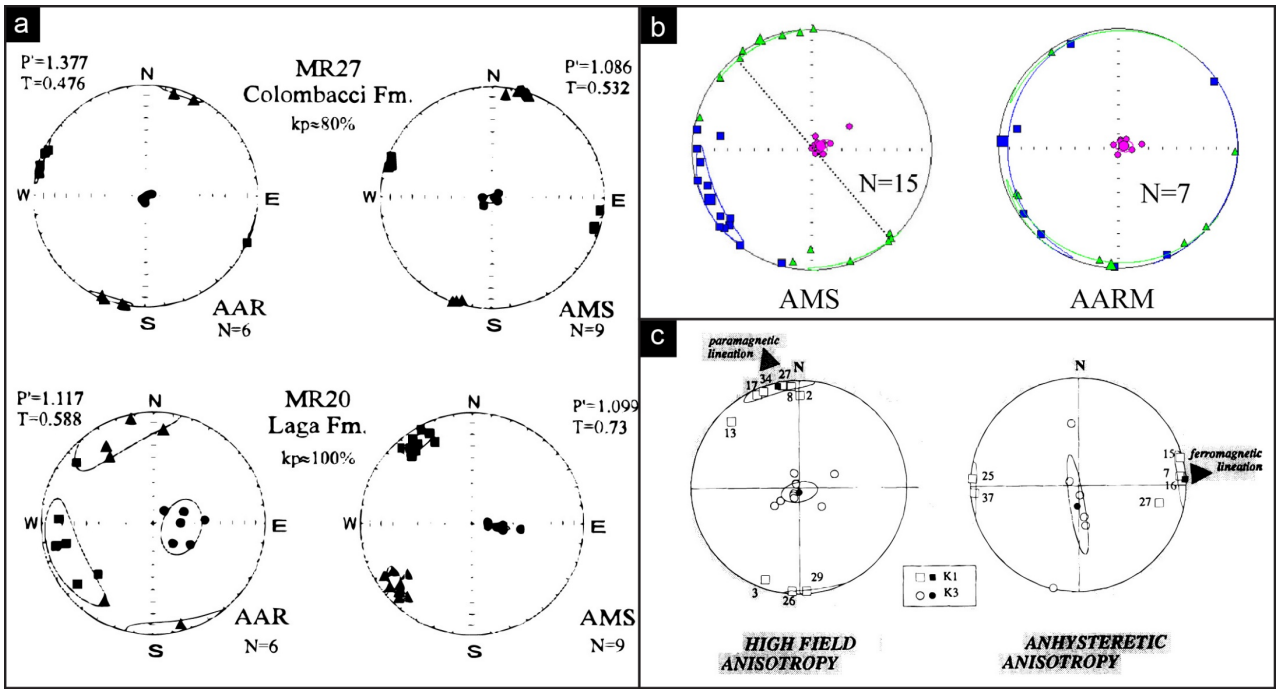

Figure 2.8. Comparisons between AMS and anisotropy of anhysteretic remanent magnetization (AARM) subfabrics. (**a**) AMS and AARM show the same orientation (Sagnotti et al., 1998). (**b**) AMS reveals a deformation/tectonic fabric while AARM preserves a sedimentary fabric (Levi et al., 2014). (**c**) Para- and ferromagnetic subfabrics recording different deformation stages (Aubourg et al., 1995).

In fact, ferromagnetic minerals might register the last deformation event while AMS remarks sedimentary or previous deformation processes, suggesting a more efficient reorientation of ferromagnetic minerals under certain conditions (Jackson, 1991; Mattei et al., 1997; Hrouda et al., 2018). Variations may also be associated with the difference response to deformation by planar and granular ferromagnetic minerals, which can give intersection or shear-related lineation, respectively (Román-Berdiel et al., 2019). In addition, the grain-size of ferromagnetic minerals can affect their efficiency in responding to an external stress. For example, larger grains (activated in lower coercivity windows) can show a higher degree of preferred orientation, as they can rearrange their orientation upon direct contact with the matrix (**Figure 2.9a**; Jackson et al., 1989). In contrast, finer particles located within the pore may remain free to move for a certain period without being forced to align under the effect of an external stress. Remanence-bearing minerals having different grain-size can acquire a fabric during different deformation steps (**Figure 2.9b**; Aubourg & Robion, 2002). Ferromagnetic minerals can also show isotropic fabric, suggesting no specific alignment within the matrix or that their content is significantly low to affect the total AMS fabric (**Figure 2.9c**; Nakamura & Borradaile, 2001; Pueyo-Anchuela et al., 2010; Issachar et al., 2015).

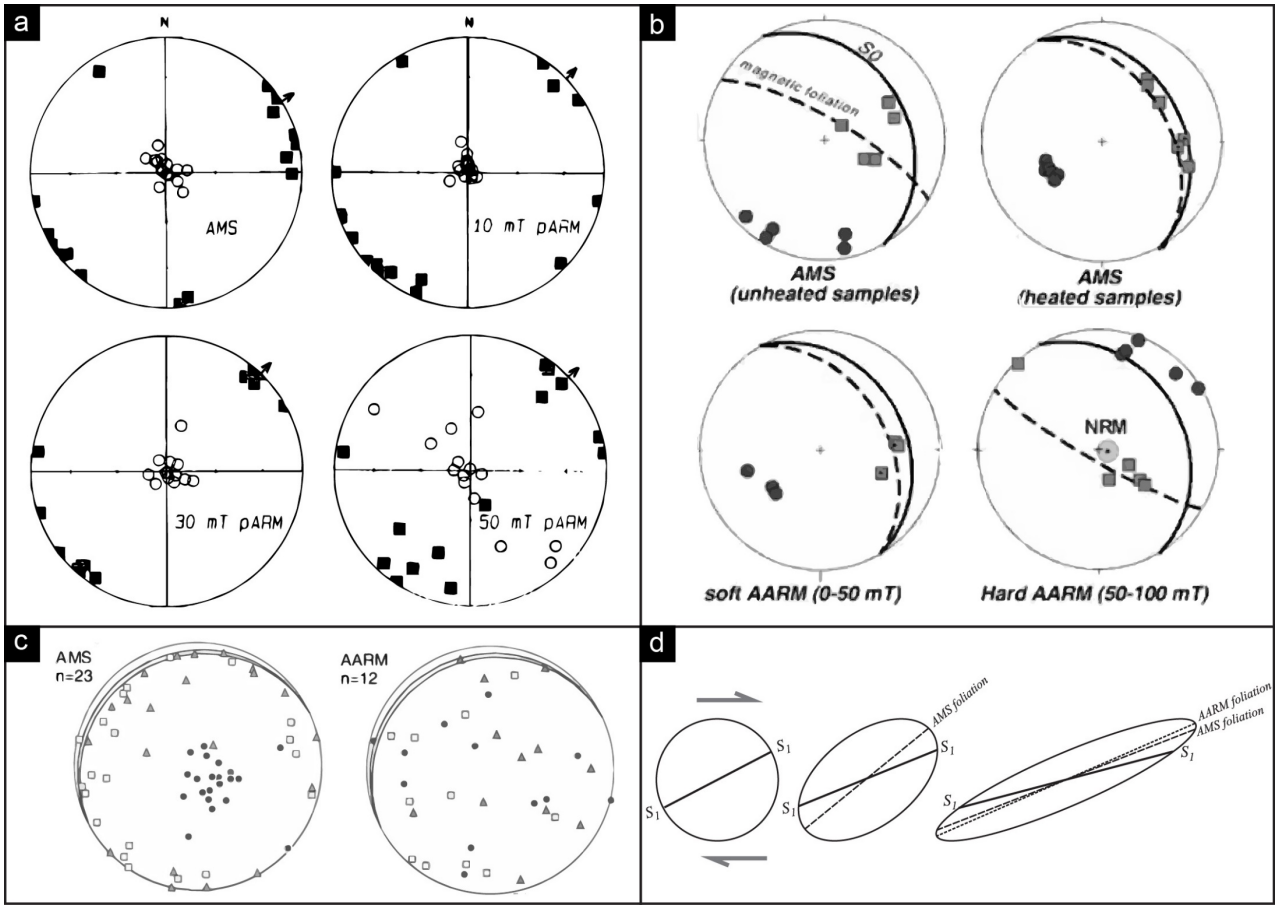

Figure 2.9. (**a**) Different clustering of k_{max} depending on the grain-size and coercivity of magnetic minerals (Jackson et al., 1989) (**b**) Distinct registration of the deformation stages by paramagnetic minerals and subpopulations of ferromagnetic grains (Aubourg & Robion, 2002) (**c**) Isotropic ferromagnetic fabric not affecting the total AMS (Pueyo-Anchuela et al., 2010). (**d**) Differential development of AMS and AARM fabrics at different steps during progressive non-coaxial deformation (Borradaile & Jackson, 2010).

The ferromagnetic subfabric can also show interchanged principal axes than the AMS revealing the presence of inverse fabric or abnormal/intermediate fabric (Aubourg et al., 1995, 1999; Rochette et al., 1992; Pueyo-Anchuela et al., 2012; Tokiwa & Yamamoto, 2012). Discrepancy between AMS and anisotropy of anhysteretic remanent magnetization (AARM) foliation with the cleavage plane can be used as petrofabric shear indicators to unravel non-coaxial strain history and/or distinguish between coaxial and non-coaxial deformation (**Figure 2.9d**; Borradaile & Henry, 1997; Ferré et al., 2004).

Moreover, the magnetic fabric heterogeneity also depends on lithology and/or fluid-rock interactions and associated alteration or neoformation of ferromagnetic minerals (e.g., Casas-Sainz et al., 2017; Román-Berdiel et al., 2019). Indeed, in sediments and clay units, the formation of new mineral by changes in redox conditions or fluid circulation (e.g., iron sulfides or iron oxides) may modify the magnetic fabric (Mattei et al., 1997). Separation of ferromagnetic subfabrics can also unravel the preferred orientation of newly formed minerals associated with seismic frictional heating (Yang et al., 2020). Therefore, characterization of magnetic mineralogy across shear zones is essential to better constrain the deformation history and unveil possible faulting-related processes.

Localized and intense shearing can induce grain fining and mechanical reduction of ferromagnetic particles from multidomain to single domain (SD) or even superparamagnetic particles (SP), producing increased susceptibility (Chou et al., 2014; Yang et al., 2020). Frictional heating during seismic slip might also generate high susceptibility and remanence intensity due to the formation of magnetite by thermal decomposition of siderite and clay minerals (**Figure 2.10**a; Yang et al., 2012; Mishima et al., 2009). Rock magnetic analysis also enables to define the peak temperature due to the frictional heating (Yang et al., 2012; Yang et al., 2016). The interaction between fault rock and circulating fluid during the seismic cycle with the precipitation of Fe-bearing minerals in fault breccias, leading to relative enrichment with respect to the wall rocks and thus increased susceptibility (**Figure 2.10b**; Tanikawa et al., 2008; Chou et al., 2012; Yang et al., 2013; Yang et al., 2020). For example, interaction with coseismic fluids can induce the decomposition of pyrite to pyrrhotite and/or siderite to magnetite (Tanikawa et al., 2008; Chou et al., 2012; Yang et al., 2018). Subsequent cooling of hot coseismic fluids can also result in goethite enrichment (Chou et al., 2012). In contrast, decreased susceptibility and magnetization intensity was also observed approaching fault-zones, suggesting magnetite depletion and incorporation of the Fe^{2+} into Fe-rich clay minerals (**Figure 2.10c**; Yang et al., 2016). Lower values of rock magnetic proxies of mineral concentrations and grain-sizes might also be induced by anaerobic methane oxidation during drainage of fluids, resulting in the reduction of greigite to paramagnetic pyrite (Greve et al., 2021).

Finally, frictional heating and the neoformation of ferromagnetic minerals could produce a new chemical remanent component and/or induce thermal remagnetization, making fault zones possible magnetic recorders of seismic events (**Figure 2.10d**; Chou et al., 2012; Yang et al., 2020).

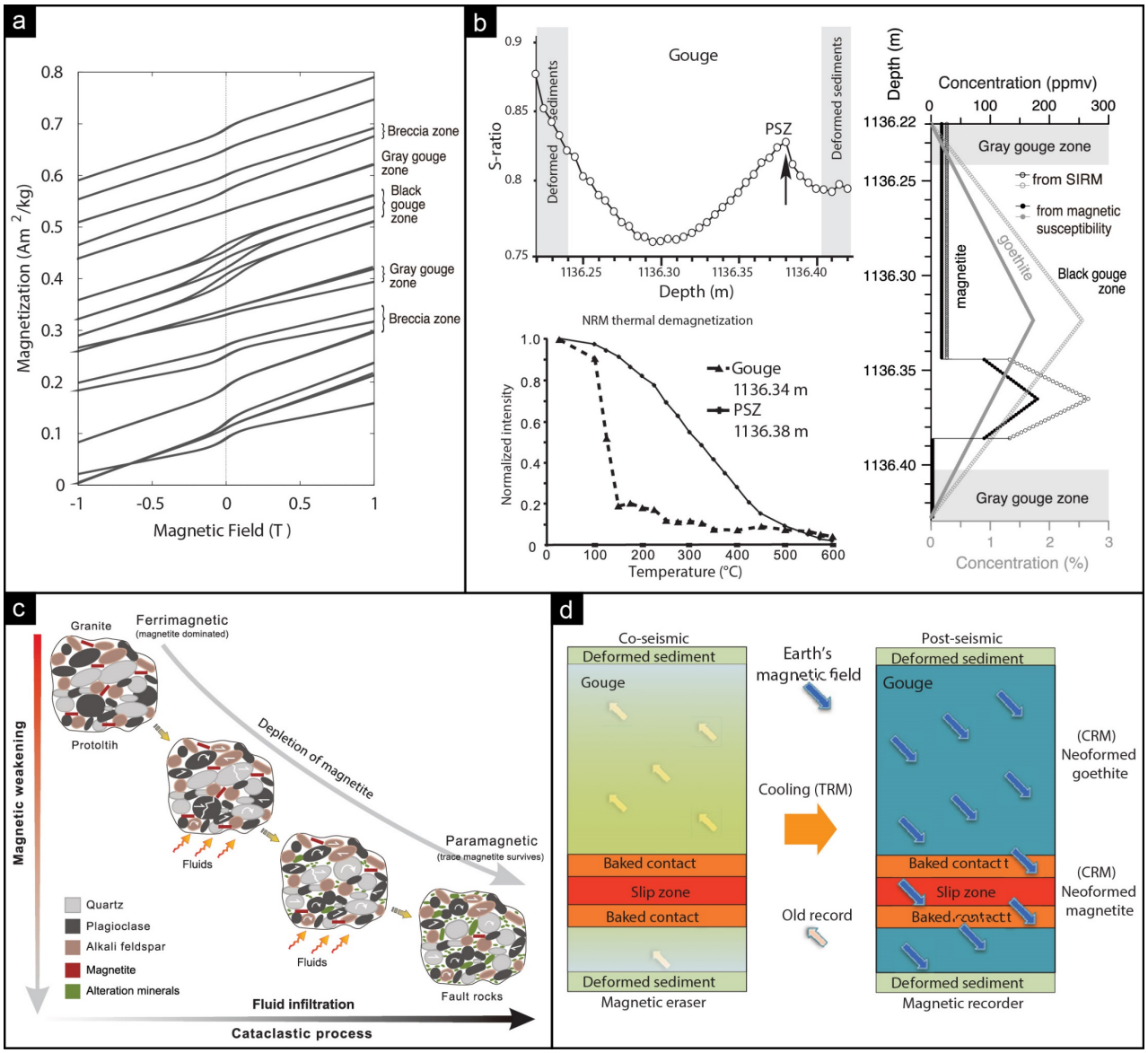

Figure 2.10. (**a**) Hysteresis loops showing dominant low-coercivity component (e.g., magnetite) in the Black gouge in contrast to the dominant paramagnetic behaviour of the Gray gouge, Breccia zone and wall rocks (Mishima et al., 2009) (**b**) Data revealing the occurrence of goethite in the Black gouge with magnetite enrichment along the principal slip zone (PSZ; Chou et al., 2012; Yang et al., 2020). (**c**) Conceptual sketch of depletion of magnetite to paramagnetic clay minerals due to fluid-rock interaction (Yang et al., 2016). (**d**) Remagnetization process in the fault gouge during the seismic cycle (Chou et al., 2012).

Chapter 3

METHODOLOGY

Magnetic minerals are sensitive to changes in the stress regime and physicochemical conditions in fault zones. Magnetic fabric studies are excellent tools to investigate the deformation path in shear zones, even detecting incipient deformation well before other strain indicators. Moreover, magnetic mineralogy characterizations can provide information on thermal and fluid circulation history. Nevertheless, the analysis of magnetic properties is only occasionally included in studies of fault rocks. This Chapter provides an overview of the methodology applied in this thesis to investigate the rock magnetic signature of faults rocks. Details are given on the experimental conditions/parameters, and data processing approaches used. The content of this Chapter integrates the methodology published in Robustelli Test & Zanella, 2021. The main findings from the selected case studies are reported in the following chapters.

3.1 Sampling strategy

The objective of this work is to detect existing variations in the rock magnetic signature of fault rocks and to understand their link to faulting processes. Since convergent margin shear zones are complex and heterogeneous, high-density sampling close to the main tectonic structures is required to have a reliable estimate of the deformation path and faulting-associated mineralogical changes. Sampling was performed at progressively increasing distance from the main thrust planes, depending upon the structural complexity and lithological changes. Multiple sites 50 cm–1 m thick were samples at each locality, showing no significant variations of the deformation pattern at the mesoscale. Efforts were made to select homogeneous sites in terms of pervasiveness of tectonic structures and deformation intensity. The sampling scheme and specimen preparation were adapted to lithological variation and intensity of deformation, as well as outcrop conditions: (i) in hard rocks, as lithified sandstones, we took at least 3 oriented hand-samples. Blocks were drilled to obtain standard cylindrical specimens (Φ = 25 mm, h = 23 mm); (ii) In highly deformed mudstones and carbonatic rocks, it was impossible to drill and prepare standard cylindrical specimens. We oriented small lithons of 5-20 cm size. To obtain significant statistical analysis, at least 8–12 hand-samples were collected at each site. Lithons were thus cut into cubes, mostly equidimensional, preserving the sample orientation.

From each block several specimens were prepared at the laboratory. After weighing, specimens were fixed and centered in standard 8cc plastic cubes with non-magnetic plasticine; (iii) For heterogeneous chaotic (block-in-matrix) units, as broken formation and mélanges, we took oriented hand-samples from the matrix. Specimens were prepared by pressing standard plastic non-magnetic cubes into the wet oriented hand-samples.

3.2 Magnetic mineralogy investigation

Rock magnetic experiments were performed on selected specimens for assessing the ferromagnetic phases and possible mineralogical variations across the shear zones. Thermomagnetic susceptibility (χ–T) curves were measured using a MFK2-FA system equipped with a CS4 furnace. Samples were heated up to 700 °C in argon with a heating rate of 11 °C/min, and then cooled to room temperature. The isothermal remanent magnetization (IRM) acquisition curves were obtained with progressively increasing field steps up to 1.5 T, on selected specimens from each site. The back-field curves were performed to detect the coercivity of remanence (B_{cr}). We applied the cumulative log-Gaussian function by the online software MAX UnMix (Maxbauer et al., 2016b) to discriminate magnetic components based on their mean remanence coercivity (Bh) and the dispersion parameter (DP) (Kruiver et al., 2001; Heslop et al., 2002). In addition, we calculated the remanence ratios (S-ratios) which are proxies of the relative contribution of high-versus low-coercivity minerals (Thompson & Oldfield, 1986; King & Channell, 1991; Liu et al., 2019). Variations in the ratio can be associated with several causes, such as lithological changes, diagenetic processes (Bloemendal et al., 1992) or changes in the magnetic properties of rocks induced by deformation, frictional heating and/or fluid-rock interaction in slip zones (Chou et al., 2012; Yang et al., 2020). We also tested the occurrence of different magnetic components by the thermal demagnetization of IRM experiments (Lowrie, 1990) on 25 selected specimens. The IRMs were imparted using fields of 1.5, 0.6, and 0.1 T, along z, y, and x axis, respectively. Then, specimens were stepwise thermally demagnetized up to 600 °C or 700 °C to define the unblocking temperatures associated with the soft, medium, and hard coercivity fractions. After each heating step, magnetic susceptibility was measured to check thermally induced mineralogical changes. Increase in susceptibility mainly results from magnetite or titanomagnetite formation from minerals such as clays, iron sulfides, carbonates, or other (hydro-)iron oxides (Urrutia-Fucugauchi, 2007). These thermochemical transformations may occur between 200 °C and 500 °C. In contrast, a decrease in susceptibility is commonly associated with oxidation, such as hematization of magnetite at high temperature (>500 °C in sediments). Bulk magnetic susceptibility was measured with an MFK2-FA at three operating frequencies (976, 3904 and 15616 Hz) as a function of increasing field from 2 A/m to 700, 350 and 200 A/m respectively. Field variations of the magnetic susceptibility may provide additional information on the dominant mineralogy and detect the presence of iron-sulfides. Para- and diamagnetic minerals, as well as pure magnetite show field-independent susceptibility (Jackson et al., 1998; Hrouda, 2002; Hrouda et al., 2006). Very slow increases and decreases with field have been reported from MD and SD magnetite respectively, although very weak and in general not significant (Hrouda et al., 2006). Instead, Ti-magnetite-, pyrrhotite- and hematite-bearing rocks

show strong variations with increasing field (e.g., Worm et al., 1993; Jackson et al., 1998; Hrouda, 2002; Pokorný et al., 2011). In addition, we calculated the frequency dependent magnetic susceptibility ($\chi_{fd\%}$) as $\chi_{fd\%} = [(\chi_{lf} - \chi_{hf})/\chi_{lf}]*100$ (Dearing et al., 1996), where χ_{lf} and χ_{hf} are the magnetic susceptibility measured at low (975 Hz) and high (15616 Hz) frequencies in a field intensity of 75 A/m. The frequency dependence of magnetic susceptibility is used to identify the contribution of superparamagnetic (SP) particles over the SD and MD grains (Thompson & Oldfield, 1986; Maher, 1988; Dearing et al., 1996; Maxbauer et al., 2016a). In specimens dominated by SP ferrimagnetic grains, $\chi_{fd\%}$ values from about 6 to 17% have been recorded (Dearing et al., 1996; Maxbauer et al., 2016a). Hysteresis loops were run at room temperature with a Vibrating Sample Magnetometer (VSM, Lake Shore 7410) with a maximum applied field B_{max} = 1 T, to further investigate the rock magnetic properties and estimate the magnetic domain-state (i.e., grain-size of magnetic minerals) (Day et al., 1977; Dunlop, 2002a, 2002b). Interpretation of hysteresis loops was performed with HystLab software (Paterson et al., 2018). Advanced processing options (e.g., automatic loop centering, drift and high-field slope corrections and loop fitting) were applied following the approach described by Paterson et al. (2018) and suggestions from Jackson & Solheid (2010). The hysteresis parameters (saturation magnetization (M_s), saturation remanent magnetization (M_{rs}) and coercivity (H_c)) were then extracted and plotted as M_{rs}/M_s versus H_{cr}/H_c (i.e., Day plot - Day et al. 1977; Dunlop, 2002a, 2002b), allowing to estimate the domain-state.

3.2.1 Low- and high-temperature experiments and SEM-EDS analysis (Case study from the SVU – Chapter 5)

Additional mineralogical experiments were performed for the SVU. In this intraplate shear zone, geochemical composition of tectonic veins suggested changes in permeability, fluid source, and circulation pathways during the major seismic cycles (Vannucchi et al., 2008, 2010; Cerchiari et al., 2020). To investigate how fluids may have induced changes in the magnetic properties, we performed high- and low-temperature experiments on selected specimens collected at increasing distance from the basal décollement. Low-temperature measurements were conducted using a Quantum Designs Magnetic Properties Measurement System (MPMS-XL) at the Institute for Rock Magnetism (IRM) at the University of Minnesota. Field cooled (FC) remanence experiments were performed by applying a 2.5 T field while cooling the specimens from 300 to10 K. The evolution of the low temperature SIRM (LT-SIRM) was studied as the specimens warms back to 300 K in zero field. Then, after cooling the specimens to 10 K in zero field, a LT-SIRM at 2.5 T was imparted. The remanence was measured while warming up to room temperature in zero field (i.e., zero-field cooled (ZFC)). Subsequently, a SIRM of 2.5 T was imparted at room temperature (RT-SIRM at 300 K) and remanence behaviour was monitored during a cooling-warming cycle (300 – 10 – 300 K) in zero field. This procedure is particularly suitable for identifying the presence of diagnostic magnetic phase transitions indicative of magnetite (Verwey transition, T_V ~ 120 K; Verwey, 1939; Muxworthy & McClelland, 2000), hematite (Morin transition, T_M ~ 260 K; Morin, 1950; Özdemir et al., 2008) or monoclinic pyrrhotite (Besnus transition, T_B ~ 34 K; Dekkers et al., 1989; Rochette et al., 1990). Additional information on magnetic particles grain-size or magnetic phases concentration might be assessed

trough several parameters (e.g., δFC/δZFC, Moskowitz et al., 1993; Carter-Stiglitz et al., 2004; R_{LT}, Smirnov, 2009; G%, Aubourg et al., 2021; see APPENDIX I for equations). Then, χ–T curves were performed in argon with heating-cooling cycles at increasing elevated temperatures (increments of 50 °C from 150 to 350 °C and then 700 °C) using a KLY-2 equipped with a CS2 furnace at the IRM. Under the assumption that cycles at temperature lower than the maximum temperature experienced in nature are reversible, this approach has been used as a rock magnetic "geothermometer" to infer frictional heating in fault zones (Yang et al., 2016, 2020). We implemented this experiment performing hysteresis cycles at room temperature after stepwise thermal treatment at increasing maximum temperature. The thermal treatment was performed in vacuum with incremental steps of 100 °C from 150 up to 650 °C. Hysteresis parameters (M_s, M_{rs}, H_c) were extrapolated with HystLab to assess variation in the magnetic properties of the samples as temperature increases.

Scanning electron microscope (SEM) observations coupled with energy dispersive spectrometry (EDS) measurements were performed at selected sites, from both the footwall and hangingwall and at different distance from the basal décollement. Compositional data points were collected using a SEM JEOL IT300LV, EDS Oxford Instruments Inca Energy 200, X-act SDD detector. Operating conditions are 15keV with 5nA current and EDS process time of 1 µsec, 10^5 counts/sec, and live time of 50 sec. The obtained elements analysis was used to assess (semi-quantitatively) the composition of the different mineralogical phases, in particular iron-bearing para- and ferromagnetic minerals and to evaluate the presence of iron sulfides.
The overall information might help in constraints the possible thermochemical reactions occurred along the plate boundary, including the estimation of potential post-seismic fluid-rock interaction.

3.3 AMS data and statistical treatments

For each specimen, the AMS was measured on a KLY-3 Kappabridge (AGICO). Measurements were accepted only with F-statistic tests of anisotropy higher than 5. In this case, a specimen is defined as statistically anisotropic within the 95% of likelihood excluding the hypothesis of rotational symmetry (Hext, 1963). Since outliers may skew the mean tensors orientation, we computed the mean values of the AMS scalar parameters and excluded values (5.7% of the total specimens from the SVU, 16.6% from the OAS, and 6.9% from the ELAW) characterized by ± 2σ of their mean for further analyses. This criterion allows a reduction in the scatter of the AMS parameters, which is induced by specimens with unconventional small size. We processed the data with the software ANISOFT 4.2 (Chadima & Jelínek, 2008). The AMS represents the preferred orientation of all para- and ferromagnetic minerals in rocks, and the mean magnetic susceptibility (k_m) is controlled by the relative abundance of all rock-forming minerals. To compare the results among different lithologies and fragments, we calculated the mass magnetic susceptibility (χ_m). The corrected anisotropy degree (Pj; see APPENDIX I for equation) reflects the eccentricity and stretching of the magnetic ellipsoid (Borradaile & Jackson, 2004, 2010). Its magnitude depends on the magnetic phases responsible for the AMS and the intensity of their preferred orientation. The shape of the ellipsoid (T) reflects the shape and/or crystallographic preferred orientation of the dominant magnetic grains and their

distribution. The shape of the magnetic ellipsoid can also be described through the ratios between the magnitude of the principal susceptibility axes such as the magnetic lineation (L) and the magnetic foliation (F). At site level, variations in modal mineral composition and grain-sizes or the occurrence of competing AMS subfabrics, such as superposed tectonic petrofabric related to cumulative strain, result in a non-orthorhombic or mixed magnetic fabric (Borradaile, 2001; Borradaile & Jackson, 2004; Satolli et al., 2020). A non-orthorhombic fabric is characterized by confidence regions inclined to the principal planes of symmetry of the tensor due to multimodal distribution of the principal magnetic susceptibility axes (Borradaile, 2001, 2003).

To detect the possible presence of superposed petrofabric, we applied a combination of contouring and cluster analyses (**Figure 3.1**). The use of contouring and bootstrapping ensures the detection of the site's main fabric over a complex fabric (Constable & Tauxe, 1990; Borradaile & Henry, 1997). In addition, contour plots (e.g., density diagrams) allow one to roughly discriminate specimens with different orientation of principal AMS axes (Borradaile & Jackson, 2004, 2010; Aubourg et al., 2010; Robustelli Test et al., 2019; Satolli et al., 2020). To improve the evaluation of possible competing subfabrics and minimize the non-orthorhombic symmetry of mixed fabrics (Borradaile, 2001), we performed the cluster analysis at sites level, using the mixed Bingham distribution (Yamaji & Sato, 2011) separately for each principal susceptibility axis with the software Orient (Vollmer, 2015). As pointed out by Borradaile (2001), treating tensors' data as three single individual vectors produces non-orthogonal density peaks or means values, especially when the tensors are not very well aligned. This can be caused by the presence of uneven uncertainties such as the occurrence of outliers that can strongly influence the shape of the contours (Borradaile, 2003). However, if carefully treated, the use of contour plot can be useful to verify sample/site homogeneity. It is widely used in magnetic fabric works to evaluate variations in the spatial orientation of the principal susceptibility axes at site level and the presence of possible clusters. Aware of this controversy, we propose this method as particularly useful for checking bimodal distribution of the three principal directions. First, we excluded any outliers having values of the scalar parameters (Pj and T) greater than ± 2σ of their mean. Before applying any statistical treatments, we ensured to isolate any possible clusters related to changes in magnetic susceptibility, magnitude, and shape of the susceptibility ellipsoid. Then, to define the possibility of inter-site heterogeneity and detect homogeneous subpopulation of data (Borradaile, 2001), we performed density distribution using the software Stereo 32 with 10 contour intervals and cosine exponent = 40. In some cases, we observed multimodal distribution of one or more of the principal susceptibility axes which induces distortion in the calculation of the mean tensor, which in turn is physically meaningless (Tarling & Hrouda, 1993). The occurrence of competing subpopulation of specimens may lead to sub-orthorhombic confidence regions, inclined to the symmetry planes (Borradaile, 2001, 2003). To better highlight the bimodal distribution of certain principal susceptibility axes, we applied the cluster analysis separately for each axis at sites level. As previously mentioned, treating the axes separately may yield in non-orthogonal means (**Figure 3.2**) for the three principal directions (Borradaile, 2001). However, we observed the occurrence of three different behaviours:

i) Case I – all 3 axes show a bimodal distribution. The cluster analysis reported two clusters, each of those having the same number of specimens. The mean directions of the three principal axes show mutual orthogonality (**Figure 3.1a**). In this case, the cluster analysis directly distinguishes specimens belonging to a certain specific distribution;

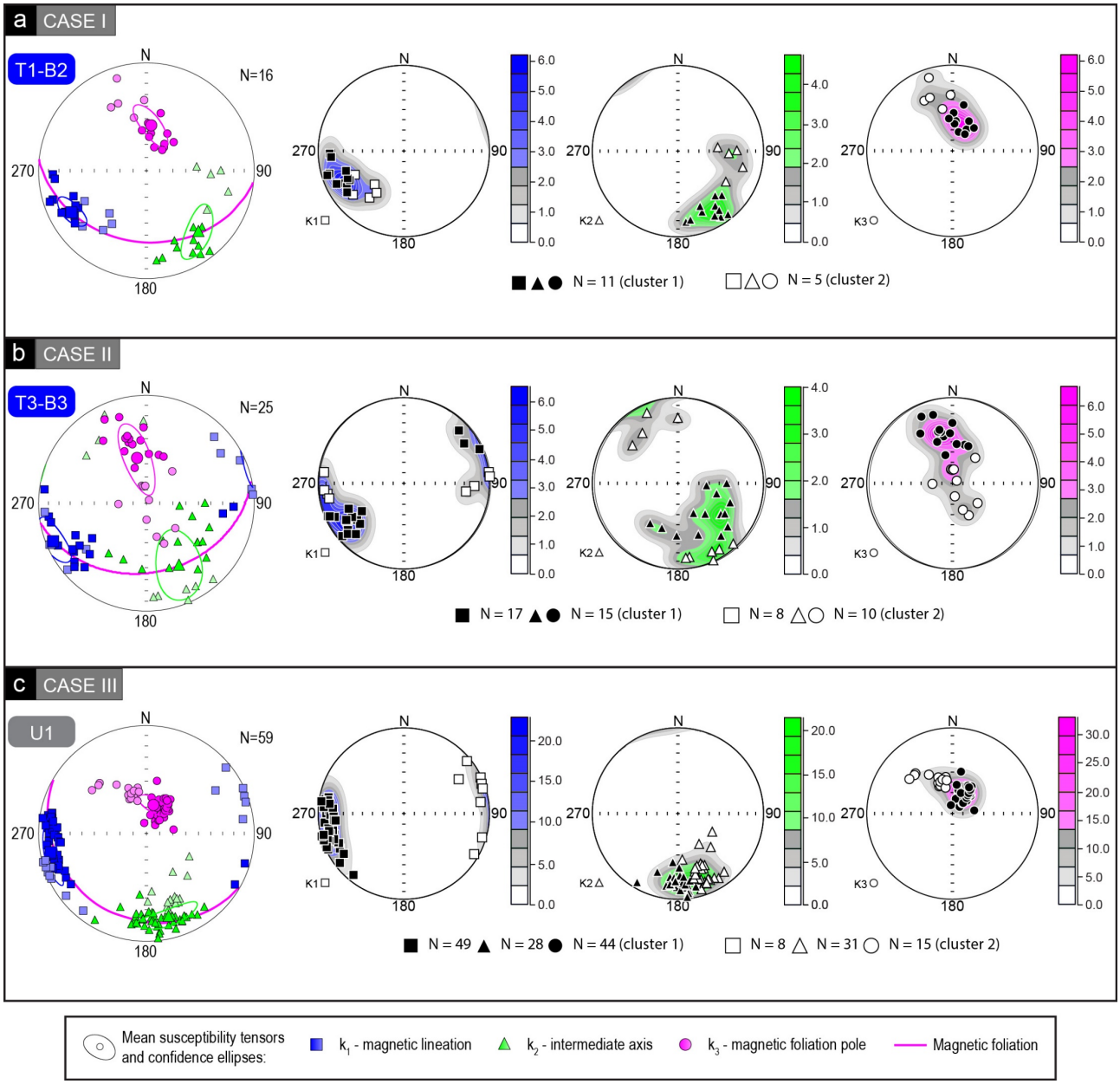

Figure 3.1. Example of the application of contour plot and cluster analysis to highlight the presence of competing subfabrics in a mixed AMS fabric at site level. Lower hemisphere equalarea projections of the AMS axes at site level (left). Different subfabric detected are reported with different shades. Contour plots and cluster analysis for each of the principal magnetic susceptibility axes separately (right). (**a**) Case I - characterized by the mutual orthogonality of the means of the three principal directions obtained by the cluster analysis; (**b**) Case II – mutual orthogonality for two of the three means; (**c**) Case III - no mutual orthogonality.

ii) Case II – only two axes show bimodal distribution, and the orthogonality is respected only between those axes (**Figure 3.1b**). The cluster analysis for the unimodal distributed axis shows different numbers of

specimens per cluster. Results of the cluster analysis were carefully evaluated and accepted when consistent with the contouring;

iii) Case III – only one axis shows bimodal distribution (**Figure 3.1c**). The cluster analysis may lead to false results, characterized by different number of non-orthogonal means. We then attribute major importance to the contour plot and/or the variations in scalar parameters.

To obtain the final subfabric the mean orientation of the AMS axes was calculated using the Jelinek's tensor statistics with the software ANISOFT 4.2 (Chadima & Jelinek, 2008). The Jelinek's statistics constrains the mutual orthogonality of the axes, essential for interpret tensors data. The reliability of the possible subfabrics must finally be verified comparing the results with the structures observed in the field.

This approach may represent a useful tool for characterize bimodal distribution of AMS data at site level. The combination with the density distribution (e.g., contour plot) is essential to avoid misleading. However, it is challenging to apply this method to strongly prolate fabrics with interspersed axes. We kindly recommended to don't use it in that cases to avoid artifacts of data treatments.

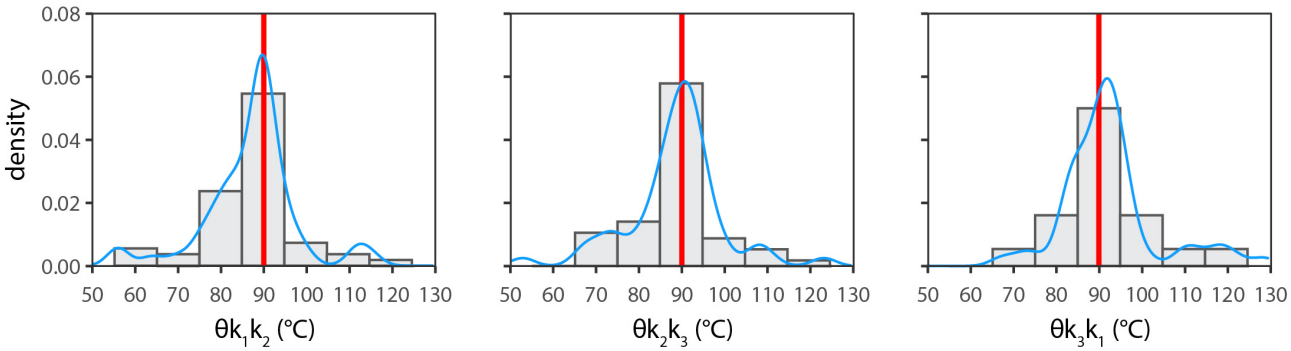

Figure 3.2. The histogram and the density distribution of the θ angles between the means of the three principal directions obtained using the Cluster Analysis.

3.4 ApARM, AARM, AIRM and High-field AMS

To isolate the orientation of remanence-bearing grains, we performed four different anisotropy of magnetic remanence (ARM) experiments on selected specimens (6 specimens for each statistical group). A combination of ApARM and AIRM experiments helps to fully characterize the ferromagnetic grains contribution to the magnetic fabric and define their dominant behaviour. First, specimens were AF demagnetized and their remanent magnetization (RM) was measured with the JR-6 spinner magnetometer, to detect the median destructive field (MDF). On the basis of this value and the coercivity distribution of the rock constituent minerals, resulted from the magnetic mineralogy investigation, we selected the AC and DC field to be applied during the remanence experiments, targeting subpopulations of ferrimagnetic grains. The anisotropy of anhysteretic remanent magnetization (AARM) and partial ARM (ApARM) were measured using different coercivity windows. ApARM experiments allow discrimination of the contribution of the different sub-populations of ferromagnetic grains (Jackson et al., 1988, 1989; Bilardello & Jackson, 2014; Biedermann et al., 2019; Biedermann, Jackson, Bilardello, & Feinberg, 2020), which may form during different episodes of deformation (Martín-Hernández & Ferré, 2007). Experiments are named as $ApARM_{40\text{-}0}$,

$ApARM_{100-40}$, and AARM depending on the different coercivity windows. To study the low-coercivity fraction (e.g., coarse magnetite grains, multidomain MD and single vortex PSD state) we applied a tumbling demagnetization in a peak AF of 60 mT. Then, we imparted the ARM in the 40–0 mT window with a bias direct field of 0.1 mT during static AF demagnetization and a decay rate of 0.01 mT/half-cycle. This procedure was repeated for the six pairs of antiparallel directions necessary to reconstruct the ARM tensor (Jelinek, 1996). For intermediate-coercivity fraction (e.g., single domain SD) we applied a tumbling demagnetization at a peak field of 100 mT and the bias field within the window 100–40 mT ($ApARM_{100-40}$). Last, an ARM was imparted at 100 mT to study the behaviour of the whole ferromagnetic component. Due to the low intensities of the remanence, we also performed the AIRM. An artificial IRM was given with a pulse magnet, with a steady field of 20 mT (for details about the procedure see Agrò et al., 2015). The intensity of the imparted magnetization is low enough to be completely demagnetized at each step.

To separate the magnetic subfabric of para/diamagnetic and ferromagnetic phases, we measured the anisotropy of high-field magnetic susceptibility (HF-AMS) at room temperature at the Laboratory for Natural Magnetism (LNM at the ETH of Zürich) using a high-field torque magnetometer (Bergmüller et al., 1994). Torque measurements were performed by rotating the specimen with an angular increment of 30° in six different fields between 1 and 1.5 T and then in the absence of an applied field (0 T). Measurements were performed in three mutually perpendicular planes for each specimen. Data were then corrected for the specimen holder. The para- and ferrimagnetic contribution to the magnetic anisotropy was separated based on their different behaviour in high-field torque measurements, using the method of Martin- Hernández & Hirt (2001). The paramagnetic signal is assumed to increase proportionally to the square of the field, while the ferrimagnetic contribution, above saturation, is independent of the field. (Hrouda & Jelinek, 1990; Martin-Hernández & Hirt, 2001, 2004; Martin-Hernández & Ferré, 2007; Biedermann, 2020). The deviatoric susceptibility tensor and relative parameters, shape of the susceptibility ellipsoid (U – difference shape factor) and degree of anisotropy (k' – mean deviatoric susceptibility), were obtained for each component.

3.5 Ternary Diagrams and comparison with mesoscale structural fabric

Ternary diagrams were designed to interrelate AMS and ARM directional data with the main structural elements (i.e., pole of the cleavage, S-C intersection, and transport direction; **Figure 3.3**). To create the ternary diagram, we defined 3 variables (**Figure 3.3a, d-e**) arranged at its vertices: In the upper vertex we have plotted the variable γ, which corresponds to the angle between the orientation of k_3 and the cleavage pole direction. We named the angle as ε, if the bedding pole is used instead of the cleavage pole. Data plotted near the upper vertex are characterized by the maximum discrepancy (γ or ε = 90°) between k_3 and the pole of the structural planes (i.e., pressure solution cleavage and/or bedding orthogonal to the magnetic foliation). On the contrary, data close to the base of the ternary diagram indicate parallelism between the magnetic foliation and the structural foliations (γ or ε = 0°). The variable α has been plotted in the lower left vertex. It represents the angle between the k_2 and the S-C intersection. This variable is called δ when referring to the angle between k_2 and the bedding cleavage intersection ("B-S"). Data plotted around this vertex are

characterized by k_2 axis on the structural foliation and orthogonal to the S-C or B-S intersection (α or δ = 90°) and thus parallel to the shear direction. In the lower right vertex, we have plotted the variable 90°-β, where β is the angle between k_1 and the transport direction projected on the cleavage plane (S plane). We call it β' when it is projected on the bedding plane. When 90°-β = 90°, k_1 and shear direction coincide (i.e., k_1 perpendicular to the S-C intersection). The 3 variables can also be modified to relate the orientations of the principal axes of the magnetic fabric ellipsoid to other structural elements, such as pseudo-bedding pole, fold-axis and extensional direction in broken formation. To determine the angles between the direction of the principal magnetic susceptibility axes and the structural elements (**Figure 3.3a**) we used the equation:

$$\theta = \cos^{-1}(\cos I_{kn} \cos D_{kn} \cos I_x \cos D_x + \cos I_{kn} \sin D_{kn} \cos I_x \sin D_x + \sin I_{kn} \sin I_x)$$

where D_{kn}, I_{kn} are declination and inclination of the principal magnetic susceptibility axis, respectively; D_x, I_x are declination and inclination of the considered structural elements.

Ternary diagrams were created using the "ggtern" package of Hamilton & Ferry (2018) written in R (R Development Core Team, 2014). This graphical representation means that the sum of the variables in each point of the ternary diagram is 100% (**Figure 3.3b-c**; Hamilton & Ferry, 2018). A data somewhere in the diagram indicates a specific quantity of the variables, where aγ + bα + c(90°-β) = 100% and the three vertices represent 100%γ, 100%α and 100%(90°-β) respectively. This configuration constrains the mutual orthogonality of the 3 principal susceptibility axes at the three vertices of the diagrams which represent three end-members of magnetic fabric associated with different deformation stages and/or mechanisms (e.g., tectonic fabric associated to LPS and low or high degree of non-coaxial strain). The diagrams are subdivided into different areas according to the contributions of the three end-members (**Figure 3.3d-e**). The upper vertices correspond to fabric with the magnetic foliation orthogonal to the cleavage and/or bedding. In our setting it represents a strongly deformed tectonic fabric induced by sub-horizontal LPS (Graham, 1966; Borradaile & Henry, 1997; Hrouda & Chadima, 2020) characterized by sub-horizontal k_3 parallel to the shortening direction and subvertical k_1 axis. For AMS data, they may also indicate the occurrence of an inverse fabric (Potter & Stephenson, 1988). The base of the diagrams indicates the parallelism between the magnetic and the structural foliations. The intersection lineation fabric (Graham, 1966; Hirt et al., 2004; Weil & Yonkee, 2009) is plotted at the lower left vertex. The magnetic foliation coincides with either the bedding or the cleavage depending on the tectonic overprint degree (Kligfield et al., 1981, 1983; Pueyo Anchuela et al., 2012), as well as the intensity of the original pre-deformational fabric (Pares & van der Pluijm, 2002; Till et al., 2010). This is also true for shear zones of low finite shear strain, where k_1 is parallel to the S-C intersection (Pueyo Anchuela et al., 2010; Casas-Sainz et al., 2018). The lower right vertex represents high degree of non-coaxial strain, where k_1 is parallel to the transport direction (Averbuch et al., 1992; Ferré et al., 2014; Casas-Sainz et al., 2018).

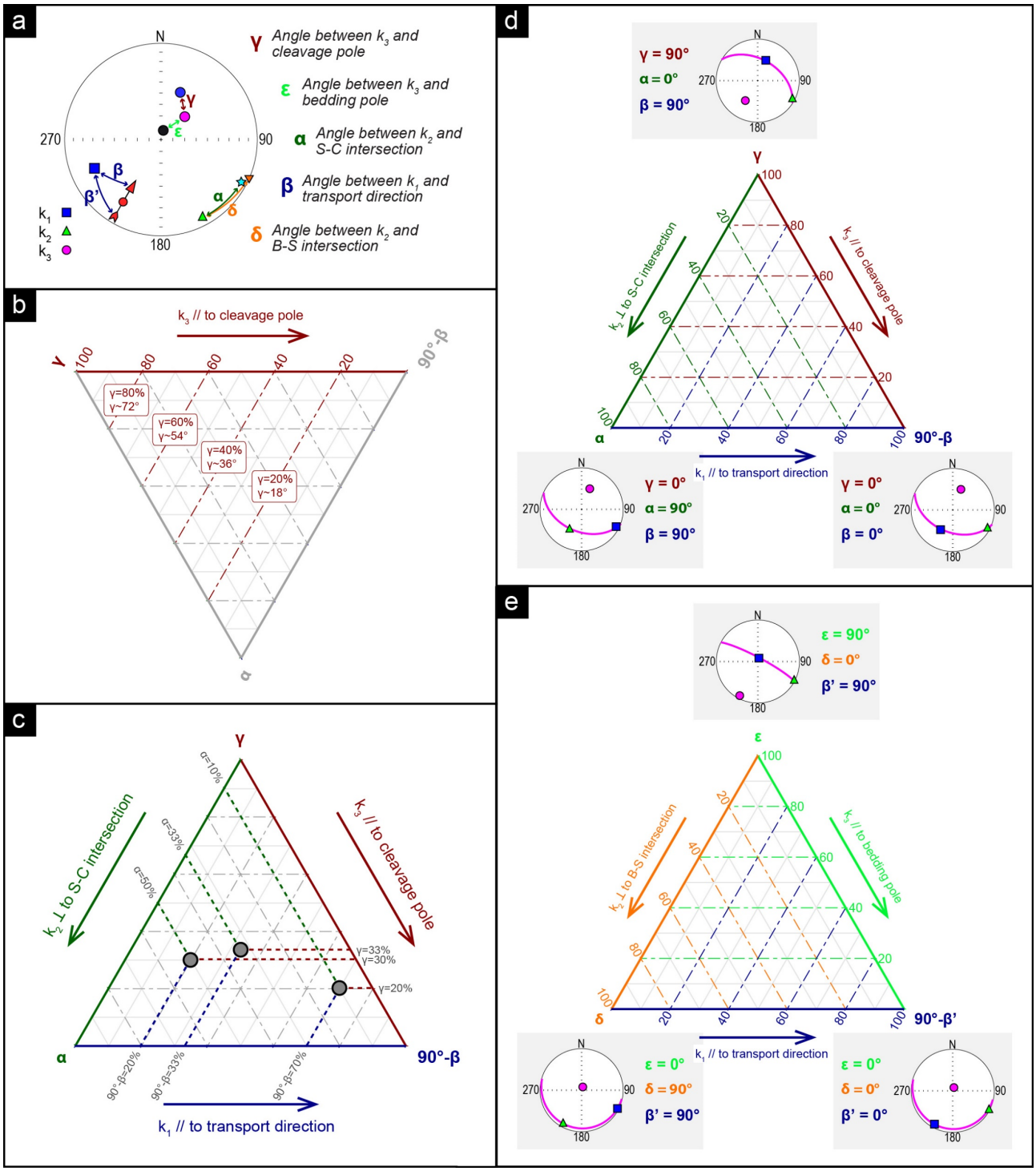

Figure 3.3. (**a**) Representation of the computed angles between structural and magnetic fabric elements (modified from Robustelli Test & Zanella, 2021); (**b**) path of a fabric with progressive parallelization of the magnetic foliation to the cleavage (modified from Hamilton & Ferry, 2018); (**c**) plot of three individual data-points, showing how the 3 computed values can be defined from the ternary diagram; Ternary diagram relating magnetic directional data with the main tectonic elements (**d**) or the main sedimentary features (**e**). Schematic representation of the magnetic fabric end-members are reported close to the vertices.

Chapter 4

FIRST CASE STUDY: The OAS thrust

This chapter reports the results of an integrated rock magnetic and structural investigation of carbonate-rich sediments (i.e., marly limestones and calcareous marls) involved in the OAS thrust. The regional distribution of maximum paleotemperature values (T_{max} ≈ 100-110 °C) suggests burial > 2 km but not exceeding 4 km (Rusciadelli et al., 2005; Aldega et al., 2007). In this context, we dealt with the magnetic properties of tectonites showing SC- or S-fabric depending on the different degree of simple to pure shear deformation and the position within the curved shape thrust (Calamita et al., 2012). The content of this Chapter has been partially published in Satolli et al., 2020 and is integrated here with subfabric separation and detailed mineralogical investigation to constrain the progressive evolution of the magnetic signature in upper crustal fault zones associated with different deformation regimes.

4.1 Geological setting

The Triassic to Miocene sedimentary successions of the Northern Apennines were deposited on the Adria paleomargin (Ciarapica & Passeri, 2002) and involved in the Neogene–Quaternary orogenesis during the convergence between Africa and Europe (e.g., Boccaletti et al., 2005). The study area is located in the Pliocene outer thrust of the Northern Apennines, known as the Olevano-Antrodoco-Sibillini (OAS) thrust **Figure 4.1**). The outer thrust shows a curved shape defined by frontal NW-SE- trending and oblique NNE-SSW-trending thrust ramps to the north and to the south of its apical zone, respectively. To the north, the OAS juxtaposes the Jurassic–Cretaceous carbonate platform and pelagic sequence to the Oligocene-Miocene hemipelagic marly succession (Scaglia Cinerea, Marne con Cerrogna and Laga Fms.) belonging to the Umbria-Marche domain. To the south the footwall is represented, instead, by a persistent carbonate platform domain (Lazio-Abruzzi domain). The Jurassic-Eocene sequence was deposited on the Adria paleomargin during the opening of the Tethys ocean. Starting from the middle–late Miocene, the deformation switched from extension to compression in a context of positive inversion tectonics, where pre-thrusting normal faults were reactivated with different geometries (e.g., Tavarnelli et al., 2004; Butler et al., 2006; Calamita et al., 2012). The southern NNE-SSW trending sector of the OAS reactivated the Lower Jurassic normal fault that

separated the carbonate platform from the pelagic domains (Ancona-Anzio fault, Castellarin et al., 1982); after its emplacement, it was antiformally folded by anticlines developed in its footwall (Alberti et al., 1996). During the Quaternary, post-orogenic extension, characterized by hinterland-dipping NW–SE-trending normal faults with associated intermontane basins and seismicity, affected the axial zone of the Northern Apennines belt (Calamita et al., 2000; Di Domenica et al., 2012).

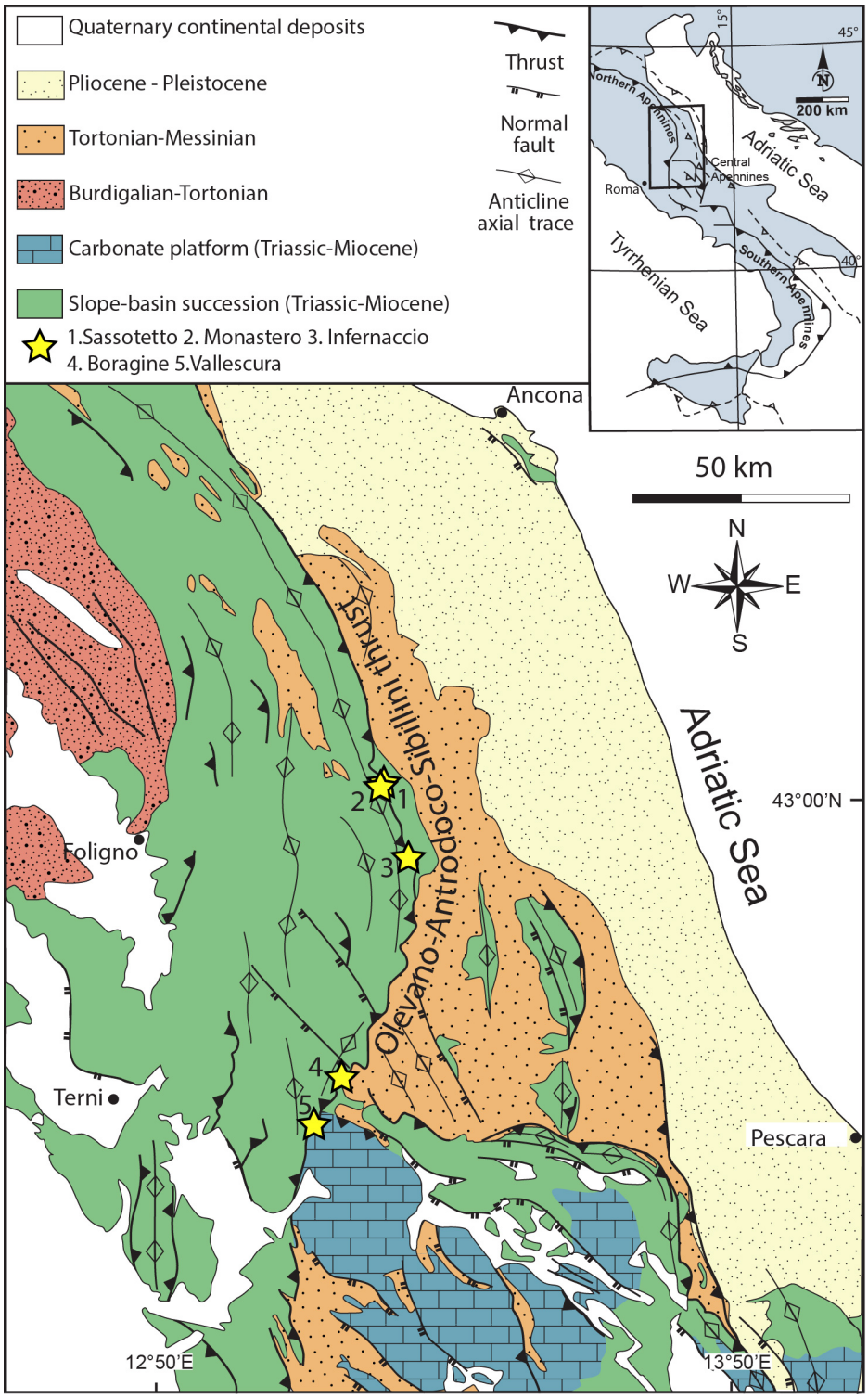

Figure 4.1. Schematic geological map of the Northern Apennines (Italy) with the studied localities (yellow stars), modified after Calamita et al. (2012). The curve-shaped Olevano-Antrodoco-Sibillini thrust is the outer front of the Northern Apennines.

In the Northern Apennines, brittle-ductile tectonites have been previously documented (Koopman, 1983; Lavecchia, 1985; Calamita et al., 1987; Ghisetti, 1987; Calamita, 1991; Calamita et al., 1991, 2012; Alberti et al., 1996; Pierantoni, 1996; Tavarnelli, 1997, 1999; Pace et al., 2015). They are usually associated with the outer thrust, showing different characteristics along two differently oriented thrust ramps (Calamita et al., 2012). The NNE-SSW-trending oblique thrust ramp is characterized by the presence of S tectonites, while the NW-SE trending frontal ramp is characterized by the presence of SC tectonites. The combination of simple and pure shear, thus the degree of non-coaxiality of these shear zones has been quantified through the kinematic vorticity number, allowing to discriminate simple-shear- and pure-shear-dominated deformation (Xypolias, 2010; Calamita et al., 2012).

Tectonites are mostly located in Scaglia Rossa, Scaglia Cinerea and Marne con Cerrogna Formations. The Scaglia Rossa Fm. (Lower Turonian-middle Eocene) predominantly consists in pink and red limestones and marly limestones with chert bands and nodules, and average 20 cm bed thickness. It can be divided in 4 members: (i) Red/ pinkish limestones with dark/red chert; (ii) Pinkish/reddish limestones without chert; (iii) Marly limestones without chert; (iv) Red marly limestones with cherts. The Cretaceous/Paleogene boundary is between facies (ii) and (iii) that are also grouped in the same member in some geological maps. The non-carbonatic component is represented by quartz, mica-illite, montmorillonite, hematite, magnetite and occasionally pyrite (Arthur & Fischer, 1977; ISPRA, 2007). After the Scaglia Rossa Fm., there is a transition from pelagic to turbidite sedimentation with an increase of the marly component. The Scaglia Cinerea Fm. (Upper Eocene- Lower Miocene) is represented by greyish/ greenish marly limestones and marls with thin bedding. It can be divided in 3 facies: (i) Grey/reddish limestones; (ii) Greyish/greenish marls; (iii) Greyish marls and clay. The Marne con Cerrogna (Burdigalian-middle Tortonian) consists of medium to thickly bedded alternating marls, calcareous marls and clay marls, intercalated with calcareous turbidites (Centamore & Micarelli, 1991).We sampled tectonites from different sectors of the Northern Apennines (**Figure 4.1**; **Figure 4.2**) in order to characterize their magnetic fabric at several localities on the frontal (Sassotetto, Monastero, Infernaccio) and oblique (Boragine, Vallescura) ramps of OAS thrust. From each locality, 1 to 5 sites were sampled and studied. Both site size and sampling strategy were decided based on the homogeneity and pervasivity of the tectonic structures as well as on the outcrop conditions. However, in order to obtain significant statistical analysis, at least 10 oriented hand samples of 10–20 cm lithons were collected at each site. Sites were named accordingly to the locality (first letter: S = Sassotetto; I = Infernaccio; M = Monastero; B = Boragine; V = Vallescura), the lithology (second and third letters: SR = Scaglia Rossa Fm.; SC = Scaglia Cinerea Fm.; MC = Marne con Cerrogna Fm.) and the distance from the fault plane (progressive numbers with the distance increment) or sublocality. Along the frontal thrust ramp, the hanging wall was sampled at Sassotetto at ca. 15–20 m from the main thrust, while the footwall was sampled at Monastero at ca. 15 m (MSC1) and ca. 45 m (MSC2), and at Infernaccio at ca. 30 m below the main thrust. From the oblique thrust ramp at Boragine and Vallescura, we sampled different levels at a progressively increasing distance of 15–20 cm from the main thrust. In both localities, 2 sites in the hanging wall into the Scaglia Rossa Fm. and 3 sites in the footwall into the Marne con Cerrogna Fm. were sampled.

All collected blocks were oriented in situ with a compass and an inclinometer. From each block several specimens were prepared at the laboratory, weighed and centered into plastic boxes (2 cm × 2 cm × 2 cm) where they were fixed with non-magnetic plasticine. A total of 271 oriented specimens was obtained from 14 sites.

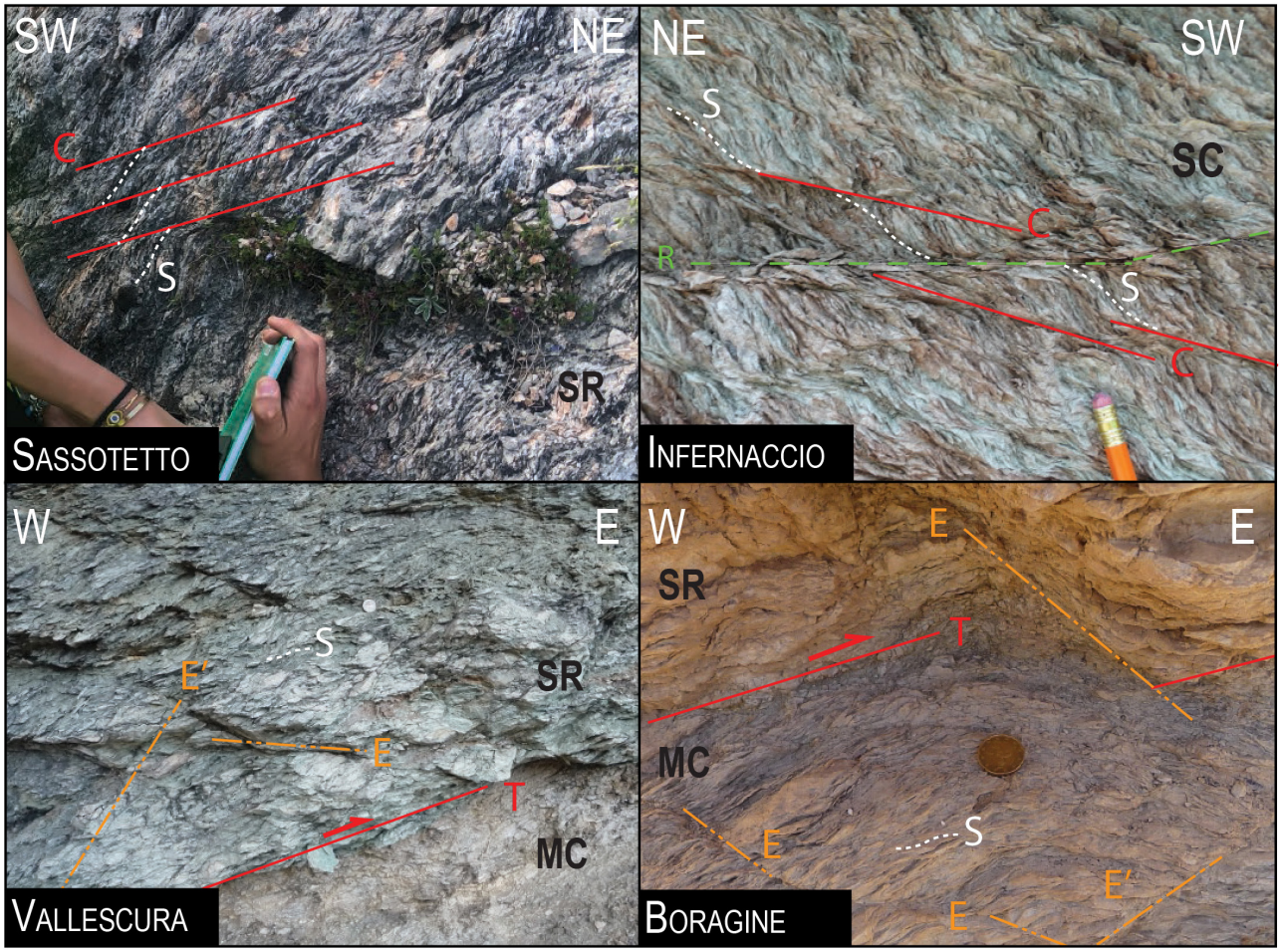

Figure 4.2. Detail view of the shear zones along the frontal (Sassotetto and Infernaccio) and oblique (Vallescura and Boragine) ramp of the Olevano-Antrodoco-Sibillini thrust (Northern Apennines, Italy). C = C shear planes; S = cleavage planes; T = thrust plane; E, E' = extensional planes; R= Riedel planes; SR = Scaglia Rossa Fm.; MC = Marne con Cerrogna Fm.; SC = Scaglia Cinerea (modified from Satolli et al., 2020).

4.2 Structural data

4.2.1 Shear zones along frontal thrust ramps

The SC tectonites show centimeter-to-decameter spaced C shear planes with calcite-bearing shear veins sub-parallel to the main thrust and centimeter-spaced S pressure solution cleavage, identifying spaced and elongated sigmoidal-shaped calcareous lithons (**Figure 4.2**). Millimeter- to centimeter-scale tension veins filled with calcite are perpendicular to the S foliation and low-angle synthetic R planes are also present. Sassotetto and Monastero are located at the hanging wall and footwall of the same thrust shear zone, respectively. Sassotetto was sampled in the Scaglia Rossa Fm. and shows C planes oriented at 250°/ 24° and S fabric oriented at 231°/57° (**Figure 4.3**). Monastero is located in the footwall of the same thrust zone in the

Scaglia Cinerea Fm. and shows C planes oriented at 232°/27° and S planes oriented at 242°/54°. Infernaccio is also located in the footwall of the thrust shear zone juxtaposing the Scaglia Rossa on the Scaglia Cinerea Fm. Here, the kinematic analysis shows C planes oriented at 230°/20° and S planes oriented at 254°/61° (Calamita et al., 2012) while synthetic R planes are oriented at 248°/09°. In this sector, the S-C intersection is NW-SE with a slip vector indicating a NE displacement direction (**Figure 4.3**).

4.2.2 Shear zones along oblique thrust ramps

The S surfaces are sub-parallels to the main thrust plane, identifying marly–calcareous lens-shaped lithons. The foliation is more pervasive in the marls and shales lithotypes of the Marne con Cerrogna and is decimeter-spaced in the marly/calcareous Scaglia Rossa Fm. (**Figure 4.2**). Furthermore, synthetic and antithetic extensional structures displace the main thrust surface and the associated shear zone. At Boragine the thrust plane (T) is oriented 334°/29° and the S surfaces are oriented 303°/22°, with a NW-SE-trending S/T intersection (**Figure 4.3**). Synthetic and antithetic plane E and E' are oriented 057°/37° and 274°/ 42°, respectively (Calamita et al., 2012; Turtù et al., 2013). At Vallescura the thrust plane is oriented 302°/30° and the S surfaces are oriented 250°/29°. Synthetic and antithetic planes E and E' are oriented 394°/44° and 243°/57°, respectively (Calamita et al., 2012). In both localities, the N60–70 transport direction (Calamita et al., 2012) differs from the S-SSW computed slip vector (**Figure 4.3**).

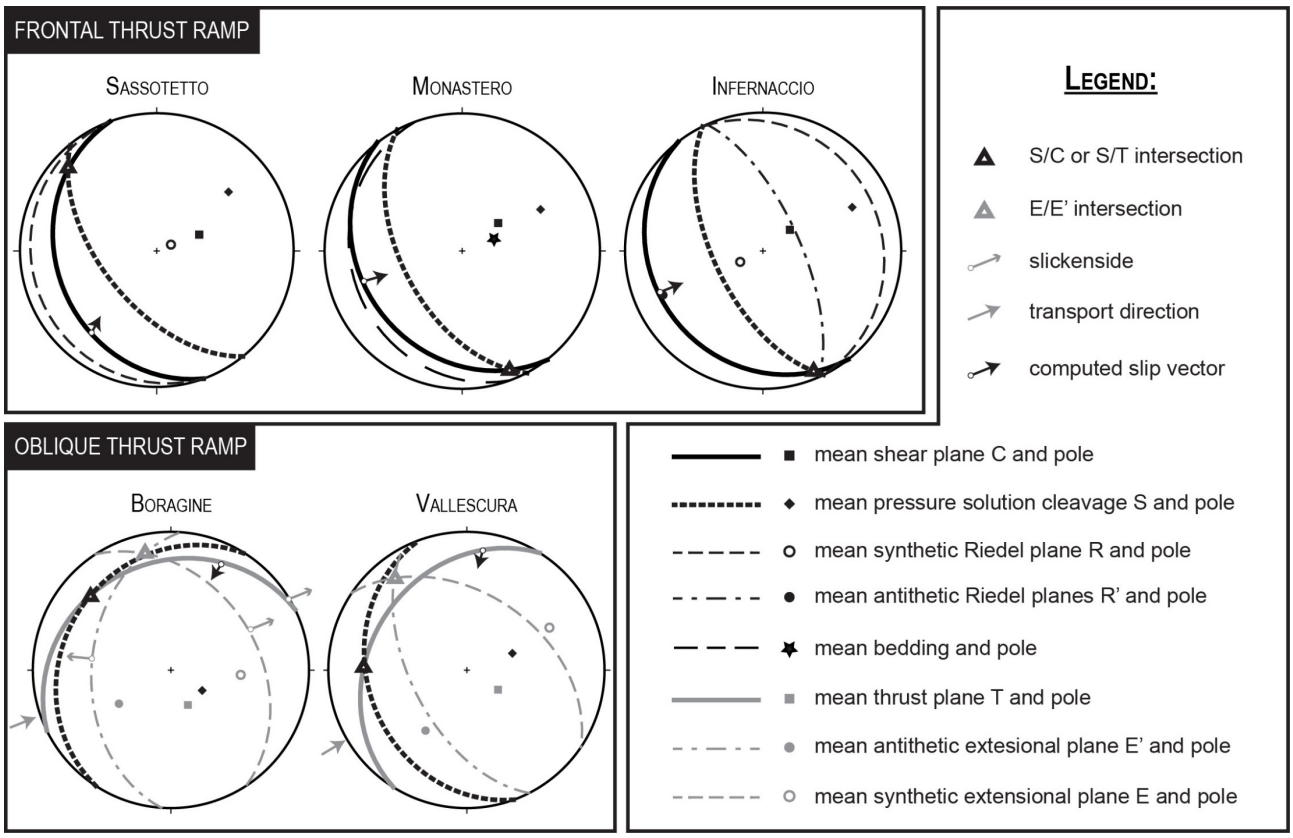

Figure 4.3. Summary of the structural data for each studied locality integrated with data from the literature (Calamita et al., 2012; Turtù et al., 2013; Pace et al., 2015; Satolli et al., 2020).

4.3 Results

4.3.1 Magnetic Mineralogy

Thermomagnetic susceptibility curves were performed on selected samples of each lithological unit (**Figure 4.4a**). Marly sediments (Scaglia Cinerea and Marne con Cerrogna Fms.) are dominated by paramagnetic minerals, as magnetic susceptibility decreases with increasing temperature (Hrouda et al., 1997) up to 400-500 °C (see, MSC2 and BMC1 in **Figure 4.4a**). The heating curves trend shows a subsequent increase in susceptibility followed by a progressive decrease up to ~ 580 °C, suggesting the formation of ferromagnetic phases from the paramagnetic minerals (Hrouda, 1994; Hrouda et al., 1997). In fact, a significant increase in susceptibility is observed in the cooling curves. In contrast, the Scaglia Rossa Fm. show no significant changes in K_m until 400 °C followed by a rapid increase up to 500 °C and a loss in susceptibility around 600 °C, suggesting a significant contribution of the ferromagnetic component, presumably magnetite.

IRM acquisition curves of the Scaglia Cinerea Fm. and most of samples of the Scaglia Rossa Fm. saturate between 0.2 and 0.3 T, suggesting the dominance of low-coercivity components (**Figure 4.4b**). In contrast, acquisition curves of the Marne con Cerrogna Fm. display a rapid increase up to 0.1 T but do not saturate at 1.5 T. This trend indicates the presence of a complex mixture of low- and high-coercivity phases.

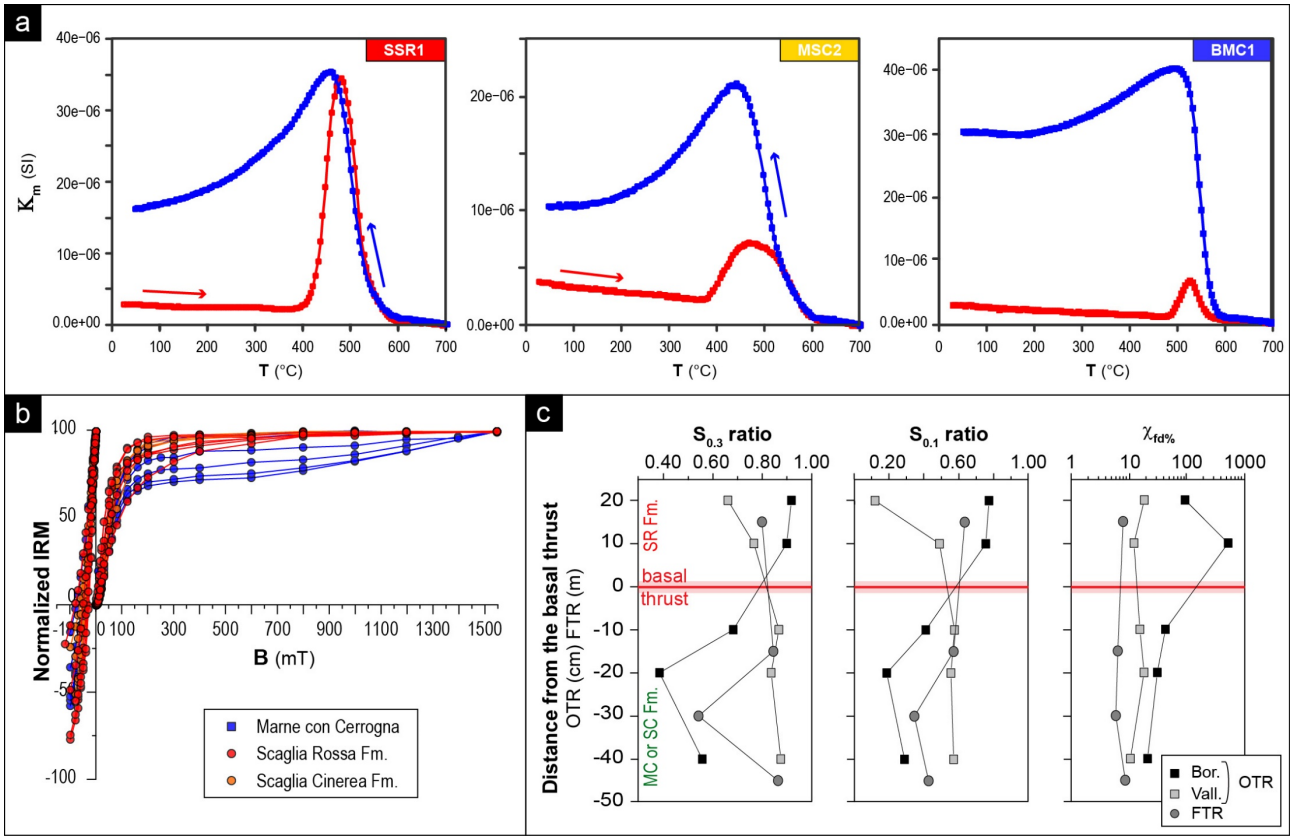

Figure 4.4. (**a**) Thermomagnetic susceptibility curves; (**b**) isothermal remanent magnetization acquisition and backfield curves; and (**c**) plots of S-ratios and frequency-dependent magnetic susceptibility ($\chi_{fd\%}$) versus distance from the basal décollement.

The S-ratios values ($S_{0.3}$ < 0.80 and $S_{0.1}$ < 0.60; **Figure 4.4c**) indicate a relevant contribution of high-coercivity phases in the Marne con Cerrogna Fm., which are located in the footwall of the OAS at Vallescura and Mt. Boragine. Instead, values ~ 0.90 are observed in the Scaglia Cinerea Fm. (footwall of the frontal thrust ramp) suggesting the dominance of low-coercivity phases such as magnetite. Considerable differences in the S ratios of the Scaglia Rossa Fm. are observed between Mt. Boragine and Vallescura. Changes in the values indicate variations in the relative contribution of low- and high-coercivity fractions and the occurrence of different members of the Scaglia Rossa Fm.. The $\chi_{fd\%}$ is generally low, except for the Scaglia Rossa Fm. at Mt. Boragine, where the contribution of superparamagnetic minerals should be taken into account (**Figure 4.4c**).

The presence of variable assemblages of low-and high-coercivity components is clearly visible from the deconvolution of the IRM acquisition curves (**Figure 4.5a**). All lithologies show a dominant low-to-medium coercivity component (Bh = 24-54 mT; $\log_{10}$(B) =1.39-1.74; **Figure 4.5a**). Furthermore, the following components are documented: (i) two high coercivity components in the Scaglia Rossa Fm., one at Bh = 261-394 mT ($\log_{10}$(B) = 2.42-2.60; specimens SSR1-04D and CSR2-04B in **Figure 4.5a**) and a less represented one at Bh = ca. 1100 mT ($\log_{10}$(B) = 3.05); (ii) a low coercivity (Bh = 13 mT; $\log_{10}$(B)= 1.14) and a high coercivity (Bh = 417 mT; $\log_{10}$(B) = 2.62) component in the Scaglia Cinerea Fm. (specimen ISC1-09C); (iii) a very high coercivity component in the Marne con Cerrogna Fm. (Bh = 2213 mT; $\log_{10}$(B) = 3.35; specimen BMC2-02 A in **Figure 4.5a**).

Nevertheless, Lowrie (1990) experiments reveal the dominance of soft fractions as carrier of the remanent magnetization. All lithologies show a dominant low-coercivity component that is demagnetized around 600 °C, and less represented medium and high coercivity components (**Figure 4.5b**). In the Scaglia Rossa and Scaglia Cinerea Fms., a slight drop of magnetization around 300 °C is shown on the X and Y axis (Specimens SSR1-09A and ISC1-11B in **Figure 4.5b**) and the high coercivity component can show an increase of magnetization at temperatures higher than 500 °C (specimens VSR1-07A and ISC1-11B in **Figure 4.5b**).

According to these results we interpret the dominant component as magnetite, save for some specimens of Scaglia Rossa Fm. where the hematite is predominant (e.g., specimen CSR2-04B). Furthermore, the drop at 300 °C might reflect the presence of iron sulfides, while the increase of the high-coercivity component magnetization at 500 °C might reflect the presence of siderite and its alteration with heating (Pan et al., 2000). Whereas the highest coercivity component in the Marne con Cerrogna Fm. may indicate goethite, that however is not clearly documented in the Lowrie's diagrams.

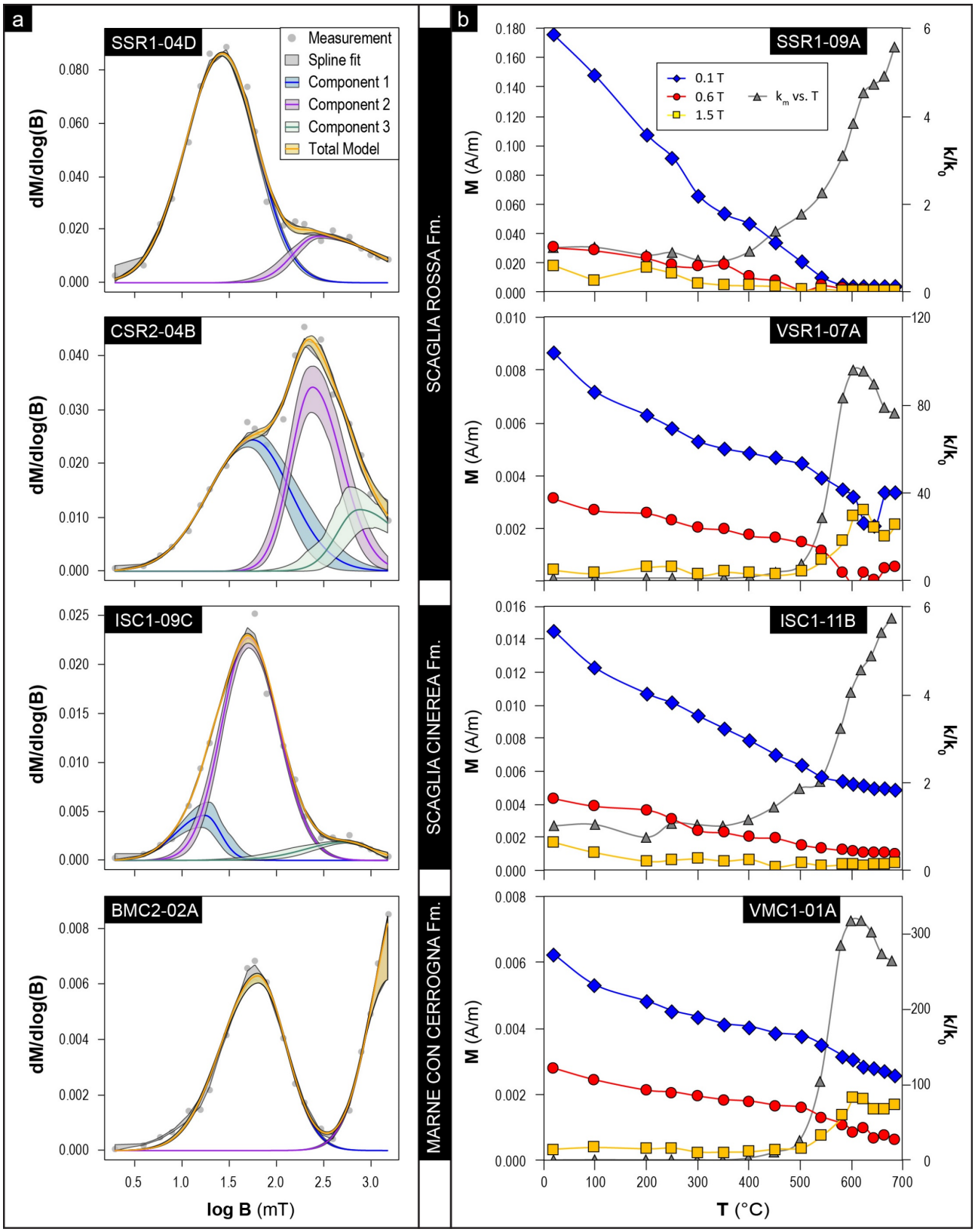

Figure 4.5. (**a**) Coercivity distribution and unmixing of isothermal remanent magnetization (IRM) acquisition curves (Maxbauer et al., 2016b); and (**b**) thermal demagnetization of three-component IRMs and normalized magnetic susceptibility (k/k_0) versus temperature.

For all the lithologies, no significant variation of magnetic susceptibility with field was observed (**Figure 4.6a**), suggesting the substantial contribution of paramagnetic minerals or magnetite to the bulk magnetic

susceptibility (Hrouda, 2002). At the very low fields we observed high noise level, which is commonly associated to samples having high content in paramagnetic minerals. Therefore, variation of susceptibility with field was evaluate calculating the variation index V_a (see, APPENDIX I; Hrouda et al., 2006). Overall, the V_a values display a mean of about -0.37 ± 8.09, which agrees with paramagnetic or magnetite (MD or SD) bearing rocks (Hrouda et al., 2006).

The hysteresis loop of the Marne con Cerrogna Fm. is characterized by a diamagnetic high-field slope with a ferromagnetic signal clearly visible after the high-field slope correction (**Figure 4.6b**). In contrast, the Scaglia Cinerea Fm. reveal a dominant paramagnetic contribution at high field with a discernible ferromagnetic signal. The Scaglia Rossa Fm. reveals a narrow hysteresis loop with a minor influence of the non-remanence bearing matrix (i.e., para- and diamagnetic component). After high-field slope correction the ferromagnetic signal reach saturation between 0.3 to 0.5 T and show B_c values < 50 mT, confirming the dominance of low-coercivity components (**Figure 4.6b**). The shape of the corrected hysteresis loops varies from considerably narrow to wasp-waisted. Based on hysteresis parameters, most of samples are distributed along the mixing curves between SD and MD magnetite grains (**Figure 4.6c**).

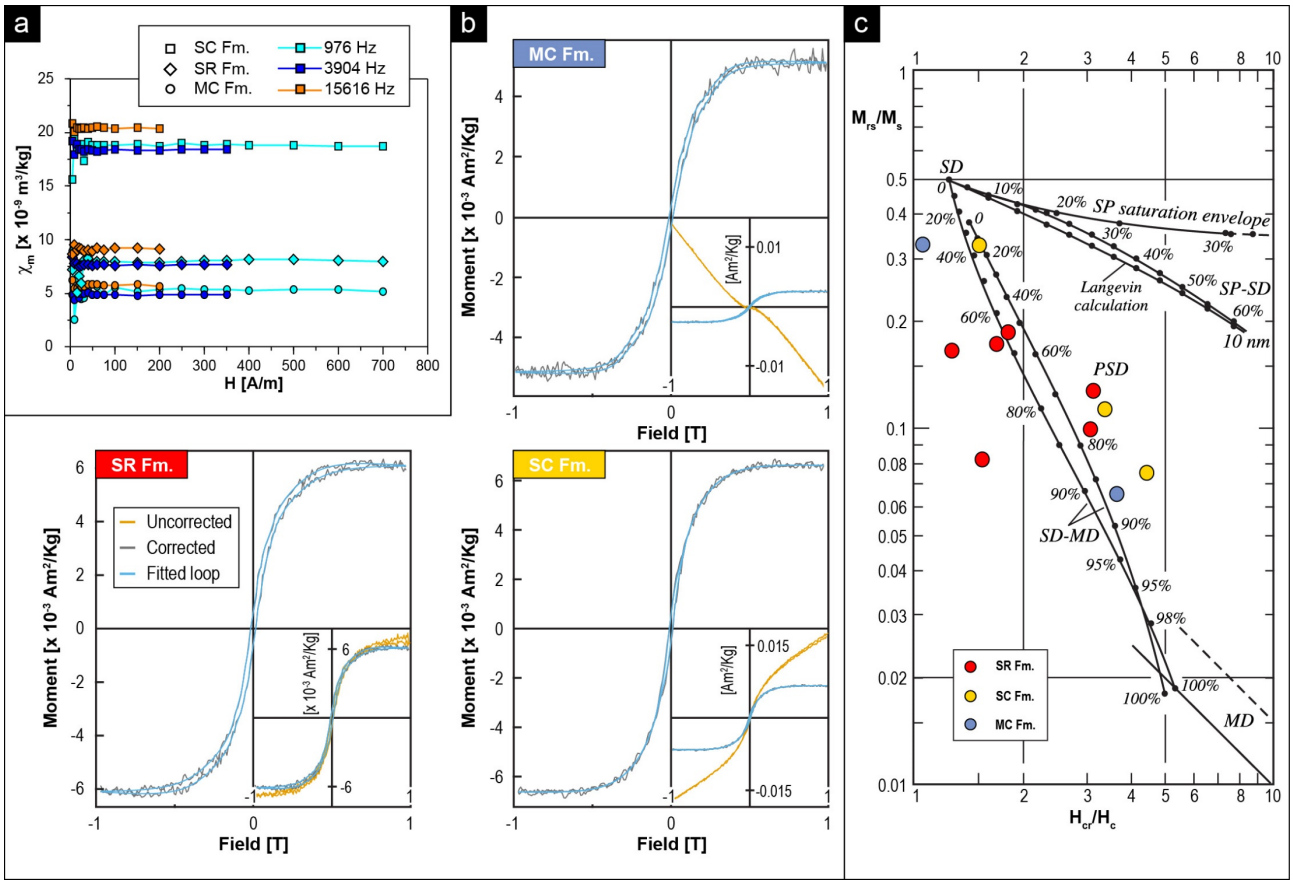

Figure 4.6. (**a**) Field and frequency variations of the mass magnetic susceptibility for representative lithologies; (**b**) Hysteresis loop for representative samples after correction and fitting. Insets show both raw and corrected data; (**c**) Day et al. (1977) plot of the hysteresis ratios M_{rs}/M_s and B_{cr}/B_c with mixing curves after Dunlop (2002a, 2002b).

4.3.2. AMS

All the sampled lithologies show consistent Pj and T parameters (**Table 4.S 1**; **Figure 4.7b, c**). Their magnetic ellipsoids are mainly neutral to slightly oblate with mean T = 0.136 ± 0.307. Overall, Pj is moderate with mean values of Pj = 1.058 ± 0.053. Mass-susceptibility is generally low (mean value χ_m = 11.8 ± 12.27 [x 10^{-9} m^3kg^{-1}]) but varies depending on the lithology (**Figure 4.7a**): χ_m = 28.80 ± 15.11 [x 10^{-9} m^3kg^{-1}] in the Scaglia Cinerea Fm.; χ_m = 8.22 ± 5.61 [x 10^{-9} m^3kg^{-1}] in the Marne con Cerrogna Fm., and χ_m = 5.77 ± 5.16 [x 10^{-9} m^3kg^{-1}] in the Scaglia Rossa Fm.. Significative low values of magnetic susceptibility in the Scaglia Rossa Fm. were also reported in previous studies (Mattei et al., 1995). These values indicate that the magnetic fabric is dominated by the contribution of paramagnetic minerals such as clay minerals (Tarling & Hrouda, 1993; Borradaile & Henry, 1997; Evans et al., 2003), but less represented ferromagnetic (sensu latu) minerals are also documented. Instead, in the Scaglia Rossa Fm. diamagnetic minerals are the main carrier of the magnetic fabric, probably also due to the high pervasivity of calcite veins, and the occasional occurrence of siderite which can cause inverse fabric (Rochette, 1988; Evans et al., 2003; Almqvist et al., 2009).

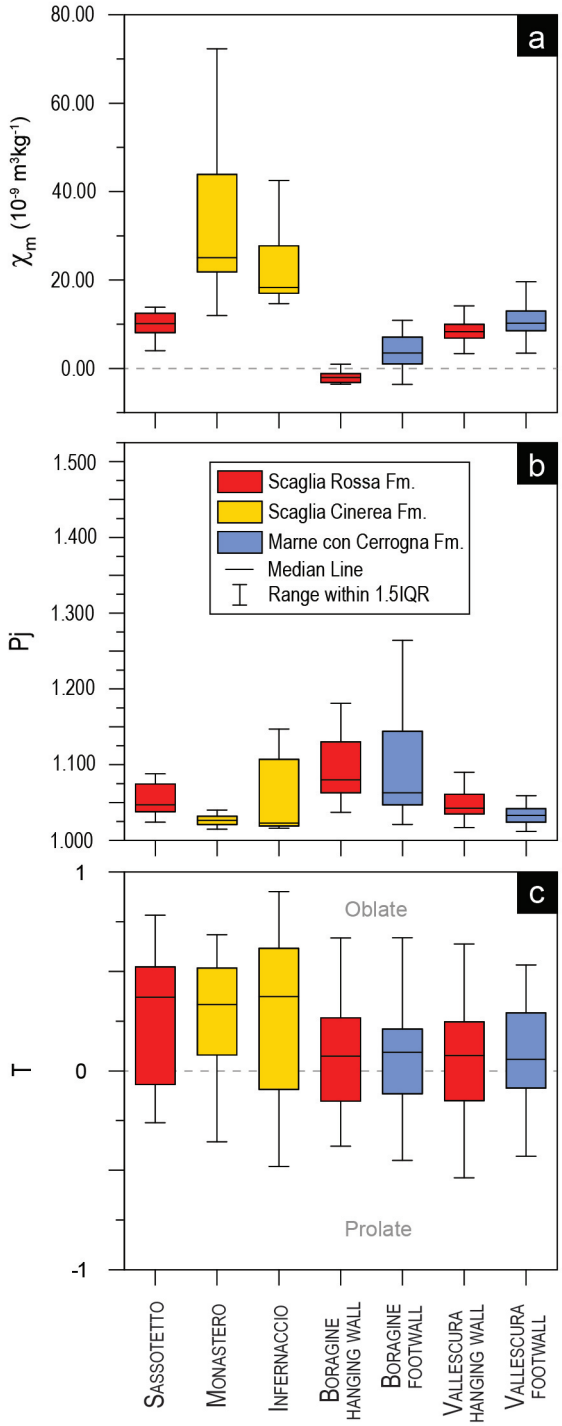

Figure 4.7. Box-and-whisker plots of the (**a**) mass magnetic susceptibility (χ_m), (**b**) corrected anisotropy degree (Pj) and (**c**) shape parameter (T) for the studied localities. Central boxes include values between the lower and upper quartiles (modified from Satolli et al., 2020).

4.3.2.1. AMS from the frontal thrust ramps

All sites show a well-defined magnetic fabric with clustered k_3 and slightly dispersed k_1 and k_2 axes. The shape of the ellipsoid is mainly oblate with T values up to 0.902. The degree of anisotropy is moderate, ranging from 1.015 to 1.147. Variations of Pj occur in relation to the different sampled lithologies (**Figure 4.8**) and distances from the main thrust (**Figure 4.7b**).

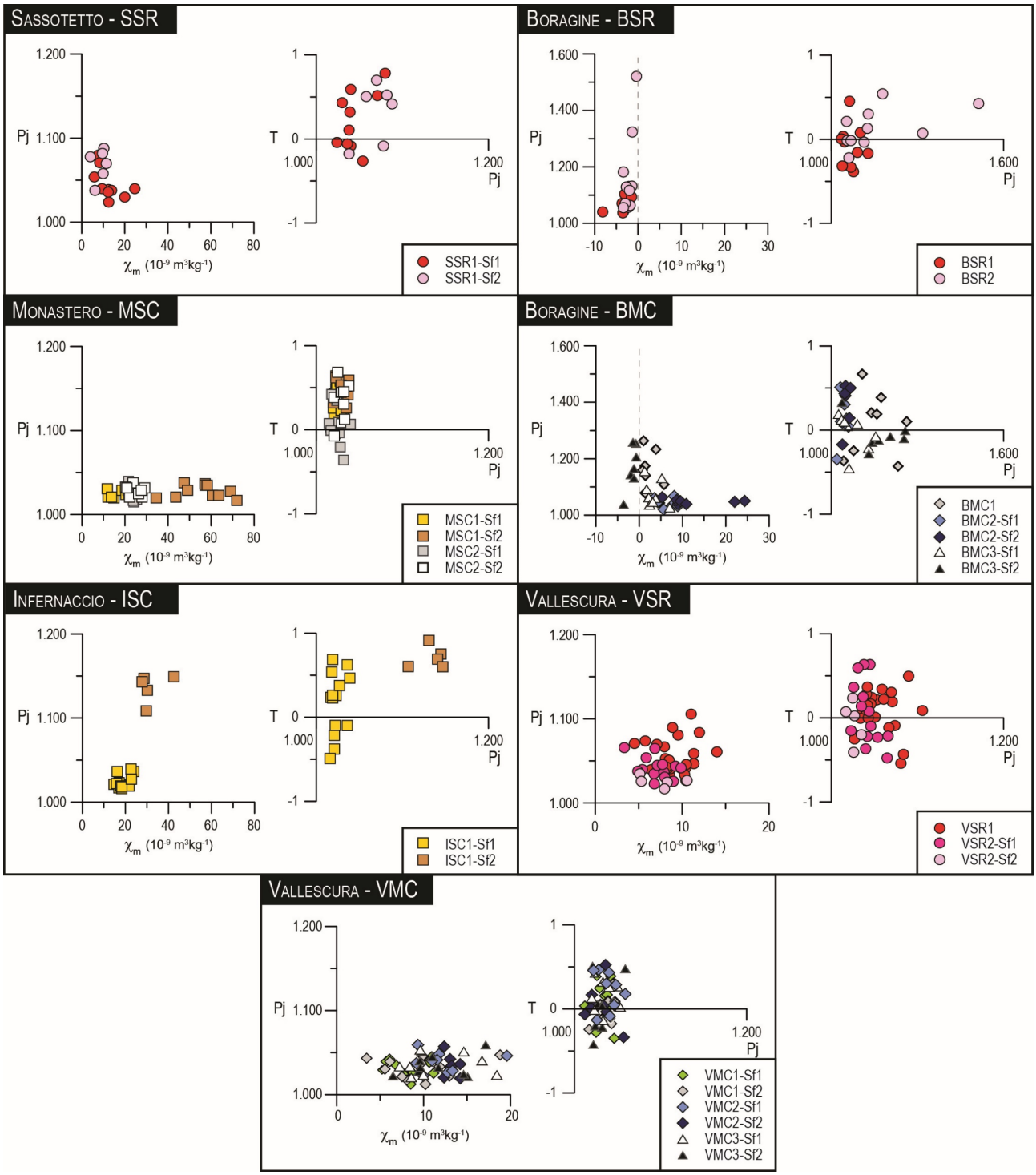

Figure 4.8. Corrected anisotropy degree (Pj) vs. mass susceptibility (χ_m) and shape parameter (T) vs. corrected anisotropy degree (Pj) plots for the various localities. Different symbols correspond to different lithologies: circles and stars for Scaglia Rossa Fm., squares for Scaglia Cinerea Fm. and lozenges and triangles for Marne con Cerrogna Fm. (modified from Satolli et al., 2020).

The magnetic foliation is mostly WSW-dipping at medium to high angle, save for site MSC2 (see **Figure 4.9**), which shows a S-dipping sub-horizontal magnetic foliation.

The SC tectonites at Sassotetto (**Figure 4.9**) show an oblate magnetic fabric T = 0.785 ± 0.340. The magnetic foliation is SW-dipping and steeply inclined. Two different subfabrics have been detected:

i. subfabric 1 is characterized by a lower anisotropy degree and higher χ_m (**Table 4.S 1**; **Figure 4.8**). The magnetic fabric is slightly oblate with a N-S trending magnetic lineation; ii. subfabric 2, characterized by higher Pj and lower χ_m, shows an oblate fabric with a sub-horizontal NW-SE trending k_1 axis.

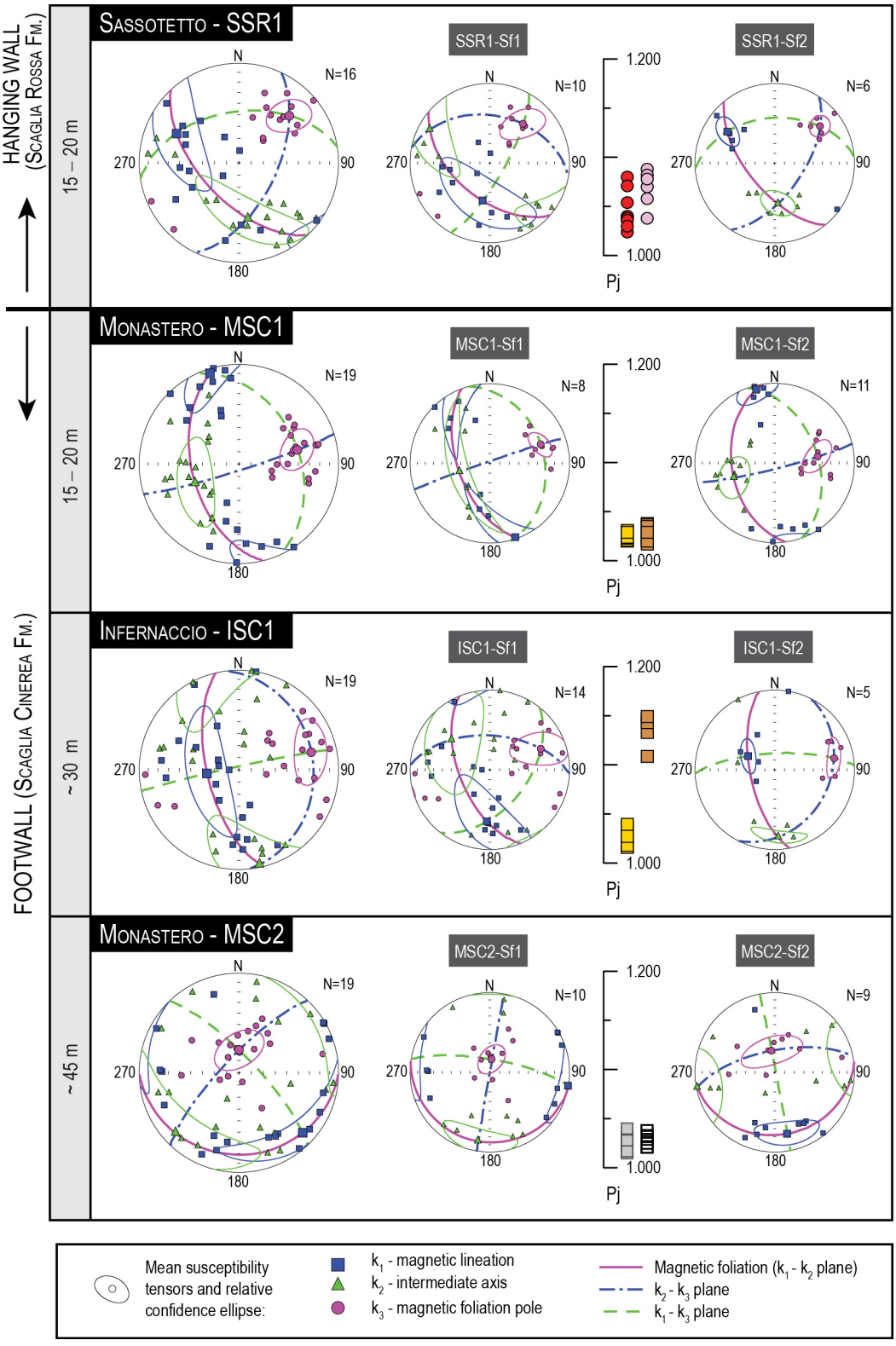

Figure 4.9. Magnetic fabric from the frontal thrust ramp at Sassotetto, Monastero (sites MSC1 and MSC2) and Infernaccio (modified from Satolli et al., 2020). Equal area projections in geographic coordinates of the principal magnetic susceptibility axes at site level (left) and relative subfabrics (middle and right). The Pj values are reported for comparison.

Both sites from Monastero (**Figure 4.9**) show two overlapping magnetic fabrics. Site MSC1 is characterized by a steep WSW-dipping magnetic foliation and k_1 axis N-S trending. The plot of χ_m versus Pj reveals two clusters corresponding to two subfabrics with consistent magnetic foliation and lineation (**Figure 4.8**, **Figure 4.9**): i. subfabric 1 (MSC1-Sf1) is characterized by lower Pj and χ_m values, and a higher dispersion of k_1 and k_2 axes on the magnetic foliation plane; ii. instead, subfabric 2 (MSC1- Sf2) shows well grouped axes.

Site MSC2 displays a sub-horizontal S-dipping magnetic foliation. Here, the two subfabrics (see MSC2-Sf1 and MSC2-Sf2 in **Figure 4.9**) show consistent k_3 but different mean k_1 and k_2 axes orientations. The different axes orientation is associated with variations in shape parameter (T). Subfabric 1 is characterized by a slightly oblate ellipsoid ($T = 0.158 \pm 0.230$) and a sub-horizontal E-W trending magnetic lineation, while subfabric 2, showing a N-S trending magnetic lineation, is neutral with $T = 0.052 \pm 0.240$.

Infernaccio shows the superposition of two subfabrics (see ISC1-Sf1 and ISC1-Sf2 in **Figure 4.9** and **Figure 4.8**) that differ in terms of AMS scalar parameters and k_1 axes orientations: i. subfabric 1 displays a neutral fabric with dispersed k_1 and k_2 axes and a sub-horizontal magnetic lineation mainly N-S trending, lower Pj values and high variability of shape parameter ranging from −0.481 to 0.678; ii. subfabric 2 is characterized by well grouped axes with E-W trending k_1, and strongly oblate fabric and high anisotropy degree.

4.3.2.2. AMS from the oblique thrust ramp

The magnetic fabric is represented by a mixed AMS fabric, with mainly neutral to slightly oblate magnetic ellipsoid ($T = 0.077 \pm 0.269$) (**Table 4.S 1**; **Figure 4.7**). The k_3 axes are mostly grouped, while k_1 and k_2 are dispersed on the magnetic foliation. The anisotropy degree is moderate with mean value of $Pj = 1.066 \pm 0.064$. χ_m values significantly vary between localities. This in turn determines the differences in magnetic fabric configuration.

Boragine is characterized by significant changes of χ_m values between lithologies. Specimens from the Scaglia Rossa Fm. (sites BSR1 and BSR2 in **Figure 4.10** and **Figure 4.8**) are mainly diamagnetic, with $\chi_m = -1.73 \pm 2.60$ [x 10^{-9} m^3kg^{-1}]. The three sites from Marne con Cerrogna Fm. show higher values, with a maximum value of 24.35 [x 10^{-9} m^3kg^{-1}]. This significantly affects the configuration of the AMS fabric at this location.

Sites BSR1 and BSR2, located above the main thrust, display an EW-trending subvertical magnetic foliation with dispersed k_1 and k_2 axes (**Figure 4.10**). Despite higher and positive χ_m values (ranging from 0.74 to 5.73 [x 10^{-9} m^3kg^{-1}] see **Figure 4.8**), site BMC1 from Marne con Cerrogna Fm. shows a similar mixed fabric with a sub-vertical E-W trending magnetic foliation. Here, specimens display k_1 axes E-W to SW-NE trending at medium angles.

The other two sites from Marne con Cerrogna Fm., BMC2 and BMC3, are characterized by a fabric with a sub-horizontal magnetic foliation. The ellipsoid shapes are slightly oblate and prolate, respectively. The site BMC2 might be characterized by the presence of two neutral subfabrics with the same orientation of the

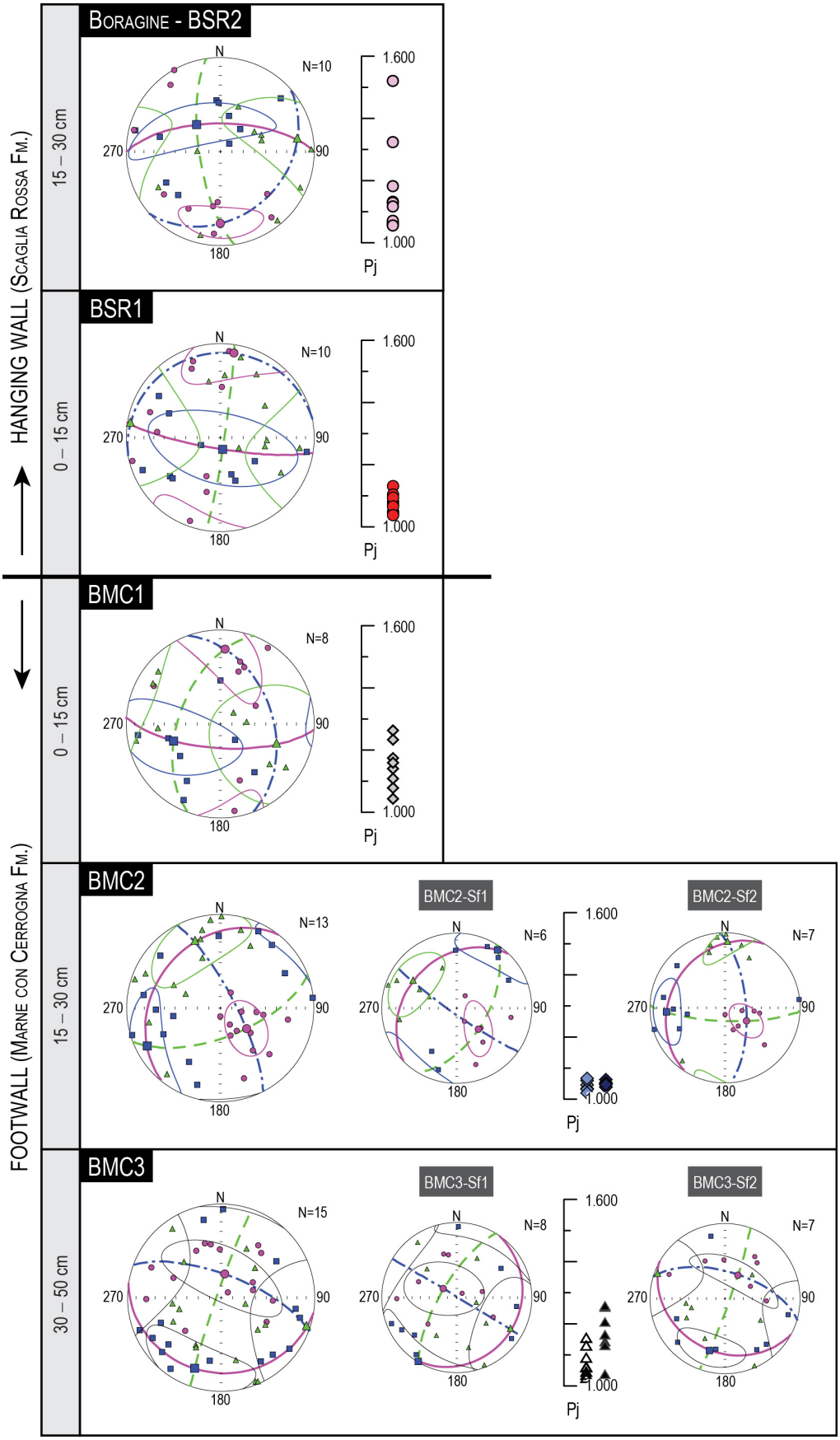

Figure 4.10. Magnetic fabric from the oblique thrust ramp at Boragine (modified from Satolli et al., 2020). Equal area projections in geographic coordinates of the principal magnetic susceptibility axes at site level (left) and relative subfabrics when detected (middle and right). The Pj values are reported for comparison. Legend as in **Figure 4.9**.

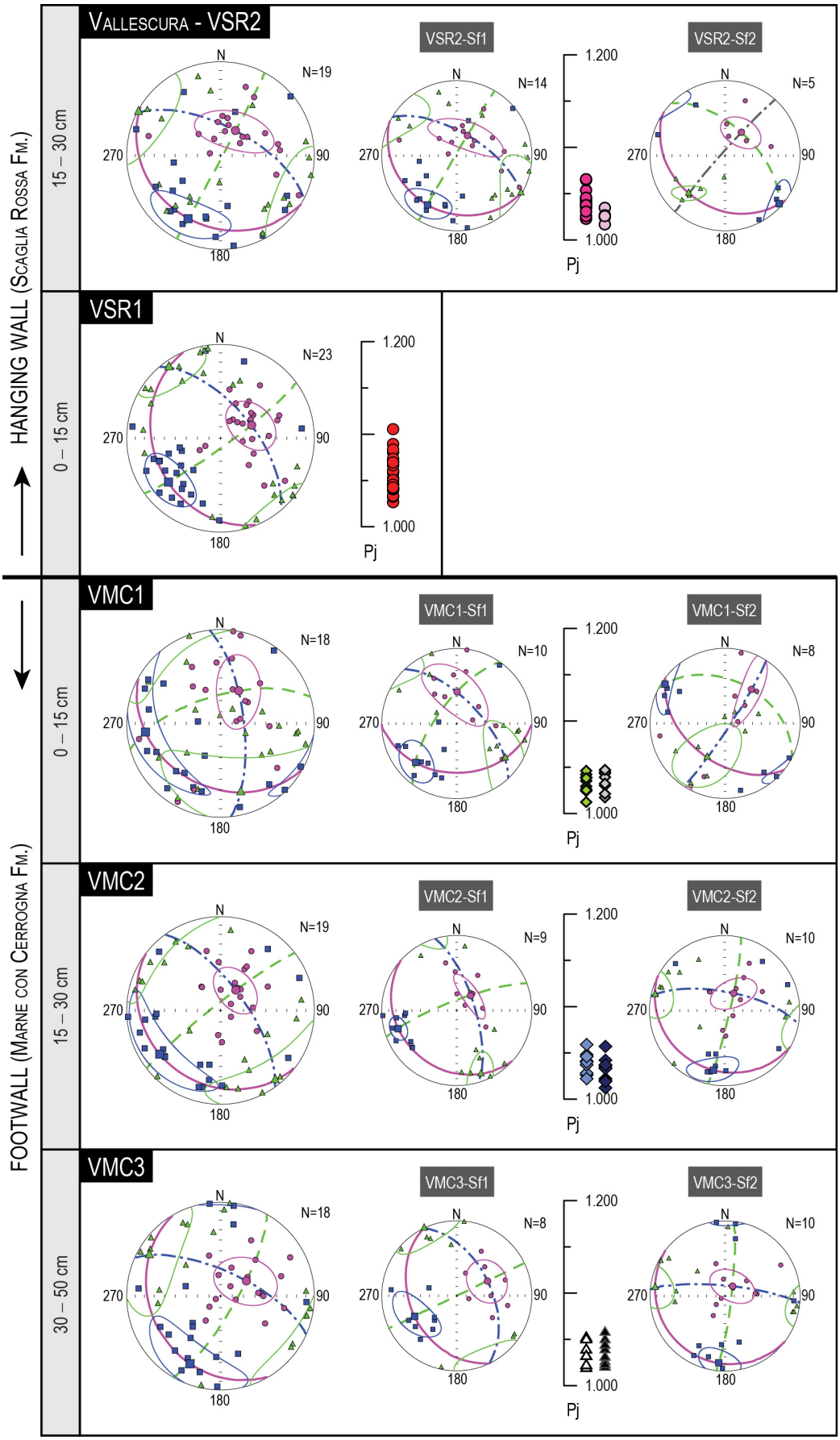

Figure 4.11. Magnetic fabric from the oblique thrust ramp at Vallescura (modified from Satolli et al., 2020). Equal area projections in geographic coordinates of the principal magnetic susceptibility axes at site level (left) and relative subfabrics when detected (middle and right), The Pj values are reported for comparison. Legend as in **Figure 4.9**.

magnetic foliation. The k_1 axes form an angle of about 122° between subfabrics. Instead, at site BMC3 specimens with negative χ_m values (BMC3-Sf1 in **Figure 4.10**) define a prolate subfabric characterized by higher Pj.

All sites from Vallescura have a consistent magnetic fabric (**Figure 4.11**). Overall, the AMS fabric shows a magnetic foliation SW-dipping at low angle with slightly dispersed k_1 and k_2 axes. The Pj values are moderate (Pj = 1.040 ± 0.017) and the shape parameter is slightly oblate with mean values T = 0.283 ± 0.264 (**Figure 4.8**).

Two different subfabrics are detected at sites level: i. subfabric 1, characterized by a magnetic foliation SW-dipping and sub-horizontal SW-NE to WSW-ENE trending magnetic lineation; ii. subfabric 2 shows a sub-horizontal magnetic foliation and NW-SE to N-S trending k_1 axes.

Subfabric 1 dominates the main fabric. It strongly affects the orientation of both magnetic foliation and lineation. Furthermore, k_1 and k_3 axes show counterclockwise (CCW) and clockwise (CW) rotations when the distance from the main thrust increases, in the hanging wall and footwall respectively. Instead, subfabric 2 shows consistent configuration close to the main thrust with a NW-SE-trending magnetic lineation. In the footwall, k_1 rotates by 116° CCW passing from site VMC1 to VMC2, when increasing the distance from the thrust.

4.3.3 AARM, AIRM and HF-AMS

Anisotropy of magnetic remanence (ARM) experiments were conducted on selected samples showing representative patterns/subfabrics. The selection was based on the orientation of the principal magnetic susceptibility axes, their relationship to meso-scale structural elements (see, 4.4 Discussion), and structural position.

The results reveal well-defined magnetic fabrics for all detected patterns and different ApARM experiments (**Figure 4.12**). Overall, the Pj values of ARM experiments increase significantly compared with the AMS values (**Figure 4.S 1**; **Table 4.S 2**). The different ApARM and AIRM experiments do not show large variations in Pj at the site/subfabric level. Only the AIRM for subfabric MSC2-SF1 (Stage A in **Figure 4.S 1**) and the $ApARM_{100\text{-}40}$ for VSR1 (Stage E// in **Figure 4.S 1**) show higher values than the other ARM experiments, probably due to local variations. No general trend was also observed in T variations (**Figure 4.S 2**; **Table 4.S 2**). In the frontal thrust ramp, significant changes in the shape parameter were observed for subfabrics MSC2-SF1 (Stage A in **Figure 4.S 2**) and SSR1-SF1 (Stage E_{FTR} in **Figure 4.S 2**), where T changes from prolate/neutral for AMS to predominantly oblate for all ApARM and AIRM experiments. In the oblique thrust ramp, the mean T values reveal neutral fabric for both AMS and all ARM experiments. In contrast, oblate fabric was observed for $ApARM_{100\text{-}40}$.

The F-test reveals lower values for samples with remanent magnetization intensity < 1e-05 $Am^2\ Kg^{-1}$, with no direct correlation with the different coercivity window of the ARM experiments (**Figure 4.12c**). AIRM

shows the highest F-test values, generally above 3.48 (lower threshold of statistically anisotropic samples within the 95% probability range). Overall, the F-test values are quite low and suggests a low content in ferromagnetic minerals. No relationship with the ARM coercivity window or lithology is observed for the Scaglia Rossa and Scaglia Cinerea Fms. (**Figure 4.12d**). In contrast, most of the samples from the Marne con Cerrogna Fm. reveal significantly low F-test values for $ApARM_{40\text{-}0}$, which might contribute to the greater dispersion of A_1 and A_2 axes for this subfabric.

After removing the few outliers with the lowest F-test and Pj > ±2σ, anisotropy of magnetic remanence experiments from the frontal thrust ramp show well-clustered axes at the subfabric level (**Figure 4.12a**). The subfabric MSC2-SF1 shows sub-vertical A_3 axes that coincide with the direction of k_3, while A_1 axes are interspersed in the sub-horizontal plane (e.g., bedding plane). In contrast, AIRM fabric displays agreement between the orientation of axes I_1 and k_1, but I_3 slightly differs from k_3.

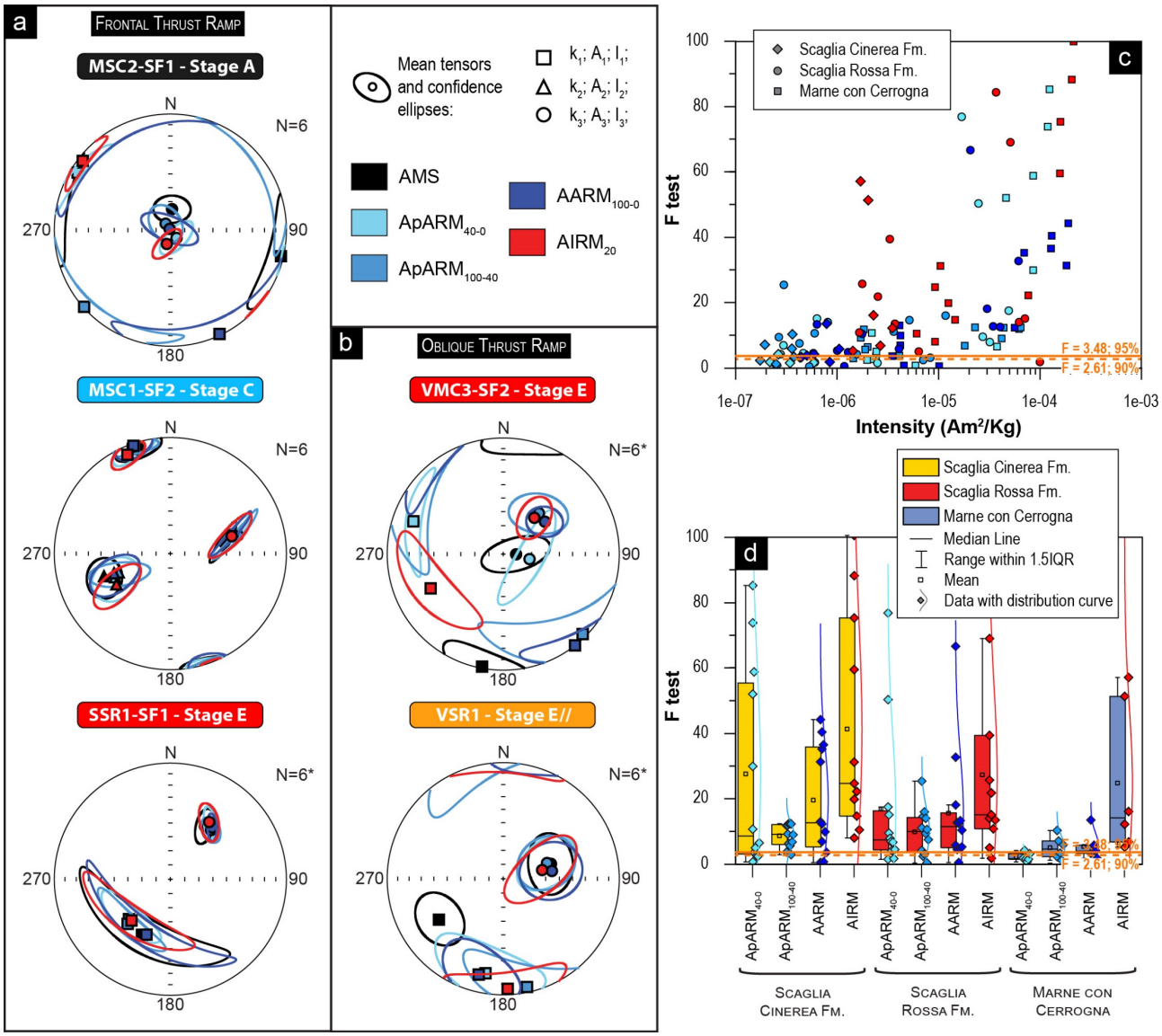

Figure 4.12. Principal directions and confidence ellipsoids of the anisotropy of magnetic remanence (ARM) experiments in: (**a**) Frontal Thrust ramp; (**b**) Oblique thrust ramp. Variations of the F-test versus remanent magnetization (**c**). Box-and-whisker plot with data and normal distribution curves of the F-test among lithologies and ARM experiments (**d**).

The orientations of the principal axes for MSC1-SF2 and SSR1-SF1 are well-concentrated and statistically indistinguishable from those of the AMS, suggesting the same orientation among ferromagnetic minerals activated by the different ARM and AIRM experiments.

In the oblique thrust ramp, fabric variations among AMS and ARM experiments are more visible (**Figure 4.12b**). For VMC3-SF2, ARM experiments show a steeper magnetic foliation than AMS. Only $ApARM_{40\text{-}0}$ shows A_3 axes coincident with k_3. A_1 is congruent among ARM experiments but rotated about 50°-60° with respect to k_1 (**Figure 4.12b; Table 4.S 2**). The AMS and AARM experiments for subfabric VSR1-SF1 show common magnetic foliations, but again the magnetic lineation is differently oriented from the k_1 strike.

To investigate the response of paramagnetic minerals and iron oxides to different deformation regimes, few samples from the representative patterns were subjected to high-field torque magnetometer measurements. The selected samples were taken from the Scaglia Cinerea and Scaglia Rossa Fms.. The high-field AMS indicates that the anisotropy is controlled by 70 ± 11% paramagnetic minerals and a minor ferromagnetic fraction of 30 ± 11%.

The high-field paramagnetic ($HF\text{-}AMS_{para}$) and ferromagnetic ($HF\text{-}AMS_{ferro}$) subfabrics for MSC2-SF1 show subvertical k_3 coaxial with those of the low-field AMS (LF-AMS) and the A_3 axes (**Figure 4.13a**). The k_3 and A_3 axes agree with the pole of the bedding (**Figure 4.13b, c**), while k_1 and k_2 for both $HF\text{-}AMS_{para}$ and $HF\text{-}AMS_{ferro}$ are interspersed within the bedding plane. The absence of a preferred direction for the k_1 and A_1 axes in the bedding plane is well illustrated by the scattering of data along the lower side of the ternary diagram (**Figure 4.13b**).

For the Subfabric MSC1-SF2 (**Figure 4.13a**) the principal axes of the $HF\text{-}AMS_{para}$ and $HF\text{-}AMS_{ferro}$ agree with the direction of the LF-AMS and ARM experiments. Thus, all tensors show a common magnetic foliation consistent with the S planes (compare **Figure 4.13a** and **Figure 4.13b**) with the maximum axes sub-parallel to the S-C intersection. In fact, data are clustered at the lower left vertex of the ternary diagrams (**Figure 4.13c**).

For the Scaglia Rossa Fms., $HF\text{-}AMS_{para}$ is generally coaxial with the LF-AMS, regardless of the different AMS pattern. In contrast sample SSR1_4B where display k_1 and k_2 axes of $HF\text{-}AMS_{para}$ and $HF\text{-}AMS_{ferro}$ at a high angle or exchanged with LF-AMS. In addition, the $HF\text{-}AMS_{ferro}$ for VSR1 reveals the same axes orientation as ARM experiments, having particular agreement with the $ApARM_{100\text{-}40}$ (**Figure 4.13a**).

4.4 Discussion & comparison with structural data

Magnetic fabric analysis revealed straightforward correlations with structural data (**Figure 4.14**; **Figure 4.15**). It was possible to infer 6 different AMS fabrics, named from A to F according to the intensity of deformation; symbols * and // indicate inverse fabric and parallelism with transport direction, respectively. In the following, we report the comparison between AMS and structural data at site level.

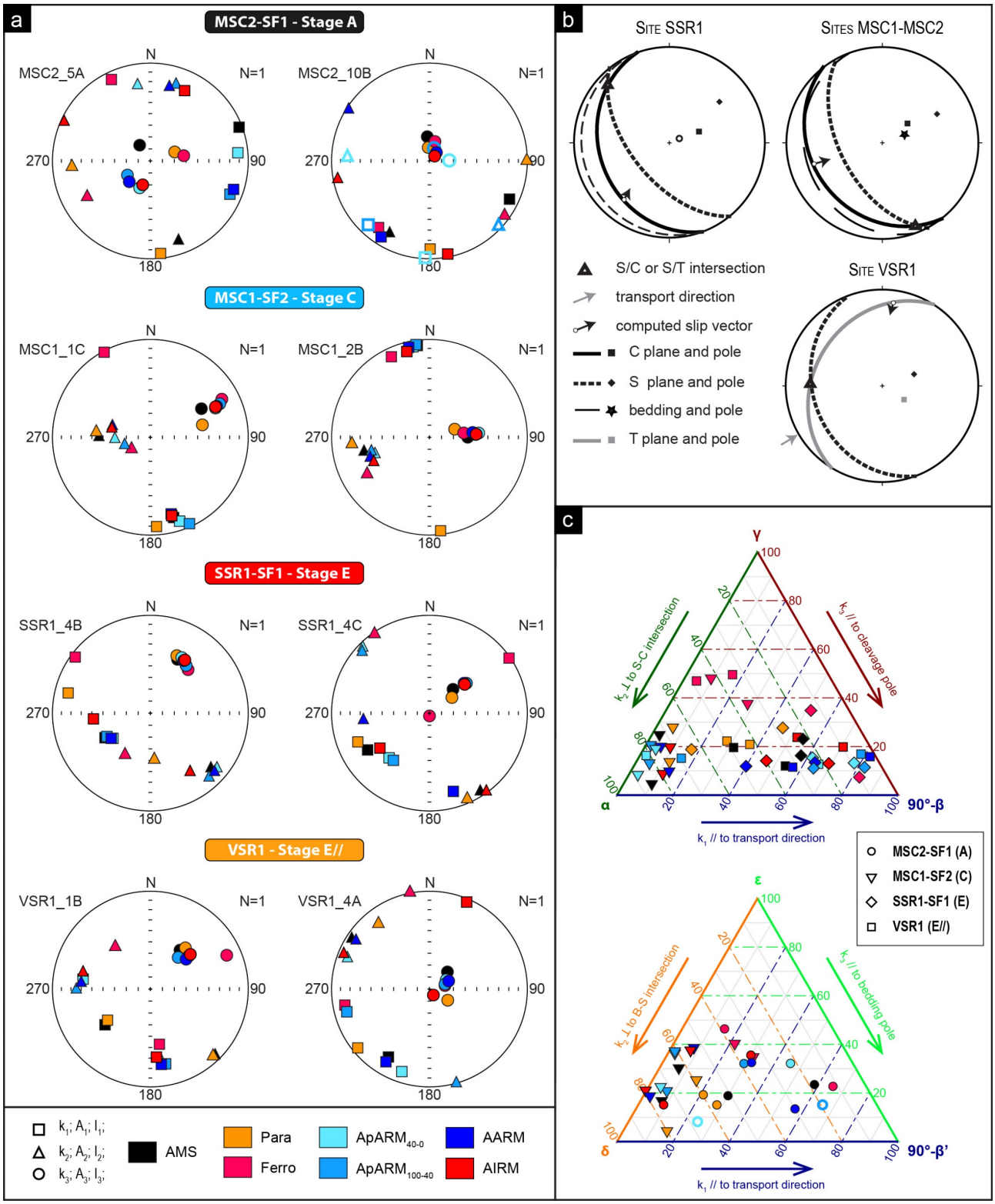

Figure 4.13. (**a**) Stereoplots of the principal directions of the low-field anisotropy of magnetic susceptibility (AMS), anisotropy of magnetic remanence (ARM) experiments and the paramagnetic and ferromagnetic components of the high-field AMS for representative samples, classified after stages. Open symbols represent data with F-test lower than 5; (**b**) Summary of the structural data (see **Figure 4.3** for details); (**c**) Ternary diagrams (see **Figure 3.3** for parameters details) relating structural and anisotropy of magnetic susceptibility and remanence data.

At Sassotetto, subfabric 1 is represented by a magnetic foliation parallel to the pressure solution cleavage, where k_1 is close to the direction of the slip vector. This subfabric may represent an advanced stage of

deformation with k_1 parallel to the transport direction (Stage E, **Figure 4.14**). In the same locality, subfabric 2 shows k_1 and k_3 consistent with S/C intersection and S pole, respectively. It represents the early stage of shearing with k_1 at the S/C intersection (Stage C, **Figure 4.14**).

At Monastero, a different magnetic fabric is documented in sites MSC1 and MSC2, sampled at 15 m and 45 m from the main thrust, respectively. In site MSC1, k_1 is at the S/C intersection and the magnetic foliation is parallel to the S plane. In particular, subfabric 1 reveals the coincidence between k_3 and S pole, but k_1 axes are dispersed in the foliation plane parallel to S. Subfabric 2, instead, reveals a better clustering of k_1, aligned with the S/C intersection. Here, the two subfabrics may represent the same process of earlier deformation stages (Stage C) with a better definition of the tectonic fabric in subfabric 2 due to higher χ_m values.

In site MSC2, subfabric 1 shows a horizontal magnetic foliation consistent with the bedding and moderate dispersion of k_1 and k_2 axis, representing the preserved sedimentary fabric of the Scaglia Cinerea Fm. (Stage A, **Figure 4.14**). In subfabric 2, k_2 and k_3 are dispersed on a girdle and k_1 is at the S/C intersection. This configuration might represent the early stage of deformation (Stage B), where the sedimentary fabric is partially preserved and k_1 corresponds to the intersection lineation between bedding and cleavage. In fact, in incipient deformation stages the magnetic foliation remains parallel to the bedding while the magnetic lineation becomes perpendicular to the bedding-parallel shortening. When the deformation increases, the magnetic foliation poles create a girdle parallel to the shortening (Hrouda & Chadima, 2020). Furthermore, principal axes of maximum susceptibility are particularly sensitive to tectonic shortening, as they develop a magnetic lineation that mimics the intersection of bedding and tectonic flattening plane (Parés, 2015).

At Infernaccio, subfabric 1 shows the parallelism between magnetic foliation and S plane, and k_1 is moving toward the slip vector direction (Stage D, **Figure 4.14**). On the contrary, subfabric 2 reveals k_1 axes at high angle in respect to the S/C intersection and sub-parallel to the slip vector (Stage E, **Figure 4.14**).

Where the magnetic lineation is mainly defined by paramagnetic carriers, it evolves from parallelism to the S/C intersection during earlier deformational stages to parallelism to the slip vector in advanced stages (Parés et al., 1999; Pueyo Anchuela et al., 2010).

The configuration of subfabric 1 is consistent between Sassotetto and Infernaccio, differing only by 24° in the magnetic foliation orientation. Instead, subfabric 2 shows an increment in k_1 axis inclination. On the contrary, at Monastero a change in magnetic foliation dipping angle is visible in both subfabrics. Particularly, subfabric 1 shows a 61° CW rotation of the magnetic lineation associated with the verticalization of the magnetic foliation from site MSC1 to site MSC2. In both sites, subfabric 2 shows a consistent sub-horizontal N-S trending magnetic lineation. Only an increment in the magnetic foliation dipping is here visible.

Overall, the simple-shear-dominated deformation regime (Calamita et al., 2012) from the frontal thrust ramp shows a magnetic foliation parallel to the S or in between S and C planes and k_1 parallel to the S/C intersection or to the slip vector, depending on the degree of deformation (from Stage C to E). Sedimentary

features and early stage of cleavage development (Stages A and B) are also visible at site MSC2 (45 m from the thrust).

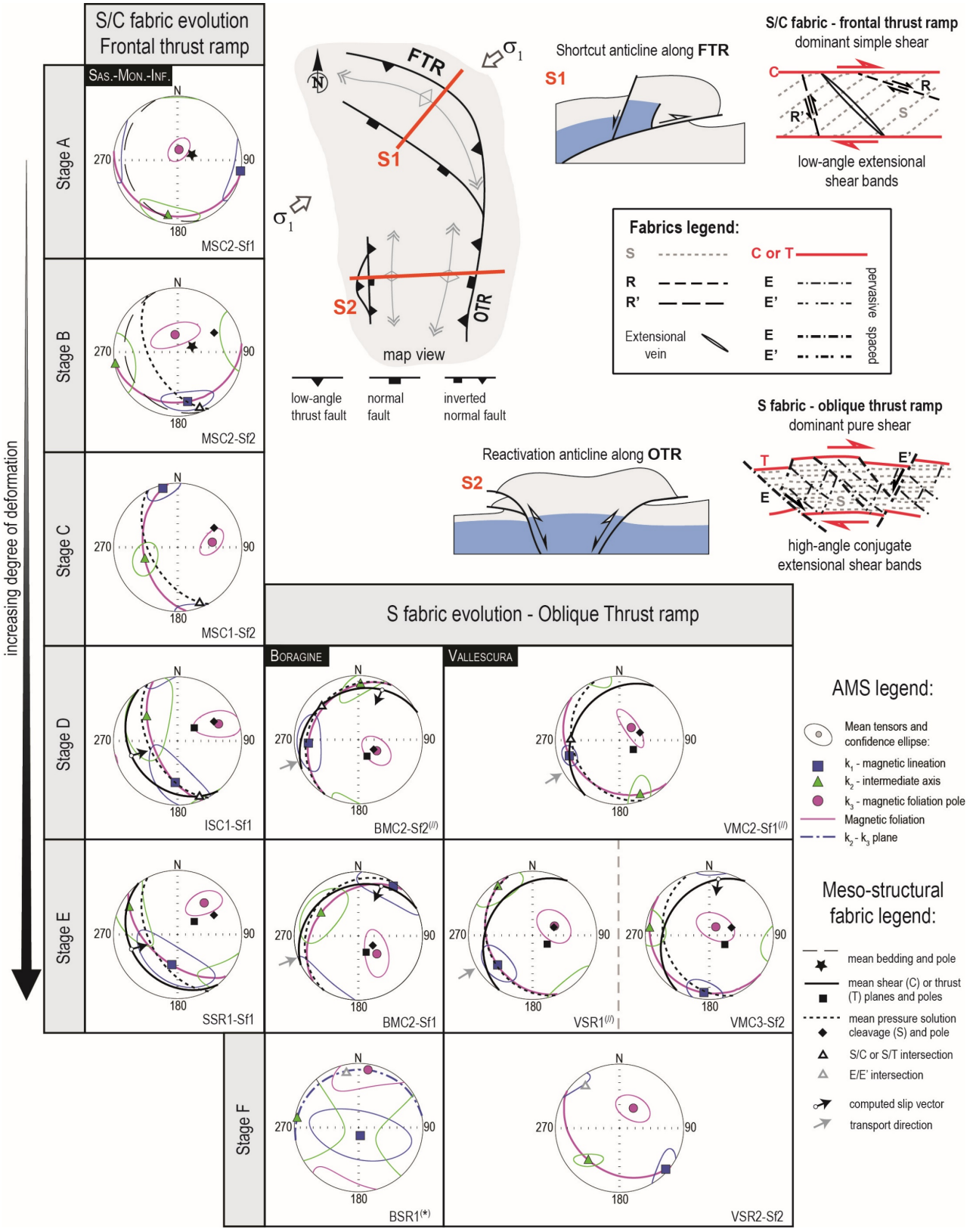

Figure 4.14. Summary of magnetic fabric stages and comparison with structural data. Representative examples from the different deformation regimes are reported (modified from Satolli et al., 2020). Conceptual diagram of the different types of shear deformation fabric (ZX section of strain ellipses) related to frontal (FTR) and oblique (OTR) thrust ramps (modified from Calamita et al., 2012; Pace et al., 2015; Satolli et al., 2020)

In particular, the interrelation between the AMS directional data and the main structural elements (i.e., pole of the cleavage, S-C intersection, and transport direction) of the different AMS fabrics (Stages A to E) are clearly visible in the ternary diagrams (**Figure 4.15a, b**; see details for plotting the diagrams in 3.5 Ternary Diagrams). Specimens from the advanced tectonic stages (Stages C to E; **Figure 4.15a**) are distributed along the lower side of the ternary diagram, confirming good parallelism between magnetic foliation and cleavage.

Data clustered around α and 90°-β vertices reflect the progressive rotation of k_1 from parallel to the S-C intersection (Stage C) to aligned with the transport direction (Stage E), respectively. In addition, the presence of specimens clustered in the lower central portion of the ternary diagram showed the occurrence of samples with a magnetic lineation at an intermediate orientation between S/C intersection and the slip vector (Stage B; **Figure 4.15a**). Stage A and B reveal slightly high values of the ε angle (i.e., angle between the magnetic foliation and the bedding), suggesting a magnetic foliation partially offset the bedding plane (**Figure 4.15b**). The distribution of Stage D data near the left side of the diagram indicates a progressive concentration of the k_1 axis at the intersection lineation (between bedding and cleavage).

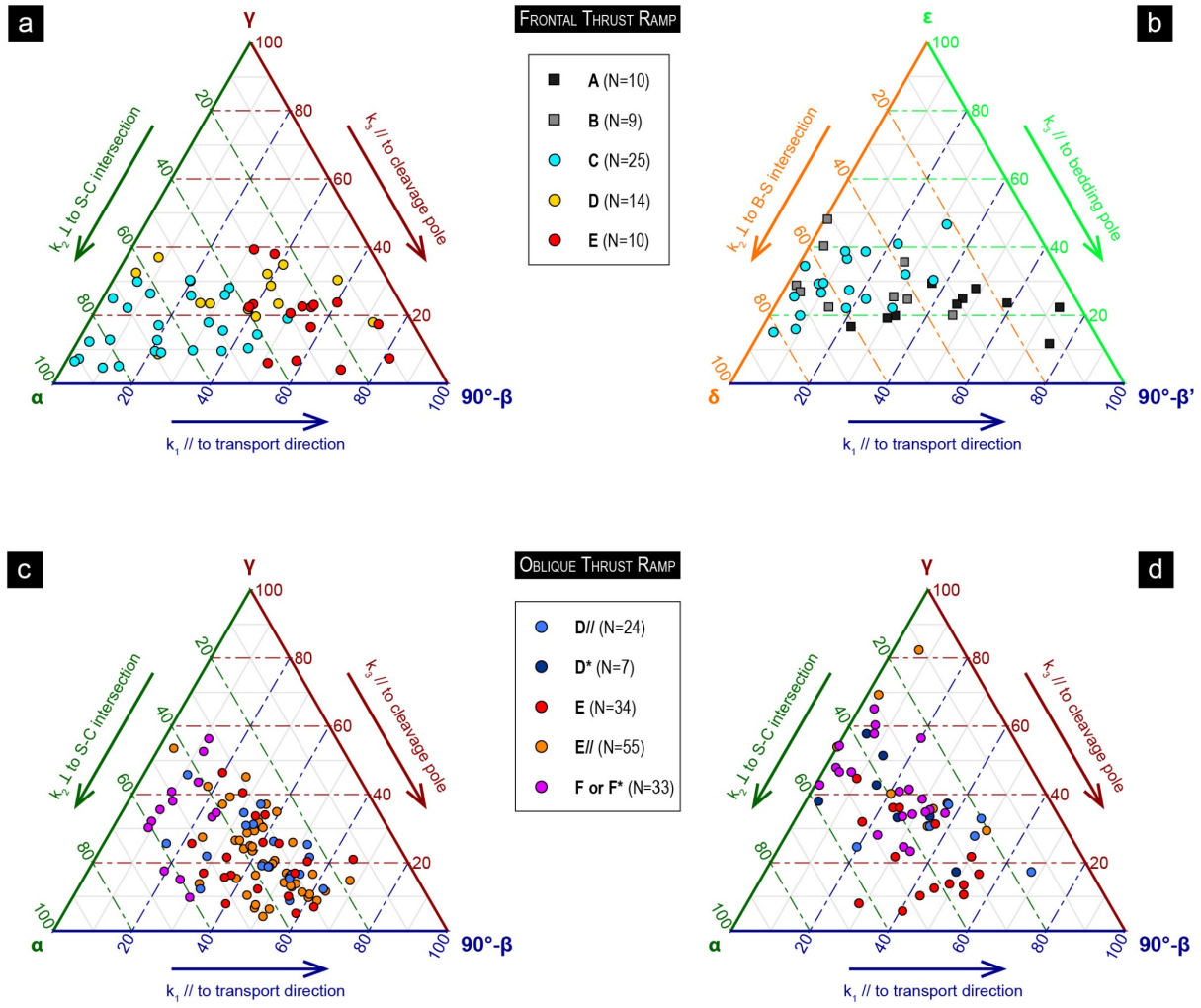

Figure 4.15. Ternary diagrams (see **Figure 3.3** for parameters details) relating structural and anisotropy of magnetic susceptibility (AMS) data from the Frontal thrust ramp (**a-b**), classified after stages; data from the oblique thrust ramp at Vallescura (**c**) and Boragine (**d**).

At Vallescura and Boragine, the sampling was done across the thrust plane, both in the hanging-wall and footwall block. In the hanging-wall block of Vallescura, site VSR1 and subfabric 1 of VSR2 show the magnetic foliation consistent with the S plane and k_1 parallel to the transport direction (Stage E//, **Figure 4.14**). Subfabric 2 of site VSR2 reveals a k_1 axis coincident with the E-E' intersection (Stage F, **Figure 4.14**).

In the footwall block, also VMC1 magnetic fabric shows a parallelism between magnetic foliation and S plane. Subfabric 1 is characterized by a fan dispersion of k_2 and k_3 and k_1 parallel to the transport direction (Stage E//), while subfabric 2 reveals k_1 axis parallel to the E-E' intersection (Stage F). In both VMC2 e VMC3 the subfabric 1 is characterized by the parallelisms between magnetic foliation and S planes, and k_1 is grouped in an intermediate orientation between the S/ T intersection and the transport direction (Stage D//). On the contrary, in both sites, subfabric 2 shows a parallelism between magnetic foliation planes and S planes. The k_1 axes are N-S trending and may indicate a parallelism with the inferred slip vector (Stage E//).

At Boragine most sites show low bulk magnetic susceptibility values (k_m), close to the instrumental limit. This might have caused problems related to mean tensors and their confidence ellipses calculation. For that reason, only site BMC2, characterized by high χ_m values, is considered reliable for further interpretations. However, for the sake of completeness, we reported the comparison between AMS and structural data for all sites.

In the hanging wall, sites BSR1 and BSR2 show highly scattered axes, with k_1 mostly subvertical and dispersed on an E-W girdle. In both sites k_3 is partially grouped at the E-E' intersection (Stage F*). At site BMC1, k_2 and k_3 axes are highly dispersed along a N-S girdle, while k_1 axes are grouped in the transport direction (Stage E//).

At site BMC2, subfabric 1 shows a magnetic foliation intermediate between S and T planes and k_1 has a double tendency to parallelize with the direction of the slip vector and the transport direction (Stage E or E// in **Figure 4.14**). Subfabric 2 is characterized by a magnetic foliation parallel to S planes and k_1 intermediate between S/T intersection and the slip vector (Stage D//, **Figure 4.14**).

Finally, in BMC3, subfabric 1 shows a subhorizontal magnetic foliation with interspersed k_2 and k_3 axes, while k_1 are mostly grouped with double tendency in the slip vector and the transport directions. Subfabric 2 shows high dispersed k_1 and k_2 axes, while k_3 is grouped at high angle from N to E. The fabric is inverse and k_3 might be considered to assume an orientation intermediate between the directions of the slip vector and the inferred slip vector.

In this pure-shear-dominated deformation regime (Calamita et al., 2012) the magnetic foliation is mostly parallel to S as most of samples are distributed in the lower side of the ternary diagram (**Figure 4.15c**). In addition, the presence of specimens scattered toward the upper vertex might be assigned to the local high content in diamagnetic minerals at some sites from Boragine (**Figure 4.15d**).

Overall, k_1 (or k_3 in case of possible inverse fabric) reveal different specific orientations: i. parallel to the slip vector (Stage E or E*); ii. parallel to the transport direction (Stage E//); iii. in between the S/T intersection

and the slip vector (Stage D// or D*); iv. parallel to the E-E' intersection close to the main thrust (Stage F or F*).

The different orientation of k_1 with respect to the structural elements is emphasized by the distribution of the data in the ternary diagrams (**Figure 4.15c, d**). In fact, at Vallescura, Stage E or E// data are clustered near the lower right side, where the partial discrepancy between the orientation of k_1 and the transport corresponds to the distance from the 90°-β vertex (**Figure 4.15c**). In contrast, at Boragine, the presence of data close to the γ vertex for Stage E// might indicate the presence of inverse or mixed fabric (**Figure 4.15d**). All samples associated to Stages D are distributed in the center of the diagram, indicating incomplete parallelization of both magnetic foliation and lineation to the cleavage and transport direction, respectively. Finally, Stage F fabric shows magnetic foliation at a high angle to the cleavage. The data distributed close to the left side of the diagram suggest that the k_1 axis is subparallel with a direction slightly different to the S-C intersection. In fact, the E-E' intersection is rotated only 20° with respect to the S-C intersection.

In addition, the relationships between the para- and ferromagnetic (s.l.) subfabrics and the petrofabric of tectonites reveal variation of the individual subpopulation of grains in recording changes in deformation regimes associated with frontal and oblique thrust ramps.

Along the frontal thrust ramp, the ferromagnetic and paramagnetic subfabrics generally agree with the AMS axes orientations and show similar geometric relationships with the structural fabric (**Figure 4.16**). The sedimentary origin of Stage A fabric is emphasized by the configuration of the ferromagnetic subfabrics. All subpopulations of ferromagnetic grains show magnetic foliation consistent with the bedding and minimum and maximum axes randomly oriented within this plane (see the scattering of Stage A data in the ternary diagram, **Figure 4.16b**). The weak or absent preferential alignment of minerals might be ascribed to sedimentary process as deposition and/or compaction and a neglectable tectonic overprint (Mattei et al., 2004; Cifelli et al., 2005; 2009). In addition, the mean A_1 axis of the $AARM_{100\text{-}0}$ and the k_1 of the HF-AMS_{para} agreed with the bedding-cleavage (B-S intersection; **Figure 4.16b**, **Figure 4.13c** and **Figure 4.12a**), showing a similar pattern as the Stage B (early stage of incipient deformation). This configuration might reveal that paramagnetic minerals and a certain subpopulation of ferromagnetic grains were more sensitive to tectonic overprint (Sun et al., 1995; Hrouda et al., 2018).

The magnetic fabrics consistent with advanced deformation stages (Stage C and E) reveal coaxial para- and ferromagnetic subfabrics (see, **Figure 4.13a** and **Figure 4.12a**) with strong parallelism with the structural elements (**Figure 4.16a**). These features indicate that different minerals recorded the same deformation (Biedermann et al., 2016). In particular, those fabric have a common magnetic foliation parallel to the S planes and magnetic lineation parallel or orthogonal to the shear direction for Stage C and E, respectively (clusters close to the δ and 90-β vertex in **Figure 4.16a**). The complete alignment of the different magnetic minerals (s.l.) at stage level might indicate that each mineral followed the same evolution trend with changes in orientation depending only on incremental deformation approaching the main thrust planes.

In the oblique thrust ramp, the AMS configuration mostly depends on the orientation of the paramagnetic minerals, while the subpopulations of ferromagnetic grains show variable contribution to the total fabric but reveal different deformation stages (**Figure 4.16a**, **Figure 4.13c** and **Figure 4.12b**). In fact, AMS and HF-AMS_{para} show magnetic foliation between S and C planes and the maximum axis consistent with the transport direction or slip vector for Stage E and E//, respectively (see, **Figure 4.12b** and **Figure 4.13**). In contrast, subpopulations of ferromagnetic grains are generally coaxial with each other but with different configurations (**Figure 4.16a** and **Figure 4.12b**). Ferromagnetic grains of Stage E show a steeper magnetic foliation consistent with the extensional plane and a magnetic lineation sub-parallel to the E-E' intersection (compare **Figure 4.12b** and **Figure 4.3**), revealing the same pattern of Stage F recorded by a few AMS subfabric at both Vallescura and Mt. Boragine (see, **Figure 4.14**). Stage E// samples show magnetic foliation in common with the AMS and sub-parallel to the S planes (**Figure 4.16a** and **Figure 4.13a-b**), but differently from the AMS the maximum axes agree with the calculated slip vector rather than the transport direction. These configurations reveal variable sensitivity of ferromagnetic minerals in recording the deformation in a pure-shear-dominated regime.

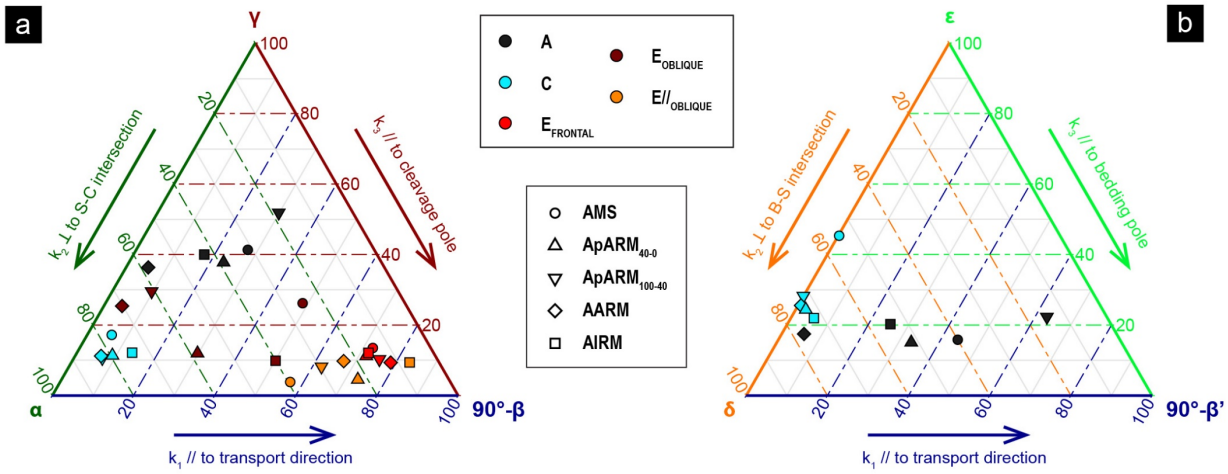

Figure 4.16. Ternary diagrams (see **Figure 3.3** for parameters details) relating structural and mean anisotropy of magnetic remanence (ARM) data.

4.5 Conclusions

We investigated the magnetic fabric in shear zones from 2 sectors of the Northern Apennines fold-and-thrust belt, characterized by different combinations of simple and pure shear involving calcareous and marly rocks (Calamita et al., 2012; Pace et al., 2015): the OAS frontal thrust ramp and the OAS oblique ramp.

The documented magnetic fabric shows similar evolution in all the deformation regimes, depending upon the increasing of deformation (lower vorticity number) and proximity to the main thrust (**Figure 4.14**). Six different fabrics were identified:

A. sedimentary fabric characterized by magnetic foliation-bedding parallelism (Hrouda & Chadima, 2020, and references therein);

B. an early stage of deformation with k_1 at the intersection between bedding and S plane (so called intersection lineation; Hrouda & Chadima, 2020);

C. magnetic foliation parallel to S and k_1 parallel to the S/C intersection, progressively evolving with the deformation increments (Parés et al., 1999; Pueyo Anchuela et al., 2010) in stage D;

D. magnetic foliation parallel to S and k_1 (or k_3 in case of possible inverse fabrics documented in the Boragine sector) intermediate between S/C intersection and the slip vector. In case of pure-shear-dominated regime, k_1 is intermediate between S/T intersection and the transport direction;

E. the magnetic foliation shows a double tendency to parallelize either the S or the C planes, and k_1 is parallel to the slip vector or the transport direction (in case of pure shear component);

F. documented in pure-shear-dominated deformation regime only, shows the parallelism between k_1 (or k_3 in case of possible inverse fabrics) axis and extensional planes intersection.

These results show that the magnetic fabric is more sensitive to the simple shear deformation, as the magnetic lineation tends to parallelize mostly with the computed slip vector. Under this case, para- and ferromagnetic minerals are coaxial and record the same deformation stages.

In pure-shear dominated regimes, the magnetic lineation becomes parallel to the transport direction when the deformation is really intense (sites at less than 15–30 cm from the thrust plane). This behaviour is also recorded by paramagnetic minerals, while the ferromagnetic subfractions exhibit different deformation stages.

These results suggest that it is fundamental to use a combination of density diagrams and cluster analysis on AMS data in order to discriminate subfabrics linked to different events. Moreover, separate the contribution of paramagnetic and ferromagnetic subpopulation of grains is suggested to constrain the progressive evolution of the magnetic fabric in different deformation regimes.

In this way, the potential of magnetic fabric as a tool to unravel different sedimentary or tectonic features and better understand the faulting processes is enhanced.

Chapter 5

SECOND CASE STUDY: The SVU

The SVU is a well-studied exhumed analogue of shallow subduction megathrust (4-5 km of burial and Tmax ≈ 120–150 °C) involving tectonic slices of mainly marly and clay-rich units (Reuter et al., 1991; Remitti et al., 2007; Vannucchi et al., 2008; Carlini et al., 2013). This shear zone provided an opportunity to study the heterogeneities in the rock magnetic signature across an intraplate shear zone and their relationships to strain partitioning and/or localization (results have been published in Robustelli Test & Zanella, 2021 and supported here by an additional case study from the SVU). Moreover, geochemical data on shear veins recorded the circulation of different fluids during the seismic cycle and its variable influence on deformation. Then, a detail characterization of the magnetic mineralogy to reveal evidence of fluid-rock interaction along intraplate shear zones is also reported.

5.1 Geological setting

The Sestola-Vidiciatico Tectonic Unit (SVU), in the Northern Apennines (**Figure 5.1a, b**), represents a plate boundary shear zone, accommodating the displacement between the overriding European plate and the underlying Adria microplate from the early to middle Miocene (Vannucchi et al., 2008; Remitti et al., 2013). The SVU is interpreted as an exhumed analogue of the shallower portion of a subduction megathrust (up to 5 km of vertical burial and maximum temperature about 120–150 °C) related to the evolution of an erosive margin (Mittempergher et al., 2018, and references therein). It consists of a complex subduction zone mélange that is about 200–500 m thick (Cerchiari et al., 2020), currently separating the overthrusting late Cretaceous-early Eocene accretionary prism (Ligurian and Subligurian Units) from the underthrusting Tuscan/Umbrian Units of the Adriatic microplate (**Figure 5.1c**) (Vannucchi et al., 2008). The map-scale mélange consists of reworked blocks and slices, up to several hundreds of meters in size, of: (a) External Ligurian/Subligurian Units derived from the pre-existing accretionary complex (e.g., Argille a Palombini and Varicolored shales); (b) Late Eocene-middle Miocene shaly and marly deposits of the prism slope (e.g., Civago marls, Fiumalbo shales, and Marmoreto marls); and (c) debris flows deposit of the frontal sedimentary prism. The tectonic slices are bounded by wavy anastomosing shear surfaces, sub-parallel to the

roof and basal décollement. At local scale, each block can be mapped as single tectonic slice that exhibits a different degree of internal deformation depending on its deformation history and lithification state prior to involvement in the intraplate shear zone. In fact, partially unconsolidated material, such as slope sediments, are the most affected by the stress regime within the megathrust shear zone (Remitti et al., 2007; Vannucchi et al., 2008, 2012). The pile of tectonic slices is displaced by normal faults that allowed the exhumation of portions of the chain preserving their original structural relationship (Remitti et al., 2012).

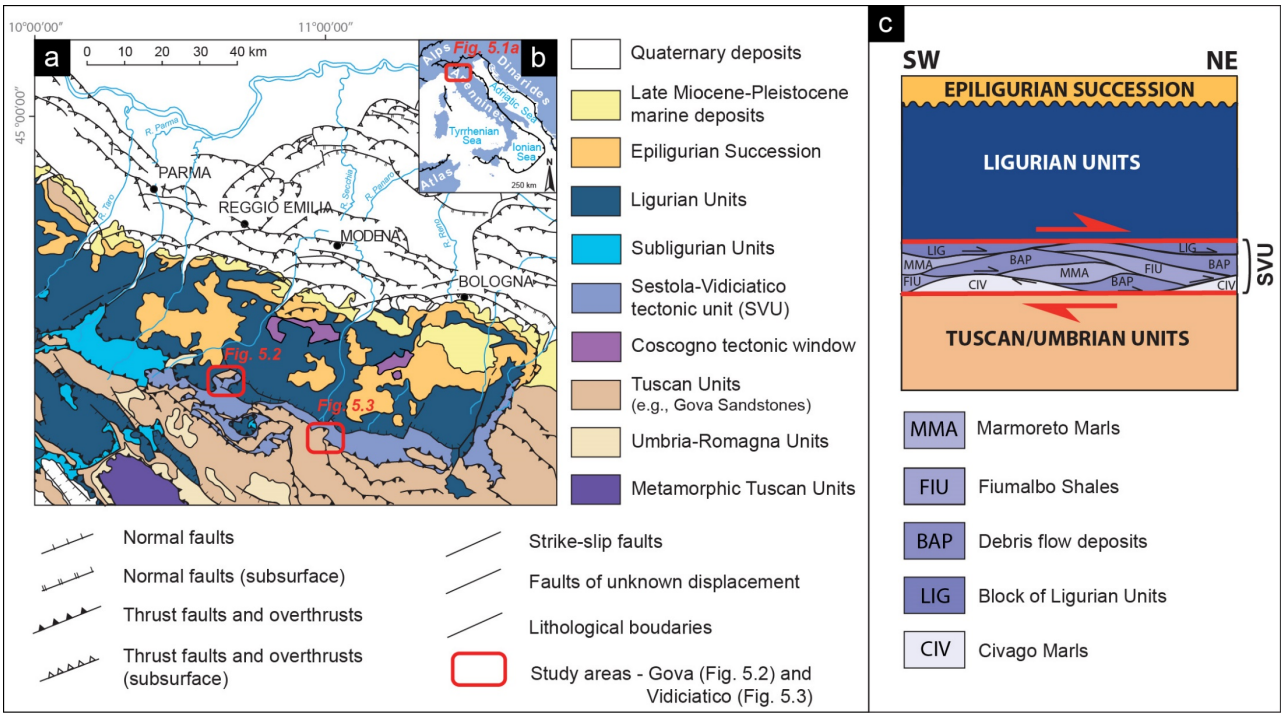

Figure 5.1. (**a**) Structural sketch map of the Northern Apennines (modified from Remitti et al., 2013) and its location in northern Italy (**b**); (**c**) simplified stratigraphic and tectonic relationships in the Apennine intraplate shear zone.

To detect existing variations in strain across intraplate shear zone by rock magnetic signatures, we sampled 29 sites across two sectors exposing the basal thrust of the SVU. Overall, the main target consists of blocks of slope sediments, as their structural fabric closely reflects the tectonic regime of the intraplate shear zone (Vannucchi et al., 2012).

5.1.1 The Gova Tectonic Window

The Gova tectonic window (see location in **Figure 5.1a**) exposes the contact between the Tuscan/Umbrian Units below the Ligurian Units. One of the best-exposed sections of the basal décollement of the SVU is located at the Cadignano Bridge (44°20′12.08″N–10°31′37.99″E). Here, the hanging wall is composed of superposed tectonic slices of slope deposits, whose contacts are marked by calcite shear veins (**Figure 5.2a, b**; Remitti et al., 2012). The kinematic indicators on the basal thrust reveal a mean top to NE transport direction (**Figure 5.2c**). The bedding of marly units is completely disrupted by the pervasiveness of shear surfaces into rhombohedral to lens shape lithons, resulting in a well-developed SW-dipping pressure-solution cleavage. The latter is cut at high angle by extensional veins related to high fluid pressure and hydraulic fracturing (Vannucchi et al., 2010; Remitti et al., 2012; Cerchiari et al., 2020). The footwall corresponds to

early Miocene foredeep deposits of the Adria sedimentary cover (Gova sandstones; Plesi, 2002; Cornamusini et al., 2018) composed by undeformed turbiditic layers intercalated with debris flow and slumps with blocks of Ligurian units. Conjugate sets of strike-slip faults were observed in the first 10 m below the basal contact (**Figure 5.2e**). Just below the contact there is an intruded layer of sheared sandstones, sandwiched between the footwall and the hanging wall, providing evidence for incomplete lithification of the foredeep turbidites when the thrust activated (Remitti et al., 2012).

Sites were located both in the footwall and hanging wall and were named according to the tectonic position (U = Underthrusting sediments; S = Sheared sandstones; and B = Plate boundary shear zone) and numbered by progressive distance from the main thrust (i.e., U1, U2, and U3 at increasing distance from the basal thrust; **Figure 5.2d**). The sampling scheme and site extensions were adapted to lithological variation and intensity of deformation. Based on the high homogeneity of the Gova sandstones, we sampled three sites (1–2 m thick) in the underthrusting sediments, at increasing distance from the basal thrust. In the shear sandstones, we sampled three different blocks along the deformed body to detect any possible fabric variations. In the first tectonic slice of the SVU, we sampled three parallel transects, perpendicular to the basal thrust up to the tectonic contact with the overthrusting slice of Fiumalbo shales (**Figure 5.2a**). The name of the sites is preceded by the number of the transect (i.e., T1-B1; **Figure 5.2d**). Each transect is composed by multiple sites (50 cm–1 m thick), without significant variations at the mesoscale (**Figure 5.2b**). We assume each site as homogeneous in terms of pervasiveness of tectonic structures and deformation intensity since the shear surfaces show the same features at all the scales. We took at least 8–12 oriented hand-samples of 5–20 cm size to ensure a significant statistical analysis.

Sandstone blocks were drilled out to give standard cylindrical specimens (Φ = 25 mm, h = 23 mm), for a total of 123 from the footwall and 29 from the sheared sandstones. For the Civago marls, it was impossible to prepare cylindrical specimens due to the pervasivity of the structures. The marly lithons were thus cut into cubes, mostly equidimensional, preserving the sample orientation. Then, specimens were fixed and centered in standard 8cc plastic cubes with non-magnetic plasticine, obtaining a total of 323 specimens.

5.1.2 The Vidiciatico sector

The deepest portion of the SVU is exposed at Vidiciatico (Vannucchi et al., 2008; 44°10'16.13"N–10°51'42.42"E, see location in **Figure 5.1a**). The main thrust is WNW-dipping at a low angle (~ 30 °) and sub-parallel to the bedding of the foredeep turbidites of the footwall (**Figure 5.3b**). The present-day attitude of the SVU basal thrust is related to the subsequent tilting associated with the exhumation (Remitti et al., 2007). The turbidites of the footwall are poorly deformed with the local presence of shear veins (Mittempergher et al., 2018). The hanging wall includes lenticular-shaped tectonic slices composed by marly rich sediments of the prism slope (e.g., Marmoreto Marls and/or Civago Marls), sedimentary breccias/mélanges (debris flow deposits), and components from the accretionary prism (e.g., Argille a Palombini or Varicolored shales) (Plesi et al., 2002; Vannucchi et al., 2010).

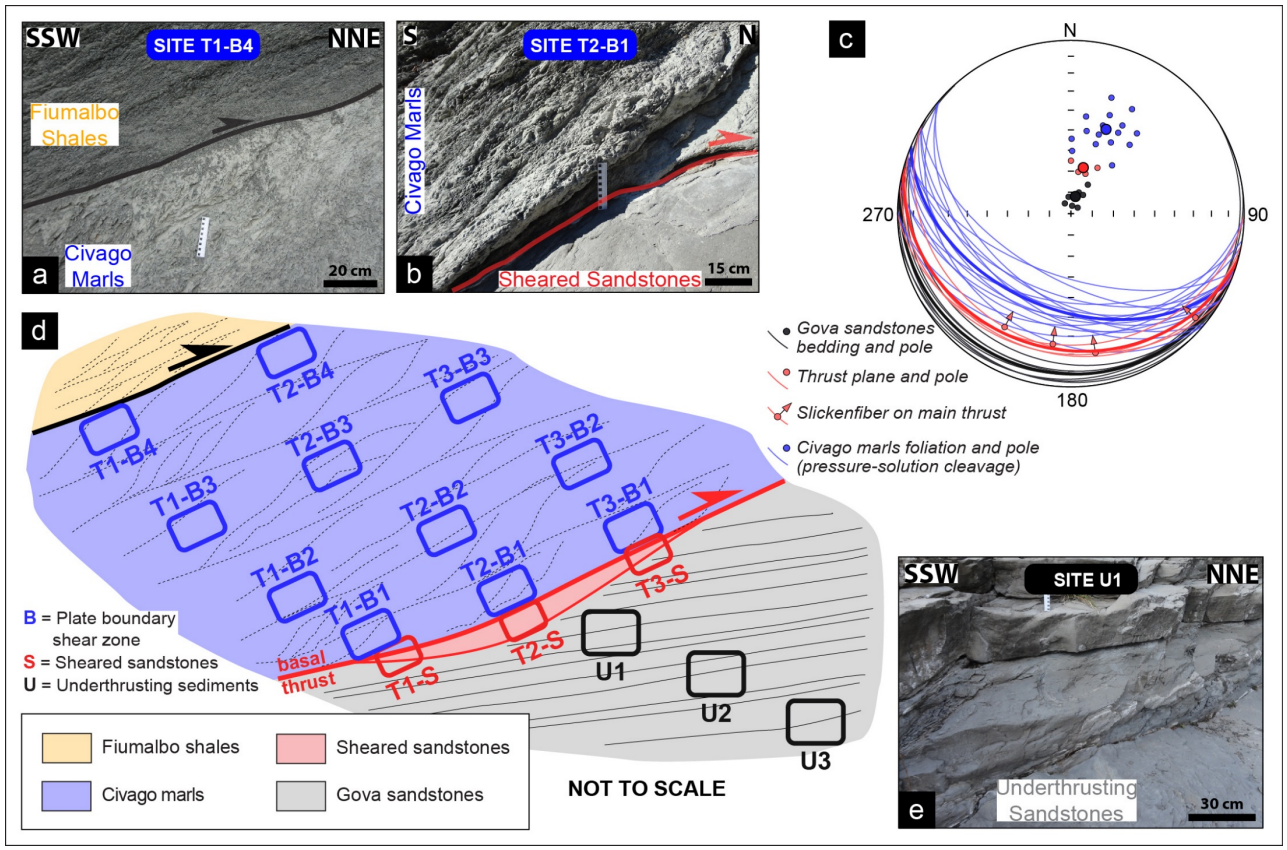

Figure 5.2. (**a**) close-up of the tectonic contact between the Civago marls and the overthrusting Fiumalbo Shale; (**b**) detail of the basal décollement of the Sestola-Vidiciatico Tectonic Unit; (**c**) equal-area projection (lower hemisphere) of the mesoscale structural data (integrated from Remitti et al., 2012); (**d**) sketch of the sites position where, U = underthrusting sediments, S = sheared sandstones, and B = plate boundary shear zone; and (**e**) foredeep turbidites of the footwall cut by strike-slip faults.

The accretionary prism components show a block-in-matrix fabric typical of broken formation (**Figure 5.3f**). This fabric is due to the superposition of two generations of folds that produced a penetrative scaly fabric (Vannucchi and Bettelli, 2002; Vannucchi et al., 2010). The debris flow deposits occur as a polymictic sedimentary breccia characterized by blocks of limestones, sandstones and shales immersed in a pelitic matrix (**Figure 5.3g**). The presence of anastomosed surfaces within the matrix has been associated with dewatering and compaction (Vannucchi et al., 2010). The marly domains show a penetrative fabric, consisting of rhombohedral shape lithons (**Figure 5.3a, e**), related to diffuse shearing that occurred during the early stage of deformation (Mittempergher et al., 2018; Cerchiari et al., 2020). This fabric is cut by localized shear zones sub-parallel to the main faults, suggesting the partitioning of the deformation along main and secondary faults (Cerchiari et al., 2020). Slickenlines on the main faults indicate a dominant top to NE transport direction (**Figure 5.3c**). In addition, two sets of extensional veins are detected and reveal crosscutting relationships with shear veins, suggesting cyclical activation and stress-switching during the evolution of the SVU (Cerchiari et al., 2020). The set of fault-parallel extensional veins reveal high fluid pressure and failure at low differential stress (Mittempergher et al., 2018). Instead, the fault-perpendicular veins, which are folded and shortened, indicate fault-parallel flattening.

The geochemical signature (REE composition; see details in Cerchiari et al., 2020) and stable isotope analysis (^{13}C and ^{18}O composition; see Vannucchi et al., 2020) of the shear veins suggest changes in permeability and drainage of deeper hot exotic fluids in disequilibrium with the fault zone during major seismic events. Instead, the onset of extensional regime during post-seismic and reloading phases produces extensional veins cemented by local fluids in equilibrium with the wall-rocks.

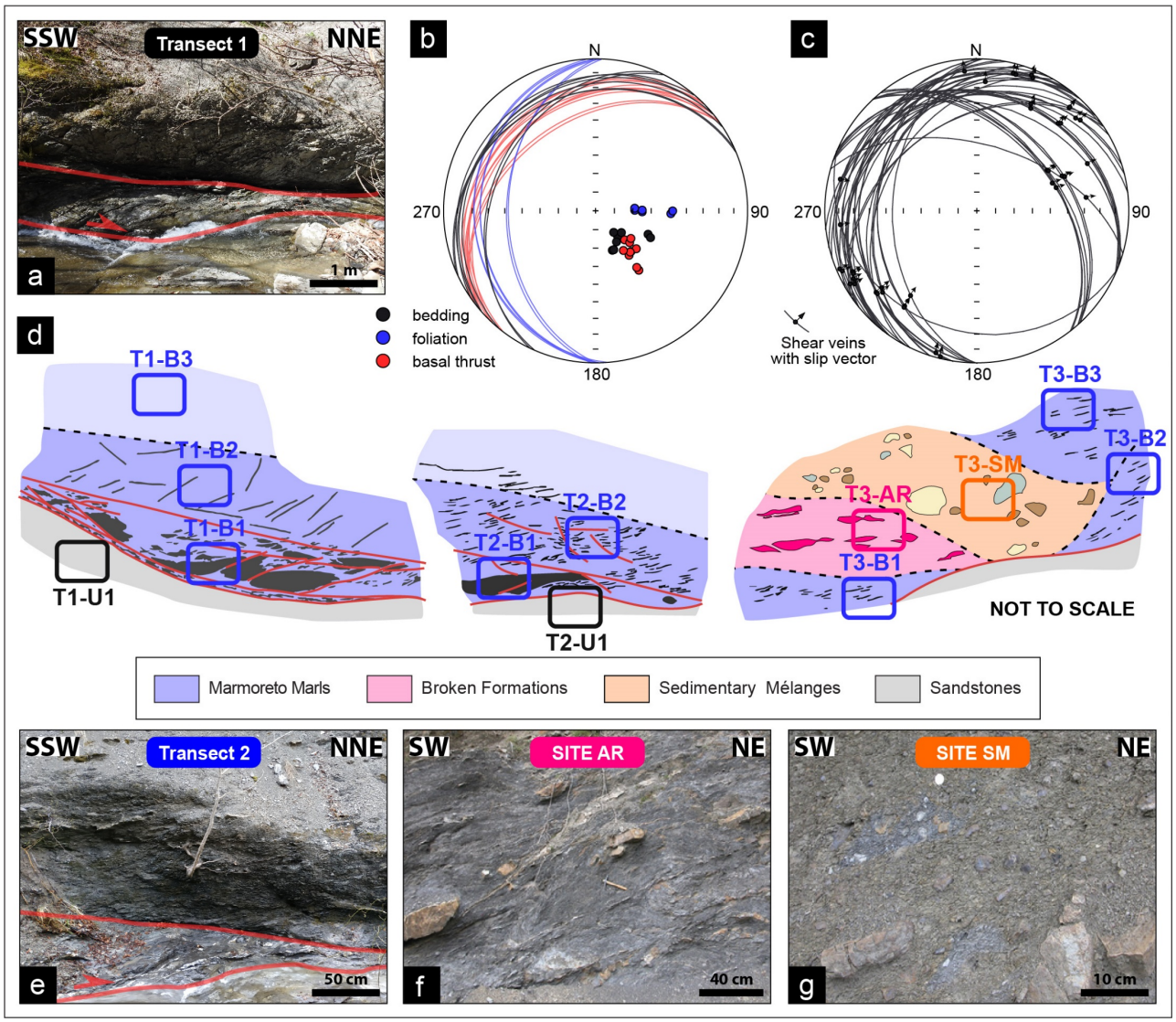

Figure 5.3. Details of the basal décollement of the Sestola-Vidiciatico Tectonic Unit (**a; e**); (**b**) Equal-area projection of the (lower hemisphere) of the mesoscale structural data (**c**) and shear veins with relative slip vectors (integrated from Mittempergher et al., 2018; Cerchiari et al., 2020); (**d**) sketch of the sites position where, U = underthrusting sediments, B = plate boundary shear zone, AR = broken formation, and SM = sedimentary mélange; Close-up of the meso-scale fabric of the broken formation (**f**) and sedimentary mélange (**g**).

Oriented hand-samples were taken from both footwall and hangingwall of the SVU through three transects perpendicular to the basal thrust (see sampling scheme in **Figure 5.3d**). Two sites were sampled in the foredeep turbidites of the footwall. Oriented blocks were drilled out to obtain standard paleomagnetic cylinders (Φ = 25 mm, h = 23 mm), for a total of 37 specimens. Within the SVU, each transect is composed by multiple sites, located at a progressively greater distance from the basal thrust (**Figure 5.3d**). Tectonic

slices of Marmoreto Marls were sampled along transect 1 and 2. Transect 3 also comprises broken formations and sedimentary mélanges. Site names include the transect number, an acronym referring to the structural position or origin of the tectonic slice (U = Underthrusting sediments; B = Plate boundary shear zone; AR = Argille a Palombini or Varicoloured shales - i.e., Broken Formation; SM = Sedimentary Mélange). The sites are then numbered according to their progressive distance from the main fault plane (e.g., T1-B1, T1-B2 and T1-B3). Twelve oriented hand-samples were taken for each site, by sampling the rhombohedral lithons in marly domains or the matrix in case of broken formation and sedimentary mélanges. We also collected few samples from the boudins immersed in the matrix of the Broken formation. Samples were then cut into cubes, obtaining a total of 268 specimens of marls, 37 from the broken formation and 31 from the sedimentary mélange.

5.2 Results

5.2.1 Magnetic Mineralogy

Thermomagnetic curves show a decrease in susceptibility up to 400 °C (**Figure 5.4a**), suggesting the dominance of paramagnetic behaviour. Then, the susceptibility increases until 500 °C and smoothly decreases to zero around 580 °C, indicating the presence of magnetite. Cooling curves are shifted toward higher susceptibility, consistently with the neoformation of magnetite.

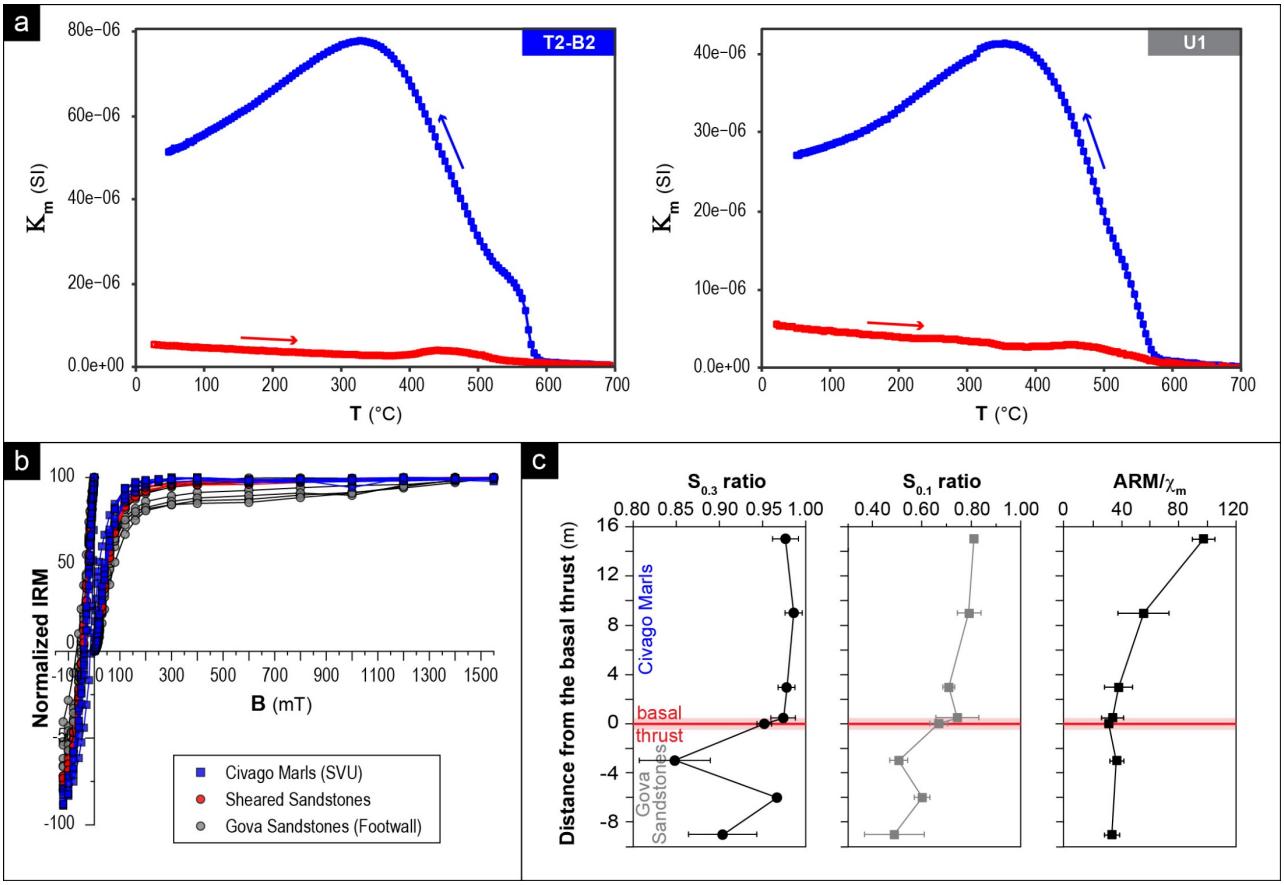

Figure 5.4. (**a**) Thermomagnetic susceptibility curves; (**b**) isothermal remanent magnetization acquisition and backfield curves; and (**c**) plots of S-ratios and anhysteretic remanent magnetization (ARM)/χm versus distance from the basal décollement.

IRM experiments suggest different coercivity phases assemblage in the lithologies (**Figure 5.4b** and **Figure 5.5a**). The Civago marls saturate around 0.2 T, indicating the dominance of low-coercivity phases (**Figure 5.4b**). The Gova sandstones show a mixture of low- and high-coercivity minerals. In fact, after an initial increase up to 0.2 T the IRM do not saturate at the peak-field of 1.5 T. A similar trend is observed for foredeep turbidites and some marly samples at Vidiciatico (**Figure 5.5a**). The Marmoreto Marls typically saturate below 0.2 T (**Figure 5.5a**). The sedimentary mélange and broken formation show IRM curves that saturate at 0.3-0.4 T, suggesting the dominance of low-coercivity minerals such as magnetite.

The S-ratios values (**Figure 5.4c** and **Figure 5.5b**; **Figure 5.S 1** and **Figure 5.S 2**) agree with the dominance of low- to medium-coercivity phases such as magnetite, within the shear zone. In the sandstones, the S-ratios decrease and are consistent with an increase in the abundance of high-coercivity minerals (**Figure 5.4c** and **Figure 5.5b**). The lowest S-ratios (< 0.80) occur at Vidiciatico in the tectonic slices located farther from the basal thrust (**Figure 5.5b**), indicating significant amount of high-coercivity minerals, particularly at site T1-B3. The ARM/χm ratio (**Figure 5.4c** and **Figure 5.5b**) suggests the occurrence of coarse-grained magnetite, in agreement with the MDF values (**Figure 5.S 1** and **Figure 5.S 2**).

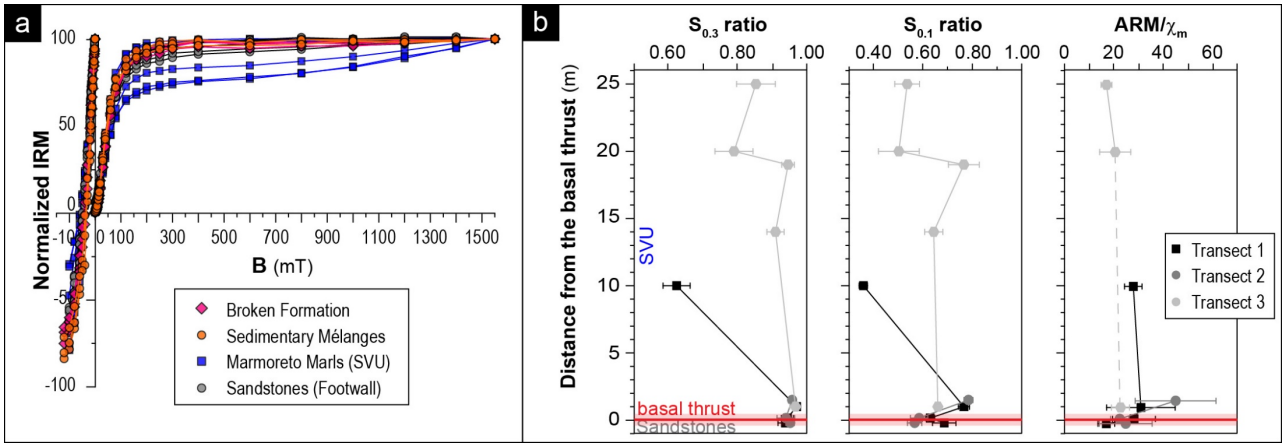

Figure 5.5. (**a**) Isothermal remanent magnetization acquisition and backfield curves; (**b**) plots of S-ratios and anhysteretic remanent magnetization (ARM)/χm versus distance from the basal décollement.

The deconvolution of the IRM acquisition curves show best-fit models characterized by the occurrence of three components (**Figure 5.6a** and **Figure 5.7a**; **Figure 5.S 1** and **Figure 5.S 2**): (a) a low-coercivity component consistent with detrital magnetite; (b) an intermediate-coercivity phase, suggesting the presence of a mixture of magnetite grains with different origin and grain-size; and (c) a high-coercivity component, such as hematite or goethite (Dunlop & Özdemir, 1997). The relative contribution and the occurrence of the components varies among lithologies and with structural position (**Figure 5.S 1** and **Figure 5.S 2**).

The sandstones in the footwall locally show a significant contribution (up to 35%) of high-coercivity phases. On the contrary, in both sheared sandstones and marly domains, component three decreases (<15%) in favour of intermediate-coercivity phases (Component 2 > 70%), while the abundance of the detrital magnetite remained stable around 5%–15% in the sandstones and turns out to be higher in the marly sediments (~20%; see samples T1-B4 in **Figure 5.6a** and T3-B1 in **Figure 5.7a**). The Marmoreto marls can

also show a significant contribution of high-coercivity components (40%-45%; T1-B3 in **Figure 5.7a**; **Figure 5.S 2**). Broken formation and sedimentary mélanges show similar components, with low and intermediate coercivity phases retaining at least the 80% of the IRM and a variable contribution of Component 3 less than 15%.

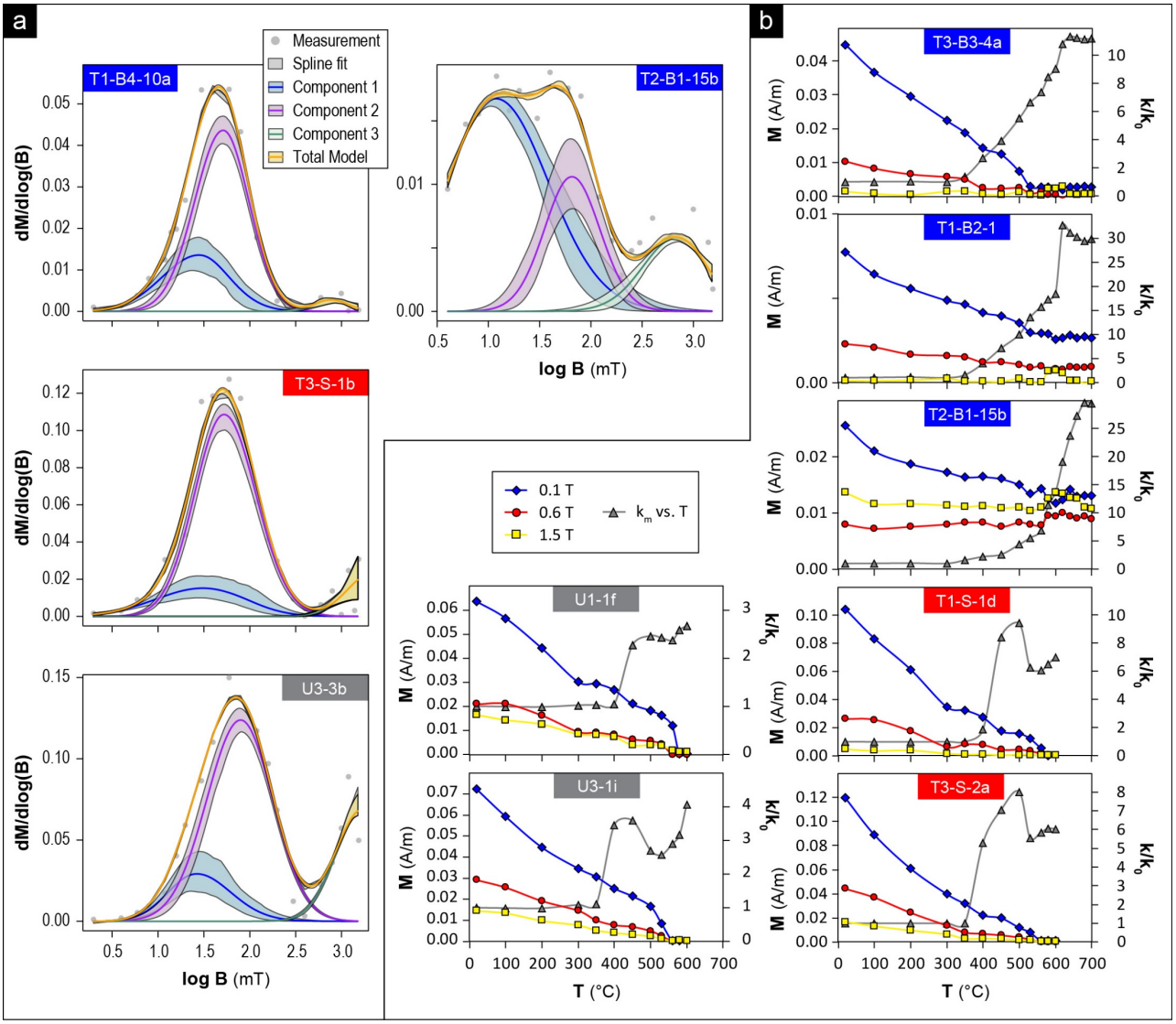

Figure 5.6. (**a**) Coercivity distribution and unmixing of isothermal remanent magnetization (IRM) acquisition curves (Maxbauer et al., 2016) of representative samples from the SVU cropping out at the Gova Tectonic window; and (**b**) thermal demagnetization of three-component IRMs and normalized magnetic susceptibility (k/k_0) versus temperature.

The Lowrie (1990) experiments (**Figure 5.6b** and **Figure 5.7b**) always show the predominance of the soft fraction (< 0.1 T), with the remanent magnetization almost completely removed at 560–580 °C. The drop around 300–350 °C in some specimens suggests the occurrence of iron sulfides (Weaver et al., 2002) and is locally detected in both sandstones and the SVU sediments (**Figure 5.S 1** and **Figure 5.S 2**). An additional drop is visible at 400–500 °C which may be associated with the presence of minor titanomagnetite. The relevance of hard and intermediate fractions varies among lithologies. A significant contribution of the hard fraction was observed in the Gova sandstones (U1-1f and U3-1i **Figure 5.6b**) and in a few samples of Marmoreto marls (T1-B3-4a in **Figure 5.7b**). In contrast, the hard fraction is almost negligible in the other

lithologies. At Gova, a relative increment can be recognized in the Civago marls with the proximity to the basal thrust (T2-B1; **Figure 5.6b**). In addition, a significant contribution of the intermediate fraction can be observed in the broken formation (T1-AR-10b in **Figure 5.7b**), with the remanence of this component almost completely erased at 350 °C, suggesting the presence of remanence-bearing iron-sulfides or Ti-magnetite. The sharply increase of k_m above 300–400 °C may be associated with a continuous oxidation effect. For the sandstones, this increment is compatible with the alteration of iron sulfides (i.e., pyrite and/or greigite) into magnetite (Mullender et al., 1993; Weaver et al., 2002). Instead, the breakdown of iron-bearing clay minerals may be a reasonable thermochemical reaction accountable for the formation of new magnetite for the marly domains (van Velzen & Zijderveld, 1992; Hirt et al., 1993). The formation of new hematite, induced by thermal treatments, is visible between 580 °C and 700 °C.

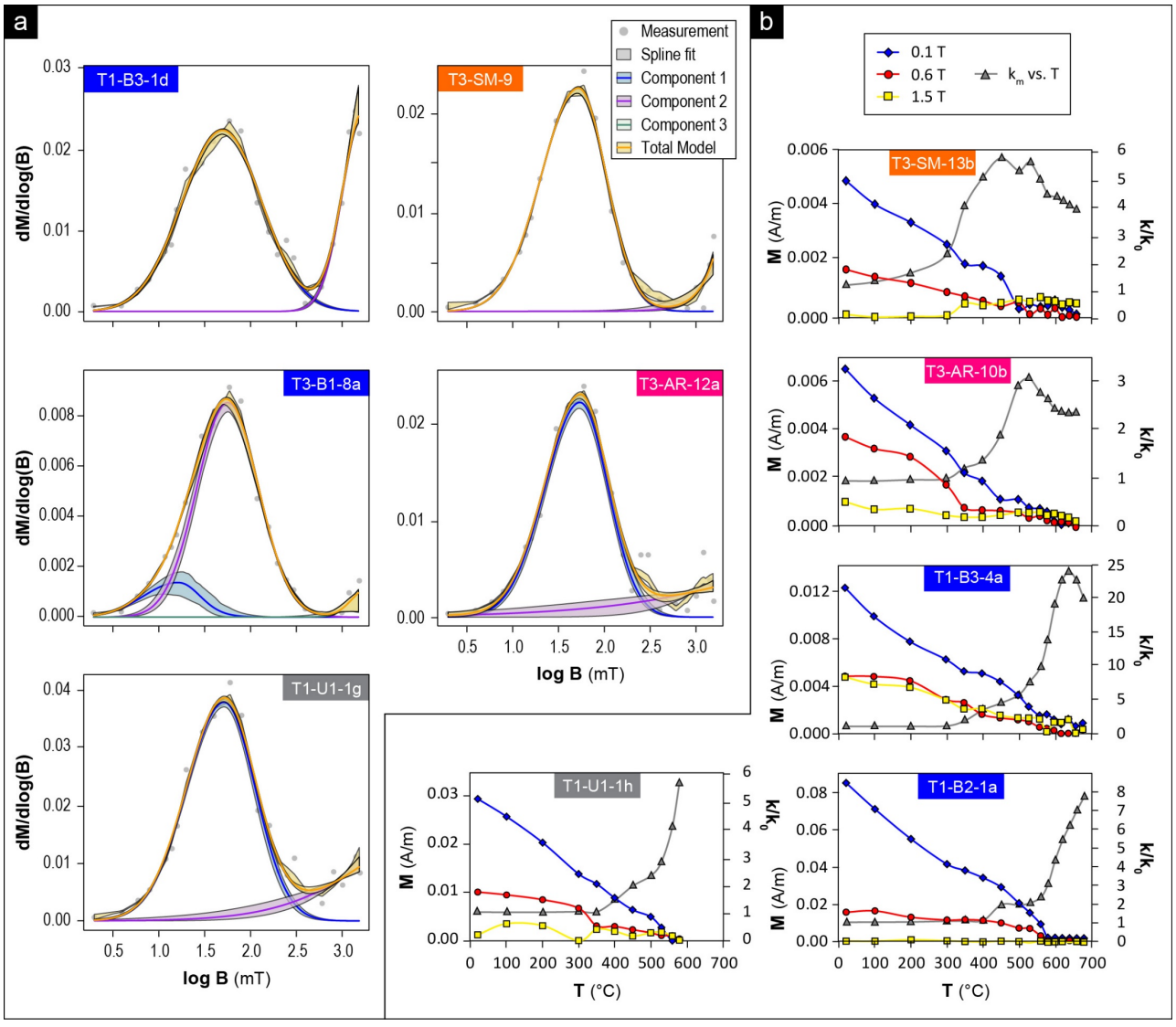

Figure 5.7. (**a**) Coercivity distribution and unmixing of isothermal remanent magnetization (IRM) acquisition curves (Maxbauer et al., 2016) of representative samples from Vidiciatico; and (**b**) thermal demagnetization of three-component IRMs and normalized magnetic susceptibility (k/k_0) versus temperature.

No significant variation of χ_m was observed as the field increased (**Figure 5.8a, b**; $V_a \sim \pm 0.50$, **Figure 5.S 1** and **Figure 5.S 2**), indicating the dominance of paramagnetic minerals or magnetite (Hrouda, 2002; Hrouda

et al., 2006). Few samples show variation in magnetic susceptibility with frequency, but the $\chi_{fd\%}$ is typically less than 6% (**Figure 5.S 1** and **Figure 5.S 2**) allowing dominance of SP particles to be excluded (Maxbauer et al., 2016).

Hysteresis loop at room temperature show a prevailing paramagnetic behaviour (**Figure 5.8c**), which causes a high noise level. In fact, in some samples the ferromagnetic component was neglectable or not sufficient to confidently define the hysteresis parameters. Overall, the hysteresis curves saturated between 0.3-0.6 T and show a narrow shape indicating the presence of low coercivity phases such as magnetite.

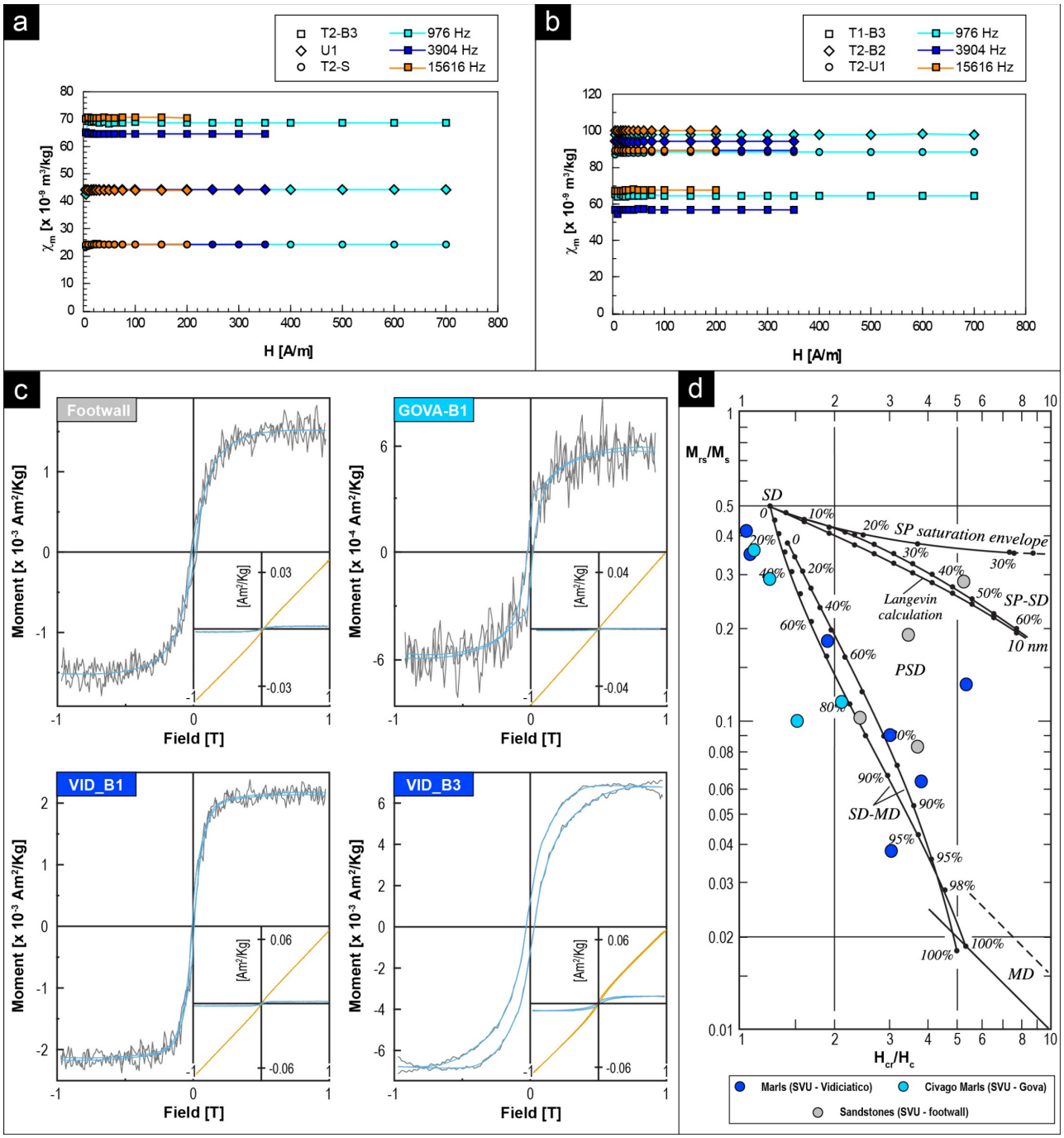

Figure 5.8. (**a**) Field and frequency variations of the mass magnetic susceptibility for representative lithologies; (**b**) Hysteresis loop for representative samples after correction and fitting. Insets show both raw and corrected data; (**c**) Day et al. (1977) plot of the hysteresis ratios M_{rs}/M_s and B_{cr}/B_c with mixing curves after Dunlop (2002a, 2002b).

Few samples from the Marmoreto marls (VID-B3 in **Figure 5.8c**) show a wider loop with a wasp-waisted shape, suggesting the presence of a mixture of low- and high-coercivity phases (Roberts et al., 1995). Based on hysteresis loop parameters, the marly domains revealed a mixture of SD and MD magnetite grains (**Figure 5.8d**) with no significant variation between Vidiciatico and Gova sector. The foredeep turbidites from the footwall also show some samples with the possible presence of SP particles.

5.2.1.1. Low- and high-temperature experiments and SEM-EDS analysis

Field-cooled (FC) and zero field-cooled (ZFC) remanence curves display a continuous decay of remanence during warming (**Figure 5.9** and **Figure 5.10**). Overall, the FC curves reveal higher magnetization than ZFC and converge at 250-300 K, suggesting the occurrence of goethite (Liu et al., 2006). In addition, most of samples show a subtle drop at ~ 124 K, consistent with the Verwey transition (T_v) of magnetite (Verwey, 1939; Muxworthy & McClelland, 2000). T_v values at around 120 K are likely related to the presence of inorganic detrital magnetite (Chang et al., 2016; Jackson and Moskowitz, 2021). The absence of a clearly visible T_v in some samples (**Figure 5.9a, c** and **Figure 5.10a-c**) may be associated with the occurrence of Ti-magnetite or more oxidized magnetite into maghemite (Chang et al., 2013). In addition, T_v becomes more visible when the FC and ZFC curves are less spaced. The remanence loss through the Verwey transition (δ; see APPENDIX I; Moskowitz et al., 1993) is < 0.4 or < 0.8 for δ_{ZFC} and δ_{FC}, respectively. At Gova, the remanence loss is less pronounced at a greater distance from the basal décollement (**Figure 5.9a**; δ_{FC} = 0.36; δ_{ZFC} = 0.28) and is higher in the shear sandstones (**Figure 5.9b**; δ_{FC} = 0.44; δ_{ZFC} = 0.39) . Similar behaviour was observed along transect 2 at Vidiciatico with maximum values of the δ ratio (δ_{FC} = 0.73; δ_{ZFC} = 0.25) detected near the basal décollement (**Figure 5.10c**). In contrast, along transect 1, the Verwey transition is weak and maximum values were observed in the underthrusting sediments and at site T1-B2 (**Figure 5.10a-b**). The delta-delta ratio (δ_{FC}/δ_{ZFC}) ranges from 1.12 to 2.96, suggesting the presence of PSD to SD magnetite grains (Housen & Moskowitz, 2006). The δ_{FC}/δ_{ZFC} increases close to the basal décollement at Gova and at transect 2 at Vidiciatico. In contrast, transect 1 at Vidiciatico shows a reverse trend with maximum values of about 2.16 at a greater distance from the basal thrust plane, at Site T1-B3.

The ratio of the SIRM at 20 K between FC and ZFC (R_{LT}; see APPENDIX I; Smirnov, 2009) varies among lithologies. Sandstones reveal values of about 2.56 ± 0.57, which becomes 1.74 in the shear sandstones. In the marly sediments, R_{LT} strongly varies between 1.18 and 4.37, confirming the presence of SD to PSD magnetite grains (Smirnov, 2009). R_{LT} displays higher values close to the basal décollement at Gova and transect 2 at Vidiciatico. In contrast, along transect 1, R_{LT} increases with distance from the main thrust plane.

The RT-SIRM cooling curves show an initial gradual increase in magnetization, followed by a faint to well-developed loss in magnetization at ~ 120 K and then increases continuously down to 10 K (**Figure 5.9** and **Figure 5.10**). The shear sandstones at Gova show two drops in the cooling curves at 126 and 247 K, consistent with the Verwey and Morin transition, respectively (**Figure 5.9b**). A similar trend is seen in the footwall at Vidiciatico (**Figure 5.10b**). Overall, upon warming, the remanence is not recovered passing through the Verwey transition and monotonically decrease from 120 to 300 K.

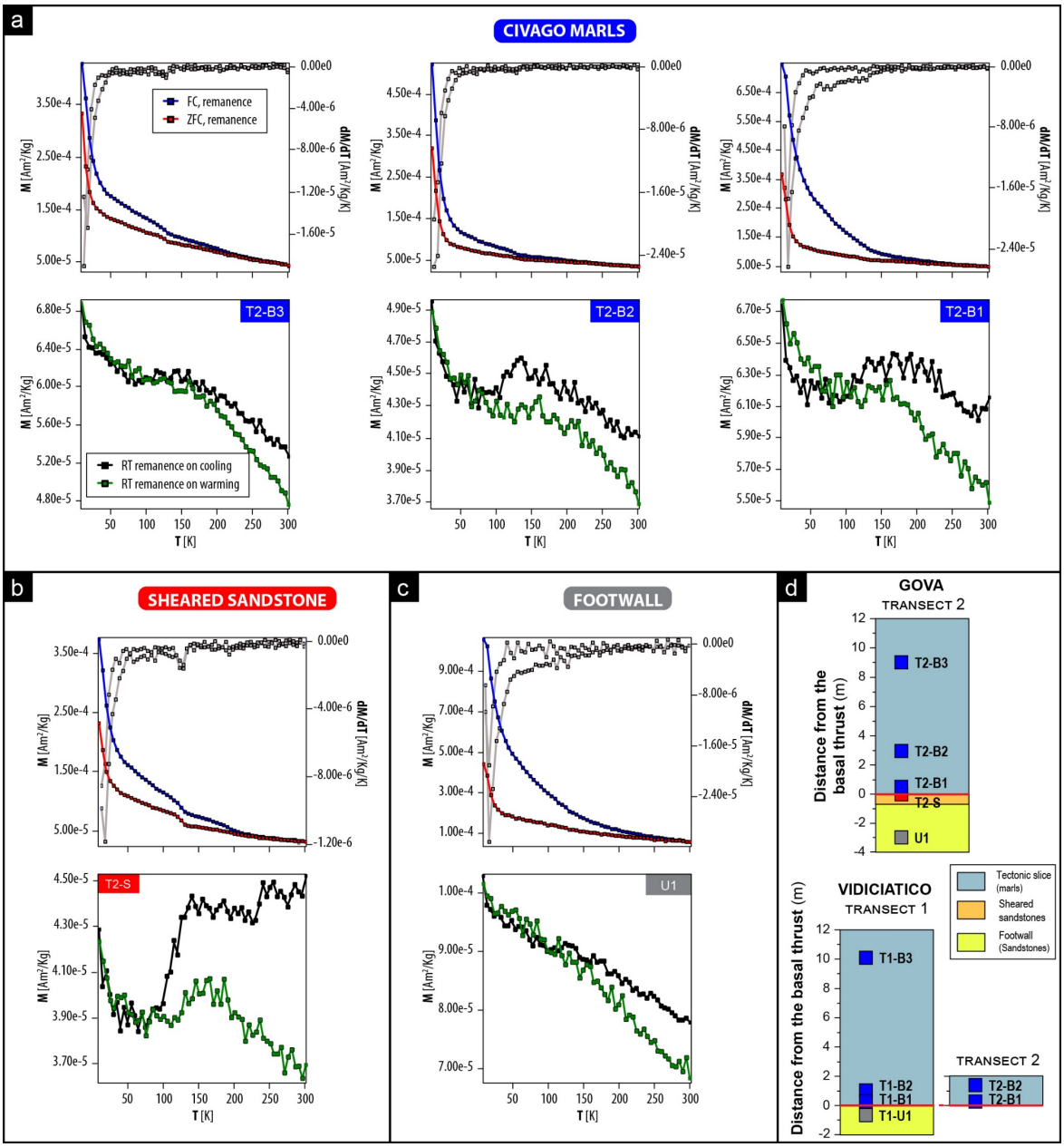

Figure 5.9. Representatives FC-ZFC with first derivative and RT-SIRM remanence curves from the Gova Sector: (**a**) Civago marls; (**b**) sheared sandstones; (**c**) sandstones from the Footwall. (**d**) Relative position of samples in respect to the thrust surface for both Gova and Vidiciatico sectors.

The remanence magnetization on the cooling curves increases by more than 7%, indicating that goethite constitutes an appreciable part of the SIRM (Dekkers, 1989). Marly sediments reveal increases in magnetization of about 14 ± 1%, while sandstones can also show a significant loss of SIRM during cooling to 10 K (**Figure 5.9b** and **Figure 5.10b**). At Gova (**Figure 5.9**), few samples shows a monotonic increase in magnetization and a faint inflection close to the T_v with magnetization increases > 30% in the footwall and at site T2-B3 (**Figure 5.9a, c**). At Vidiciatico, the increases in magnetization are generally less intense, with higher values (~ 11%) close to the basal décollement (**Figure 5.10a, c**). The goethite proxy (G%; see APPENDIX I; Aubourg et al., 2021) is significantly higher at Gova, where it ranges from 7% to 20%. In contrast, at Vidiciatico G% is typically < 11%. At both Gova and Vidiciatico, G% decreases with proximity to the basal décollement and increases with distance.

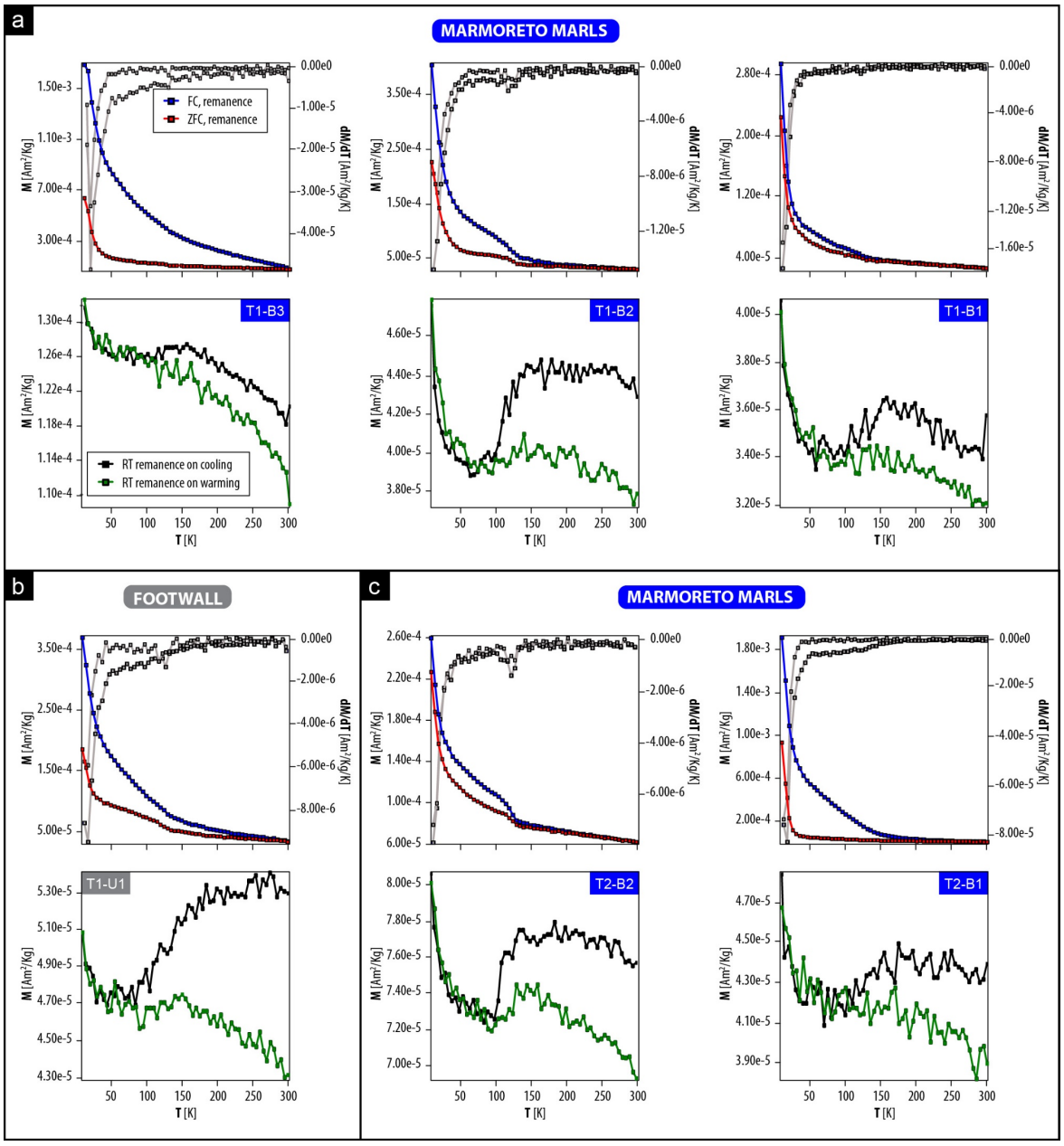

Figure 5.10. Representatives FC-ZFC with first derivative and RT-SIRM remanence curves from the Vidiciatico Sector: Marmoreto marls from Transect 1 (**a**) and 2 (**c**); (**b**) sandstones from the Footwall. Relative position of the samples are reported in **Figure 5.9d**.

The stepwise thermomagnetic susceptibility cycles are almost reversible up to a maximum temperature of 350 °C (**Figure 5.11** and **Figure 5.12**), suggesting no new generation of ferromagnetic grains. In fact, at the lowest temperature steps, most samples reveal low or neglectable values (< 9%) of the alteration indices (A_{50} and $\delta_{\chi curve}$%; see APPENDIX I; Hrouda, 2003; Yang et al., 2016). Only a few samples of marly sediments start to alter at about 350 °C (T2-B1 in **Figure 5.11a** and T2-B3 in **Figure 5.12a**), showing A_{50} = 20-22% and $\delta_{\chi curve}$% = 19-31%. Overall, the heating-cooling cycle at the 700 °C step show irreversible curves. The heating curves at the 700 °C step exhibit a paramagnetic hyperbolic behaviour from room temperature up to 350-400 °C (**Figure 5.11** and **Figure 5.12**), following the Curie-Weiss Law (Hrouda et al., 1997). The χ starts to increase above ~ 350 °C and reaches maximum values between 500 and 550 °C, suggesting the

thermal decomposition of iron-bearing paramagnetic minerals, such as pyrite and/or clay minerals (Tanikawa et al., 2008; Yang et al., 2016). The magnitude of the increase in χ varies significantly depending on the lithology (**Figure 5.11** and **Figure 5.12**). The sheared sandstones reveal a slight increase in χ with values at 550 °C lower than the initial susceptibility (**Figure 5.11b**). In contrast, the sandstones of the footwall show a sharp increase in χ at about 400 °C (**Figure 5.11c** and **Figure 5.12b**).

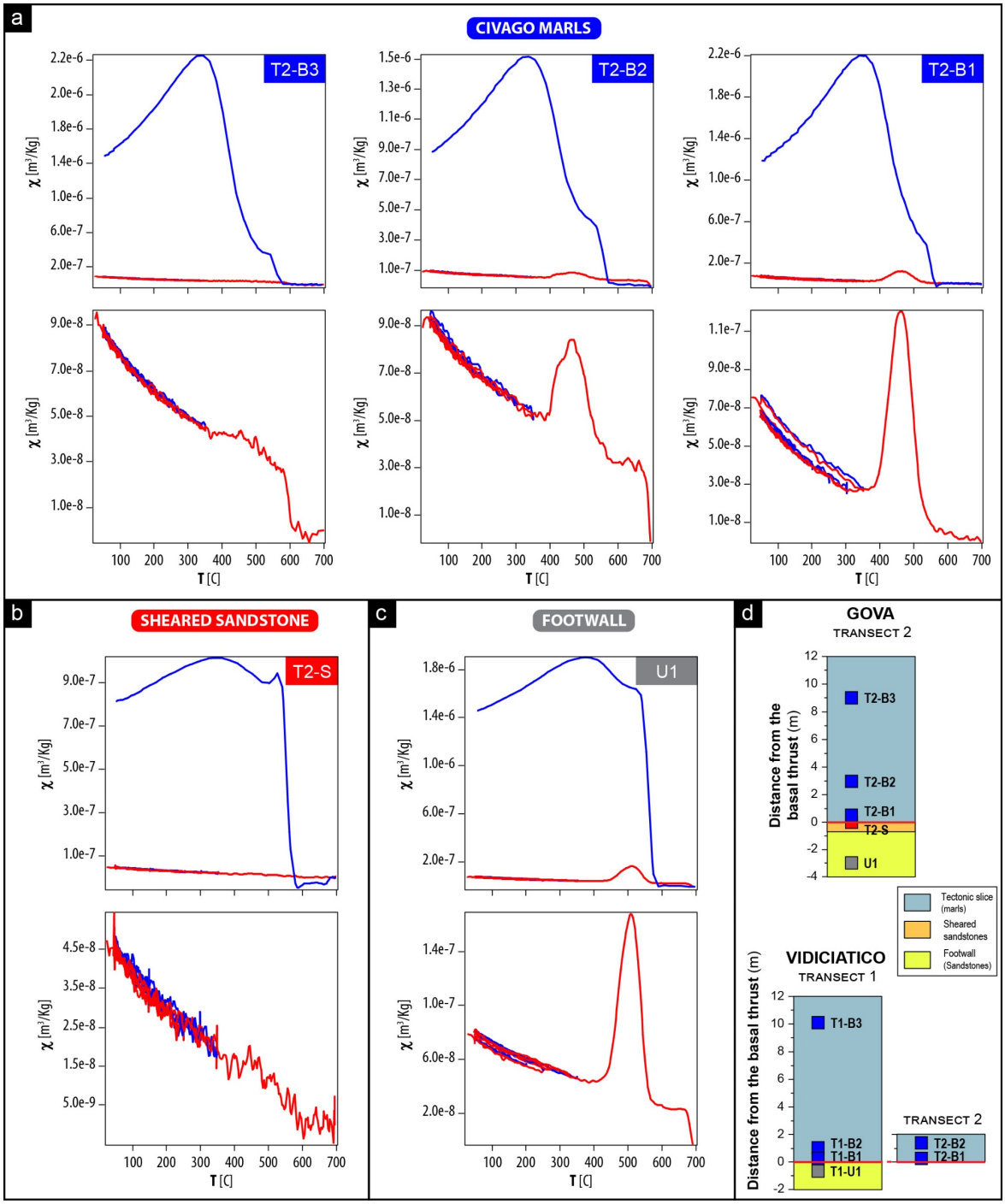

Figure 5.11. Representatives stepwise thermomagnetic susceptibility curves from the Gova Sector: (**a**) Civago marls; (**b**) sheared sandstones; (**c**) sandstones from the Footwall. Details on the heating curves and the heating-cooling cycles at T_{max} < 350 °C are reported. (**d**) Relative position of samples in respect to the thrust surface for both Gova and Vidiciatico sectors.

In the marly sediments at Gova and along transect 2 at Vidiciatico, χ increases at 350 °C, but the magnitude of this increase diminishes with distance from the thrust (**Figure 5.11a** and **Figure 5.12c**). In contrast, transect 1 shows an opposite trend, with faint to neglectable increase in χ upon heating in proximity to the basal thrust plane (**Figure 5.12a**). In most samples, χ becomes nearly zero at about 600 °C, indicating the presence and/or new formation of magnetite. Some specimens show a significant loss of χ at 580-600 °C but reaches zero at 700 °C, suggesting the local presence of hematite (e.g., Samples T2-B2 and U1 in **Figure 5.11a, c** and T1-U1 in **Figure 5.12b**).

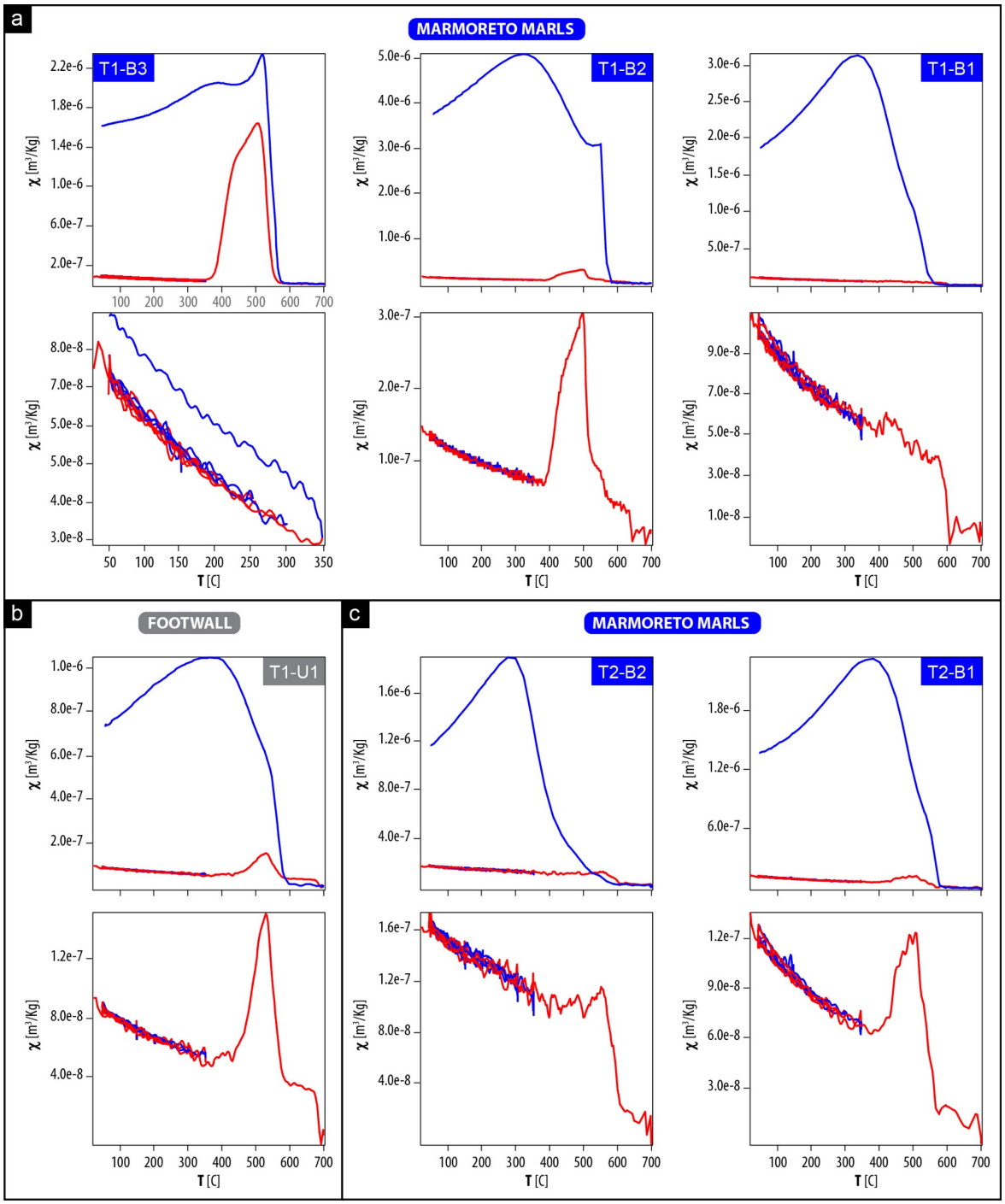

Figure 5.12. Representatives stepwise thermomagnetic susceptibility curves from the Vidiciatico Sector: Marmoreto marls from Transect 1 (**a**) and 2 (**c**); (**b**) sandstones from the Footwall. Samples position are reported in **Figure 5.11d**.

Upon cooling, χ increases abruptly, suggesting significant neoformation of magnetite during the thermal treatment. Different behaviours were observed in the cooling curves. At Gova, we observed variations depending on the lithology. In sandstones, χ increases sharply at 580-600 °C to an order of magnitude higher and then slightly increases showing maximum values at 350-400 °C (**Figure 5.11b-c**). Marly sediments show an initial rapid increase in susceptibility between 580 and 550 °C, followed by a monotonic increase with decreasing temperature, reaching a peak in χ between 300 and 350 °C (**Figure 5.11**). The sandstones at Vidiciatico exhibit intermediate behaviour with a minor increase in susceptibility between 600 and 550 °C (**Figure 5.12b**). Along transect 1 (**Figure 5.12a**), the increase in χ at 580 °C becomes sharper with distance from the basal décollement. In particular, T1-B3 reaches maximum χ at 500 °C. In contrast, along transect 2, the maximum χ shifts to a lower temperature (~ 300 °C) at greater distance from the thrust (**Figure 5.12c**).

Hysteresis loops after stepwise thermal treatments reveal low saturation magnetization (M_s) up to 350 °C with values < 1.84 (x 10^{-3} Am^2/kg). At low temperature steps, before high-field correction, the signal is dominated by paramagnetic behaviour and shows slight changes in M_s with increasing T_{max} (**Figure 5.S 3**). M_s strongly increases after the 450 °C step, revealing the formation of ferromagnetic phases, which leads to a common final product for all lithology at the 650 °C step. Overall, the M_s values after the 650 °C step are two orders of magnitude higher than the initial values (**Figure 5.13a**). At the 650 °C thermal step, the hysteresis loops are pot-bellied, showing a shape parameter $\delta_{hyst} < 0$. The occurrence of $B_c < 30$ mT suggests the neoformation of low coercivity minerals (e.g., magnetite) as the final product.

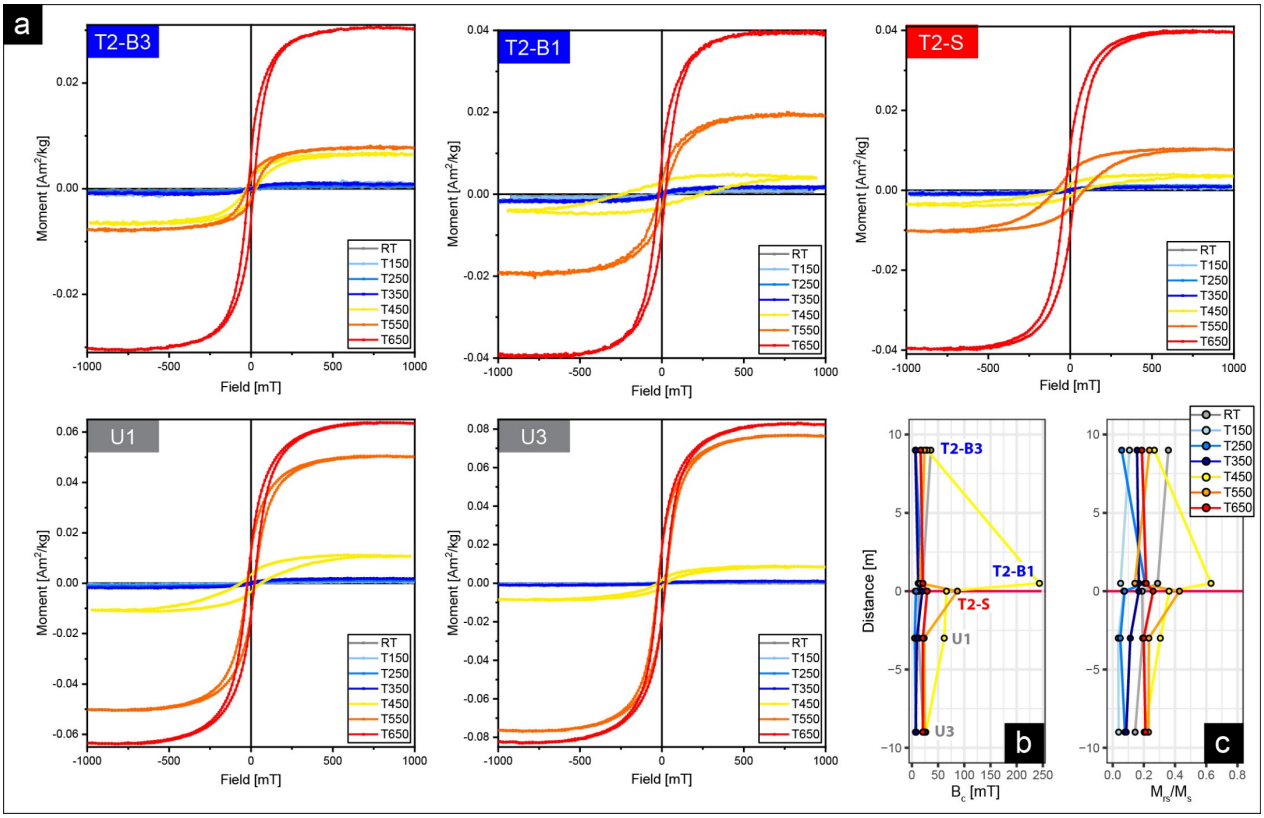

Figure 5.13. (**a**) Hysterisis loops after stepwise thermal treatment at a progressively higher maximum temperature. Loop are corrected for the high-field slope. Raw data are reported in **Figure 5.S 3**. Hysteresis paramenters vs. distance from the basal décollement: (**b**) B_c and (**c**) M_{rs}/M_s. See **Figure 5.11d** for samples position.

Different trends were observed in the evolution of the hysteresis loops between lithologies and with distance from the main thrust plane (**Figure 5.13**).

In the footwall, the hysteresis loop becomes wider at 450 °C and the coercivity (B_c) increases (**Figure 5.13a**). B_c changes from < 10 mT to 35 mT and 62 mT at site U3 and U1, respectively (**Figure 5.13b**). Thereafter, the loop thins and B_c progressively decreases during the 550 and 650 °C temperature steps, showing values of about 20 mT. In contrast, M_s increases significantly after the 550 °C step to maximum values of 8.28 (x 10^{-2} Am^2/kg). The variation of M_{rs}/M_s with temperature remarks the progressive mineralogical transformations and exhibits maximum values at the 450 °C step (**Figure 5.13c**). In addition, site U1 shows a greater increase in B_c and M_{rs}/M_s than site U3. The sheared level of sandstones shows increase in B_c from the 450 °C step with a maximum value of 87 mT at the 550 °C step (**Figure 5.13b**). The shape of the hysteresis loop changes from wasp-waisted with δ_{hyst} values close to 1 to pot-bellied with δ_{hyst} about 0.1 at the 550 °C step (**Figure 5.13a**). M_s increases strongly only during the last thermal step.

In the marls, we observed a different behaviour depending on the distance from the basal thrust. At a greater distance (Site T2-B3 in **Figure 5.13a**), B_c reaches a maximum value of 29 mT at the 450 °C step. The magnetization after the increase at 450 °C remains almost stable (~ 7 x 10^{-3} Am^2/kg) and then increases significantly at the last thermal step. The shape of the hysteresis loop is slightly wasp-waisted (δ_{hyst} < 0.5) and becomes pot-bellied at the 650 °C thermal step (**Figure 5.13a**). In contrast, close to the basal thrust, at the 450 °C step, B_c is 243 mT (**Figure 5.13b**), suggesting the neoformation of high-coercivity minerals such as hematite probably SD (Özdemir & Dunlop, 2014). At this step, the M_{rs}/M_s ratio shows the highest value of 0.63 (**Figure 5.13c**), consistent with that of hematite (Özdemir & Dunlop, 2014). After the 550 °C step, the coercivity turn back to lower values (~ 15 mT).

The petrographic observations performed using SEM-EDS analysis revealed the presence of iron-sulfides microcrysts (**Figure 5.14**). In fact, EDS analysis confirm the occurrence of pyrite (FeS2; **Figure 5.14e**).
In the marly domains from the hanging wall of the SVU, pyrite occurs either as isolated framboids (1 to 10 μm in diameter) or as large aggregated of framboids (~ 150 μm; **Figure 5.14a, b**). At the tips of the aggregates, smaller grain framboids are distributed along the dissolution seams, which might be associated to porphyroblastic or porphyroclastic structures (Passchier & Trouw, 2005).

Instead, within the sandstones, pyrite framboids are usually isolated and dispersed between clay minerals or within the carbonate matrix, with no preferred orientation or specific spatial distribution (**Figure 5.14c, d**).

5.2.2 AMS

The mass magnetic susceptibility varies among lithologies (**Table 5.S 1** and **Table 5.S 3**; **Figure 5.15a** and **Figure 5.16a**), ranging from 30.9 to 220.8 (× 10^{-9} m^3kg^{-1}). These values agree with a high content of paramagnetic minerals, such as clay minerals or phyllosilicates. A predominance of the paramagnetic minerals of the matrix on the total AMS has to be considered (Rochette, 1987; Evans et al., 2003).

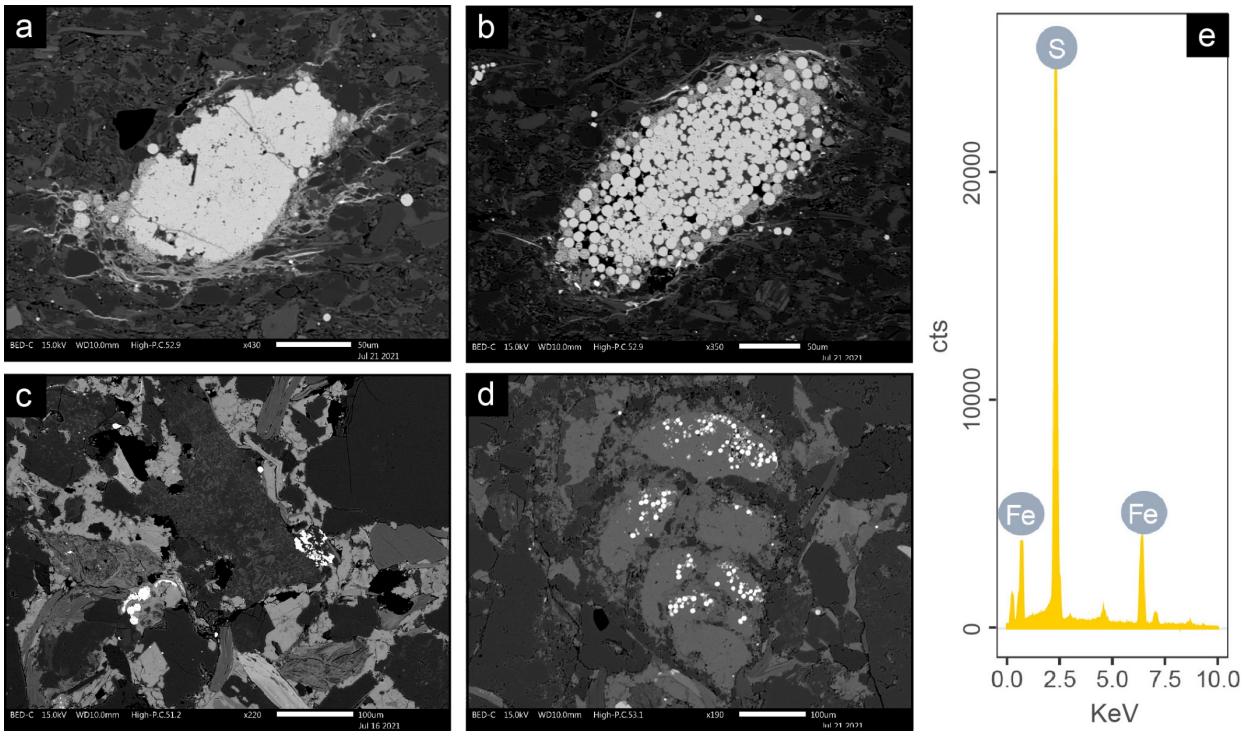

Figure 5.14. Backscattered SEM image of: (**a-b)** large aggregates of framboidal Pyrite within the SVU marly domains; isolated framboids in the foredeep turbidites (**c-d**). (**e**) Representative EDS spectrum of pyrite framboids.

The turbiditic sandstones from the footwall of the SVU show low values with a mean of χ_m = 56.1 ± 15.7 (× 10^{-9} m^3kg^{-1}). The Gova Sandstones shows two clusters of χ_m values (**Figure 5.15d**), unrelated to the distance from the thrust and variations in the AMS scalar parameters (Pj and T, **Figure 5.15b, c**). The sheared sandstones layer displays variations between areas, with a significant lower mean at Site T2-S. In the footwall at Vidiciatico, the χ_m differs considerably between the two sites, with higher values at Site T2-U1 (χ_m = 88.9 ± 16.4 [× 10^{-9} m^3kg^{-1}]; **Figure 5.16a** and **Table 5.S 3**). In contrast, the marly domains of the hanging wall reveal a wider range of values, from 45.0 to 144.8 (× 10^{-9} m^3kg^{-1}). The Civago marls show an increase in χ_m with distance from the thrust plane (**Figure 5.15d**). In the Marmoreto Marls, slight variations are observed among sites with no clear correlation with structural position (**Figure 5.16d**). The sedimentary mélange displays uniform and on average higher values of χ_m = 105.8 ± 7.4 (× 10^{-9} m^3kg^{-1}). Instead, the Broken formation reveals significant variability and the highest values, with χ_m spanning from 58.9 to 220.8 (× 10^{-9} m^3kg^{-1}) (**Figure 5.16d**).

At Gova, the footwall is characterized by neutral to oblate AMS ellipsoids and low to moderate anisotropy degree (Pj = 1.064 ± 0.009; T = 0.318 ± 0.168; **Figure 5.15b, c**). The sheared level displays the lowest Pj (~1.039 ± 0.013). The magnetic fabric is oblate at the tips of the sheared body, while in the central portion T shows a transition from oblate to prolate (Transect 2 **Figure 5.15e**). At Vidiciatico, the foredeep turbiditic sandstones reveal a neutral to oblate magnetic fabric with moderate to high Pj (**Figure 5.16b, c**). Remarkable differences in Pj are observed between sites, with the highest values (~ 1.152) found at Site T2-U1 (**Figure 5.16e**).

In the hanging wall, slight variation in AMS scalar parameters are observed as a function of the different origin of the tectonic slices (**Figure 5.15** and **Figure 5.16**). In the Civago marls slices, Pj varies from low to high (between 1.015 and 1.245; **Figure 5.15b**), with the lowest values detected in the central portion of the tectonic slice, between 3 and 9 m from the basal thrust. No notable dependence of Pj on the rock composition can be inferred. T is oblate in most specimens being neutral and prolate only in a minor number of specimens, mostly located along Transect 2 and 3 (**Figure 5.15e**).

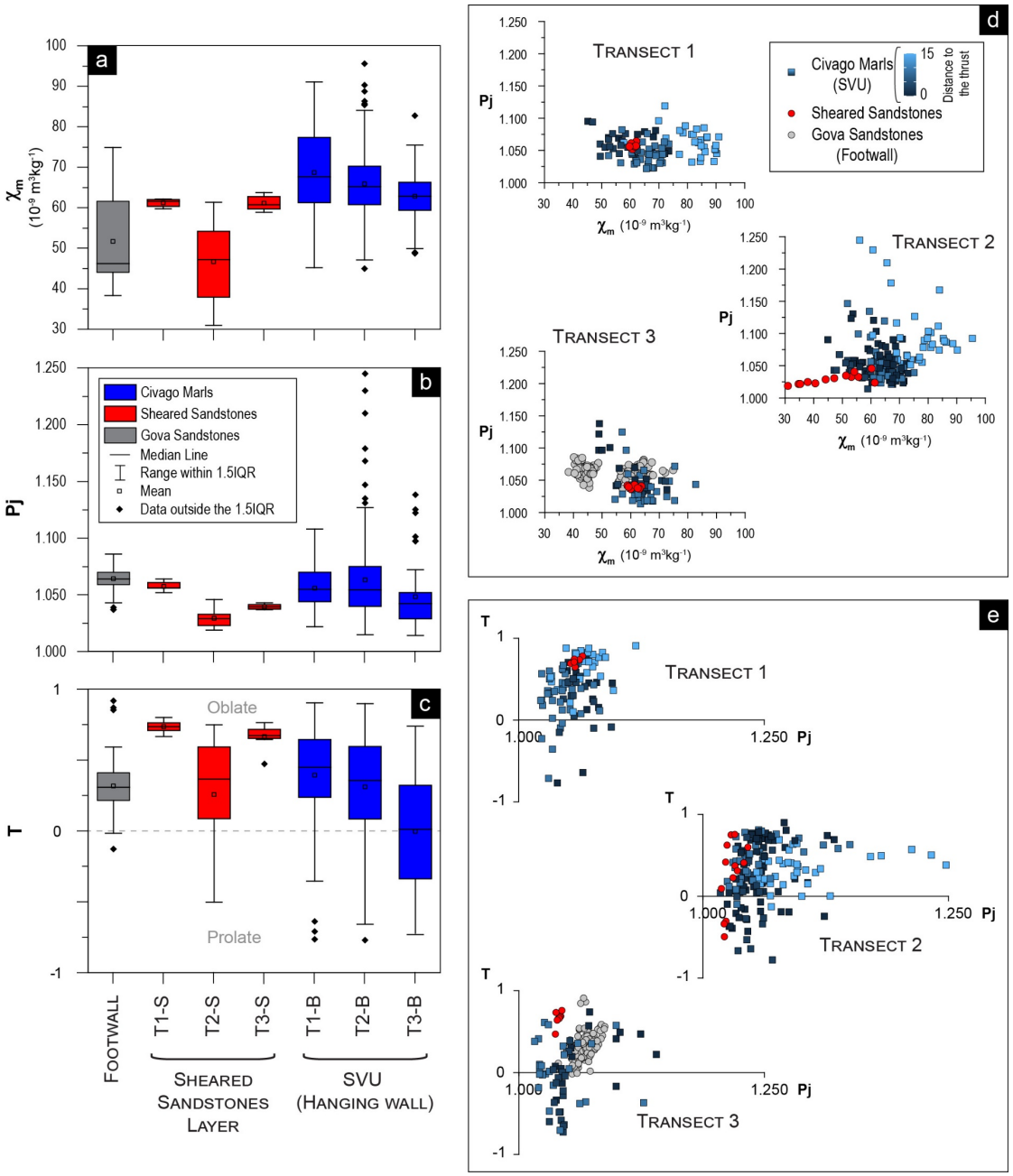

Figure 5.15. Variations of the anisotropy of magnetic susceptibility scalar parameters among transects from the Gova Tectonic window: Box-and-whisker plots of the (**a**) mass magnetic susceptibility (χ_m), (**b**) corrected anisotropy degree (Pj) and (**c**) shape parameter (T); (**d**) Pj versus χ_m; and (**e**) T versus Pj.

Marmoreto marls show AMS scalar parameters comparable to those of the other marly domains. The highest Pj values was detected close to the main thrust plane at Transect 2 (**Figure 5.16d**), where the magnetic fabric is strongly oblate. In the other transects, the shape of the magnetic ellipsoid changes from neutral to oblate

according to the distance from the main thrust faults (**Figure 5.16e**). The sedimentary mélange shows a neutral shape of the magnetic ellipsoid with moderate degree of anisotropy (T = 0.290 ± 0.306; Pj = 1.052 ± 0.017). In contrast, the Broken formation reveals a strongly oblate fabric with the highest Pj values (~ 1.225).

We did not observe variations in AMS parameters related to unconventional dimension and shape imperfections of the specimens (Cañón-Tapia & Pinkerton, 2000; Almqvist et al., 2020). We thus assume that variations in AMS data are related to changes in mineralogy and/or deformation intensity. In the following paragraphs, AMS axis orientations and variations of the scalar parameters will be discussed by sector, describing separately each transect.

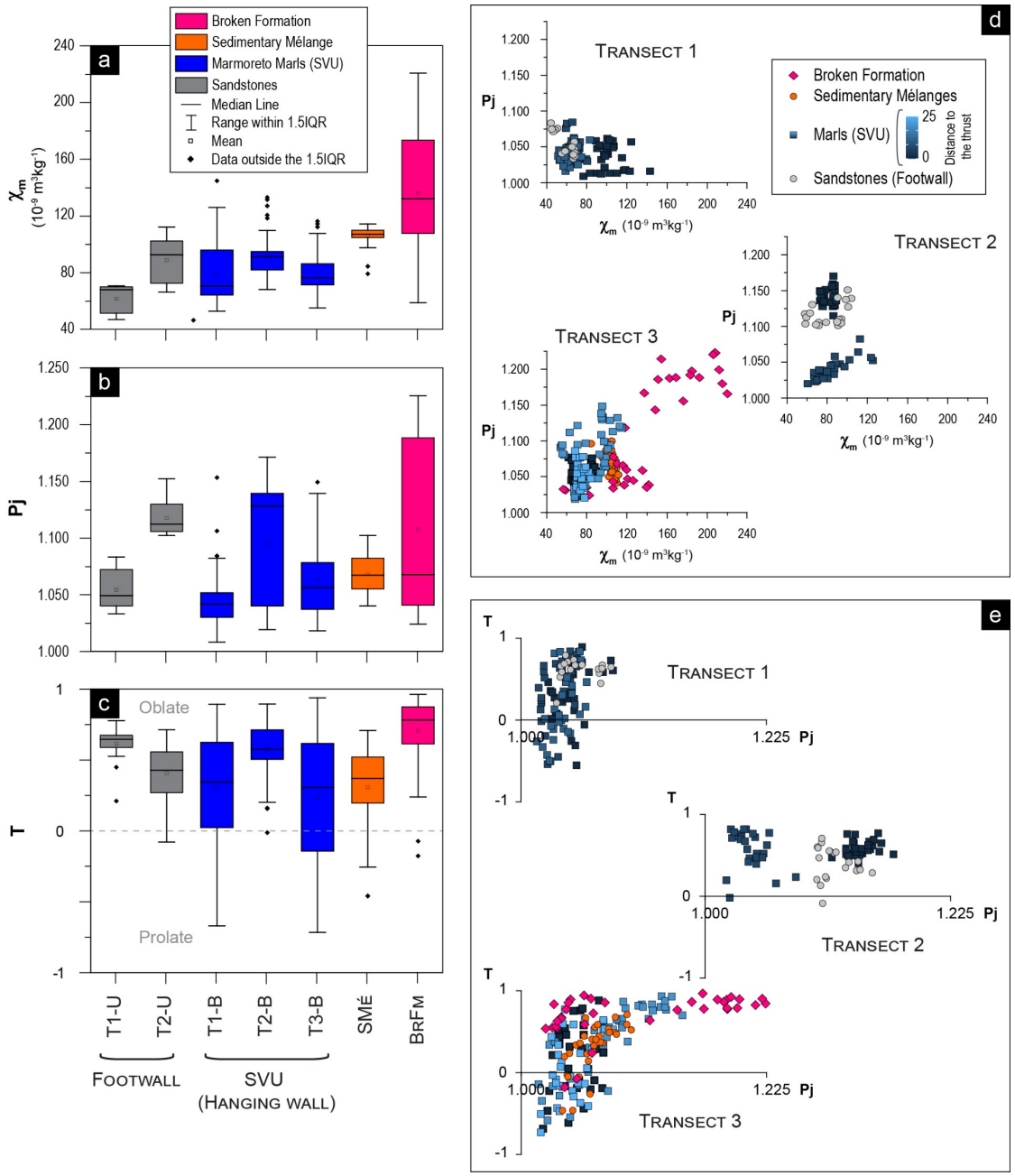

Figure 5.16. Variations of the anisotropy of magnetic susceptibility scalar parameters among transects from Vidiciatico: Box-and-whisker plots of the (**a**) mass magnetic susceptibility (χ_m), (**b**) corrected anisotropy degree (Pj) and (**c**) shape parameter (T); (**d**) Pj versus χ_m; and (**e**) T versus Pj.

5.2.2.1 The Gova Tectonic Window

5.2.2.1.1 Footwall

χ_m and T vary slightly among sites, while Pj remains constant (**Figure 5.17**). The magnetic fabric changes from neutral to oblate in the first 3 m below the basal thrust. At all sites, the magnetic fabric is well-defined with a sub-horizontal magnetic foliation and an E-W trending magnetic lineation. In addition, at site U1, some specimens display a deviation of k_3 axis toward NW, resulting in the deflection of k_1 and k_2 from the mean magnetic foliation (U1 light-toned axes **Figure 5.17**).

5.2.2.1.2 Transect 1

The sheared sandstones are characterized by a low Pj and a strongly oblate ellipsoid (**Figure 5.17**). Into the SVU, both χ_m and T display a relatively small decrease in the first 3 m above the basal thrust, followed by a higher susceptibility and a higher degree of oblateness in the upper part of the tectonic slice; Pj does not vary greatly. Throughout transect 1, the magnetic fabric is oblate, showing well-grouped axes with a SW- to SSW-dipping magnetic foliation and mainly SW-plunging k_1 (**Figure 5.17**). Furthermore, Site T1-B4 reveals a mixed fabric characterized by a high dispersion of k_1 and k_2 axes and two main clusters of k_3. By contouring and cluster analysis, most of specimens can be associated to two subfabrics showing a well-defined SSW-dipping magnetic foliation and k_1 axis trending E-W and NE-SW (heavy-toned colors **Figure 5.17**; Sf1 and Sf2 **Table 5.S 1**). In addition, the k_3 cluster at WNW suggests a third subfabric (light-toned axes **Figure 5.17**), characterized by a steeply dipping magnetic foliation and a sub-horizontal N-S trending k_1 axis.

5.2.2.1.3 Transect 2

The sheared sandstones show a neutral magnetic fabric with low Pj (**Figure 5.18**). On the contrary, into the SVU most of sites reveals an oblate fabric with relatively high Pj. A significant drop is observed in all AMS parameters at site T2-B2. The magnetic fabric of the sheared level is well-defined and characterized by a steeply dipping magnetic foliation and a horizontal E-W trending magnetic lineation. The SVU is characterized by the occurrence of complex magnetic fabrics. Site T2-B1 shows a mixed magnetic fabric with highly dispersed k_1 and k_2 axes. Three different subfabrics were detected: (a) a dominant neutral subfabric showing a S-dipping magnetic foliation and sub-horizontal E-W trending magnetic lineation (heavy-toned colors **Figure 5.18**; Sf1 Site T2-B1 **Table 5.S 1**); (b) an oblate magnetic fabric with a magnetic foliation that strikes NW-SE and a SW-plunging k_1 axis (Sf2 Site T2B1 **Table 5.S 1**); and (c) an oblate magnetic fabric showing a S- to SE-dipping magnetic foliation associated to a magnetic lineation from N-S to NW-SE trending. At 3 m to the fault zone there is a drop in the AMS parameters (T2-B2), in which the magnetic fabric is prolate and characterized by a NE-SW trending magnetic lineation. The presence of non-orthorhombic confidence regions is due to the superposition of subfabrics. In the upper part of the tectonic slice the magnetic fabric is again oblate and Pj increases. Both sites T2-B3 and T2-B4 display a slight dispersion of AMS axes. These configurations suggest variations in the relative contribution of two

competing fabric between sites. In fact, the magnetic lineation preserves a dominant attitude along an E-W to NE-SW direction, while the magnetic foliation shifts from SW-dipping at site T2-B3 to mostly S-dipping close to the contact with the Fiumalbo shale.

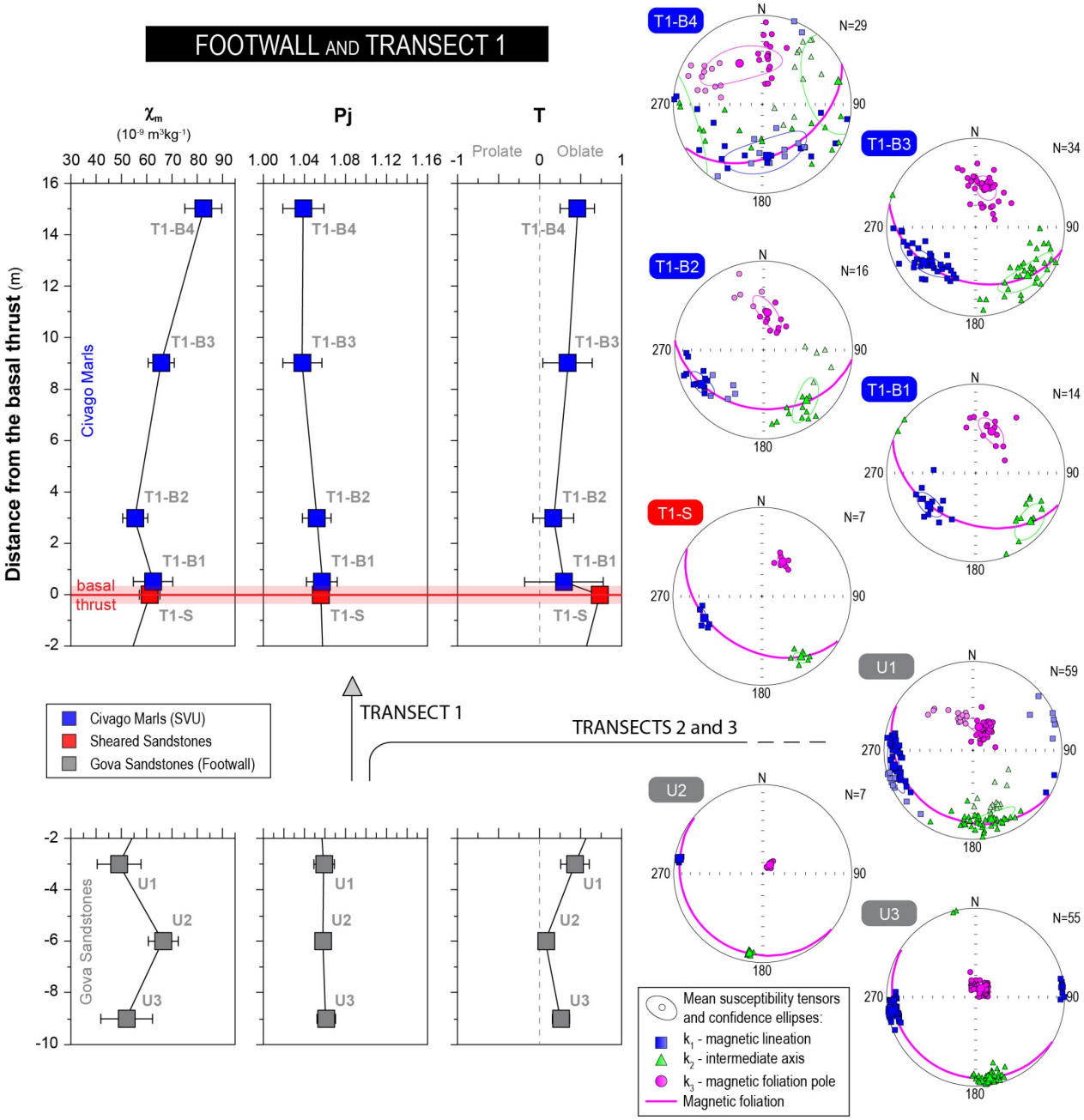

Figure 5.17. Magnetic fabric from the footwall and Sestola-Vidiciatico Tectonic Unit Transect 1, Gova Tectonic window. Plots of χ_m, Pj, and T versus distance from the basal décollement (left). Stereoplots (lower hemisphere equal-area projections) of the principal magnetic susceptibility axes at site level (right). Different subfabric detected by the cluster analysis are reported with different shades.

5.2.2.1.4 Transect 3

The magnetic fabric of site T3-S is oblate with a low Pj (**Figure 5.18**). The maximum principal susceptibility axes are well-clustered with sub-horizontal E-W trending magnetic lineation. The magnetic foliation is S-dipping at an intermediate angle. At the base of the Civago marls, the magnetic fabric is well-defined and

oblate with a high Pj. The magnetic foliation is SSW-dipping and the magnetic lineation trends NE-SW. In the central portion of the tectonic slice, the magnetic fabric changes into prolate and Pj decreases. At site T3-B2, k_1 axes are well-group toward SW, while k_2 and k_3 are dispersed on a NW-SE trending girdle.

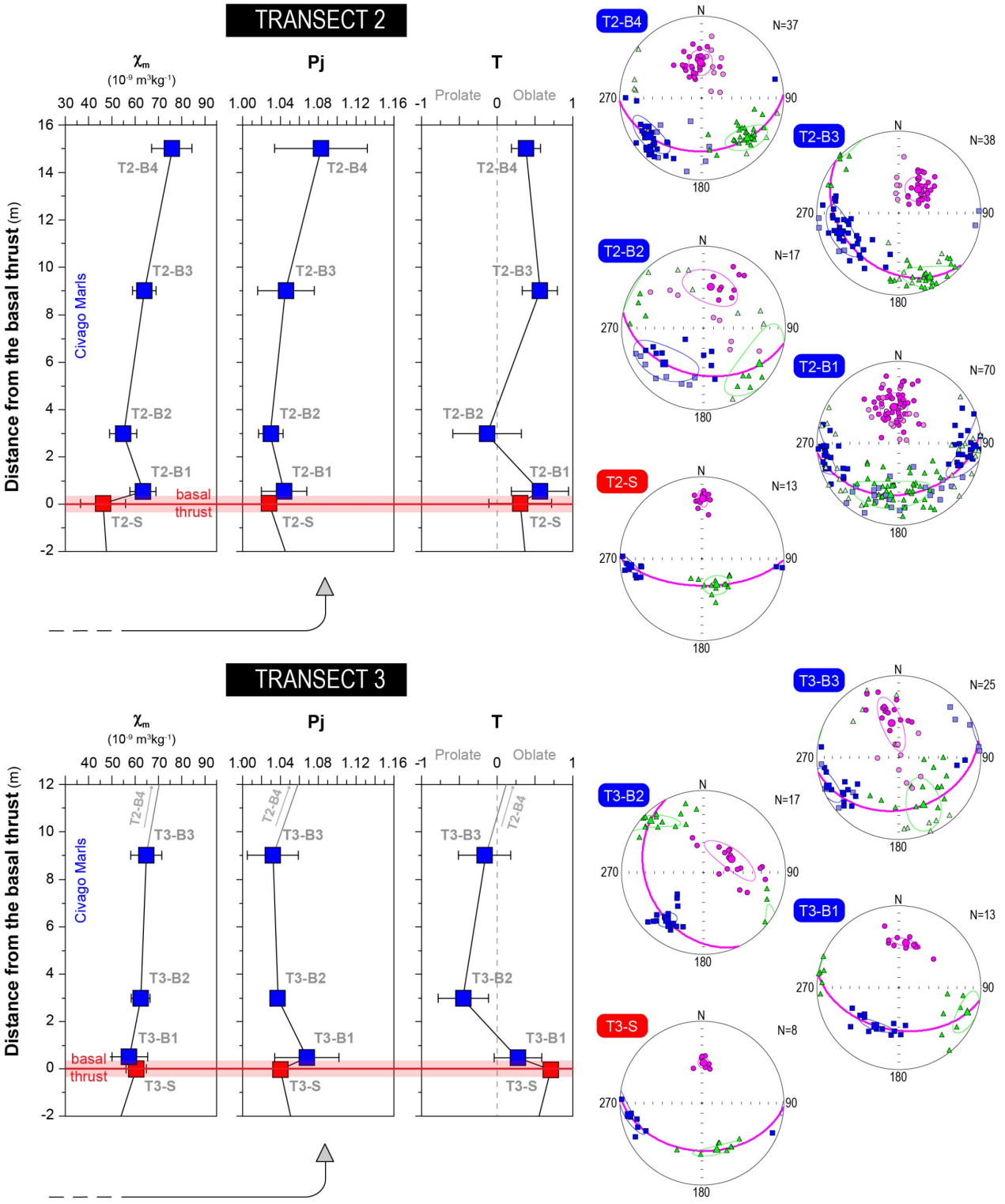

Figure 5.18. Magnetic fabric from the Sestola-Vidiciatico Tectonic Unit Transect 2 and 3, Gova tectonic window. Plots of AMS parameters versus distance from the décollement (left). Lower hemisphere equal-area projections of the AMS axes at site level (right). Legends as in **Figure 5.17**.

Site T3-B3 reveals a slightly prolate mixed magnetic fabric with a dominant WSW-trending magnetic lineation. Here, the scattering of k_3 and k_2 axes is related to the superposition of two different patterns. Most data follow the dominant oblate fabric with SSE-dipping magnetic foliation, while few specimens show a sub-horizontal magnetic foliation and a prolate shape.

In general, the footwall reveals high data consistency with a prevailing sub-horizontal magnetic fabric with an E-W trending k_1 (U_{Main} **Figure 5.19**). The small deflections result from a secondary pattern ($U_{Strike\ slip}$) contributing for the 32% at site U1. In the sheared sandstones, the main trend reveals a dominant ENE-WSW striking magnetic lineation. Variations in the magnetic foliation among portions produce the scatter in the total AMS. The magnetic fabric of sites T2-S and T3-S shows a consistent S-dipping magnetic foliation at high-angle. Instead, at site T1-S the magnetic foliation is SW-dipping, in agreement with the main pattern observed into the SVU. In the megathrust shear zone, the magnetic fabric shows significant heterogeneities. By contouring and cluster analysis we discriminate 5 main patterns (**Figure 5.19**). Pattern 1, characterized by an oblate fabric with an E-W magnetic lineation, is mostly localized in the middle/upper portion of the tectonic slice. This pattern is also preserved in most specimens from Site T2-B1. Pattern 2 is the dominant magnetic fabric into the SVU. It shows an oblate ellipsoid with a SW-dipping magnetic foliation and a SW-plunging magnetic lineation. Pattern 3, in the first meter of the Transect 2 (Sf3 Site T2-B1 **Table 5.S 1**), shows N-S trending k_1 and SSE-dipping magnetic foliation. Pattern 4 is observed in the central portion of the tectonic slice along Transect 2 and 3; it includes specimens with prolate to slightly triaxial AMS ellipsoid with a well-defined NE-SW trending magnetic lineation and interspersed k_2 and k_3 axes. A specific subfabric, named Pattern 5, was observed at site T1-B4 (Sf3 Site T1-B4 **Table 5.S 1**) and may be considered as local disturbance/variation.

5.2.2.2 The Vidiciatico sector

5.2.2.2.1 Transect 1

The sandstones of the footwall show an oblate magnetic fabric, characterized by low Pj and sub-horizontal magnetic foliation (Transect 1 in **Figure 5.20**). The χ_m shows a bimodal distribution coupled with a different orientation of the principal magnetic susceptibility axes. Specimens with lower χ_m values display a magnetic fabric with well-clustered AMS axes and sub-horizontal magnetic lineation with NW-SE trend. In contrast, the magnetic fabric of samples with higher χ_m shows a significant scattering of k_1 and k_2 on the magnetic foliation plane.

Within the SVU, the magnetic fabric is strongly oblate in the first 2 meters above the basal thrust, followed by an increase in χ_m. At a greater distance from the thrust (~ 10 m) the χ_m decreases and the magnetic fabric becomes prolate. Pj shows a slight increase near the main fault plane. Variations in the AMS scalar parameters are associated with changes in the magnetic fabric configuration. Sites T1-B1 and T1-B2 show a well-defined oblate magnetic fabric, characterized by a sub-horizontal W- to WNW-dipping magnetic foliation and a dominant NW-SE oriented magnetic lineation. In contrast, few samples from site T1-B1

(light-toned axes **Figure 5.20**) reveal sub-horizontal k_1 axes clustered at WSW, suggesting the presence of a second subfabric. In addition, the magnetic foliation becomes flatter with the proximity to the thrust plane.

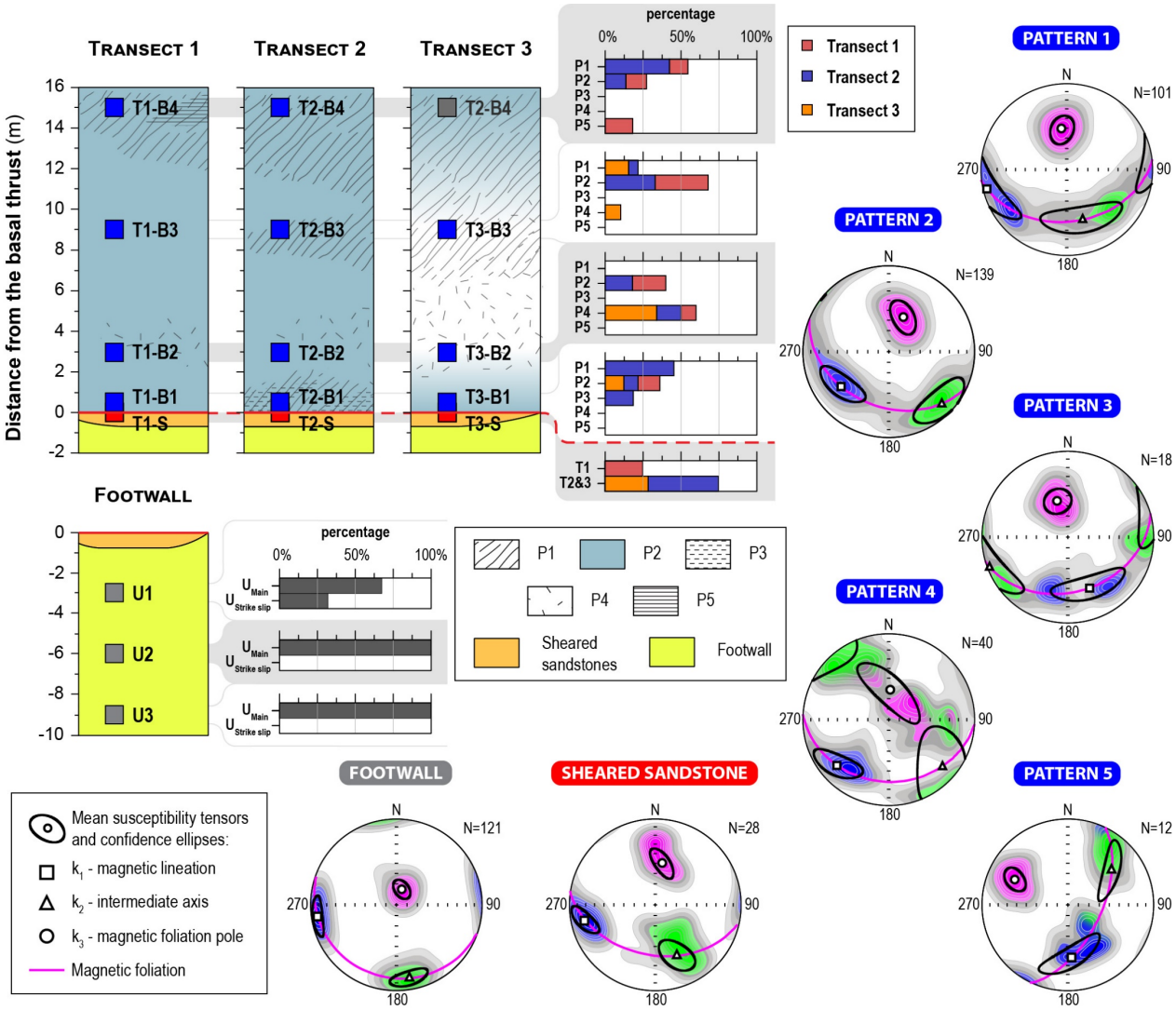

Figure 5.19. Distribution of the principal magnetic fabric detected in the footwall and Sestola-Vidiciatico Tectonic Unit transects from the Gova Tectonic window. Percentage histograms of pattern occurrence for levels at different distance from the main thrust. Lower hemisphere equal-area projections of the principal magnetic susceptibility axes with relative contour diagrams.

At ~ 10 m from the basal thrust (Site T1-B3), we observed a mixed magnetic fabric with a well-defined sub-horizontal magnetic lineation trending NW-SE and a magnetic foliation dipping toward NE at a high angle. The total fabric reflects the AMS configuration carried by most of the specimens (Subfabric 2 in **Table 5.S 3**). A minor subfabric is also registered, showing sub-vertical k_3 axes (light-toned axes **Figure 5.20**).

5.2.2.2.2 Transect 2

χ_m and T agree among sites, revealing a dominant oblate magnetic fabric along Transect 2 (**Figure 5.20**). Instead, Pj decreases significantly with distance from the basal thrust (**Table 5.S 3**). In both footwall and hanging wall, there is a prevailing magnetic fabric showing a NW-dipping magnetic foliation and a common

orientation of the k_1 axes at WNW to N. Site T1-B2 reveals the presence of an additional subfabric characterized by a higher Pj and magnetic foliation dipping toward W at a low angle (light-toned axes in **Figure 5.20**). Subfabric 2 shows a sub-horizontal magnetic lineation clustered at WSW.

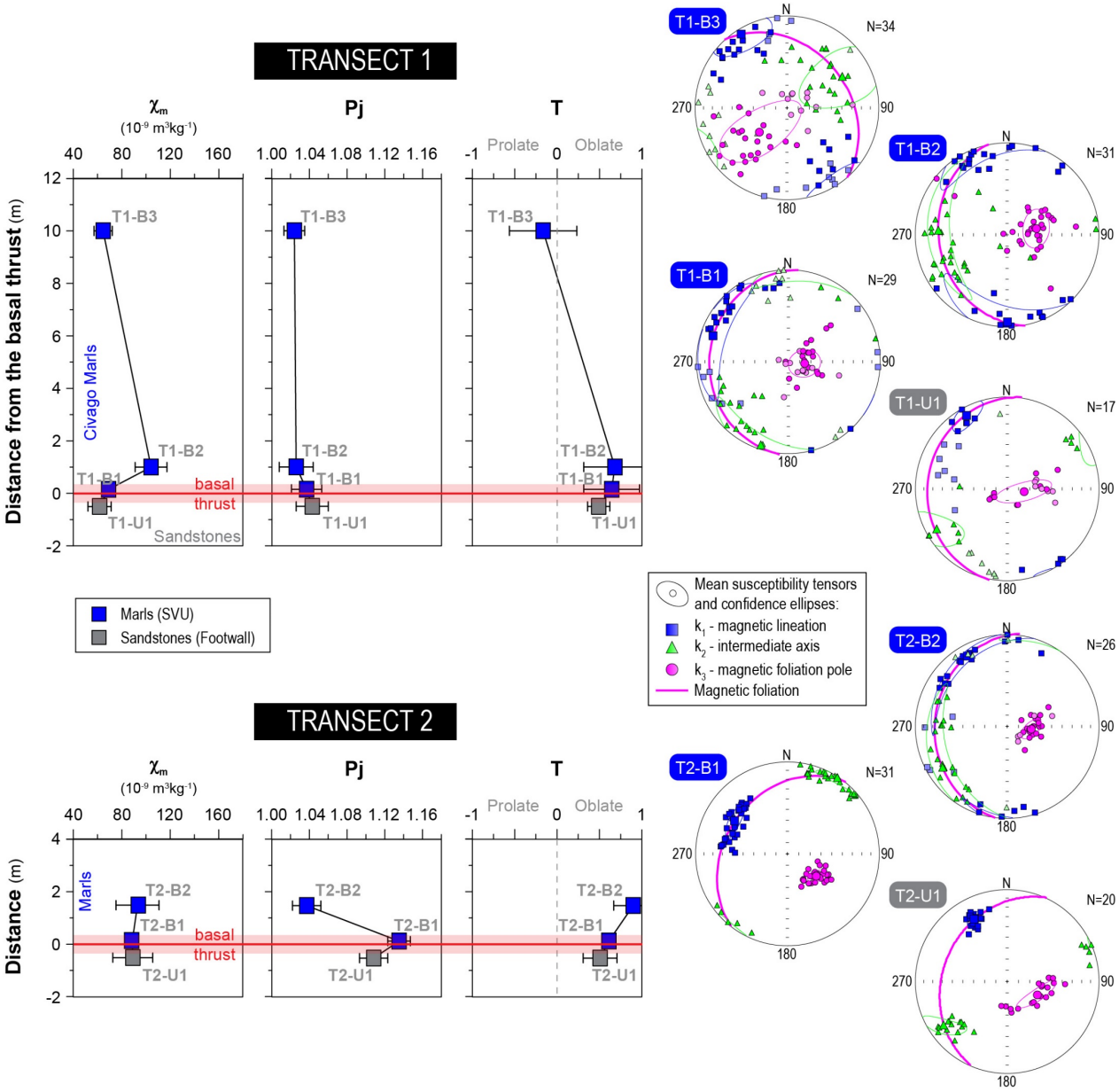

Figure 5.20. Magnetic fabric from the Sestola-Vidiciatico Tectonic Unit Transect 1 and 2, Vidiciatico sector. Plots of AMS parameters versus distance from the décollement (left). Lower hemisphere equal-area projections of the AMS axes at site level (right). Legends as in **Figure 5.17**.

5.2.2.2.3 Transect 3

Along Transect 2, the variation in magnetic fabric pattern and relative parameters is closely related to the origin of the tectonic slice. Here, the distance to the thrust fault is relevant only for marly domains. In fact, tectonic slices of marls show comparable values of both χ_m and Pj, while T is the only parameter that shows significant variation, shifting from oblate to prolate with increasing distance from the basal thrust (Site T3-

B3 in **Figure 5.21**). The orientation of the principal magnetic susceptibility axes also changes at greater distance from the thrust.

Sites T3-B1 and T3-B2 show a common mixed magnetic fabric with a WNW- dipping magnetic foliation. The k_1 axes reveal a bimodal distribution: (a) well-clustered toward NNW (heavy-toned axes in T3-B1 and T3-B2 stereoplots in **Figure 5.21**) or (b) slightly scattered around the SW direction (light-toned axes in **Figure 5.21**). At the Site T3-B2, we observed an additional subfabric (Subfabric 3 in **Table 5.S 3**; opened symbols in **Figure 5.21**) displaying the same axis orientation as at the Site T3-B3. The latter shows a prolate magnetic fabric characterized by a subvertical magnetic foliation and k_1 axes grouped in the NNE direction.

The varicolored shales of the Broken formation display a total mixed magnetic fabric consistent with that of the marly deposits. Two main subfabric were observed to share the same magnetic foliation dipping toward WNW at a low angle (Site T1-AR **Figure 5.21**), while the k_1 axes show a bimodal orientation trending NW or SW for subfabric 1 and 2, respectively (**Table 5.S 3**). In contrast, the boudins display a different fabric configuration, characterized by subvertical magnetic foliation. The only common feature with the total fabric is the orientation of the magnetic lineation toward NW.

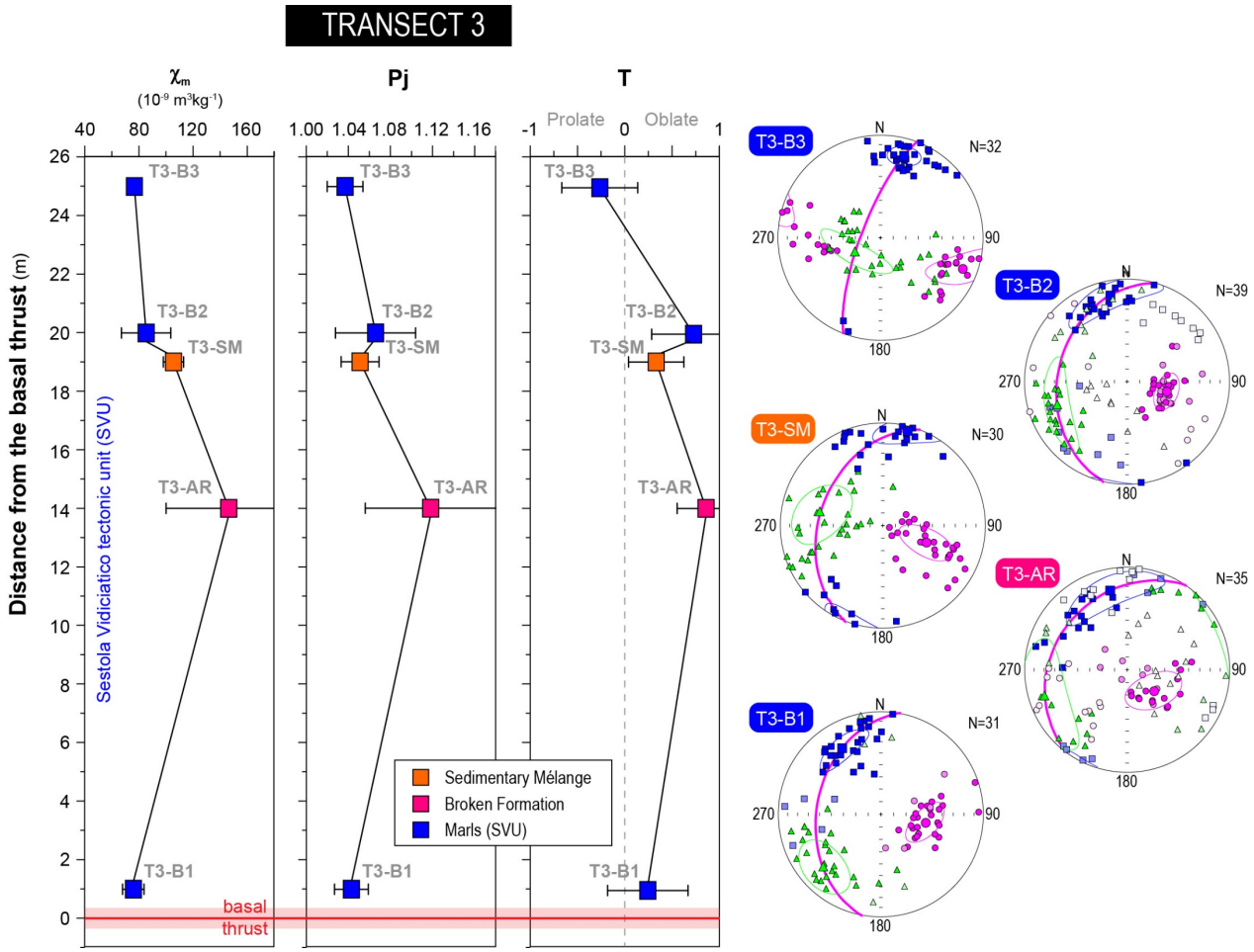

Figure 5.21. Magnetic fabric from the Sestola-Vidiciatico Tectonic Unit Transect 3, Vidiciatico sector. Plots of AMS parameters versus distance from the décollement (left). Lower hemisphere equal-area projections of the AMS axes at site level (right). Legends as in **Figure 5.17**.

The sedimentary mélange shows a neutral to slightly oblate magnetic fabric with a low Pj (**Figure 5.21**). The k_3 axes are SE-plunging at different angles, defining a slightly inclined NW-dipping magnetic foliation. The magnetic lineation is well-grouped and trends to NNE, while the k_2 axes partially deviate from the magnetic foliation plane.

Overall, the footwall shows the occurrence of two different subfabrics characterized by a common NW-dipping magnetic foliation and differing for the distribution of the principal susceptibility axes (**Figure 5.22**): (a) a dominant (81% of the specimens) neutral to slightly oblate subfabric showing well clustered k_1 axes NW-SE oriented and k_2 and k_3 slightly dispersed on a girdle; (b) the remaining 19% of the specimens exhibit an oblate fabric with magnetic lineation rotated in the WNW direction. The latter case is slightly represented in the footwall but appears to be dominant at site T2-B1, just above the basal décollement (compare stereoplots T2-B1 and Sf2 T1-U1, light-toned axes, **Figure 5.20**; **Table 5.S 3**)

Within the SVU, the magnetic fabric can be grouped in 4 main patterns depending on the orientation of the principal magnetic susceptibility axes (**Figure 5.22**). Pattern 1 is the main recurrent fabric, occurring all over the shear zone up to the farthest site from the basal thrust. It consists of an oblate fabric with a WNW-dipping magnetic foliation and a slightly inclined NW-plunging magnetic lineation, oblique to the foliation strike. An exception is the tectonic slice of the sedimentary mélange, which reveals a specific magnetic fabric different from all other patterns detected. This fabric is characterized by a NW-dipping magnetic foliation at an intermediate angle and a sub-horizontal NNE-trending magnetic lineation (T3-SM **Figure 5.20** and **Figure 5.22**). Pattern 2 is localized along the main and the secondary fault planes. It has a common magnetic foliation with Pattern 1, but the magnetic lineation is partially clustered in the SW-NE direction. In addition, Pattern 1 reveals a slight scattering of the k_1 axes within the foliation plane. Pattern 1 and Pattern 2 are also occurring in the broken formation matrix, contributing about 43% and 22%, respectively, to the total AMS of this tectonic slice (**Figure 5.22**; **Table 5.S 3**). Pattern 3, characterized by a steep NE-dipping magnetic foliation and SE-NW directed magnetic lineation, dominates (65%) the magnetic fabric at site T1-B3, about 10 meters from the basal thrust (**Figure 5.22**). This pattern is also preserved in the boudins of the broken formation (T3-AR, Sf3 Boudins; **Table 5.S 3**). Finally, Pattern 4 is characterized by a prolate magnetic fabric showing sub-horizontal k_3 axes clustered to NW and a magnetic lineation NE-trending. Pattern 4 is typical of site T2-B3 about 20 m from the thrust plane. This fabric is also recorded (~ 23%) at site T2-B2 at the contact with the overlaying marly tectonic slice where T2-B3 is located (see sampling scheme in **Figure 5.3d**).

5.2.3 AARM, AIRM and HF-AMS

The ARM fabrics are mostly well-defined for all patterns, showing slight but significant differences (**Figure 5.23** and **Figure 5.24**). The local occurrence of high within-site scatter may be related to the low RM intensity (typically $\ll 40 \times 10^{-6}$ Am^2 Kg^{-1}), suggesting low concentration of ferrimagnetic minerals. About 36% of specimens reveal low F-test values (< 2.61, the limit of statistically anisotropic specimens within the 90% of likelihood), which are independent to RM intensity, ARM window, and lithologies (**Figure 5.23d, e**

and **Figure 5.24d, e**). In particular, around the 63% of samples from the sandstones at Vidiciatico and the shear sandstones at Gova reveal isotropic fabrics. However, after removing few outliers (Pj > ±2σ), the ARM fabric has well-defined mean axes clustered at pattern level (**Figure 5.23a-c**). Pj and T values strongly vary at site and pattern levels (**Table 5.S 2** and **Table 5.S 4**). Overall, Pj tends to be equal to or slightly higher than AMS (**Figure 5.S 4** and **Figure 5.S 6**). Only at site T2-B1 at Vidiciatico Pj decreases significantly. Occasionally, AIRM show the highest Pj values. T decreases for almost all patterns, showing a neutral to prolate fabric for all the remanence-bearing grains (**Figure 5.S 5** and **Figure 5.S 7**). The exceptions are the patterns P4 (at both Gova and Vidiciatico) where the magnetic fabric changes from prolate for AMS to neutral or oblate for ARM experiments.

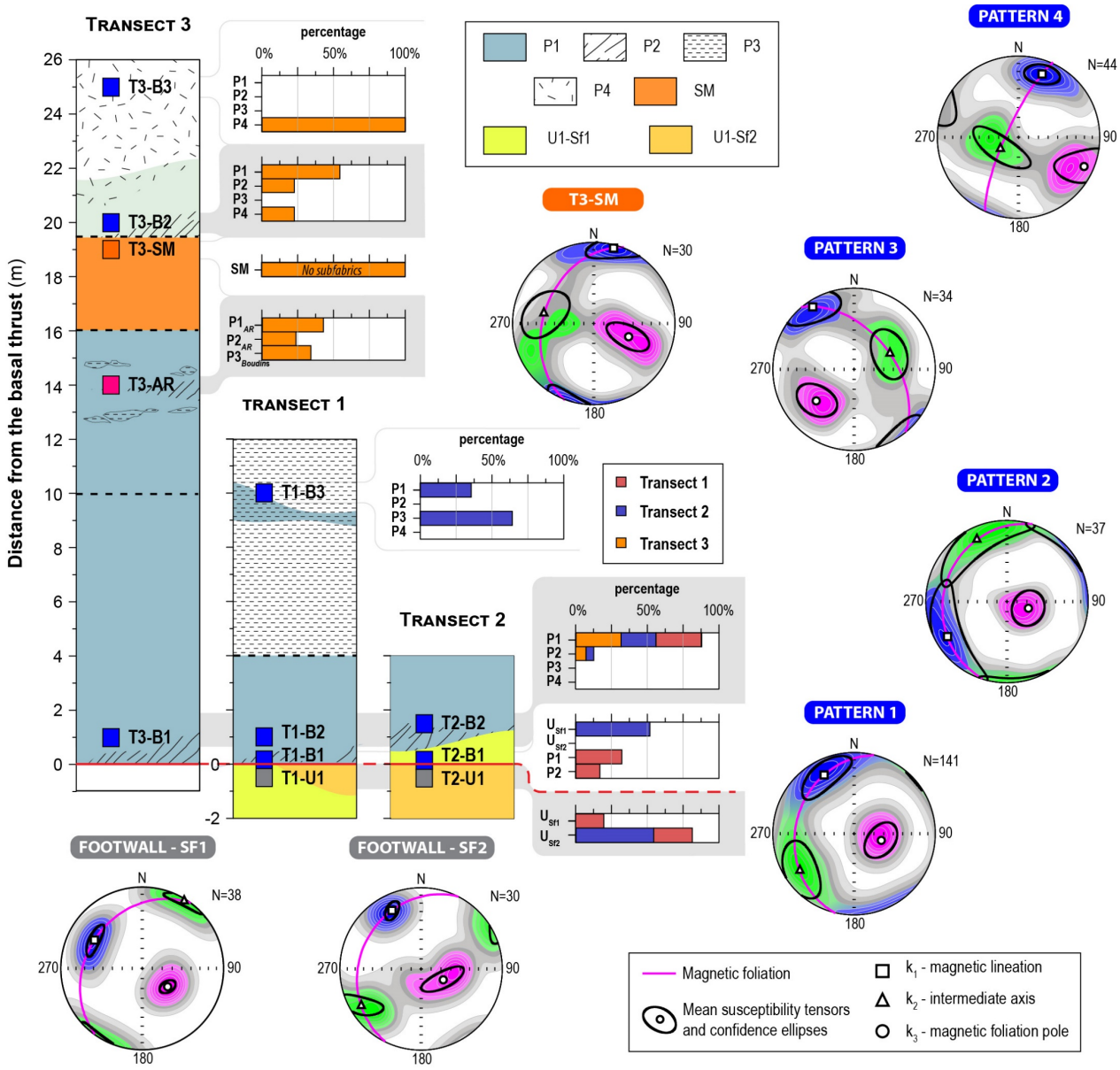

Figure 5.22. Distribution of the subfabrics detected in both footwall and hanging wall of the SVU from the Vidiciatico sector. Percentage histograms of pattern occurrence depending on the relative distance from the main thrust. Lower hemisphere equal-area projections of the principal magnetic susceptibility axes with relative contour diagrams.

5.2.3.1 The Gova Tectonic Window

For Pattern 1, the ApARMs and AARM display maximum (A_1) and minimum (A_3) axes inverted to the AMS ones (**Figure 5.23a**), suggesting the presence of SD magnetite (Rochette, 1988; Rochette et al., 1999) or MD grains rotated in respect to the other ferro- and paramagnetic grains (Biedermann et al., 2020). The orientations of the principal axes at Pattern 2 are statistically indistinguishable from the AMS. The only exception is the $ApARM_{100-40}$, where A_3 is sub-horizontal and A_1 moves toward the k_3. Pattern 3 reveals overlapping A_1 axes, however A_2 and A_3 are switched with respect to those of the AMS. ARM fabrics for Pattern 4 are all consistent and similar to those of Pattern 3. In this case, the A_1 axes are N-plunging at high-angle, whereas A_3 show the same direction of k_1. AARM and ApARMs fabrics of Pattern 5 strongly differ to the AMS, revealing a sub-horizontal NE-SW trending A_3 and vertical A_1 axes. The AIRM yields the same fabric of AMS in most of patterns, even if the principal axes scatter increase (**Figure 5.23a**). The two exceptions are Pattern 3 and 4, where I_1 is NW-SE trending and parallel or orthogonal with the related AMS configuration. The I_3 and I_2 axes are girdled in the NE-SW direction.

In the footwall and sheared sandstones, the ARM experiments show the same fabric at pattern level (**Figure 5.23b-c**). For site T1-S (Transect 1 **Figure 5.23b**), the maximum axes (A_1 and I_1) for the various coercivity components are interspersed within the magnetic foliation plane, which is the same as the AMS. In addition, for the pattern $U1\text{-}Sf2_{(strike\ slip)}$ (**Figure 5.23c**), the maximum and intermediate axes are rotated about 20° counterclockwise with respect to the AMS ones.

5.2.3.2 The Vidiciatico sector

The AARM and ApARMs show well-defined magnetic fabrics with a mostly similar axis configuration among experiments at the site level (**Figure 5.24a-b**). Within the SVU, the orientation of the principal axes of the ferromagnetic fabric appears to be related to their location along a specific transect, as well as the structural position, rather than the AMS fabric/pattern (**Figure 5.24a**). In fact, ARM fabric for AMS Pattern 1 and Pattern 2 are different if compered among the three transects. Along transect 1, the ARM experiments share the same SW-oriented magnetic lineation, which is orthogonal or parallel to k_1 of Pattern 1 and Pattern 2, respectively. Moreover, Pattern 1 shows a NE-plunging pole of the magnetic foliation (A_3) consistent with that of the AMS (k_3). In contrast, the A_1 axes of Pattern 2 are sub-horizontal, discordant with the sub-vertical k_3 of the AMS. The AIRM provides the same fabric as the AMS. At transect 2, AARM and ApARMs reveal a sub-vertical magnetic lineation (A_1) and sub-horizontal A_3 axes, showing independent orientation from the AMS fabrics. Same ARM fabrics were observed for Pattern 3. AIRM experiments are less defined and show a broad dispersed magnetic lineation N-S to NNE-SSW-trending (**Figure 5.24a**). The magnetic foliation varies from slightly dipping to sub-vertical, unlike that of AMS. Along transect 3, the anisotropy of remanence displays the same magnetic foliation as the AMS. In particular, Pattern 1 shows variations in magnetic lineation orientation depending on the coercivity window. A_1 is sub-horizontal or sub-vertical for $ApARM_{40-0}$ and $ApARM_{100-40}$, respectively, which in turn is parallel or orthogonal to k_1. In contrast, Pattern 2

has coaxial ellipsoids between AMS, AIRM and ARM experiments. Finally, for Pattern 4 all principal axes are statistically indistinguishable from the AMS (**Figure 5.24a**).

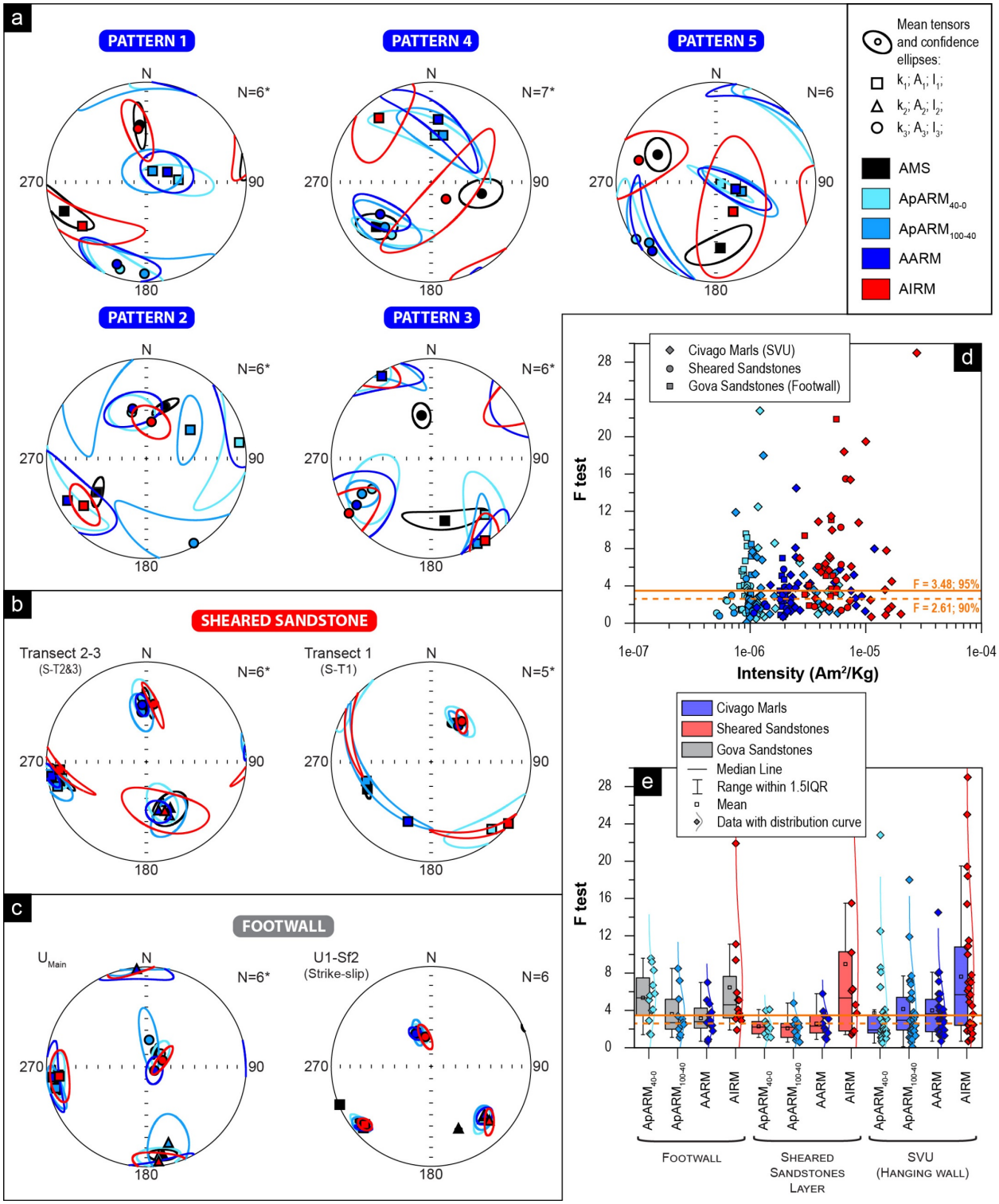

Figure 5.23. Principal directions and confidence ellipsoids of the anisotropy of magnetic remanence experiments in: (**a**) Civago marls tectonic slice; (**b**) sheared sandstones; and (**c**) sandstones of the footwall. Variations of the *F*-test versus remanent magnetization (**d**). Box-and-whisker plot with data and normal distribution curves of the *F*-test among lithologies and ARM experiments (**e**).

In the footwall, different orientation of the AMS and ARM fabrics were observed at the site level. At sites T2-U1 and T2-B1, the AMS and anisotropy of remanence experiments yield the same fabric (**Figure 5.24b**).

At site T1-U1, Subfabric 1 displays A_1 sub-parallel to k_1 with the exception of the $ApARM_{100-40}$ where A_1 is orthogonal. The magnetic foliation can be consistent or significantly different from AMS depending on the coercivity window. In contrast, ARM experiments for subfabric 2 show A_1 axes orthogonal to the magnetic lineation of the AMS, while A_3 and I_3 strongly vary in orientation (**Figure 5.24b**).

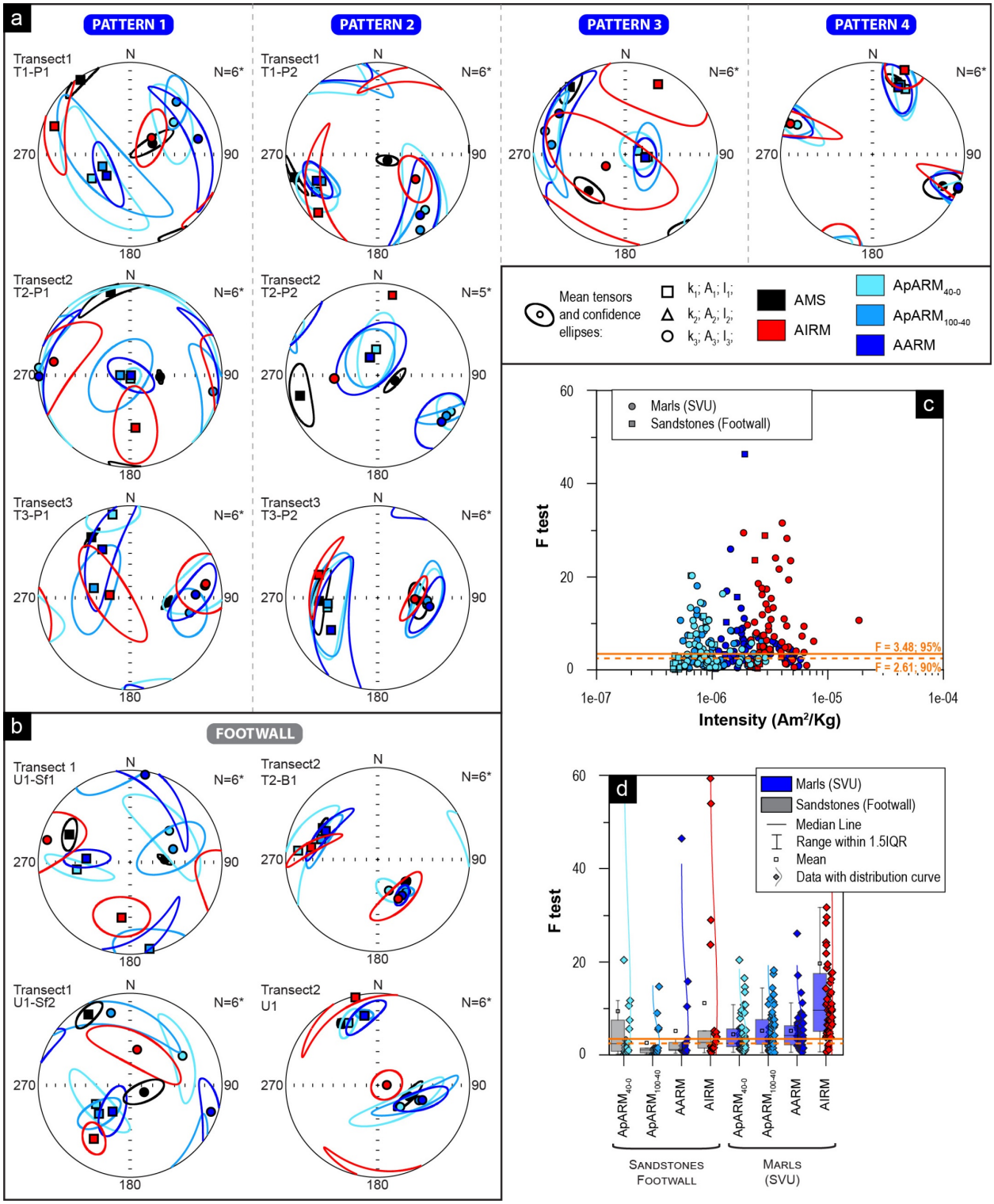

Figure 5.24. Principal directions and confidence ellipsoids of the ARM experiments in: (**a**) Marmoreto marls tectonic slices; (**b**) sandstones of the footwall. Variations of the *F*-test versus remanent magnetization (**c**). Box-and-whisker plot with data and normal distribution curves of the *F*-test among lithologies and ARM experiments (**d**).

To discern the main carriers of the AMS, we separated the para- and ferromagnetic components of the HF-AMS (**Figure 5.25**). The results indicate that the anisotropy of both sandstones and tectonized marls are dominated by the paramagnetic fraction (97 ± 34%). The ferromagnetic component appears to be neglectable (3 ± 19%). In fact, the high-field paramagnetic subfabrics (HF-AMS_{para}) are mostly coaxial with the low-field AMS for all the different patterns, confirming that paramagnetic minerals carry the AMS (**Figure 5.25a**).

In the footwall, the ARM experiments of the selected samples are mostly isotropic (open symbols in **Figure 5.25a, c**) and show a steeper magnetic foliation. The A_1 and A_2 axes are switched in respect to k_1 and k_2 of both LF-AMS and HF-AMS_{para}. In contrast, the HF-AMS_{ferro} fabric is rotated about 70 ° from the LF-AMS (**Figure 5.25a**).

Within the SVU, the HF-AMS_{para} fraction coincides with the LF-AMS, while the HF-AMS_{ferro} and ARM experiments reveal complex relationships with no general trend. Overall, the resulted ferromagnetic subfabrics (both remanence-bearing and HF-AMS_{ferro}) show at least one of the three principal axes sub-parallel with the LF-AMS (**Figure 5.25a**). The interchanges among the axes and variations in their orientation appear to be related to the microscopic structural fabric at specimen level. The HF-AMS_{ferro} subfabric can be coaxial or strongly deviate from the ARM and ApARMs experiments.

In particular, the two representative samples of Pattern 1 show similar orientation of magnetic foliation for ApARMs and Hf-$_{ferro}$, despite the different dip angles. However, maximum (A_1, I_1 and k_1) and intermediate (A_2, I_2 and k_2) axes are interchanged between the specimens, which resulted in A_1 and k_1 (HF-AMS_{ferro}) being parallel or orthogonal to those of the LF-AMS (**Figure 5.25a, c**). The samples from Pattern 2 share one of the principal axes (minimum or maximum) with the LF-AMS. The k_1 and A_1 axes are coaxial or orthogonal to each other. Instead, the minimum axes can be consistent with those of the LF-AMS or interspersed with the intermediate axes (**Figure 5.25a**).

For pattern 3, the magnetic lineation of ARM subfabrics is generally sub-vertical and NE-oriented, which in turn is orthogonal to the k_1 of HF-AMS_{para} and LF-AMS (**Figure 5.25a, c**). The magnetic foliation is also sub-vertical and can agree with or differ from that of LF-AMS. In contrast, the HF-AMS_{ferro} subfabrics have independent orientations, with sub-horizontal magnetic foliation and lineation. The k_1 have a double tendency to be parallel or orthogonal to the long axis direction of the AMS (**Figure 5.25a**).

5.2.4 Ternary

We use ternary diagrams to interrelate AMS and ARM directional data with the main structural elements (i.e., cleavage, S-C intersection, and transport direction; **Figure 5.26c-d**). The diagrams are subdivided into different areas according to the contributions of three end-members representative for AMS deformation stages (see details for plotting the diagrams in 3.5 Ternary Diagrams). The upper vertices correspond to fabric with the magnetic foliation orthogonal to the cleavage and/or bedding. In our setting it represents a strongly deformed tectonic fabric induced by sub-horizontal LPS (Graham, 1966; Borradaile & Henry, 1997;

Hrouda & Chadima, 2020) characterized by sub-horizontal k_3 parallel to the shortening direction and subvertical k_1 axis. For AMS data, they may also indicate the occurrence of an inverse fabric (Potter & Stephenson, 1988).

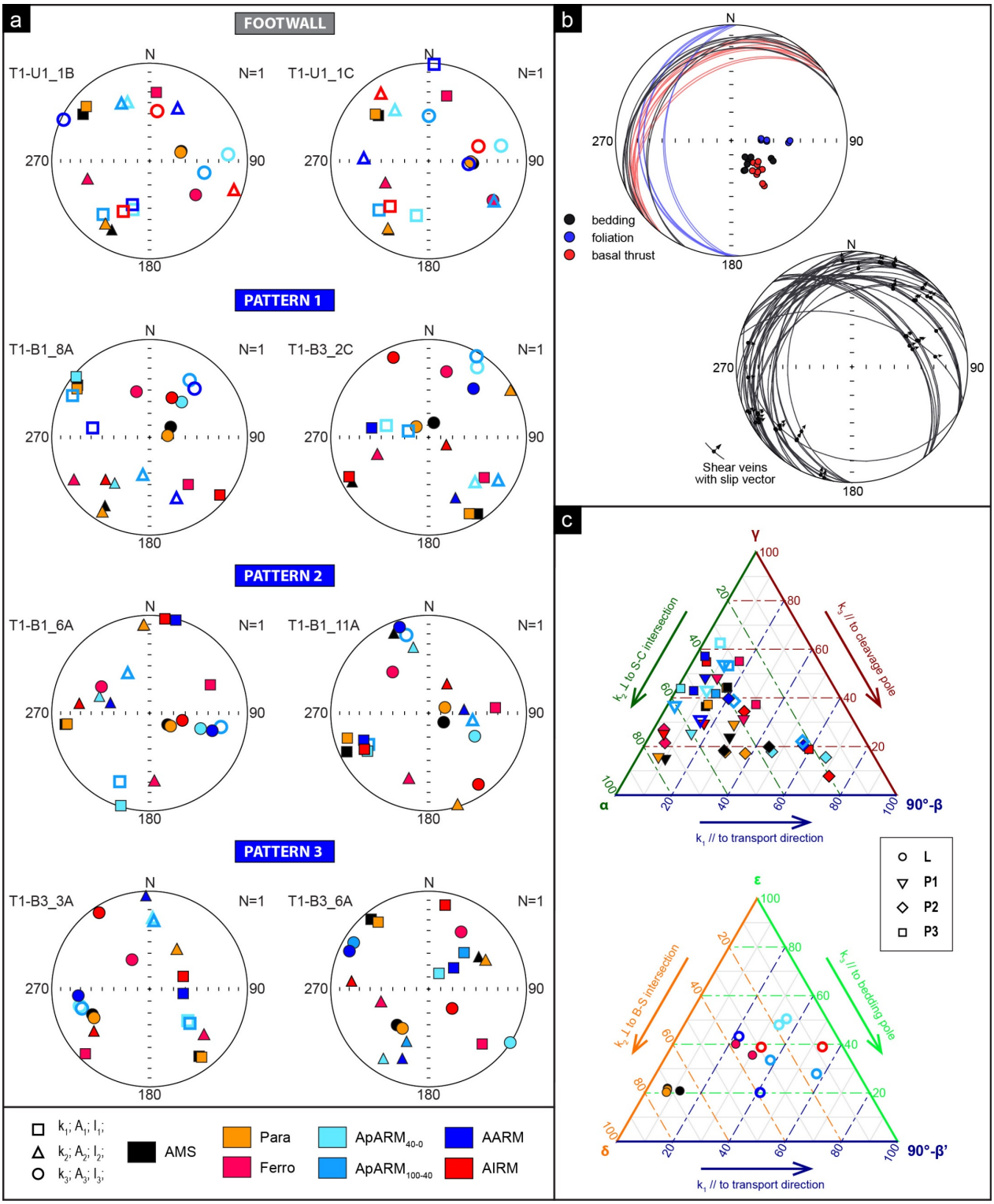

Figure 5.25. (**a**) Stereoplots (Lower hemisphere equal-area projections) of the principal directions of the LF-AMS, ARM experiments and the paramagnetic and ferromagnetic components of the high-field AMS for representative samples, classified after patterns. Open symbols represent data with F-test lower than 5; (**b**) Summary of the structural data (see **Figure 5.3** for details); (**c**) Ternary diagrams relating structural and anisotropy of magnetic susceptibility and remanence data.

The base of the diagrams indicates the parallelism between the magnetic and the structural foliations. The intersection lineation fabric (Graham, 1966; Hirt et al., 2004; Weil & Yonkee, 2009) is plotted at the lower left vertex (**Figure 5.26a, b**). The magnetic foliation coincides with either the bedding or the cleavage depending on the tectonic overprint degree (Kligfield et al., 1981, 1983; Pueyo Anchuela et al., 2012), as well as the intensity of the original pre-deformational fabric (Parés & van der Pluijm, 2002; Till et al., 2010). This is also true for shear zones of low finite shear strain, where k_1 is parallel to the S-C intersection (Pueyo Anchuela et al., 2010; Casas-Sainz et al., 2018). The lower right vertex represents high degree of non-coaxial strain, where k_1 is parallel to the transport direction (Averbuch et al., 1992; Ferré et al., 2014; Casas-Sainz et al., 2018).

5.2.4.1 The Gova Tectonic Window

Specimens from the SVU are distributed along the lower sides of the diagram (**Figure 5.26a**), showing a high consistency between the magnetic foliation and the cleavage. P1 and P2 are characterized by the progressive correspondence of k_1 with the S-C intersection and the transport direction, respectively. This is also true for the two patterns observed in the sheared sandstones (S-T1 and S-T2&3; **Figure 5.26a**). The broad data dispersion reveals the simultaneous occurrence of two end-members representative of LPS and shearing, with variable relative contribution. For Pattern 4, k_1 axes are consistent with the transport direction and magnetic foliations has a fan-like orientation. Thus, data are well-aligned and distributed toward the 90°-β vertex, suggesting competition of end-members with a progressive alignment with the shear-related fabric. Data from ARM experiments (**Figure 5.26e**) are mainly distributed in the central and upper portion of the diagram. In fact, most of the ARM fabrics reveals a magnetic foliation at high angle with respect to cleavage. Different behaviours are associated to the P1 pattern and the shear sandstones, where the deviation of A_1 axes from the shear direction is clearly visible in the ternary diagram. In the footwall, specimens mostly show a one-to-one relationship between the magnetic foliation and the bedding plane. The broad correspondence between the magnetic lineation and the B-S intersection results in data clustered toward the δ vertex. Similar consideration can be done for the ARM experiments in the footwall (**Figure 5.26f**).

5.2.4.2 The Vidiciatico sector

Good agreement between magnetic foliation and cleavage can be observed for P1 and P2, as the data are distributed close to the lower side of the ternary diagram (**Figure 5.27a**). The magnetic lineation of the patterns P1 and P2 tends to be parallel to the S-C intersection or the shear direction, respectively. In fact, the data of these two patterns are clustered at opposite vertices (**Figure 5.27a**). This behaviour is also visible for the two patterns observed in the matrix of the broken formation (P1-AR and P2-AR in **Figure 5.27a**). The presence of steep magnetic foliation for Pattern 3 and 4 is emphasized by the distribution of the data at progressively greater distance from the bottom side of the diagram (**Figure 5.27a**). In addition, P3 is clustered near the left side, suggesting agreement between k_1 and the S-C intersection. In contrast, the sedimentary mélange reveals a magnetic foliation slightly consistent with the footwall bedding, but the higher dispersion of the dataset reveals little correlation with the structural elements (**Figure 5.27b**).

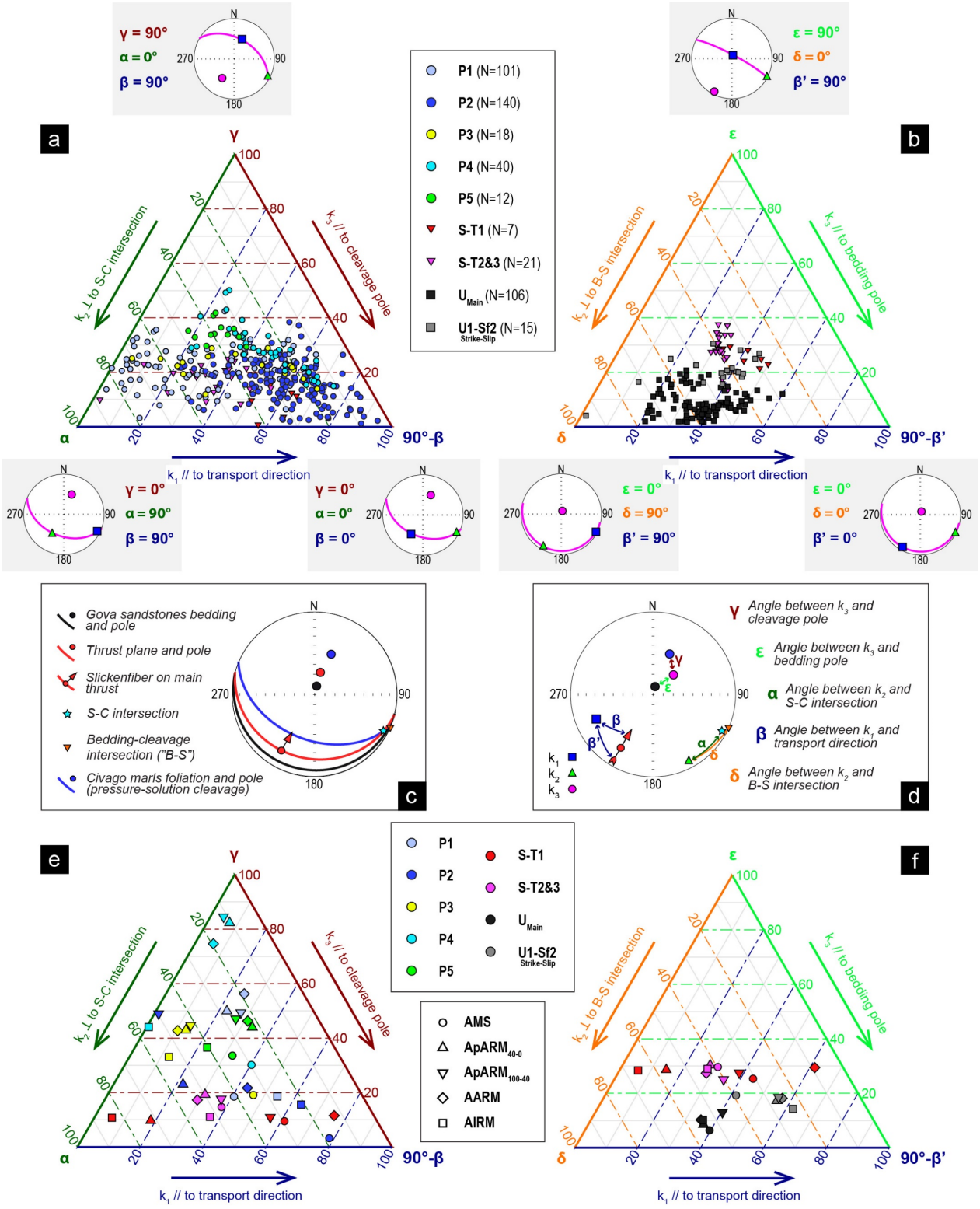

Figure 5.26. Ternary diagrams relating structural and magnetic directional data. Anisotropy of magnetic susceptibility (**a**) and mean anisotropy of magnetic remanence (**e**) data from the Civago marls and sheared sandstones, classified after pattern; data from the footwall and sheared sandstones: AMS (**b**) and ARM (**f**); schematic representation of the magnetic fabric end-members are reported close to the vertices. (**c**) Stereoplot of the mean values of mesoscale structural data (modified from Remitti et al., 2012); and (**d**) representation of the computed angles between structural and magnetic fabric elements.

The datasets of ARM experiments reveal complex relationships with respect to the structural data. Overall, the ARM subfabrics show a magnetic foliation at higher angle with respect to the cleavage than AMS, as

data are dispersed toward the central upper portion of the diagram. This is particularly visible for patterns P1 and P2 in transect 2 (T2-P1 and T2-P2 in **Figure 5.27c**) and for pattern P3. An exception is the pattern P2 along transect 3, where ARM fabrics show better consistency between the magnetic foliation and the cleavage than AMS. In addition, the maximum axis (A_1 and I_1) for P1 and P2 display a double tendency to be parallel or orthogonal to the transport direction as the data are scattered between the left and right sides of the ternary diagram (**Figure 5.27c**). The good correlation among AMS and ApARMs of P4 is reflected by the cluster of data.

The sandstones of the footwall reveal good parallelism between the magnetic foliation and lineation with bedding and B-S intersection, respectively (**Figure 5.27b**). A similar distribution of data is observed for the ARM subfabrics detected along transect 2. In contrast, subfabric U1-Sf1 and U1-Sf2 show significantly different configuration for AMS and ARMs, where the latter exhibit magnetic foliation at a high angle to the bedding plane (**Figure 5.27d**).

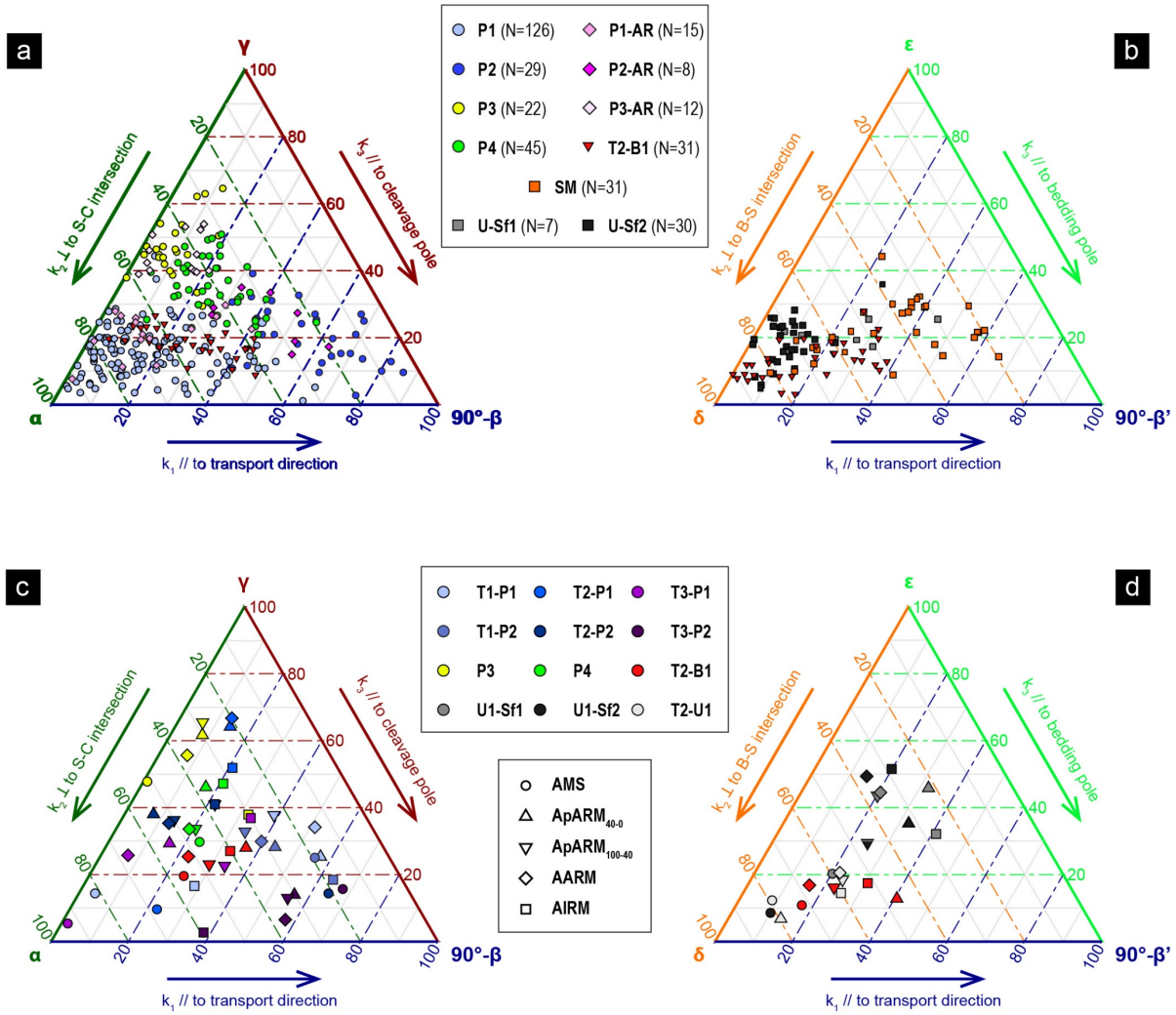

Figure 5.27. Ternary diagrams (see **Figure 3.3** for parameters details) relating structural and magnetic directional data. AMS (**a**) and mean ARM (**c**) data from the Marmoreto marls, classified after pattern; data from the footwall: AMS (**b**) and ARM (**d**).

5.3 Discussion

5.3.1 Local heterogeneities in strain recorded by AMS

Magnetic fabric is sensitive to the local variability of the strain field during faulting (Braun et al., 2015; Levi et al., 2014; Yang et al., 2020). It allows the tracking of heterogeneities in the spatial distribution of inelastic strain and strain partitioning across intraplate shear zones and thrust faults (Casas-Sainz et al., 2017, 2018; Román-Berdiel et al., 2019; Greve et al., 2020). The progressive evolution of the magnetic fabric due to an increase in deformation intensity (i.e., shearing and/or LPS) follows trends that have been demonstrated in a number of studies (e.g., Parés & van der Pluijm, 2002; Pueyo Anchuela et al., 2010; Satolli et al., 2020). The parallelism between the magnetic foliation and bedding or cleavage qualitatively reveals the degree of reworking of the original sedimentary fabric. The consistency between the magnetic lineation and the S-C intersection or the transport direction may reveal the intensity of shearing/faulting.

In the case of the SVU we observe a heterogeneous distribution of the principal axes of the AMS ellipsoids, despite the homogeneity in structural data. Conducting AMS analysis by combined contour plot and cluster analysis at the site level allows discernment of distinct subfabrics with straightforward correlations with structural data. In most patterns, the consistency between the magnetic foliation and the pressure-solution cleavage (**Figure 5.26** and **Figure 5.27**) clearly indicates a tectonic origin, with only minor influence from the original sedimentary fabric. The coherence with structural elements, coupled with the absence of correlations between χ_m and scalar parameters, allows the interpretation of AMS data in terms of local variation of strain features.

Combining the observed geometric relationships between magnetic and structural fabrics, the following can be inferred:

1. P1, with the parallelism between the magnetic lineation and the S-C intersection (**Figure 5.26a** and **Figure 5.27a**), may be associated to a lower degree of shear strain away from the main thrust faults, with dominant LPS or local contraction within the intraplate shear zone;

2. P2, which shows a k_1 parallel to the top to NE transport direction (**Figure 5.26a** and **Figure 5.27a**), indicates a high degree of non-coaxial strain with complete reworking of the initial fabric (Parés & van der Pluijm, 2002; Casas-Sainz et al., 2018). Its occurrence and distribution differ in the two localities (**Figure 5.19** and **Figure 5.22**). At Gova, P2 is recurrent throughout the shear zone, whereas at Vidiciatico its distribution is limited only close to the principal fault planes, suggesting variation in strain registration in different portions of the intraplate shear zone. Local variations were observed at Gova, with the P3 pattern showing a magnetic lineation N-S to NNW-SSE trending consistent with some of the slickenfibers detected on the main thrust faults (Remitti et al., 2012). Considering their position in the first meter from the basal thrust (T2-B1 in **Figure 5.18** and **Figure 5.19**), they may represent local variations in the accommodation of the shear along the fault plane;

3. Locally, the magnetic fabric might reflect early stage of deformation and/or previous tectonic events. In fact, P4 at Gova, characterized by a prolate fabric with a loose cluster of k_1 around the shear direction, may consist of a transitional magnetic fabric with only partial reworking of an original sedimentary or a previous pre-faulting deformation fabric. We suggest that the axes interspersion in a plane perpendicular to the cleavage (Pattern 4 in **Figure 5.19**) reveals the preservation of the lozenge-shape petrofabric formed by crosscutting normal shear faults/fractures during the initial brittle stage of deformation, when the marly sediments were not completely lithified (Remitti et al., 2007; Vannucchi et al., 2010). Similar consideration can be applied to P3 at Vidiciatico, which reveals a prolate magnetic fabric characterized by a NE-dipping magnetic foliation and a sub-horizontal NW-SE trending magnetic lineation (**Figure 5.22**). The occurrence of a magnetic lineation consistent with the S-C intersection (**Figure 5.27a**) might reveal a considerable contribution of the LPS with an incomplete reorientation of the primary magnetic fabric. Alternatively, P3 can be associated to the folding stage that occurred at the frontal part of the accretionary prism (Vannucchi & Bettelli, 2002; Bettelli & Vannucchi, 2003; Remitti et al., 2012);

4. At greater distance from the basal thrust, independent magnetic fabric can also be observed. For example, at Gova, P5 represents a local variation observed close to the contact with the Fiumalbo shale (T1-B4) and without any relationship with the structural data. Possible explanations are: (a) higher contribution of ferromagnetic minerals and the presence of a mixed/intermediate magnetic fabric (Ferré, 2002; Pueyo Anchuela et al., 2010), considering that this pattern shows the highest χ_m values; (b) percolation of ferruginous fluids (Ejembi et al., 2020); and (c) preservation of a strong original fabric. At Vidiciatico as well, we noted a magnetic fabric showing independent orientation of the AMS axes with respect to the structural elements. This fabric, called P4, appears at about ~ 20 m from the basal décollement and shows a prolate magnetic fabric with subvertical magnetic foliation (T3-B3 in **Figure 5.21** and P4 in **Figure 5.22**). Its occurrence can be related to a variety of processes, such as (a) superposition of a previous deformation fabric with the thrusting stage, (b) tilting of the magnetic fabric acquired during the soft sediment deformation while the tectonic slice was incorporated within the intraplate shear zone, (c) advanced stage of LPS, or (d) local accommodation of the deformation between tectonic slices;

5. The tectonic slice of the broken formation reveals a mixed magnetic fabric characterized by the superposition of two patterns having the same axes orientation of P1 and P2 (**Figure 5.21** and **Figure 5.27a**). This configuration suggests a good record of the strain during thrust faulting with partial to total reworking of the previous deformation fabric that produced the block-in-matrix fabric. The latter is still preserved in the boudins, which show the same fabric of the P3 at Vidiciatico. This fabric can be related to the preservation of the brittle boudinage associated with the folding stage that occurred at the front of the accretionary prism (Remitti et al., 2012);

6. The tectonic slice of sedimentary mélange reveals evidence of the original sedimentary/gravitational origin. Some specimens still show a sub-vertical k_3 and well-clustered k_1 axes (**Figure 5.21** and **Figure 5.22**), typical of imbricated fabric related to emplacement under current and subsequent compaction

(Sagnotti et al., 1994). In addition, the presence of k_3 axes plunging at high angle and k_2 axes deviating from the mean magnetic foliation plane, might reflect the local reworking of the initial sedimentary fabric. In fact, the magnetic foliation and lineation of these specimens partially agree with the cleavage and the shear direction, respectively.

The distribution of different patterns is related to the distance from the main thrust plane, but also varies between the two localities.

At Gova, Site T2-B1 is affected by strong heterogeneities which lead to a high dispersion of k_1 along the cleavage plane. This configuration may result from: (a) a dominant fraction of pure shear compared to simple shear (Kitamura & Kimura, 2012); and (b) variation in the intensity of deformation preserved by the different lithons. We prefer the latter, given the variations observed with distance. P2 and P3 patterns are detected in the first 30 cm from the basal thrust while P1 becomes dominant at greater distance. These observations also support the hypothesis of shear localization along discrete planes and the occurrence of an intersection lineation fabric when the shear is diffuse and less intense. The high fabric variability at this site can also be ascribed to the presence of a brecciated level which could be related to friction while faulting or to local high fluid pressure (Remitti et al., 2007). The variations in AMS patterns are also associated to changes in Pj and T depending on the distance from the main thrust faults (**Figure 5.17** and **Figure 5.18**). Close to the basal thrust the magnetic fabric is dominantly oblate (P2 and P3) and Pj slightly increases. In the central portion of the tectonic slice, Pj gradually diminishes, and the ellipsoids become less oblate or prolate. Thus, the presence of the patterns related to previous tectonic or sedimentary fabric (P4–P5) or less intense deformation (P1) becomes dominant. Heterogeneities were also observed between transects. Along Transect 1, where P2 is dominant, Pj and T remain almost constant. Instead, transects 2 and 3 show major changes in Pj and T, associated with a minor pervasivity of P2. We ascribe these observations to an increase in Pj and oblateness due to shear strain localization along the boundary faults.

At Vidiciatico, P1 is the dominant magnetic fabric whereas P2 is confined along the basal thrust and secondary fault planes, coupled with an increase in Pj and T (**Figure 5.22**). Again, fabric related to the early stages of deformation (P3-P4) or to the different origin of the tectonic slice (T3-SM) becomes dominant at a greater distance from the basal décollement, where Pj tends to decrease and the ellipsoid changes into prolate. Heterogeneities among transect are related to the presence of tectonic slices of different origins. For example, the occurrence of high Pj and T values in the broken formation must be associated with the original block-in-matrix fabric, as well as with a different relative concentration of ferromagnetic grains, since χ_m shows the highest values (**Figure 5.16**). In contrast, the distribution of the magnetic fabric is equivalent among transect in the first 4 m from the basal thrust, where marly sediments are the dominant components.

Overall, changes in the distribution of magnetic fabrics between the two localities might be ascribe to a different repartition of diffuse vs. localized deformation. The possible presence of previous sedimentary or tectonic fabric with unfavourable orientation should also be considered.

Between hanging wall and footwall portions of the underlying units can be dragged and intruded below the basal décollement, such as the level of shear sandstones occurring at Gova (Remitti et al., 2012). Here, the AMS shows a magnetic foliation at medium to high angles with respect to the bedding (**Figure 5.26a**). Along transect 1 the magnetic fabric shows higher Pj values with respect to the other 2 transects and is consistent with the shear-related pattern (P2). On the contrary, in transect 2 and 3 the magnetic lineation is consistent with the S-C intersection. Thus, they may have mainly registered the LPS. This configuration can also be associated to a stronger original magnetic fabric and a different degree of reworking.

Most samples from the footwall shows a magnetic foliation parallel to the bedding and a well-clustered magnetic lineation consistent with the B-S intersection. This reveals a main sedimentary fabric with dominant uniaxial overburden during underthrusting (Yang et al., 2013). The k_1 axes cluster may be associated with incipient deformation registered during the early stages of LPS (Graham, 1966; Caricchi et al., 2016). This is evident in the footwall at Vidiciatico, where the subfabric U_{Sf2} (**Figure 5.22**) shows slight but significant change in AMS configuration, with the k_1 and k_2 axes forming a girdle in the direction of LPS. In addition, a second pattern (U1-$Sf2_{(strike\ slip)}$) in agreement with the presence of strike-slip faults can be detected in the first 3 meters below the basal décollement at Gova. Variations of magnetic fabric in the footwall suggest changes in deformation regime between the plate boundary shear zone and the underthrusting sediments. In addition, the low Pj as well as a reduction of ellipsoid oblateness can be associated to a reduced degree of compaction, probably due to elevated fluid pressure (Yang et al., 2013). This agrees with a weak décollement and strain decoupling across the basal thrust (Housen et al., 1996; Yang et al., 2013; Greve et al., 2020).

5.3.2 Ferromagnetic fabric insight into the deformation history of a shear zone

ARM and LF-AMS data from the footwall are generally similar (**Figure 5.23c** and **Figure 5.24b**), indicating that para- and ferromagnetic minerals have undergone the same deformation, uniaxial vertical strain with minor contribution of local LPS due to the proximity to the décollement. In the studied lithologies, both ferrimagnetic and paramagnetic minerals are predominantly primary, of detrital origin, and are thought to have been deformed simultaneously. At Gova, the dominant fabric (U_{main}; **Figure 5.23c**) shows slight deviation of $ApARM_{100\text{-}40}$ directional data may originate from intense rearrangement of SD magnetite grains by LPS. The strong similarity between $ApARM_{40\text{-}0}$ and AARM confirms a major contribution of lower-coercivity fractions, as coarse-grain magnetite, given that two ApARM experiments should be additive (Biedermann et al., 2020; Yu et al., 2002). At Gova and transect 2 at Vidiciatico (U1-$Sf2_{(strike\ slip)}$ **Figure 5.23c** and Transect2 in **Figure 5.24b**), the presence of patterns showing rotation of A_1 and A_2 axes with respect to the LF-AMS, may be associated with a more rapid rotation of ferromagnetic minerals compared to the clay matrix (Hrouda et al., 2018; Till et al., 2010). This process is most pronounced along Transect 1 at Vidiciatico, where the A_1 axes show a double tendency to be parallel or orthogonal to the magnetic lineation of the LF-AMS (**Figure 5.24b**), revealing different overprint of the tectonic stage on the original sedimentary fabric. $HF\text{-}AMS_{para}$ yields the same fabric of the LF-AMS, whereas ferromagnetic subfabrics

show a magnetic lineation consistent with the S-C intersection or the shear direction (**Figure 5.25a**). These observations might lead to infer a different repartition of the deformation between para- and ferromagnetic minerals.

The consistent LF-AMS and AARM data in the sheared sandstones reveal a complete reorientation of both ferro- and paramagnetic minerals when the sandstone layer was dragged or intruded below the basal contact. This agrees with the non-complete lithification of the sediments when the thrusting started (Remitti et al., 2012). In fact, the original fabric of unlithified sediments can be easily disrupted by the stress application (Housen et al., 1996). Pattern S-T1 reveals an interspersion of A_1 and A_2 axes along the foliation plane (**Figure 5.23b**). We deduce a different response to the shearing by minerals having different grain-size and shape, since AARM and $ApARM_{100-40}$ show the parallelism between A_1 axes and the shear direction while $ApARM_{40-0}$ and AIRM display an intersection lineation fabric (**Figure 5.26e** and **Figure 5.26f**).

Within the brittle shear zone, ARM fabrics are more homogeneous than the LF-AMS ones, with similarities among the different patterns. Variations are related to the distance from the main thrust or the amount of tectonic reworking in the different tectonic slices. Close to the basal décollement (P2), the consistency of LF-AMS and AARM maximum axes with the transport direction indicates a major contribution of shearing and similar alignment of the para- and ferromagnetic minerals (**Figure 5.23a** and **Figure 5.24a**), suggesting shear localization. Moreover, at Gova and Transect 3 at Vidiciatico, the subpopulation of minerals in the coercivity window of the $ApARM_{40-0}$, which also dominates the AARM, shows a magnetic lineation dispersed from E-W to NE-SW. This might suggest a less efficient reorientation of coarse grains (Hirt, 2007), with a non-complete reworking from an intersection lineation to a shear-dominating fabric (**Figure 5.26e** and **Figure 5.27c**). In addition, the $HF\text{-}AMS_{para}$ is coaxial with the LF-AMS, confirming that the clay matrix is recording the thrusting stage, while the ferromagnetic subfabric can be parallel or orthogonal to the shear direction, suggesting local variations in the reorientation of the ferromagnetic minerals. The poor overlap of AARM and LF-AMS confidence ellipsoids possibly suggests that magnetite subpopulations and clay minerals have registered different stages of the non-coaxial deformation (Borradaile, 2001). This interpretation is also supported by the geometric relationships between the LF-AMS and $HF\text{-}AMS_{para}$ with the ferromagnetic subfabrics for P1 along transect 1 and 3 at Vidiciatico. Here, the clay matrix shows an intersection lineation fabric while the AARMs and $HF\text{-}AMS_{ferro}$ subfabrics reveal a progressive reorientation of the ferromagnetic grains toward the shear direction. On the contrary, the AIRM experiments are predominantly consistent with the LF-AMS and $HF\text{-}AMS_{para}$, suggesting that coarse magnetite grains registered the local variation of strain as the clay minerals. Further local variation was observed at Gova, where, despite the proximity to the basal thrust P3 remanence data show a steeply dipping magnetic foliation toward NE and a sub-horizontal magnetic lineation (**Figure 5.23** and **Figure 5.26e**). Consistent magnetic foliation is observed at P4, where the magnetic lineation is moving toward the dip direction in all the ARM experiments. This agree with synthetic Riedel developed in a shear zone, where the variation in magnetic lineation orientation can be attributed to different rearrangement degree. Moreover, the small changes among coercivity windows may indicate variable degree of reworking among magnetite subpopulation with different grain-size and shape

(Biedermann et al., 2020). Overall, at greater distance (P1 and P5 in **Figure 5.23a** and P3 in **Figure 5.24a**), the ARM directional data show a subvertical magnetic foliation, suggesting that different ferromagnetic subpopulations are recording the same process, which seems to be independent to that registered by the clay minerals. Same ferromagnetic subfabrics were detected along transect 2 at Vidiciatico (**Figure 5.24a**). From axes configuration we can associate the AARM fabrics to the formation of the subvertical extensional veins pervading the marly sediments, which in turn are related to high pressure of fluids (Remitti et al., 2012).

5.3.3 Magnetic signature of fluid-rock interaction

Fluid circulation and its interaction with the wall-rocks along convergent margin shear zones strongly influence deformation mechanisms during the seismic cycle (Sibson, 2013). At Vidiciatico, active fluid circulation was associated with changes in stress-regime during different phases of the seismic cycle (Cerchiari et al., 2020). Deeper hot exotic fluids migrated along the fault zone during the co-seismic phase associated with failure, re-shear on the main faults and switch from compressional to extensional regime. In contrast, the increased pore pressure during the post-seismic phase induced an extensional regime with drainage of local fluids in equilibrium with the wall-rocks, followed by a reloading phase with reduced fluid pressure and recover of the compressional regime (Cerchiari et al., 2020). Therefore, changes in physicochemical conditions (e.g., temperature and pH) and in the nature of circulating fluids can induce alteration and/or dissolution-precipitation processes of Fe-bearing minerals (ferromagnetic and paramagnetic) resulting in a partial or total transformation of the magnetic properties of fault rocks (Yang et al., 2020).

The results of detailed magnetic mineralogy characterization of the wall-rocks of the SVU reveal a heterogeneous distribution of primary and secondary magnetic phases that may provide insights into changes in physicochemical conditions during the complex evolution of the intraplate shear zone.

The bulk magnetic signature of the wall-rock sediments is dominated by paramagnetic minerals with a mixture of SD and MD magnetite as the predominant ferromagnetic phases (**Figure 5.4**, **Figure *5.5***, **Figure 5.6**, **Figure *5.7*** and **Figure *5.8***). The presence of a T_v around ~ 124 K supports the dominance of inorganic detrital magnetite (Chang et al., 2016; Jackson and Moskowitz, 2021), where the partially suppressed transition may be related to the occurrence of oxidized magnetite (e.g., maghemite; Moskowitz et al., 1993; Housen & Moskowitz, 2006; Chang et al., 2013). Subtle variations in grain-size and content of high-coercivity minerals (e.g., hematite and goethite) show specific relationships with structural position and distance from the main thrust planes.

Overall, low-temperature measurements testified to the local occurrence of significant goethite content (**Figure 5.9** and **Figure 5.10**), which origin may be related to fluid-rock interaction as co-seismic aqueous fluids cool during the post-seismic phase (Chou et al., 2012). In addition, the presence of goethite can be related to the breakdown of pyrite due to interaction with relatively low-temperature and high pH fluids (Yang et al., 2020). Relative enrichment in goethite varies significantly among localities and transects. At Gova and Vidiciatico transect 2, goethite content appears to increase with proximity to basal décollement

(see the variable spacing between FC-ZFC curves in **Figure 5.9** and **Figure 5.10**). In contrast, at Vidiciatico transect 1, the influence of the goethite signal on the LT-SIRM curves shows inverse trend, with potential enrichment close to the major fault separating two tectonic slices of marly sediments. The occurrence of different trends in the gothite enrichment may be associated with a complex evolution of fluid circulation along different preferential pathways depending on the fluid pressure and permeability/lithification rate of the wall-rock.

In addition, changes in ferromagnetic mineral content can be inferred from changes in SIRM and χ_m. The Civago marls (Gova tectonic window) shows a decrease in SIRM and χ_m values in the central part of the tectonic slice, with increased values approaching the boundary faults (**Figure 5.17**), suggesting slightly higher concentration of magnetite close to the main thrust planes. In the Marmoreto Marls (Vidiciatico sector), χ_m slightly increase in the first few meters from the thrust and decrease significantly at a higher distance (Site T1-B3 **Figure 5.20**), revealing possible primary differences in the magnetic mineralogy of the different tectonic slices of the marly units. Higher susceptibility close to the basal décollement is also associated with increased R_{LT}, δ_{FC} and δ_{FC}/δ_{ZFC} ratios, suggesting enrichment in SD magnetite grains. Despite the occurrence of goethite and/or maghemite that may complicate interpretation, the occurrence of ZF>ZFC curves and higher δ_{FC}/δ_{ZFC} ratios indicate a significant content in SD magnetite (Housen & Moskowitz, 2006). Moreover, at Vidiciatico transect 1, we continue to observe an inverse trend, with higher R_{LT} and δ_{FC} values close to the secondary thrust separating the tectonic units.

Different parameters change accordingly, tracing the same or an associated variation in mineralogy within the shear zone. Enrichment in goethite or magnetite content and grain-size variation with proximity to the fault planes could be related to original variations in sediments, preservation of diagenetic processes or fluid-related dissolution-precipitation. High concentration of ferrimagnetic minerals may result from the neoformation of ferromagnetic phases due to interaction with seismic fluids (e.g., Tanikawa et al., 2008). Moreover, the relatively higher magnetite content and grain-size variation may be related to thermal decomposition and grain fining caused by frictional heating (Chou et al., 2014). However, SP magnetite grains are unlikely present ($\chi_{fd\%} < 6\%$), suggesting that no grain fining has occurred. Thus, interaction with fluids may be the main cause of the variation in susceptibility according to structural position. Moreover, the lack of enrichments in pyrrhotite or hematite within the shear zone supports the absence of frictional heating, as a high content in these minerals can be produced by the decomposition of pyrite due to circulation of hot fluids during the co-seismic phase (Tanikawa et al., 2008; Chou et al., 2012; Yang et al., 2018, 2020).

In contrast, a higher content of high-coercivity components is common in the footwall, where it could represent a primary feature related to the deposition and subsequent diagenetic history of the sandstones. However, the significant enrichment in the shear level of sandstones (**Figure 5.9b**) and at the top of the footwall (close to the basal décollement), could reveal a correlation with the circulation of relatively hot fluids and their percolation within the more porous sandstones, when not yet lithified at the time of initial involvement within the SVU.

Transformations during high-temperature experiments starts at ~350°C (**Figure 5.11**, **Figure *5.12***, and **Figure *5.13***), indicating that para- and ferromagnetic-minerals sediments have potentially never experienced such a temperature (at least since the last seismic events). Alternatively, it could represent the specific temperature at which some of the occurring minerals can transform into other phases (e.g., paramagnetic clay minerals into magnetite). The thermal treatments bring to the formation of both magnetite and/or high-coercivity minerals depending on structural position, leading to some possible constraints in the presence of mineral phase enrichments due to fault-related processes. Moreover, the magnitude of the increase in χ in the heating curves (**Figure 5.11** and **Figure 5.12**) varies accordingly to the goethite content observed in the LT-SIRM, supporting correlations between different magnetic mineral assemblages and structural position. The final product of the entire heating-cooling cycle is the neoformation of magnetite, which resulted in the suppression of variations in susceptibility between sites. Thus, variations in the behaviour of the heating curves may reveal a primary and or fluid-related magnetic signature of the sediments as different concentration of certain phases, either para- or ferro-magnetic minerals.

The correlations with fluid circulation and relative structural position are strengthened by hysteresis loop data, in which depending on the distance from the main thrust plane, different intermediate products were created during step-wise thermal treatment. In fact, with proximity to the thrust, an increase in B_c and M_{rs}/M_s was observed during heating in both sandstones and mudstones, suggesting the initial formation of high-coercivity minerals such as hematite (**Figure 5.13b**). In contrast, at a greater distance from the main thrust, only magnetite was formed during the heating experiments (**Figure 5.13**). Hematite can derive from the alteration of goethite, which occurs between 240-400 °C (Dekkers, 1990; Yang et al., 2019), or from the decomposition of pyrite when altering at high temperature (Yang et al., 2019, 2020). Changes in alteration products appear to be strictly related with proximity to major thrust faults and thus associated with a fault-related processes.

Further correlations of mineralogical changes related to the faulting processes come from the SEM-EDS observations (**Figure 5.14**), which show the occurrence of different generations of pyrite with specific structural relationships within the marly units. The large aggregates of framboidal pyrite appear to be primary, associated with diagenetic processes. However, the presence of shadow-like tails (**Figure 5.14a, b**) suggests significant structural control in the neoformation of fine-grained pyrite along dissolution seams. The neoformation of pyrite may be associated with anaerobic methane oxidation due to fluid drainage (Greve et al., 2021) or even with enhanced bacterial activities in unconsolidated sediments, coeval with the development of deformation bands (Famin et al., 2021). The latter hypothesis is preferred as it does not require the contribution of frictional heating, which does not show a significant contribution in the evolution of SVU. In fact, no pseudotachylytes formation or dark gouge levels were detected, nor were magnetic mineral formations due to high-temperature alteration such as pyrrhotite.

Defining the source and progressive evolution of fluids and their interaction with the wall-rocks during seismic phases remains a challenge. However, a detailed characterization of the magnetic mineralogy could

indicate subtle but significant variations in concentration of different magnetic minerals that could reveal possible insights into the preservation of the diagenetic signature prior to involvement in the shear zone and/or interaction with fluids circulating during seismic cycle.

5.4 Conclusions

Magnetic properties of fault rocks are directly connected with the physicochemical processes occurring at intraplate shear zones (Yang et al., 2020). Strong heterogeneities were observed in brittle shear zones and still needed an explanation. Our study shows that a full characterization of the anisotropy of magnetic properties combining the unmixing of non-orthorhombic fabrics with ApARM and HF-AMS experiments is vital to obtain a robust interpretation of the heterogeneities in the magnetic signature. Our observations have also demonstrated that exhumed analogues give the opportunity to have a direct correlation with the structural elements, for example, using ternary diagrams, leading to a quantitative interrelation with the prevailing deformation processes. In the case of the SVU, this approach helps to reveal distinct subfabrics with reasonably straightforward correlations with the intensity of the tectonic reworking and the structural position within the shear zone (i.e., the proximity to the main thrust faults), and in evaluating the heterogeneous registration of strain (i.e., distributed vs. localized deformation). The unmixing of the complex AMS results helps to discern the different response of the paramagnetic minerals to the deformation. The dominance of a shear-related fabric, consistent with the top to NE transport direction, close to the basal décollement and the secondary thrust planes, suggests a shear strain localization along the main faults. In contrast distributed deformation can be inferred with distance from the thrust, where the presence of subfabrics related to less intense deformation and/or previous pre-faulting deformation fabric become significant. The anisotropy of magnetic remanence (AARM, ApARM, and AIRM) highlights the behaviour of the ferrimagnetic components, revealing different registration of the non-coaxial strain compared to the clay matrix (HF-AMS_{para}) close to the main thrust planes. It also suggests the registration of different deformation stages away from the basal thrust.

Spatial and temporal changes of the physiochemical conditions during the evolution of the intraplate shear zone were identified by detailed rock magnetic characterization of mineral assemblages. In particular, evidence of complex evolution from the partial preservation of the diagenetic signature to the fluid related processes (alteration, leaching and neoformation of minerals) during seismic cycles was observed.

Additional studies of different localities are necessary to support the emerging sub-discipline of “fault magnetism” (e.g., Yang et al., 2020) and provide a better understanding of the linkage between variations in magnetic properties and the geodynamic evolution of intraplate shear zones, since magnetic properties analysis targeting mainly brittle fault rocks are up to now scarce.

Chapter 6

THIRD CASE STUDY: The ELAW

In this chapter, I present the results obtained from non-metamorphic chaotic rock units occurring at different tectono-stratigraphic positions within the out-of sequence thrust system of the outer part of an accretionary wedge (Codegone et al., 2012; Festa et al., 2020). Those units correspond to heterogenous assemblages of clasts (Mèlanges and broken formations) of variable nature (marls, sandstones and limestones) immersed in shaly and marly matrix that have undergone low-temperature (100-110 °C) illitization (Dellisanti et al., 2008; Festa et al., 2015). This context offered a valuable chance to investigate how the rock magnetic signal can reflect the different mélange forming processes and define a criterion useful to distinguish their genesis. The contents of this Chapter were published in Robustelli Test et al., 2019 and here supplemented and further constrained by the addition of new sites and the execution of further experiments.

6.1 Geological setting

The Northern Apennines (**Figure 6.1**) imbricate thrust stack represents a good ancient analogue of modern subduction-accretion complex, resulting from the Late Cretaceous–Early Cenozoic convergence between the European continental margin and the Adria microplate following the Piedmont–Ligurian ocean closure (e.g., Boccaletti et al., 1980; Dewey et al., 1989; Marroni et al., 1998; Elter et al., 2003; Lucente et al., 2008; Festa et al., 2010; 2020; Barbero et al., 2020).

The Late Cretaceous–Early Eocene accretionary stage has been recorded in the evolution of the Ligurian Accretionary Complex, which consists of different units (i.e., Internal, External, and Subligurian units; **Figure 6.1**) containing tectono-sedimentary assemblages originally deposited in an ocean basin (i.e., Jurassic ophiolites and sedimentary cover), ocean-continental transition (OCT) zone, and thinned continental crust of the Adria margin, respectively. During this stage, related to the east-dipping Alpine subduction, a consistent part of the External Ligurian units (i.e., the Basal complex Auct.) was strongly deformed, leading to the formation of different types of chaotic units (i.e., broken formations and tectonic mélanges) (e.g., Pini, 1999;

Marroni et al., 2010; Bettelli et al., 2003; CerrinaFeroni et al., 2004; Festa et al., 2010, 2013; Remitti et al., 2011; Codegone et al., 2012; Festa & Codegone, 2013; Barbero et al., 2017, 2020).

Since the middle–late Eocene, the wedge-top basin succession of the Epiligurian units unconformably covered the Ligurian accretionary complex and the N- to NE-verging thrust-related structures, which formed during the west-dipping Apennine subduction of the thinned continental margin of Adria (e.g., Castellarin, 1994; Marroni et al., 2010). Different types of mass-transport deposit (MTDs), including sedimentary mélanges (i.e., olistostromes), occur at different stratigraphic levels within the wedge-top basins succession, marking different stages of slope instability (e.g., Bettelli et al., 1989a,b; Mutti et al., 1995; Panini et al., 2002; 2013; CerrinaFeroni et al., 2004; Pini et al., 2004; Marroni et al., 2010; Remitti et al., 2011; Ogata et al., 2012; 2014; Festa et al., 2013; 2015a,b; Festa & Codegone, 2013; Barbero et al., 2017, 2020).

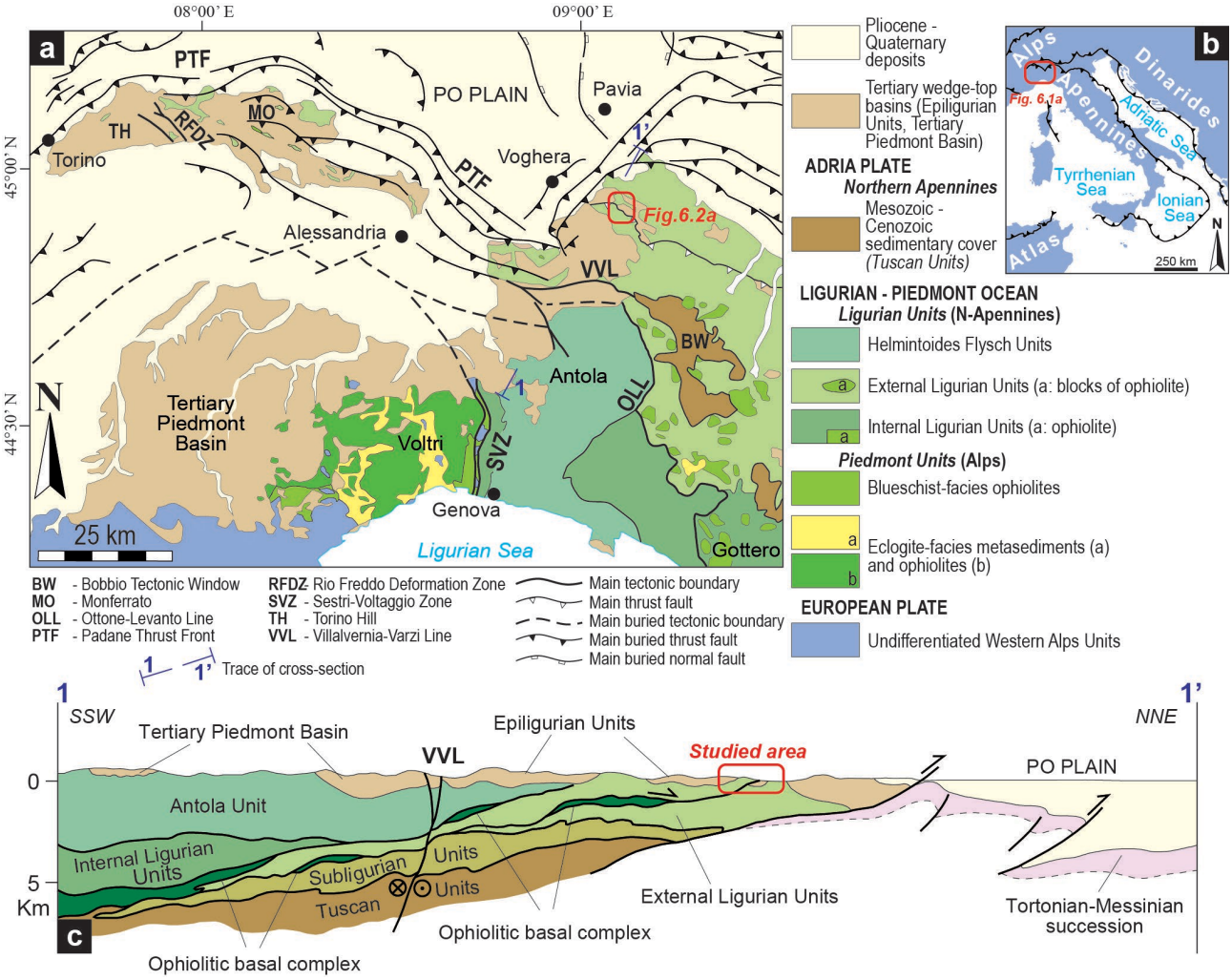

Figure 6.1. Structural sketch map (**a**) of the northwestern Italy (modified from Balestro et al., 2015 and Barbero et al., 2020); (**b**) location of **Figure 6.1a**; (**c**) geological cross section across the Northern Apennines (modified from Boccaletti & Coli, 1982)

6.2 Meso-Structural Fabrics of Chaotic Rock Units

Four different types of chaotic rock units, part of which were described in previous published papers focusing on mélange-forming processes (see Codegone et al., 2012; Festa et al., 2015), occur in different tectono-stratigraphic positions within the exhumed Ligurian accretionary complex and overlying wedge-top basins of the Epiligurian successions in the Voghera sector of the Northern Apennines (**Figure 6.2a**). Previously published structural data (Codegone et al., 2012) are integrated by new ones, allowing for the discrimination of the process of formation of four types of chaotic rock units on the basis of their different meso-to-mapscale and micro-scale diagnostic block-in-matrix fabrics (Festa et al., 2019).

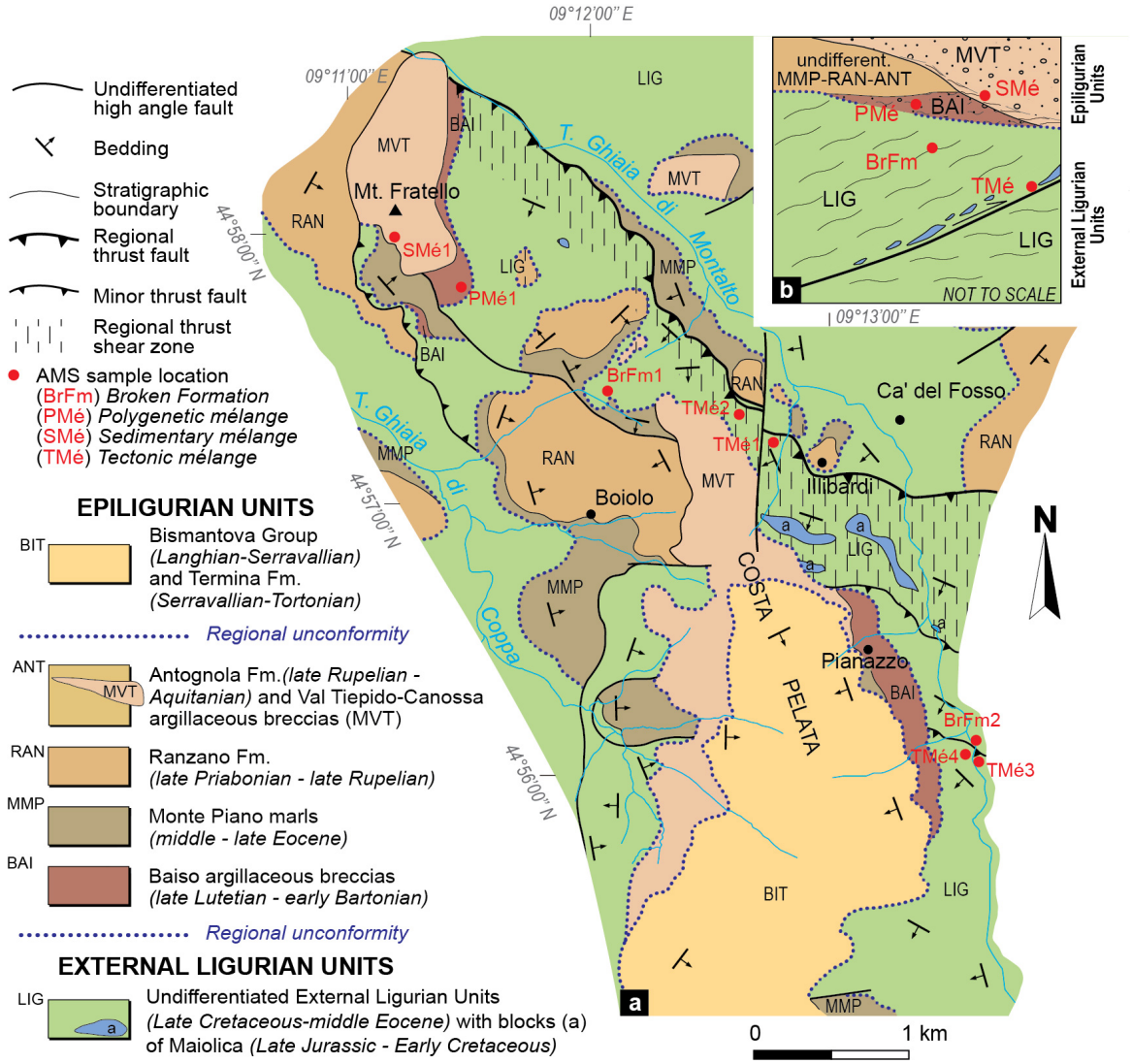

Figure 6.2. Simplified geological-structural map of the Voghera sector of the Northern Apennines (modified from (Codegone et al., 2012; Festa et al., 2015) (**a**) with location of the anisotropy of magnetic susceptibility (AMS) samples. (**b**) Schematic column (not to scale) showing the vertical piling of the different mélange and broken formation units and locations of AMS samples.

6.2.1 The Broken Formation

The broken formation (sensu Hsü et al., 1968) corresponds to the Upper Cretaceous Argille varicolori of the External Ligurian units (**Figure 6.2**), which results from the fragmentation and disruption of an originally coherent well-bedded stratigraphic succession made of varicolored clay, shale, and marl, alternating with limestone, sandstone, and manganiferous siltstone in decimeter-thick beds. Its block-in-matrix fabric was mainly acquired through layer-parallel extension/contraction occurring at the wedge front of the Ligurian accretionary complex during the Late Cretaceous–middle Eocene oceanic subduction stage (e.g., Bettelli & Panini, 1987; Pini, 1999; Bettelli & Vannucchi, 2003; Codegone et al., 2012; Festa et al., 2013; Festa & Codegone, 2013; Barbero et al., 2017).

At the mesoscale, the broken formation is characterized by pinch-and-swell structures, necking of the less competent, shaly, clayey, and marly layers, and a brittle and/or ductile bedding-parallel boudinage of centimeter- to meter-long elongated and mainly tabular bed fragments, which represent "native" (i.e., intra-formational) blocks (**Figure 6.3a**). Elongated blocks display a high aspect ratio (block long axis/short axis) with a mean value ranging from 3.7 to 4.2 (**Figure 6.4a, b**). Pinch-and-swell and boudinage structures are mainly asymmetric, defining a planar alignment that is consistent with extensional shearing in an ESE–WNW direction, as documented by the block long-axis lineation to the same direction (**Figure 6.4c**). Boudins are aligned parallel to the shaly and marly layers (i.e., the matrix) in defining a typical pseudo-bedding fashion (**Figure 6.3a**).

Meter-scale disharmonic-to isoclinal and rootless to transposed intra-layer sheath-like folds deform the broken formation (**Figure 6.3b**). They show sub-horizontal axial surfaces (**Figure 6.4c**), NW and/or SE-dipping, irregularly thickened and stretched hinge zones, and thinned and boudinaged limbs parallel to the SE (or NW)-dipping pseudo-bedding.

The block-in-matrix fabric of the broken formation indicates that deformation started just after the deposition of sediments under unconsolidated to poorly-consolidated conditions, and continued throughout progressive lithification (Codegone et al., 2012; Festa et al., 2013). Vertical compaction due to burial resulted in the formation of layer-parallel deformation, which is consistent with large-magnitude lateral spreading that resulted in flattening (mean aspect ratio from 3.7 to 4.2; see Festa et al., 2013). The coeval development of flattened structures and intra-layer sheath-like folds was commonly interpreted as the product of heterogeneous deformation at the toe of the accretionary wedge, where different deformational domains can exist (e.g., Kusky & Bradley, 1999; Festa et al., 2013).

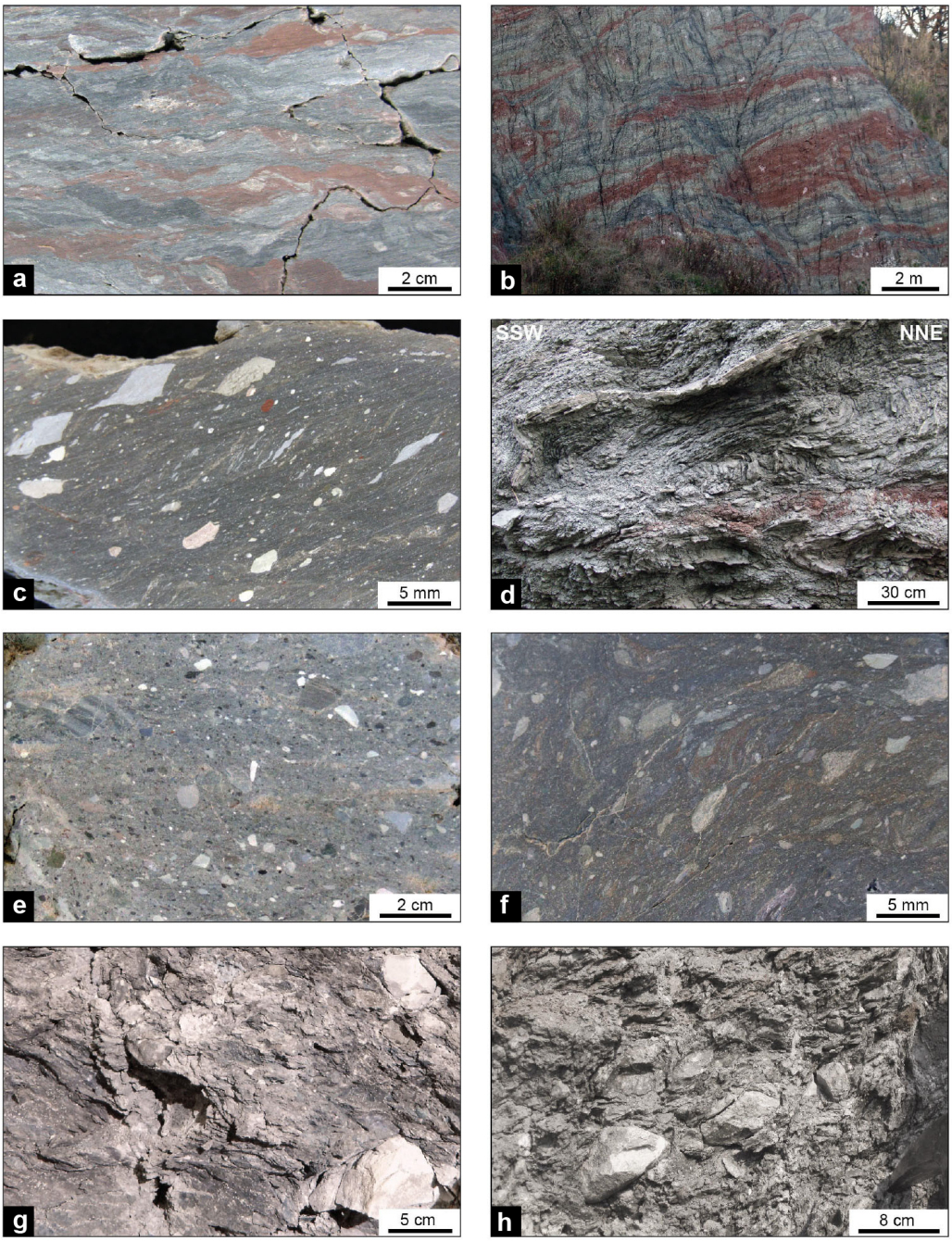

Figure 6.3. Close up view of the different hand-sample-to-meso-scale block-in-matrix fabrics of mélanges and broken formations studied. Broken formation (i.e., the Argille varicolori of the External Ligurian units): (**a**) asymmetrical brittle boudinage and pinch-and-swell structures of alternating varicolored shaly, clayey, and marly layers; (**b**) disharmonic-to-isoclinal and transposed folds with sub-horizontal axial surfaces aligned parallel to the tectonic layering and/or pseudo-bedding, which results in the development of pinch-and-swell structures and boudinage of shaly layers due to layer-parallel extension along the fold limbs. Tectonic mélange: (**c**) polished cut of the high-strain shear zone that shows millimeter-sized elongated asymmetric "exotic" clasts in a fine grained matrix. In the central part of the photograph, elongated clasts show a P-C fabric; (**d**) shear transposition and overprinting of the previously formed isoclinal folds of the broken formation that forms isolated fold hinges with axial surfaces aligned to planar northeast-verging shear zones and mesoscale thrust faults, resulting in the production of the tectonic mélange. Sedimentary mélange: (**e**) polished surface of hand sample showing the isotropic texture of the brecciated shaly matrix with irregular shaped blocks randomly distributed within the matrix; (**f**) polished surface of hand sample of the basal shear zone of the sedimentary mélange, showing the reorientation of elongated hard clasts to S-C fabric. Polygenetic mélange: (**g–h**) sub-angular to angular, and tabular clasts and blocks, centimeter- to decimeter in size, embedded in a brecciated shaly matrix, and gently reoriented by a scaly fabric related to tectonic deformation.

6.2.2 The Tectonic Mélange

Close to the main regional thrust surface (**Figure 6.2**), the NE-verging thrusting-related tectonic shearing formed a tens of meters thick shear zone. It is characterized by a block-in-matrix fabric consisting in the tectonic mixing of the broken formation (i.e., the Argille varicolori), and "exotic" elongated blocks, tens to hundreds of meters long, which represent wrenched fragments of both the hanging wall and footwall units succession (see Panini et al., 2002; Codegone et al., 2012). Thus, the final block-in-matrix fabric of the tectonic mélange represents the product of the superposition of two different tectonic events.

"Exotic" blocks, lenticular to elongated in shape, have their NE-striking long axes aligned parallel to the verging of the regional thrusting event and of mesoscale shear zones (**Figure 6.2** and **Figure 6.3c**). The mean values of their aspect ratio range from 2.3 to 2.7 (**Figure 6.4a, b**). The long-axes of the blocks embedded in the matrix are reoriented by P and R, S-C and P-C shear zones and display a strong alignment to tectonic features at all scales (**Figure 6.4c**), from millimeter-size clasts to decimeter-sized blocks. The shaly matrix is strongly affected by SW dipping R and P shears, whose mutual interlacing define millimeter- to centimeter-scale, spaced lenticular lenses (L shear lenses, sensu Naylor et al., 1986), which are wrapped by NE-verging shear surfaces. The lenses are commonly included within pervasive decimeter- to meter-wide S-C reverse shear zones, with NW strikes and W-SW dip directions that are also responsible for their reorientation. The shear transposition of the previously-formed mesoscale isoclinal folds of the broken formation (NW- to SE-oriented) produced isolated and sheared fold hinges, with axial surfaces aligned to NE-verging shear planes of the tectonic mélange (**Figure 6.3d**). The isolated folds of the broken formation thus show NE-verging and mainly NW- and locally SE-plunging fold axes (**Figure 6.3c**; see also Codegone et al., 2012). Away from the thrust faults (**Figure 6.2**), the intensity of thrust-related deformation gradually decreases, allowing a transition to the tectonic pseudo-bedding of the broken formation and/or to the original (partially preserved) bedding. The final block-in-matrix of the tectonic mélange has been interpreted as being related to the NE-verging out-of-sequence thrusting in the inner wedge of the Ligurian accretionary complex, during the late Oligocene–early Miocene collisional stage (e.g., Bettelli et al., 1989; Pini et al., 2004; Camerlenghi & Pini, 2009; Remitti et al., 2011). Exotic blocks offscraped from the footwall unit were accreted within the thrust shear zone and mixed with native blocks derived from the earlier broken formation.

6.2.3 The Sedimentary Mélange

The sedimentary mélange (**Figure 6.2**), corresponding to the upper Oligocene–lower Miocene Val Tiepido Canossa Argillaceous Breccias (see Panini et al., 2013), consists of an irregularly shaped chaotic mass-transport deposit, up to 180–200 m thick, which is internally characterized by a block-in-matrix fabric. The latter results from submarine cohesive debris flows that involve heterogeneous material sourced from the wedge of the Late Cretaceous Ligurian accretionary complex and disrupted portions of middle Eocene–Oligocene Epiligurian succession in response to out-of-sequence thrusting and the dynamic re-equilibrium of the wedge front during the collisional stage (e.g., Fagereng et al., 2011; Festa et al., 2015). The mass-

transport deposit consists of the stacking of different single debris flow, ranging from meters to tens of meters in thickness (Festa et al., 2015). Each single debris flow shows the inverse grading of the largest blocks, which range in size from decimeters to about 1 m and are bounded at the base by decimeter-thick shear zones.

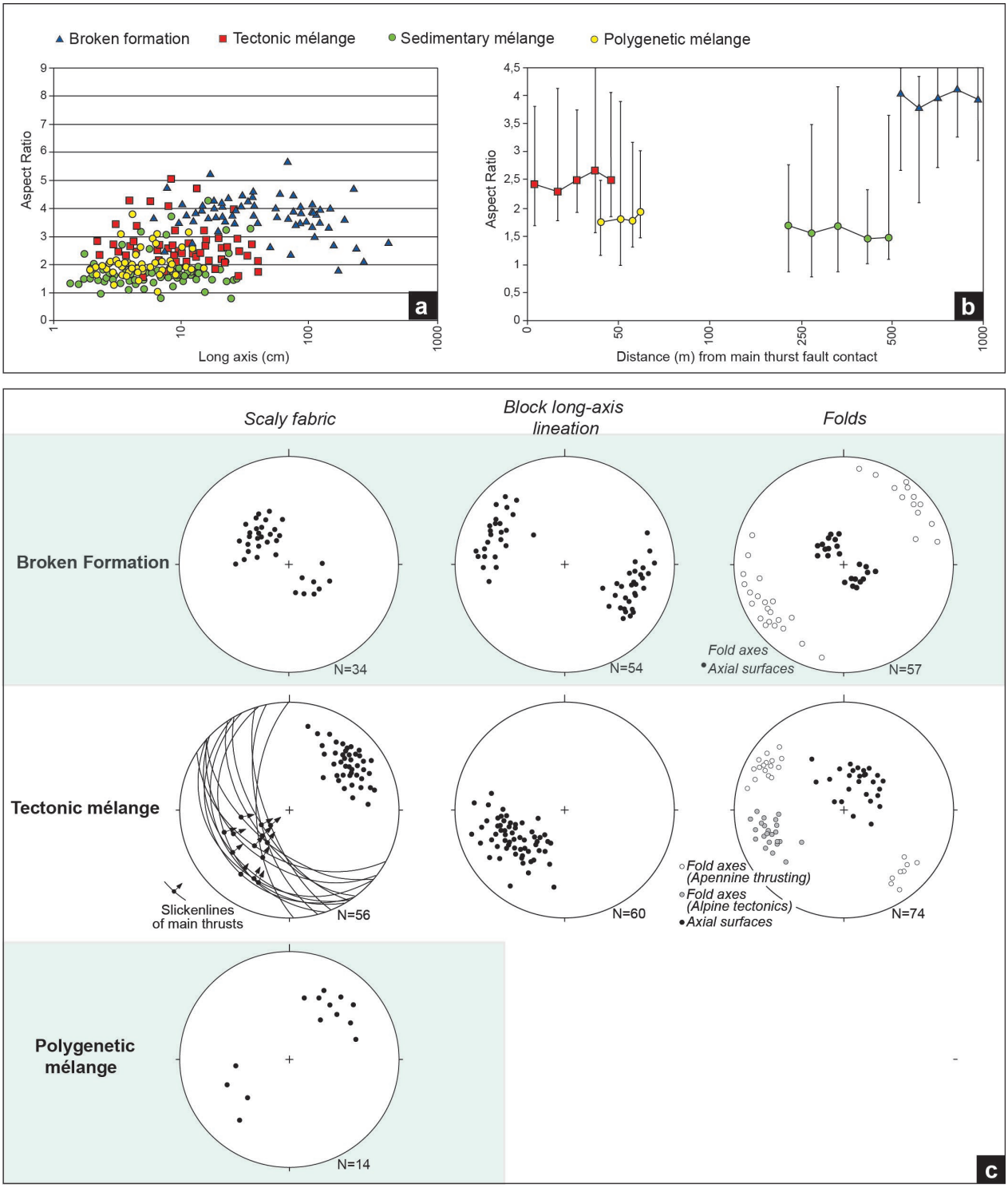

Figure 6.4. Diagrams showing block characteristics and rock fabric in different types of mélanges: (**a**) aspect ratio (block long axis/short axis) vs block long axis; (**b**) aspect ratio vs. location of chaotic units (i.e., distance from the thrust faults). Data are plotted as means with 95% error bars indicated; (**c**) mesoscale data (Schmidt net, lower hemisphere) of scaly fabric, lineation of the long axis of the blocks, and folds of broken formation, tectonic mélange, and polygenetic mélange.

At the mesoscale, the block-in-matrix fabric of the sedimentary mélange shows an isotropic fabric defined by the highly-disordered distribution and orientation of a polymictic assemblage of irregularly-shaped (angular to rounded) hard to partially-soft clasts/blocks, dispersed in a brecciated shaly matrix (**Figure 6.3e**). The clasts/blocks, which range in size from centimetres to decimetres and show different ages and origins, display a low aspect ratio, with a mean value ranging from 1.4 to 1.7 (**Figure 6.4a, b**).

The base of the sedimentary mélange and of each single debris flow is characterized by a thin horizon (5 cm to 50 cm in thickness) of sheared argillaceous breccias (**Figure 6.2b** and **Figure 6.3f**; see Festa et al., 2015, 2016). This sheared horizon, which is interpreted to be formed as the result of the mass-transport emplacement (see Pini et al., 2012; Ogata et al., 2014; Festa et al., 2012, 2015, 2016), shows a planar anisotropy defined by the alignment of elongated blocks parallel to the extensionally sheared layers and is crosscut at low angles by disjunctive extensional shear surfaces (**Figure 6.3f**). Poorly consolidated clasts commonly display extreme elongation in the direction of emplacement, with asymmetries related to simple shear (Festa et al., 2015).

The random and highly-disordered distribution of the blocks in the shaly brecciated matrix (**Figure 6.3e, f**) suggest mechanisms of translation and emplacement related to the rheological behaviour of a viscous matrix (Lowe et al., 1982; Middleton & Hampton, 1982; Mulder & Alexander, 2001). The basal and internal shear zones, which are characterized by enhanced reorientation of clasts and microclasts, matrix banding, and crude foliation, suggest a constriction plus flattening-type (i.e., prolate plus oblate) strain ellipsoid, with a prevailing component of stretching along the direction of flow and a minor component of planar flattening (see Pini et al., 2012). This agrees with a mechanism of emplacement likely related to "viscous" shear zones in a shale-dominated matrix, which is consistent with relatively slow-moving bodies (Festa et al., 2015).

6.2.4 The Polygenetic Mélange

The polygenetic mélange, which corresponds to the late Lutetian–early Priabonian Baiso argillaceous breccias (**Figure 6.2**) at the base of the Epiligurian succession (see Panini et al., 2013), differs from the Sedimentary mélange because its primary gravitationally-related block-in-matrix fabric is gently overprinted by tectonic deformation related to the late Oligocene–early Miocene northeast verging thrusting stage (see Codegone et al., 2012 for details). The primary block-in-matrix fabric of the mass transport deposits is well comparable with that of the sedimentary mélange, consisting in sub-angular to angular, and tabular clasts and blocks, centimeter- to decimeter in size, embedded in a brecciated shaly matrix (**Figure 6.3g**). However, partially elongated blocks also occur. Differently from those of the sedimentary mélange, blocks display a low to medium aspect ratio with a mean value ranging from 1.7 to 2.0 (**Figure 6.4a, b**). The matrix consists of polymictic and isotropic mud breccias with mainly rounded-to-angular and rarely elongated, millimeter-to-centimeter-sized clasts (**Figure 6.3g, h**). Independently on the scale of observation, the block-in-matrix fabric is gentle reoriented and close to minor thrust faults and shear zones, tabular blocks/clasts are aligned to pervasive S-C shears and scaly fabric, and SW-dipping and NE-verging, that overprint the originally formed mass-transport deposit (**Figure 6.3h** and **Figure 6.4c**).

6.3 Results

6.3.1 Magnetic Mineralogy

Thermomagnetic susceptibility experiments were performed on selected samples of broken formation and tectonic mélanges (**Figure 6.5a**). The heating curves reveal a hyperbolic trend up to 300-400 °C, which indicates a substantial contribution of paramagnetic minerals on room-temperature susceptibility (Hrouda et al., 1997; 2019). Thereafter, the magnetic susceptibility increases up to 400-500 °C and gradually decreases until 600 °C, likely related to the formation of new magnetite during the heating process. In fact, the cooling curves show a remarkably high susceptibility with two humps which suggest the formation of magnetite and a second ferromagnetic phase.

IRM acquisition experiments were performed for all the different chaotic rock units (**Figure 6.5b**). These curves show smooth and concave downward curvatures, indicating that a single magnetic phase dominates the remanence. Sedimentary mélanges (SMé) and the grey portion of the varicolored shales saturate between 0.2 and 0.5 T, revealing the presence of low-coercivity minerals. Samples from the broken formation show higher saturation point and thus a greater contribution of high-coercivity phases. In contrast, the red portion of the varicolored shales ($TMé_{(red)}$) does not saturate at 1.5 T, implying the dominance of high-coercivity minerals such as hematite or goethite. Variations in the content of high-coercivity phases are reflected by the S-ratios (**Figure 6.5c**), where the lowest values ($S_{0.3} < 0.3$; $S_{0.1} < -0.2$) are found in the $TMé_{(red)}$.

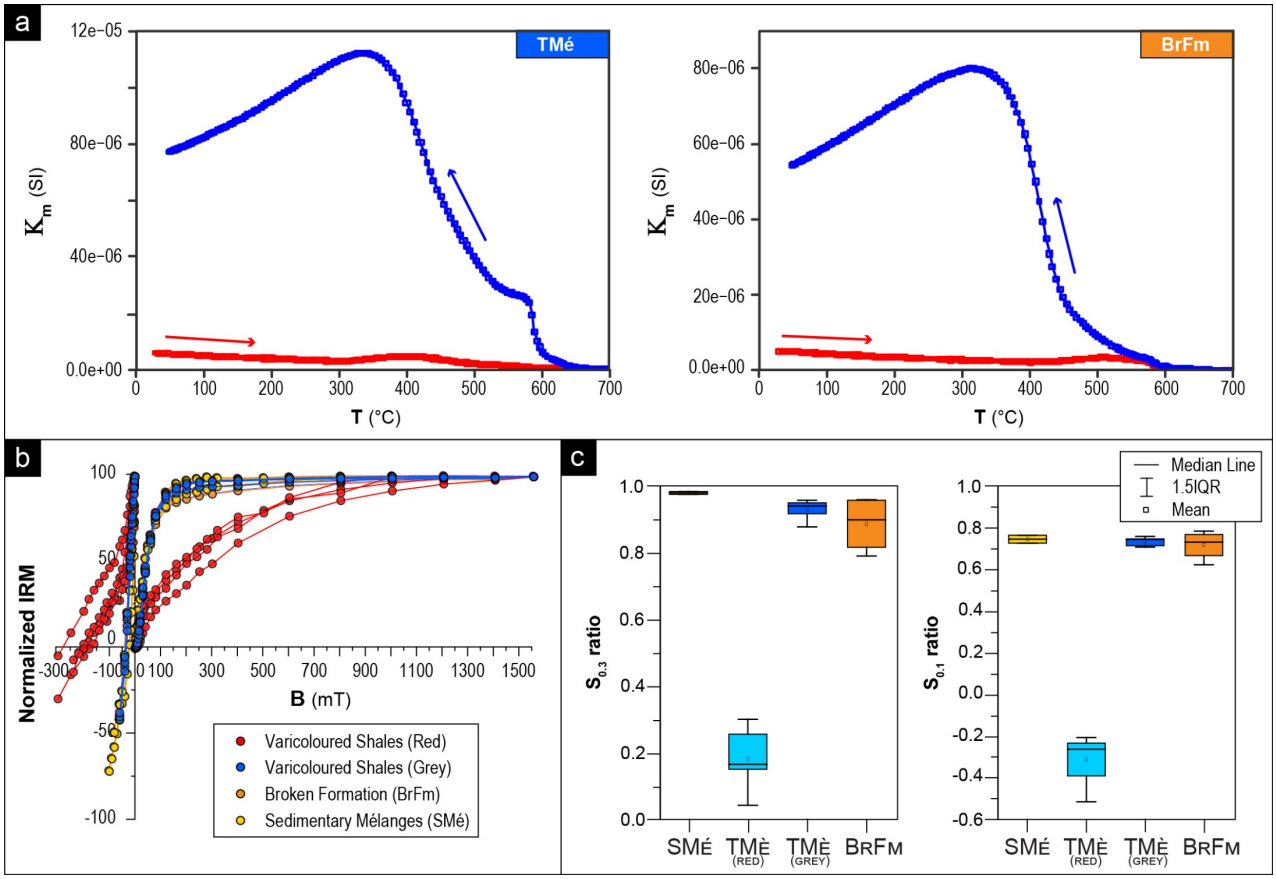

Figure 6.5. (**a**) Thermomagnetic susceptibility curves; (**b**) isothermal remanent magnetization acquisition and backfield curves; and (**c**) Box-and-whisker plots of the of S-ratios.

Deconvolution of the IRM acquisition curves shows a dominant low-coercivity component in both broken formation (BrFm) and tectonic mélanges (TMé) with a variable minor contribution (between 4% and 18%) of high-coercivity phases (**Figure 6.6a**). In contrast, some red portions of the varicoloured shales (Sample TMé4-5B) are characterized by a predominant (~ 68%) high-coercivity component with Bh = 313-546 mT ($\log_{10}$(B) = 2.50-2.75). Here, the low-coercivity component pertains to only ~ 30%.

The Lowrie (1990) experiments agree with the predominance of soft fractions, such as magnetite, for both broken formation and tectonic mélanges (e.g., Samples BrFm2-1 and TMé3-2 in **Figure 6.6b**). Indeed, the remanent magnetization is almost completely lost at 580 °C. A drop is also observed at ~ 350 °C, suggesting the possible presence of iron-sulfides (Weaver et al., 2002). The contribution of hard fractions is negligible for the TMé$_{(grey)}$ (Sample TMè3-2). In contrast, its contribution is significative for the broken formation, although minor. The red portion of the varicolored shales (e.g., Sample TMé4-5B in **Figure 6.6b**) shows the dominance of the intermediate fraction and a significant contribution of both soft and hard fractions.

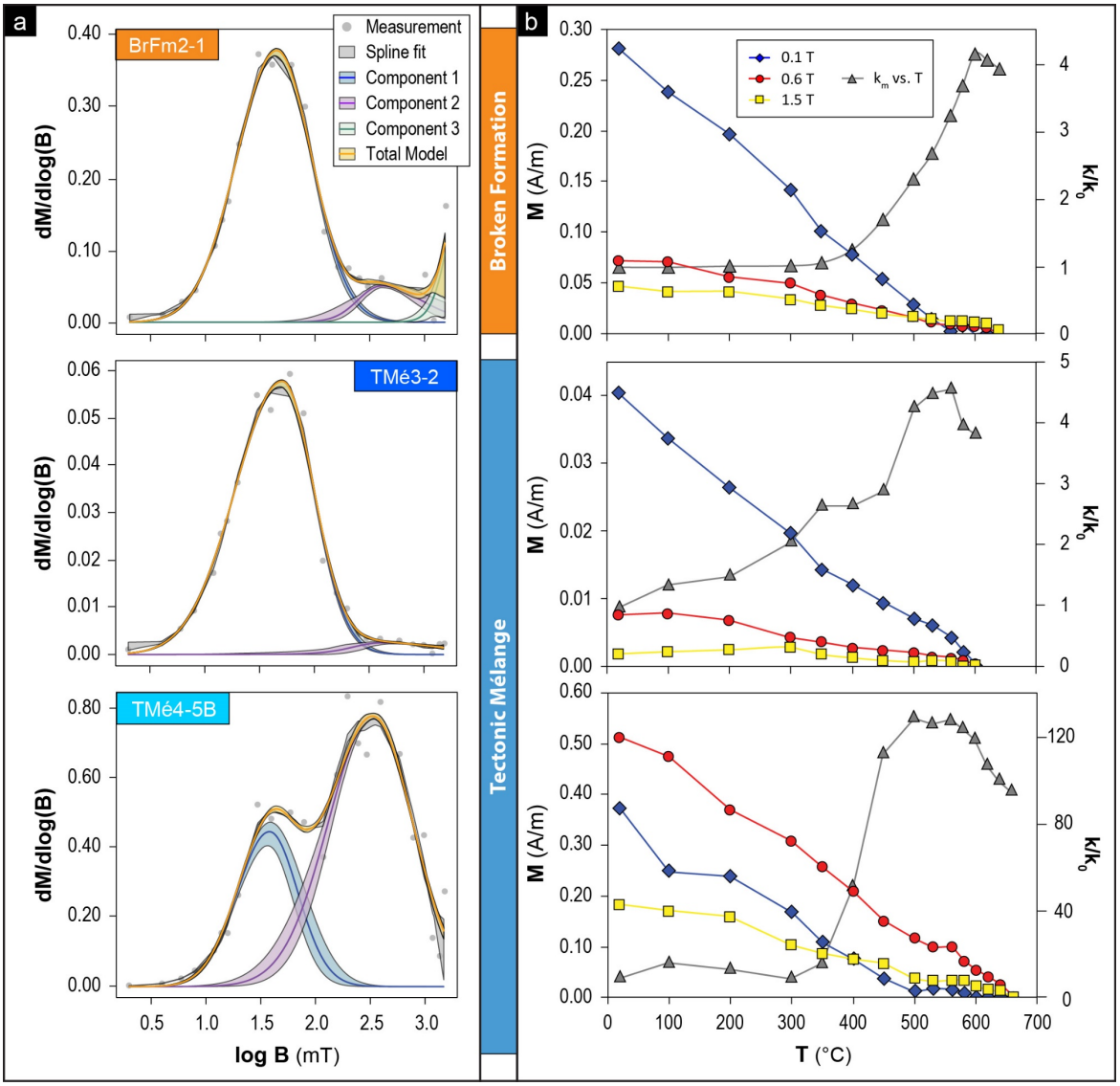

Figure 6.6. (**a**) Coercivity distribution and unmixing of isothermal remanent magnetization (IRM) acquisition curves (Maxbauer et al., 2016b); and (**b**) thermal demagnetization of three-component IRMs and normalized magnetic susceptibility (k/k_0) versus temperature.

In all chaotic rock units, the normalized magnetic susceptibility (k/k_0) increases sharply with increasing temperature at ~ 300-350 °C (**Figure 6.6b)**. This increase might indicate the formation of new magnetite from paramagnetic iron-bearing minerals such as pyrite or clay minerals (Hirt et al., 1993; van Velzen & Zijderveld, 1992). Between 500 °C and 660 °C k/k_0 progressively decreases, probably due to the formation of new hematite during the heating process.

Magnetitic susceptibility (χ_m) does not change as the field varies (**Figure 6.7a**). In addition, V_a index (see APPENDIX I) shows slight variations, with values between -2.8 and 1.49, consistent with the dominance of paramagnetic minerals or pure magnetite (Hrouda, 2002; Hrouda et al., 2006).

Chaotic rock units display hysteresis loop dominated by a paramagnetic behaviour (**Figure 6.7b**). Due to the high content in paramagnetic minerals, the data are often noisy, and resolving the ferromagnetic signal of the hysteresis loop is not always possible. After high-field slope correction, the ferromagnetic signal is generally visible. The corrected hysteresis loop for tectonic mélanges shows a very narrow shape and approaches saturation at ~ 0.4-0.5 T, which suggests the presence of low-coercivity phases (**Figure 6.7b**). In contrast, the BrFm results reveal wasp-waisted shape ($\sigma_{hyst} > 0$; Fabian, 2003) and do not saturate, indicating the presence of higher coercivity components. The M_{rs}/M_s and B_{cr}/B_c values reveal a grain-size distribution spanning across the SD to MD threshold, as the data mostly fall in the PSD domain range (**Figure 6.7c**).

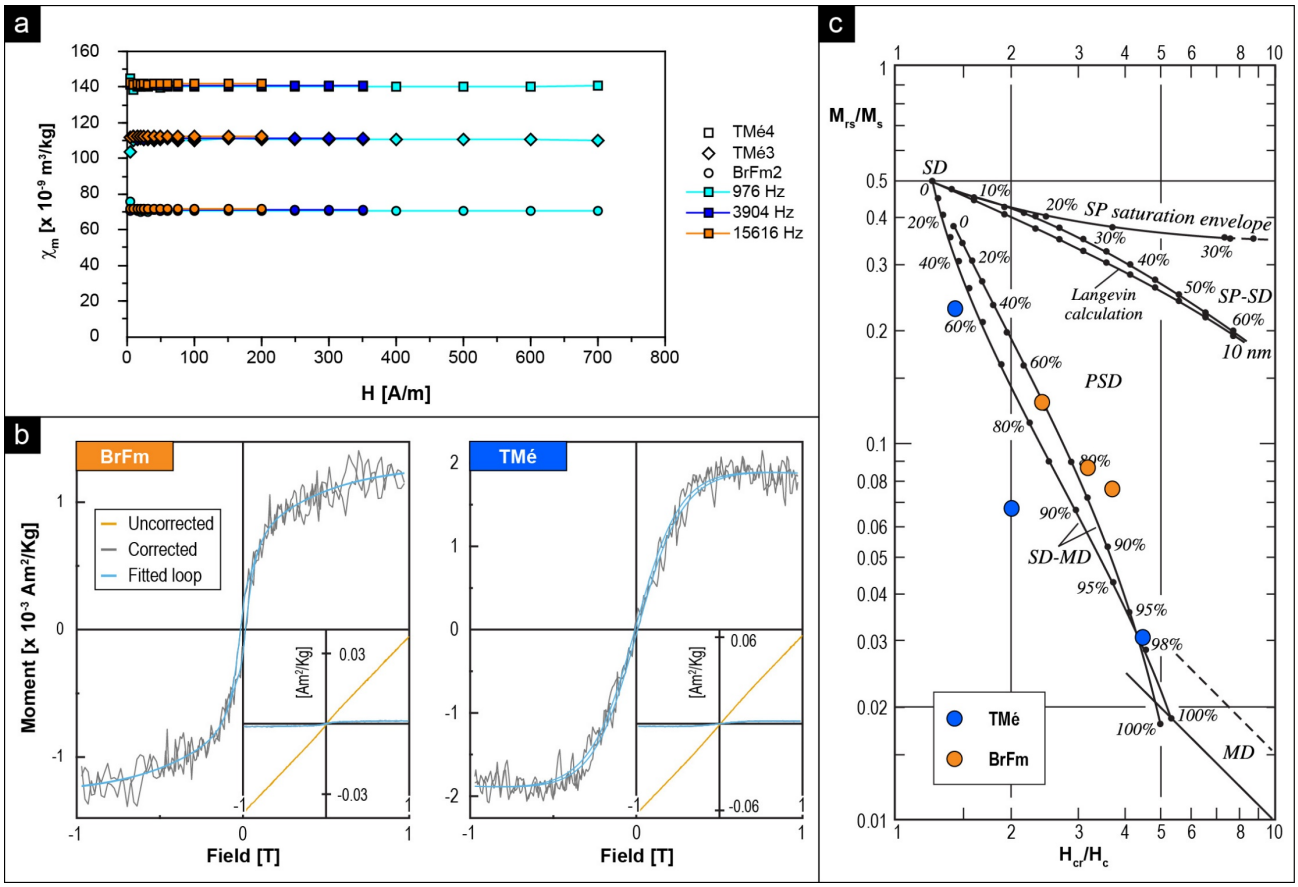

Figure 6.7. (**a**) field and frequency variations of mass magnetic susceptibility; (**b**) Hysteresis loop for representative samples after correction and fitting. Insets show both raw and corrected data; (**c**) Day et al. (1977) plot of the hysteresis ratios M_{rs}/M_s and B_{cr}/B_c with mixing curves after Dunlop (2002a, 2002b).

6.3.2 AMS

A total of 172 specimens for AMS measurements were obtained from eight selected sites where oriented hand sample of ~ 6 dm^3 were taken from the shaly, clayey, and marly matrix of the different types of chaotic rock units (see, **6.2 Meso-Structural Fabrics** for description and **Figure 6.2** for location). Specimens were derived by pressing non-magnetic plastic cubes (8 cm^3 volume) into the wet matrix of oriented hand-samples, obtaining homogeneous specimens from heterogeneously chaotic (block-in-matrix) units.

AMS results revealed low magnetic susceptibility (K_m) for all chaotic rock units, with values ranging from 26 to 236 µSI (**Table 6.S 1**; **Figure 6.8a**), suggesting a dominant control of paramagnetic minerals on the magnetic fabric (Rochette, 1987; Sagnotti, 2011). Sedimentary mélanges show the highest K_m values (**Figure 6.8a**), which range from 109 to 236 µSI. The other rock chaotic units display lower magnetic susceptibility, where the lowest values are found in the tectonic mélanges (**Figure 6.8a**). Overall, the standard deviation of the mean susceptibility is relatively low (5–25%), which is considered as evidence for specimen homogeneity.

Pj values are relatively low, ranging from 1.005 to 1.088, with low standard deviation values (0.001–0.018) (**Table 6.S 1**; **Figure 6.8b**). The largest variability of Pj is detected for both tectonic and sedimentary mélanges. In addition, the SMé revealed the highest anisotropy degree (Pj from 1.036 to 1.088; **Figure 6.8b**).

The shape parameter (T) appears to vary with the type of chaotic rock unit (**Figure 6.8c**). Broken formations and tectonic mélanges reveal a prevailing oblate magnetic ellipsoid. Sedimentary mélanges are characterized by an oblate to neutral magnetic ellipsoids (T = 0.059 ± 0.233; **Table 6.S 1**; **Figure 6.8c**). In contrast, polygenetic mélanges show the greatest variability in T values spanning from -0.584 to 0.577, with a total magnetic ellipsoid of neutral shape (**Figure 6.8c**).

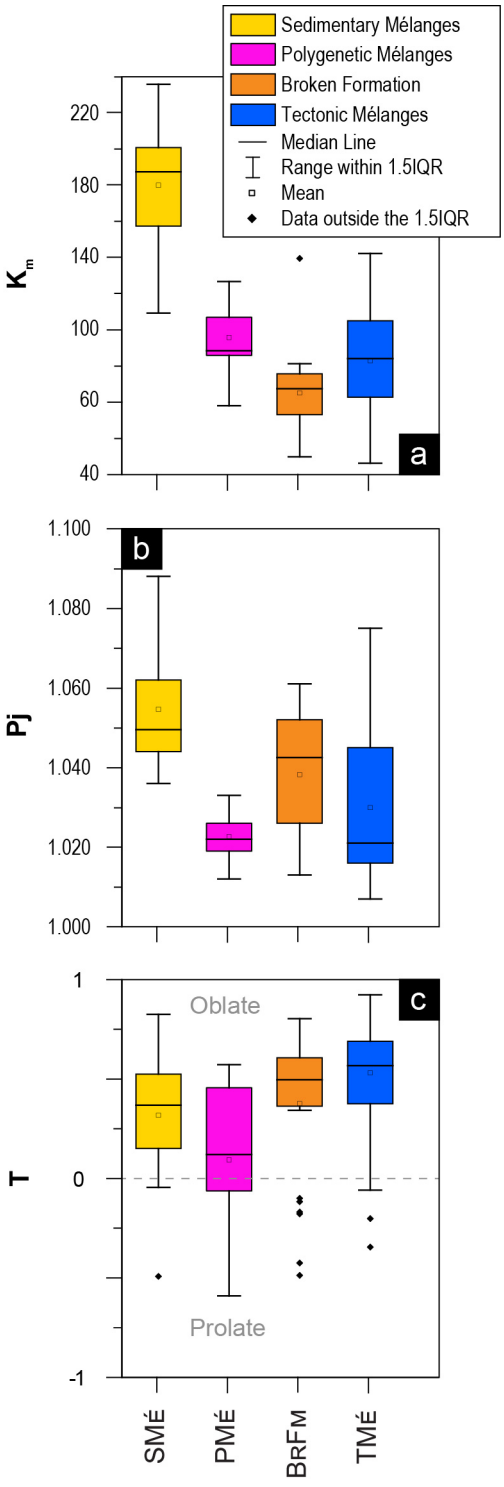

Figure 6.8. Box-and-whisker plots of the (**a**) mean magnetic susceptibility (K_m), (**b**) corrected anisotropy degree (Pj) and (**c**) shape parameter (T) for the different mélanges type.

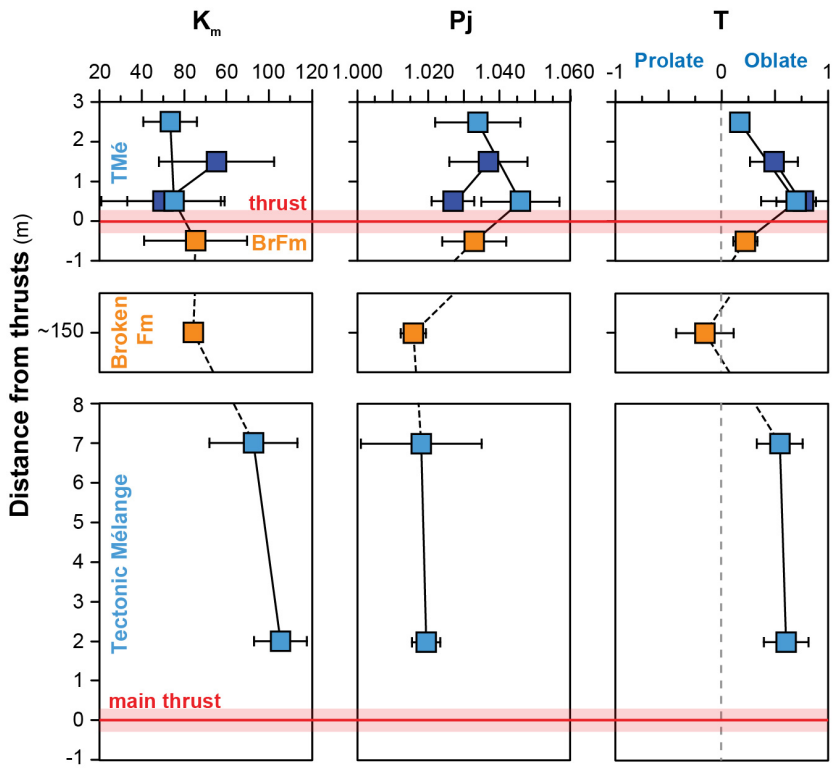

Figure 6.9. Plots of K_m, Pj, and T versus distance from the main thrust faults.

In tectonic mélanges and broken formation, K_m and AMS scalar parameters (i.e., Pj and T) display variations depending on structural position and/or distance from the main thrust planes (**Figure 6.9**).

K_m shows local variability, with no general correlation with the type of chaotic rock unit. In contrast, Pj and T exhibit a similar trend, with the lowest mean values in the broken formation located farther from the main thrust planes. In tectonic mélanges, Pj and T show a progressive increase with proximity to the main thrust faults.

Detailed analysis of the magnetic fabric divided by type of chaotic rock unit is given in the following subchapters.

6.3.2.1 The Broken Formation

The broken formation was sampled at two sites (see, **Figure 6.2**) located at different structural position and distances from the main thrust planes.

Site BrFm1 (**Figure 6.10a-c**), which is the farthest from the main thrust, showed a prolate ellipsoid ($k_1 >> k_2 \approx k_3$; $-1 \leq T < 0$; $L > F$) (orange squares in **Figure 6.10f-i**; **Table 6.S 1**) with a well-defined magnetic lineation ESE-striking. The k_2 and k_3 axes are inter-dispersed, showing a SSW- to NNE-striking distribution. The magnetic foliation is SSW-dipping and steeply inclined. Despite the limited data, two different subfabrics may be tentatively detected (**Figure 6.10b-c**):

- A neutral subfabric ($L \approx F$) showing a sub-horizontal magnetic foliation ESE-dipping and a cluster of k_1 axes ESE-striking (subfabric1 in **Figure 6.10c**);
- A prolate subfabric with a sub-vertical magnetic foliation and a cluster of k_1 axes ESE–WNW-oriented (subfabric2 in **Figure 6.10c**).

Site BrFm2 (**Figure 6.10d**), located in the footwall of a main thrust splay (**Figure 6.2**), exhibits a mixed magnetic fabric with an oblate ellipsoid ($k_1 \approx k_2 >> k_3$; $0 > T \geq 1$; $F > L$) (blue squares in **Figure 6.10f-i**; **Table 6.S 1**) that results from the combination of two different subfabric:

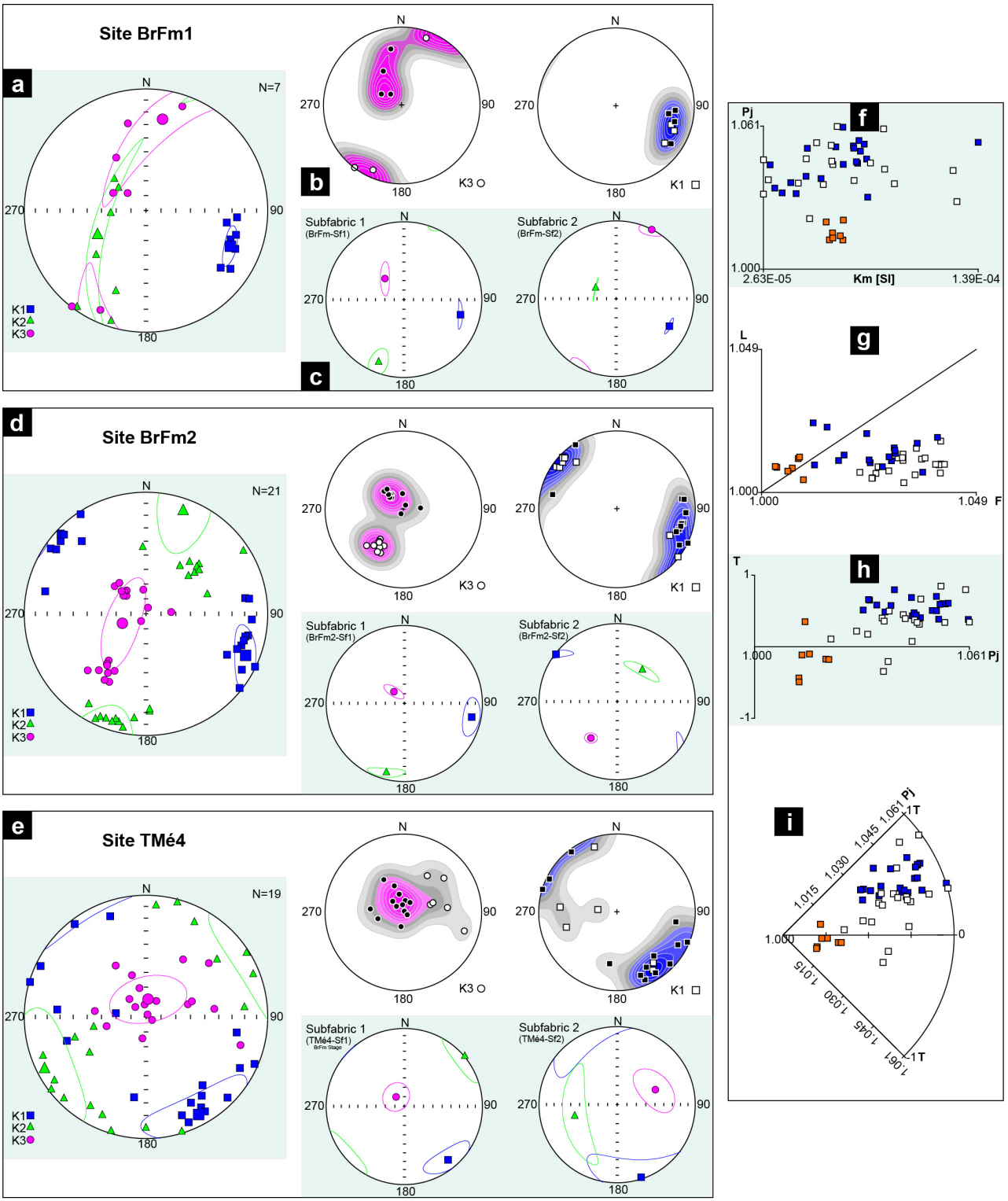

Figure 6.10. Magnetic fabric of broken formation and tectonic mélange specimens (modified from Robustelli Test et al., 2019): (**a**) stereoplots (lower-hemisphere projections) showing the shapes and attitudes of the magnetic susceptibility ellipsoids from the broken formation (site BrFm1); (**b**) density diagrams of k_1 and k_3 axes (contour interval = 10) and (**c**) relative subfabrics; broken formation site BrFm2 (**d**), and tectonic mélanges site TMé4 (**e**), AMS data. Whole diagrams for the measured magnetic fabric in which orange, blue, and white squares are respectively BrFm1, BrFm2, and TMé4 data: (**f**) anisotropy degree vs mean susceptibility; (**g**) magnetic lineation vs. magnetic foliation; (**h**) shape parameter vs. corrected anisotropy degree; (**i**) $\pi/4$ segment polar plot (see Borradaile & Jackson, 2004), in which Pj represents the radius and T the arc length.

• Subfabric 1 (BrFm2-Sf1 in **Figure 6.10c**) is characterized by sub-horizontal magnetic foliation slightly dipping to ESE and a magnetic lineation ESE-striking;

• Subfabric 2 (BrFm2-Sf2 in **Figure 6.10c**) reveals a sub-vertical magnetic foliation and horizontal k_1 axes ESE–WNW aligned.

6.3.2.2 The Tectonic Mélange

The Tectonic mélange was sampled at four sites, located at different distances from the regional NW-striking thrust shear zone (TMé1 to TMé4; see location in **Figure 6.2**). All sites showed mainly oblate magnetic fabric with a strong magnetic foliation (white squares in **Figure 6.10e-i** and **Figure 6.11**; **Table 6.S 1**).

Site TMé1, which is located within the main shear zone (**Figure 6.2**), is characterized by a well-defined steeply-dipping magnetic lineation WSW-striking (**Figure 6.11a**), and sub-horizontal k_2 axes, NW-striking. The k_1 and k_2 axes distributions roughly defined the magnetic foliation plane which is WSW-dipping. Here, two coherent subfabrics show weakly different k_3 and k_2 orientations, distributed from E-W to NE-SW and from NNW–SSE to NW-SE, respectively.

SiteTMé2, which is located about 7 m away from the main shear zone (**Figure 6.2**), showed a complex blended fabric (see Borradaile & Jackson, 2004), with a well-defined sub-vertical magnetic foliation around NNE-striking. This fabric consists of the combination of three different subfabrics, characterized by neutral to oblate ellipsoids (**Figure 6.11c** and blue squares in **Figure 6.11d-g**):

• Subfabric 1 (TMé2-Sf1) showed a sub-vertical magnetic foliation and a sub-horizontal k_3 axis, ESE and NNE-striking, respectively, while the magnetic lineation is ESE-striking;

• Subfabric 2 (TMé2-Sf2) displayed a NNE-striking sub-vertical magnetic foliation, sub-horizontal k_1 and k_3 axes NNE- and WNW-striking, respectively, and a sub-vertical k_2 axis, which weakly deviated from the magnetic foliation;

• Subfabric 3 (TMé2-Sf3) showed a sub-vertical magnetic foliation, NNE-striking, and a k_1 axis plunging at a high angle towards the S.

Site TMé3 and TMé4 are located within the shear zone of a main thrust splay (**Figure 6.2**), but different fabrics were observed at site level.

In particular, Site TMé3 (**Figure 6.11b**) reveal a WSW-dipping magnetic foliation with high dispersion of k_3 axes. Samples collected at increasing distance from the thrust plane revealed significantly different magnetic fabric:

• Subfabric 1 (TMé3-$Sf1_{0\text{-}1m}$) is representative of samples taken in the first meter from the thrust plane. The magnetic fabric is characterized by a well-defined SW-dipping magnetic foliation and a SW-striking magnetic lineation at low to intermediate angles;

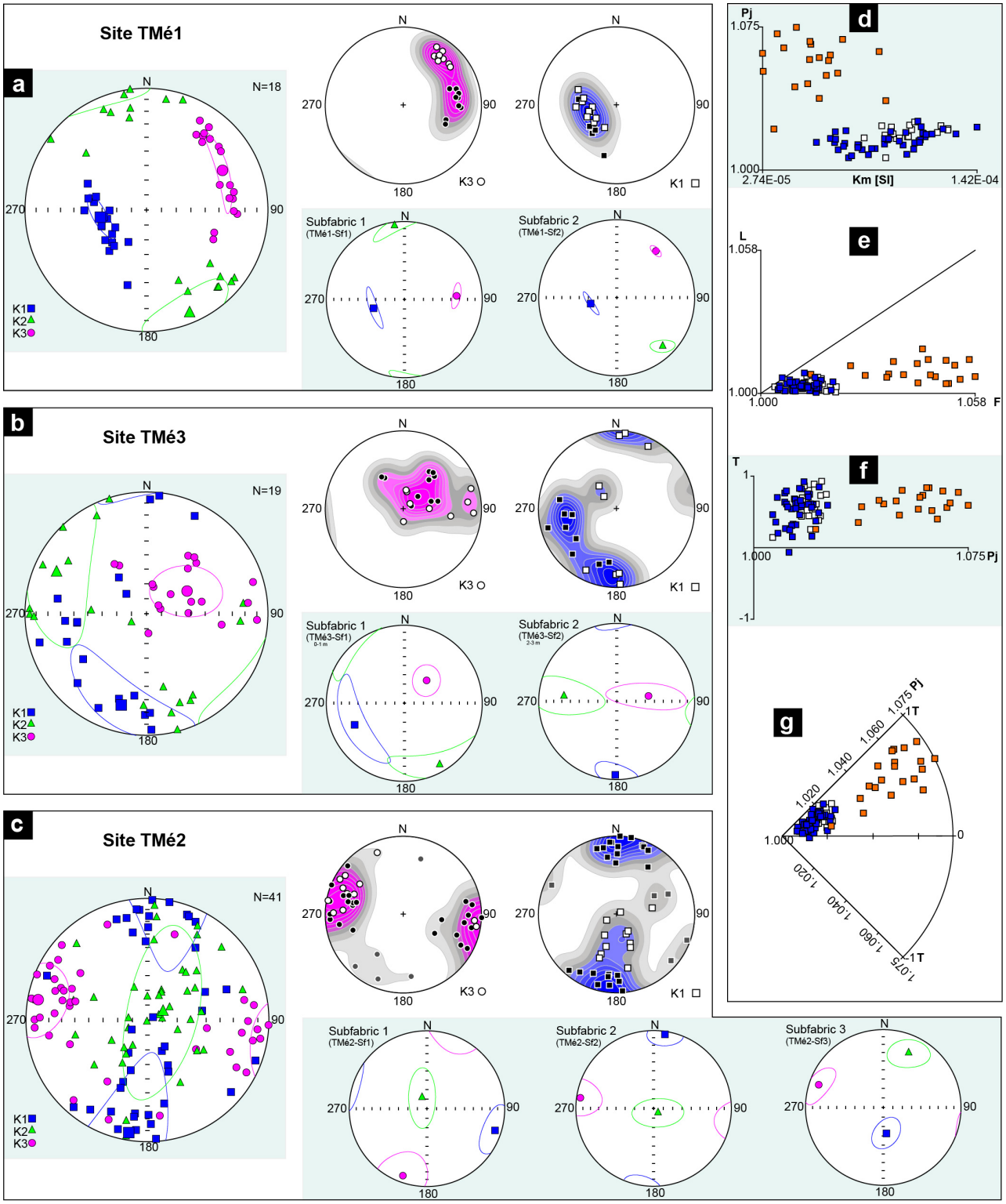

Figure 6.11. Tectonic fabric of tectonic mélange specimens (modified from Robustelli Test et al., 2019): stereoplots (lower-hemisphere projections) of the AMS data, density diagrams of k_1 and k_3 axes (contour interval = 10) and relative subfabrics for (**a**) Site TMé1, (**b**) Site TMé3, and (**c**) Site TMé2. Whole diagrams for the measured magnetic fabric in which orange, blue, and white squares are respectively TMé3, TMè2, and TMé1 data: (**d**) anisotropy degree vs mean susceptibility; (**e**) magnetic lineation vs. magnetic foliation; (**f**) shape parameter vs. corrected anisotropy degree; (**g**) $\pi/4$ segment polar plot (see Borradaile & Jackson, 2004), in which Pj represents the radius and T the arc length.

• Subfabric 2 (TMé3-Sf$2_{2\text{-}3m}$), typical of samples collected within 2-3 m from the thrust plane, displays k_3 and k_2 axes distributed along an E-W girdle. This fabric reveals a N-S-striking sub-vertical magnetic foliation and sub-horizontal k_1 axes clustered around the N-S direction.

Site TMé4 (**Figure 6.10e**) showed a sub-horizontal magnetic fabric. The k_3 axes had a bimodal distribution allowing two different subfabrics to be identified:

• Subfabric 1 (TMé4-Sf1) displayed sub-vertical k_3 axes associated with a sub-horizontal magnetic foliation and a ESE-oriented magnetic lineation;

• Subfabric 2 (TMé4-Sf2) is characterized by k_3 axes plunging toward ENE, a well-defined SW-dipping magnetic foliation and a sub-horizontal magnetic lineation SE-striking.

6.3.2.3 The Sedimentary Mélange

The magnetic fabric of the sedimentary mélange (SMé1, **Figure 6.12a-c**; see location in **Figure 6.2**) is characterized by a blended AMS fabric (see Borradaile & Jackson, 2004), with a weakly dipping magnetic foliation and an oblate to neutral magnetic ellipsoid (white squares in **Figure 6.12e-h**; **Table 6.S 1**). This fabric resulted from the combination of different samples collected within both the basal shear zone and the isotropic portion (i.e., some meters above the basal shear zone) of the sedimentary mélange, respectively (**Figure 6.12b-c**):

• The basal shear zone (Subfabric2 – SMé1-Sf2 n **Figure 6.12c**) showed a neutral to oblate subfabric with the k_1 axis SW-striking, the k_3 axis NW-plunging at a low angle, and the k_2 axis laying on the sub-vertical magnetic foliation, which is NE-striking;

• The isotropic portion (Subfabric1 – SMé1-Sf1 in **Figure 6.12c**) showed an oblate ellipsoid characterized by a well-defined magnetic foliation, SW-dipping, containing statistically-distinct k_1 and k_2 axes, SE- and SW-striking, respectively.

6.3.2.4 The Polygenetic Mélange

The PMé1 (**Figure 6.12d**, see location in **Figure 6.2**) showed a cumulative magnetic fabric with a neutral ellipsoid (orange squares in **Figure 6.12e-h**; **Table 6.S 1**) and no detectable subfabric combinations. The k_3 axis is around ENE-striking, defining a magnetic foliation WSW-dipping with different angles. The slightly gathered k_2 axes are SW-plunging at variable angles, partially deviating from the magnetic foliation plane. The clustered k_1 axes define a sub-horizontal magnetic lineation, NW-striking.

6.3.3 AARM, AIRM and HF-AMS

ApARM and AIRM experiments were performed on characteristic subfabrics observed in broken formation and tectonic mélanges. The obtained magnetic fabrics are well-defined and exhibit a close similarity to AMS patterns (**Figure 6.13**).

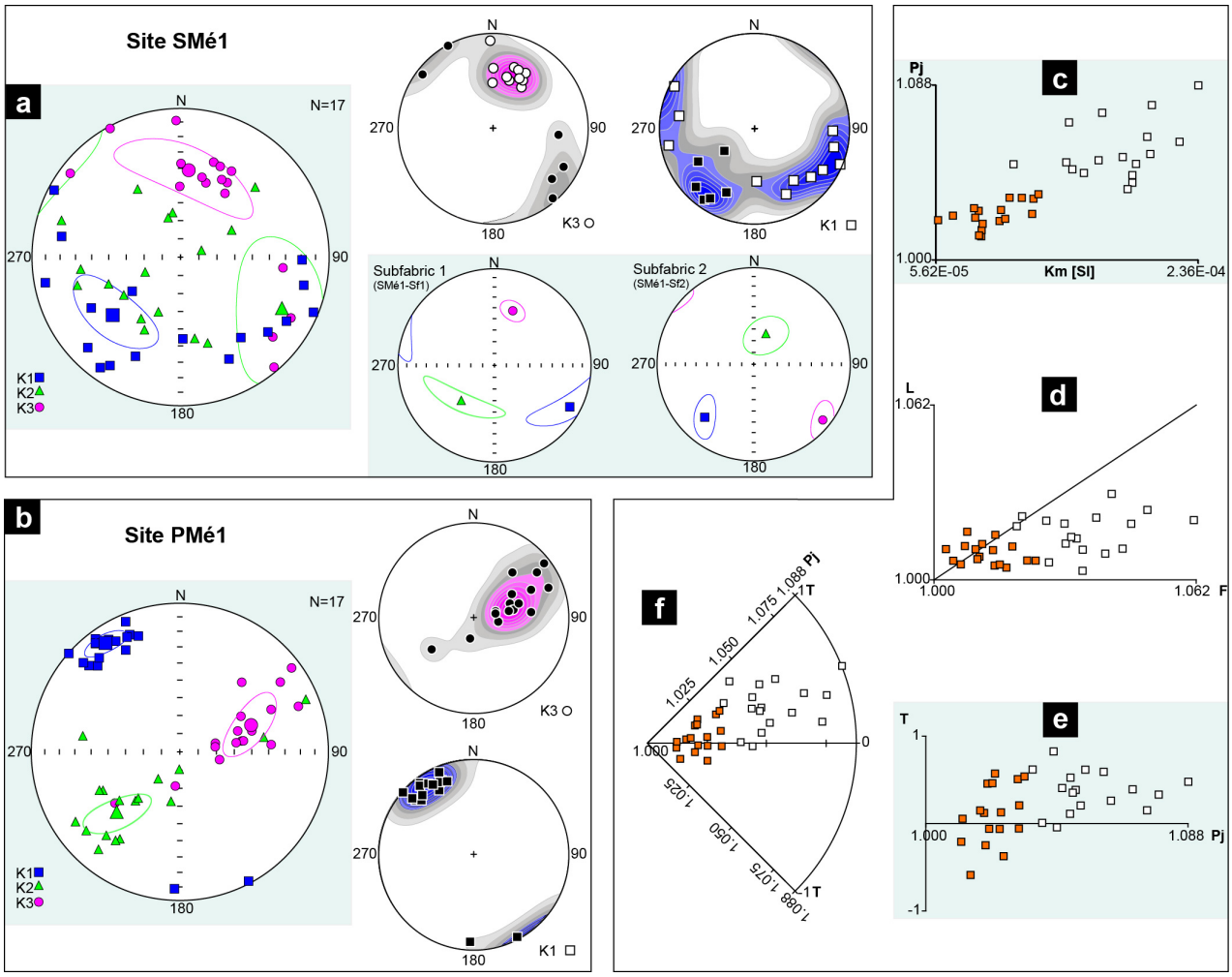

Figure 6.12. Magnetic fabric of sedimentary (SMé1) and polygenetic (PMé1) mélange specimens (modified from Robustelli Test et al., 2019): (**a**) stereoplots (lower-hemisphere projections) showing the shapes and attitudes of the magnetic susceptibility ellipsoids from site SMé1; (**b**) density diagrams of k_1 and k_3 axes (contour interval = 10) and (**c**) relative subfabrics; (**d**) and site PMé1 AMS data. Whole diagrams for the measured sedimentary fabric in which white and orange are, respectively, SMé1 and PMé2 data: (**e**) anisotropy degree vs. mean susceptibility; (**f**) magnetic lineation vs magnetic foliation; (**g**) shape parameter vs corrected anisotropy degree;(h) π/4 segment polar plot (see Borradaile & Jackson, 2004), in which Pj represents the radius and T the arc length.

In particular, ARM experiments show significantly higher Pj values than AMS. At the site/subfabric level, Pj values agreed among ARM experiments ($1.109 < Pj < 1.180$; **Figure 6.S 1**; **Table 6.S 2**). AIRM exhibit the highest Pj, typically ≥ 1.160 with peak values of about 1.295 ± 0.053 for tectonic mélanges (TMé3 subfabrics). Overall, the shape parameter (T) is lower for ARM experiments than AMS. In both the broken formation and tectonic mélange, T changes from strongly oblate for AMS to slightly neutral for ARM experiments. An exception is subfabric TMé4-SF1, where values distribution is similar for AMS and all ARM experiments. In all subfabric, AIRM show T values consistent with the AMS or slightly lower (**Figure 6.S 2**; **Table 6.S 2**).

A slight trend and correlation between F-test values and remanence intensity is visible (**Figure 6.13c**), with significantly higher F-test values for $AARM_{100\text{-}0}$ and $AIRM_{20}$. In contrast, there is no correlation with the type of chaotic rock unit (**Figure 6.13d**).

The ApARM fabrics are well-defined for all the different representative patterns (**Figure 6.13a, b**). No significant changes are visible between different ARM experiments and AMS for both broken formations and tectonic mélanges. In fact, at the subfabric level, confidence ellipsoids of the principal anisotropy axes (from AMS and ARM experiments) overlap and thus the fabrics are all statistically indistinguishable (**Figure 6.13a, b**). This configuration suggests the similar/same orientation for all subpopulations of remanence-bearing grains (of different mineralogy and grain-size) with that of the minerals carrying the AMS.

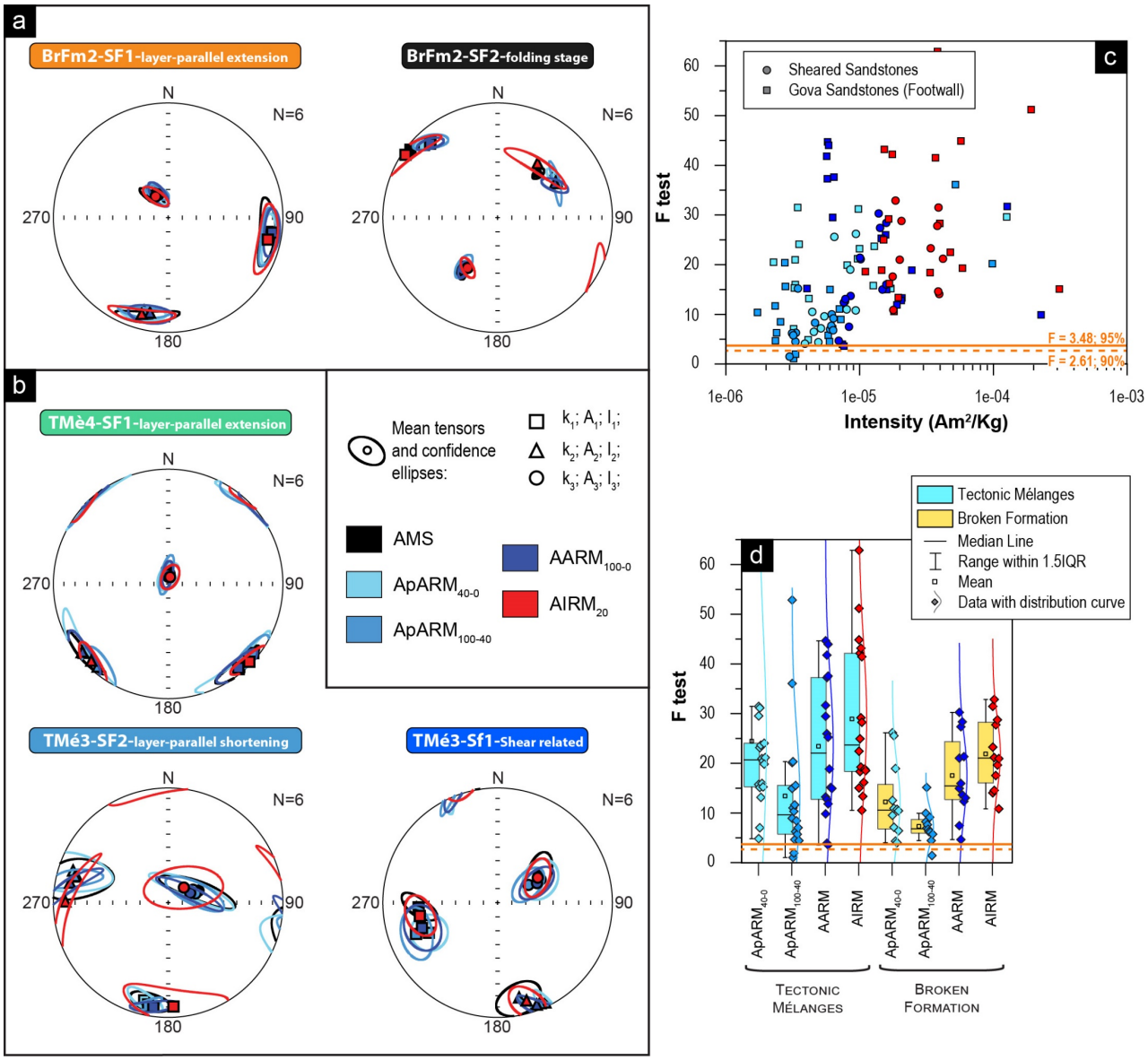

Figure 6.13. Principal directions and confidence ellipsoids of the anisotropy of magnetic remanence (ARM) experiments in: (**a**) broken formation; (**b**) tectonic mélanges. Variations of the F-test versus remanent magnetization (**c**). Box-and-whisker plot with data and normal distribution curves of the F-test among lithologies and ARM experiments (**d**).

The para- and ferromagnetic components of the HF-AMS were extracted for few representative specimens from each dominant subfabric (**Figure 6.14**). The anisotropy is dominated by the paramagnetic fraction. In fact, the average proportions of the components are 97 ± 32% paramagnetic and 3 ± 17% for the ferrimagnetic fraction.

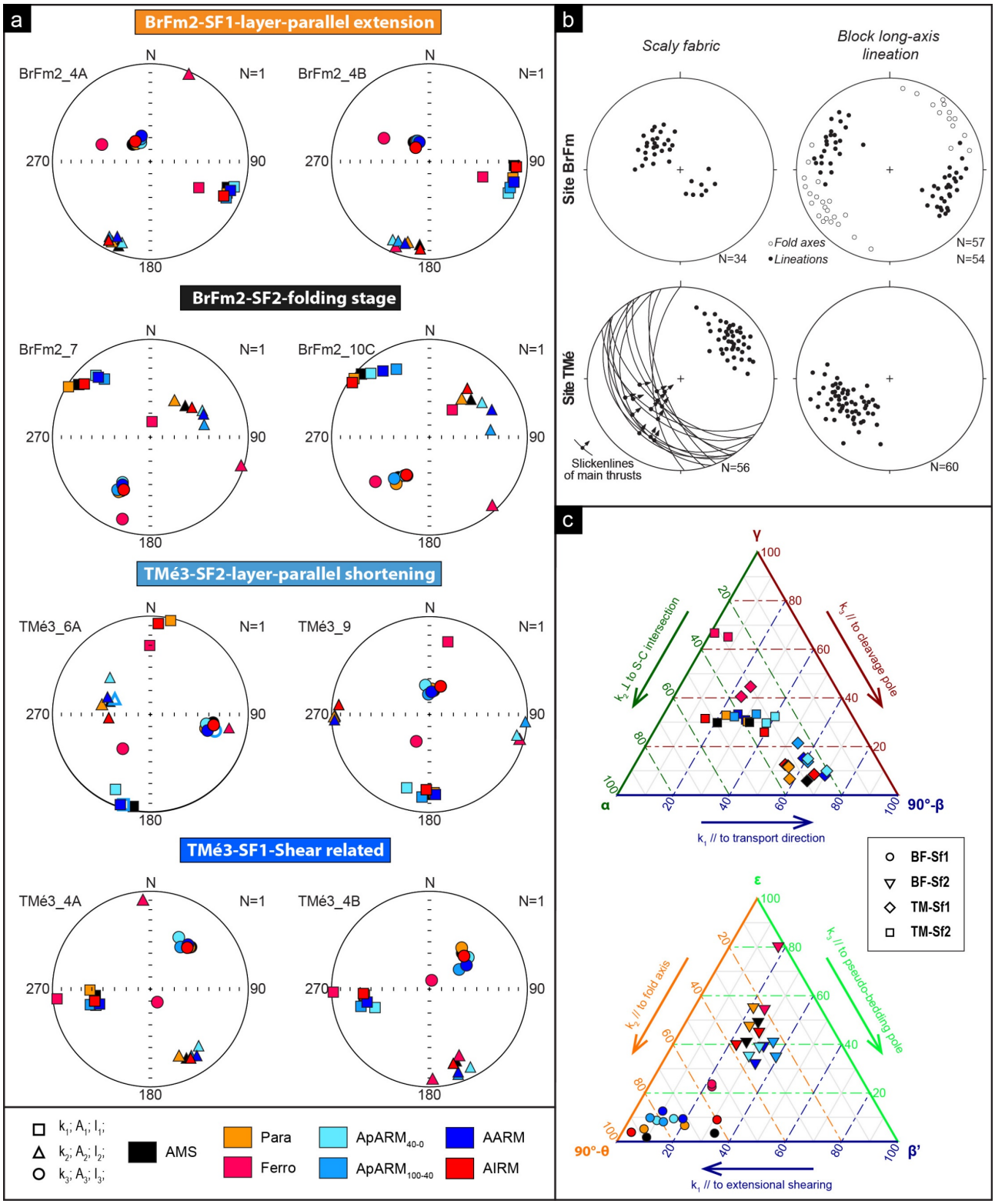

Figure 6.14. (**a**) Stereoplots of the principal directions of the low-field anisotropy of magnetic susceptibility (AMS), anisotropy of magnetic remanence (ARM) experiments and the paramagnetic and ferromagnetic components of the high-field AMS for representative samples, classified after stages. Open symbols represent data with F-test lower than 5; (**b**) Summary of the structural data (see **Figure 6.4c** for details); (**c**) Ternary diagrams (see **Figure 3.3** for parameters details) relating structural and anisotropy of magnetic susceptibility and remanence data.

The magnetic subfabrics carried by the paramagnetic (HF-AMS$_{para}$) and ferromagnetic (HF-AMS$_{ferro}$) components are coaxial with the low-field AMS (LF-AMS) (**Figure 6.14**).

Overall, all the three principal directions of AMS (both low- and high-field) and ARM experiments are subparallel. Sometimes, the HF-AMS_{ferro} components shows interchanged k_1 and k_2 axis with respect to LF-AMS (BrFm2-SF2 in **Figure 6.14**).

The presence of well-developed fabric with characteristic orientation of the paramagnetic and ferromagnetic (s.l.) grains at pattern level is clearly visible from the ternary diagram (**Figure 6.14c**). In fact, the presence of well-grouped data suggests that every pattern show same orientation for para- (HF-AMS_{para}) and ferromagnetic minerals (both HF-AMS_{ferro} and ARM experiments) with a specific configuration of the three principal axes with respect to the structural elements depending on the dominant deformation mechanism and/or type of chaotic rock unit (**Figure 6.14c;** compare **Figure 6.14a** and **Figure 6.14b**).

6.4 Discussion & correlation of the magnetic fabric with mélange forming processes

The AMS analysis enabled the definition of specific configurations of the magnetic fabric (i.e., AMS and/or ARM ellipsoids and their axes orientation) for the different types of chaotic rock unit, reflecting the forming processes (i.e., tectonic, sedimentary, and their interlink and superposition) that were previously distinguished through structural field data.

6.4.1 The Broken Formation

The AMS fabric of the broken formation (Sites BrFm1 and BrFm2 in **Figure 6.15**, **Figure 6.16**, see also **Figure 6.10a-d**) shows a NW-striking magnetic lineation (k_1) aligned with the tectonic stretching direction. The shape of the magnetic ellipsoid varies from prolate to oblate depending on the distance from the main thrust planes (**Figure 6.2**). Distribution of k_3 axes on a girdle pattern emerges from the superposition of competing subfabrics (**Figure 6.10a-d**) and defines a transitional to tectonic magnetic fabric, which is commonly associated with incipient deformation. In fact, weak-to-incipient deformation induced the progressive deviation of k_3 axes from a direction perpendicular to the bedding plane toward one parallel to the maximum tectonic shortening axis. The detected subfabrics (**Figure 6.10a-d**; **Figure 6.17b**) suggest that the magnetic fabric resulted from the combination and superposition of two different deformational mechanisms and/or differently-oriented deformational events. Since both para- and ferromagnetic minerals are coaxial (**Figure 6.14** and **Figure 6.17b-d**), we can infer that subfabrics are associated with recording distinct deformation mechanisms/stages rather than different carriers of the magnetic anisotropy.

In particular, the sub-horizontal ESE-dipping magnetic foliation of subfabric1 is subparallel to the SE-dipping pseudo-bedding, and the magnetic lineation is aligned to the NW-striking layer-parallel extension and related features (i.e., pinch-and-swell and boudinage) (BrFm1-SF1 in **Figure 6.15**; BrFm2-SF1 in **Figure 6.16**). Partial or complete parallelism between AMS and structural elements can be evaluated in the ternary diagrams (see $BrFm_{LPExt}$ in **Figure 6.17b**), where the lower left vertex represent a fabric with magnetic foliation and lineation parallel to the pseudo-bedding and the ESE–WNW extensional shearing direction, respectively. These features are well-consistent with the combination of layer-parallel extension

and vertical compaction due to burial at the wedge front of the Ligurian accretionary complex. This occurred during the Late Cretaceous–early Eocene accretionary stage in wet and partially lithified sediments (e.g., Bettelli & Panini, 1987; Pini, 1999; Bettelli & Vannucchi, 2003; Codegone et al., 2012; Festa et al., 2013).

On the contrary, the alignment of the NW-striking magnetic lineation of subfabric2 (BrFm1-SF2 in **Figure 6.15**; BrFm2-SF2 in **Figure 6.16**) to the block long-axis lineation may represent the superposition of tectonic shearing, as sediment incorporated at the toe of the accretionary wedge (e.g., Bettelli et al., 1989; Kimura & Mukai, 1991; Festa et al., 2013). In addition, the presence of a magnetic foliation at high angle to the pseudo-bedding (see, $BrFm_{Folding}$ in **Figure 6.17b-d**) might indicate the influence of LPS or folding processes.

Thus, the broken formation magnetic fabric, is well comparable with the mesoscale structural fabric, showing a coeval development of flattened, intra-layer sheath-like folds, layer-parallel extensional fabric, and asymmetric boudinage likely resulting from the heterogeneity of deformation at the toe of the accretionary wedge.

6.4.2 The Tectonic Mélange

The magnetic fabric of the tectonic mélange, showing a slightly neutral to mainly oblate AMS ellipsoid with a steep magnetic foliation (Sites TMé1 to TMé4 in **Figure 6.15**; **Figure 6.16**), revealed a transitional to tectonic- magnetic fabric. Changes in magnetic lineation (k_1) plunging angles and Pj values, approaching to the main regional-scale thrust surface (see **Figure 6.11**; **Figure 6.9**), record the progressive deformation related to tectonic shearing onto the broken formation fabric. Overall, no different orientations of para- and ferromagnetic minerals were observed, allowing the observed magnetic subfabric to be interpreted in terms of tectonic reworking.

In TMé1, located within the shear zone of the NW-striking thrusts, the alignment of a steeply-dipping magnetic foliation to the mesoscale tectonic shear surfaces (i.e., R-shear, scaly fabric, shear surfaces; compare **Figure 6.4c** and **Figure 6.11a**), is well consistent with the development of tectonically-induced mesoscale shear deformation. The parallelism between the NE-oriented magnetic lineation and the main tectonic shear direction (TMé1 in **Figure 6.15**; $TMé_{shear}$ in **Figure 6.17**) remarks the magnetic fabric formed during the late Oligocene–early Miocene out-of-sequence thrusting stage (see Codegone et al., 2012).

On the contrary, the blended magnetic fabric of site TMé2, which is located away from the NW-striking thrust and the related shear zone, represents the superposition of two tectonic subfabrics (subfabric2 and subfabric3) onto the subfabric1 (see **Figure 6.11c**). The latter is well-comparable with that of the broken formation (see subfabric2 of site BrFm1 in **Figure 6.10**, **Figure 6.11c,d** and **Figure 6.15**).

The configuration of subfabrics2 and 3, showing the reorientation of the k_1 axes (**Figure 6.11c**), may represent two stages of progressive realignment of the ferromagnetic grains and clay particles or different reworking intensity of the broken formation during thrusting. Since both para- and ferromagnetic minerals

are coaxial (**Figure 6.13b**; **Figure 6.14**) we can confidently ascribe the different pattern to varying deformation intensity.

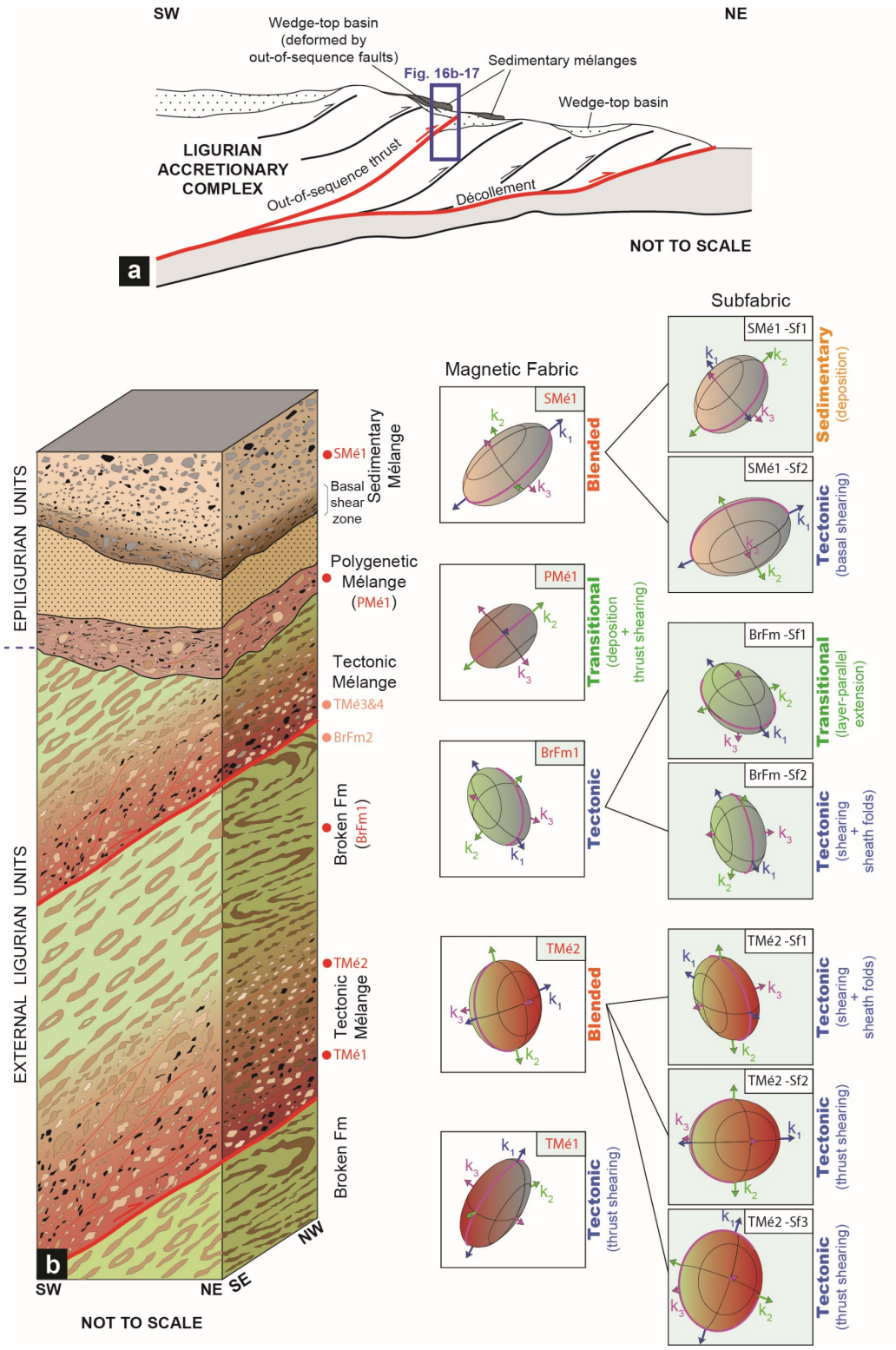

Figure 6.15. (**a**) Conceptual cross-section (not to scale) of the Ligurian accretionary complex (modified from Festa et al., 2015), the blue box represents the schematic 3D stratigraphic column of **Figure 6.15b** and **Figure 6.16**; (**b**) conceptual 3D stratigraphic column (not to scale) showing the internal arrangement and structural position of the dfferent types of mélange (tectonic, sedimentary, and polygenetic) and broken formation and related AMS ellipsoids oriented to present-day geographic coordinates (see text for explanation) (modified from Robustelli Test et al., 2019). Red and black lines in the 3D stratigraphic column represent tectonic and stratigraphic contacts, respectively.

In particular, subfabric2, which is characterized by a slightly neutral AMS ellipsoid with k_1 axis SSW-plunging at a low angle (**Figure 6.11c**), represents a transitional fabric. This is consistent with the incipient deformation stage, showing convergence of long axes (k_1) to the intersection between S and C planes. Instead, subfabric3, characterized by slightly oblate ellipsoid and k_1 axes plunging at high angle toward the south (**Figure 6.11c** and **Figure 6.15**), may represent a clearly tectonic fabric possibly related to a subsequent stage of increasing deformation, with the progressive parallelization of the k_1 axes to the shear direction.

Similar magnetic fabric behaviour was observed along a splay thrust (Sites TMé3 and TMé4; see location in **Figure 6.2**), with changes in ellipsoid shape and axis orientation depending on proximity to the main shear surface.

Samples close to the basal thrust (TMé3-$Sf1_{0\text{-}1m}$ in **Figure 6.11b** and **Figure 6.16**) reveal a good alignment between the magnetic foliation and lineation with the scaly fabric and shear direction, respectively (see, **Figure 6.17a**). In contrast, moving a few meters away from the thrust plane, the dominant subfabric (TMé3-$Sf2_{2\text{-}3m}$ in **Figure 6.11b** and **Figure 6.16**) shows parallelism between k_1 and the S-C intersection, corresponding to an intersection lineation fabric (left side of the ternary diagram in **Figure 6.17a**). The presence of a steeply inclined magnetic foliation suggests the dominance of layer-parallel shortening (LPS) at a greater distance from the thrust plane. In turn, this indicates the localization of the strain close to the basal thrust.

The latter fabric is also recorded at site TMé4 (Subfabric TMé4-Sf2 in **Figure 6.16**) with the addition of a second subfabric (TMé4-Sf1 in **Figure 6.16**) comparable with the layer-parallel extensional fabric ($BrFm_{LPExt}$) of the broken formation (BrFm1-SF1 in **Figure 6.15**; BrFm2-SF1 in **Figure 6.16**). In fact, the TMé4-Sf1 and the $BrFm_{LPExt}$ have the same geometrical relationships with the structural elements (compare BrFm2-Sf1 and TMé4-Sf1 in **Figure 6.16**), as data distribution is indistinguishable within the ternary diagram (**Figure 6.17b**). Thus, this configuration emphasizes the heterogeneity of deformation within the accretionary prism, with the presence of a domain that has preserved the previous broken formation stage and the variable pervasivity of the NE-verging thrusting stage.

6.4.3 The Sedimentary Mélange

The blended magnetic fabric (see Borradaile & Jackson, 2004) of the sedimentary mélange (SMé1 in **Figure 6.15**), characterized by an oblate to neutral ellipsoid and a high dispersion of k_1 and k_2 axes, revealed the combination of different petrofabrics. The latter axes are consistent with the internal arrangement of viscous debris flows emplaced within wedge-top basins at the top of the Ligurian accretionary wedge in the late Oligocene–Early Miocene (Remitti et al., 2011; Codegone et al., 2012; Panini et al., 2013; Festa et al., 2015).

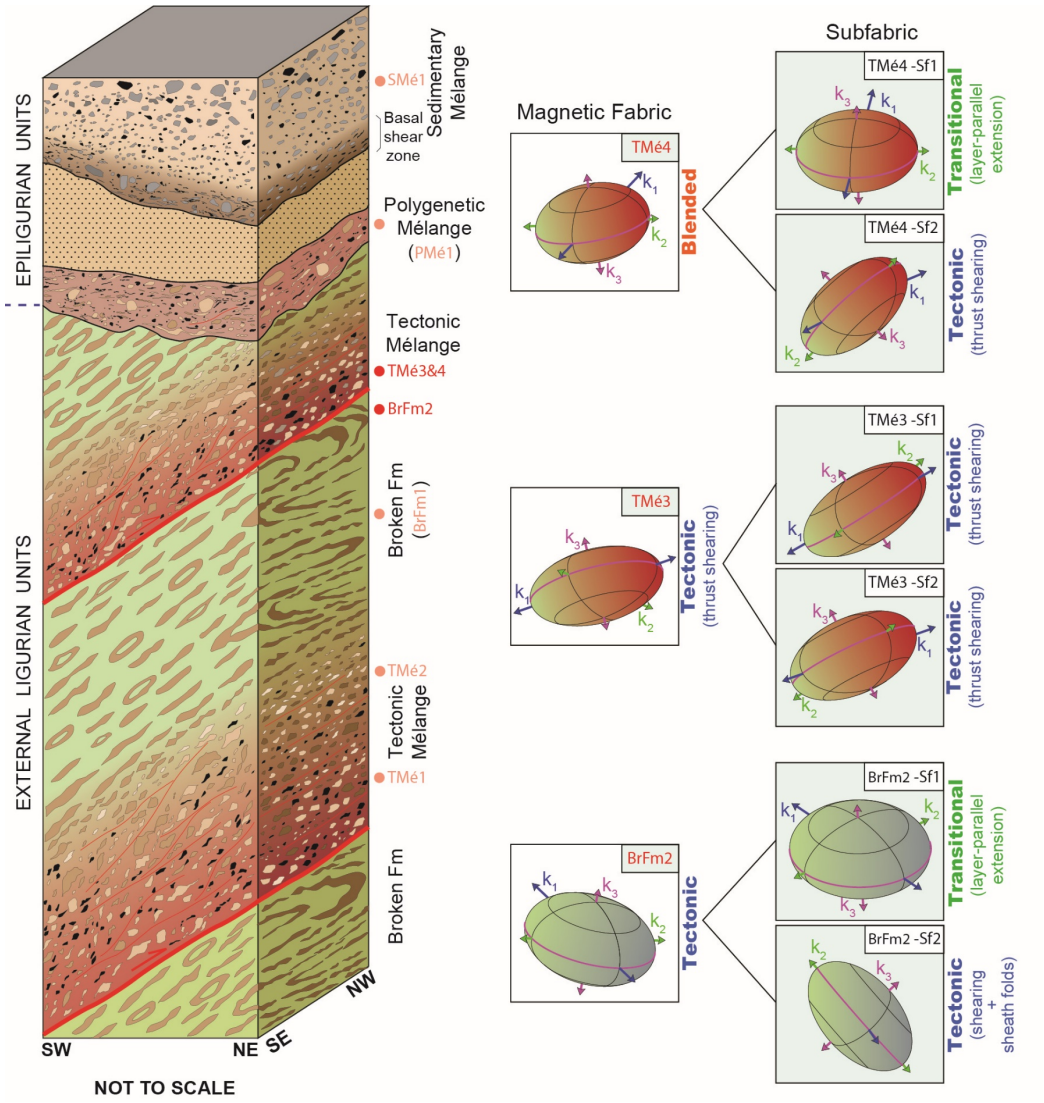

Figure 6.16. Conceptual 3D stratigraphic column (not to scale) showing the internal arrangement and structural position of the different types of mélanges and broken formation and related AMS ellipsoids oriented to present-day geographic coordinates (see text for explanation) (modified from Robustelli Test et al., 2019).

The occurrence of distinct k_1 and k_2 axes clusters (**Figure 6.12c**) revealed partially-preferred orientations of para- and ferromagnetic grains induced by sedimentary (gravitational) processes of formation. Two different mechanisms could provide this magnetic fabric: (i) depositional processes under current flow associated with grain transport by traction, in which the cluster of k_1 axes trends in the direction perpendicular to the flow (Sagnotti et al., 1994), and (ii) a weak and non-pervasive deformation associated with the emplacement of overlaying debris flow (i.e., "cryptoslumps", see also references Corin et al., 2001; Schwehr & Tauxe, 2003).

On the contrary, subfabric2 showed a slightly neutral magnetic ellipsoid (**Figure 6.12c**, **f-h**) with SW-striking k_1 axes parallel to the orientation of the clast-long axis within the basal viscous shear zone of the sedimentary mélange (see Festa et al., 2015). The magnetic lineation (k_1) is also consistent with the direction of extensional shearing. Thus, the AMS fabric reflects a significant preferred orientation of grains induced by the downslope emplacement of the sedimentary mélange as a cohesive debris flow (see, e.g., Ogata et al., 2014, 2019; Festa et al., 2015, 2016; Kuranaga et al., 2019).

6.4.4 The Polygenetic Mélange

The magnetic fabric of the polygenetic mélange (PMé1 in **Figure 6.15**) defined a neutral magnetic ellipsoid with a sub-horizontal magnetic foliation and well-clustered k_1 axes. This pattern represents a transitional fabric due to the partially tectonic reorientation of the primary fabric of the sedimentary mélange (i.e., the MTD). In fact, the occurrence of some sub-vertical k_3 axes associated with sub-horizontal k_1 and k_2 axes are well consistent with the remnant of a primary gravitationally-induced fabric, formed during the MTD emplacement. Instead, the girdle drawn by the k_2 and k_3 axes might document the role played by tectonic processes in weakly reworking the primary fabric of the sedimentary mélange. In fact, data grouped close to the lower left vertex of the ternary diagram (**Figure 6.17a**) reveal a good parallelism between magnetic and mélange foliations and the alignment of the k_1 axes with the direction of S-C structures related to the NW-verging out-of-sequence thrusting (i.e., late Oligocene–early Miocene thrusting stage, see Festa et al., 2013; **Figure 6.17a**; compare **Figure 6.4c** and **Figure 6.12b**).

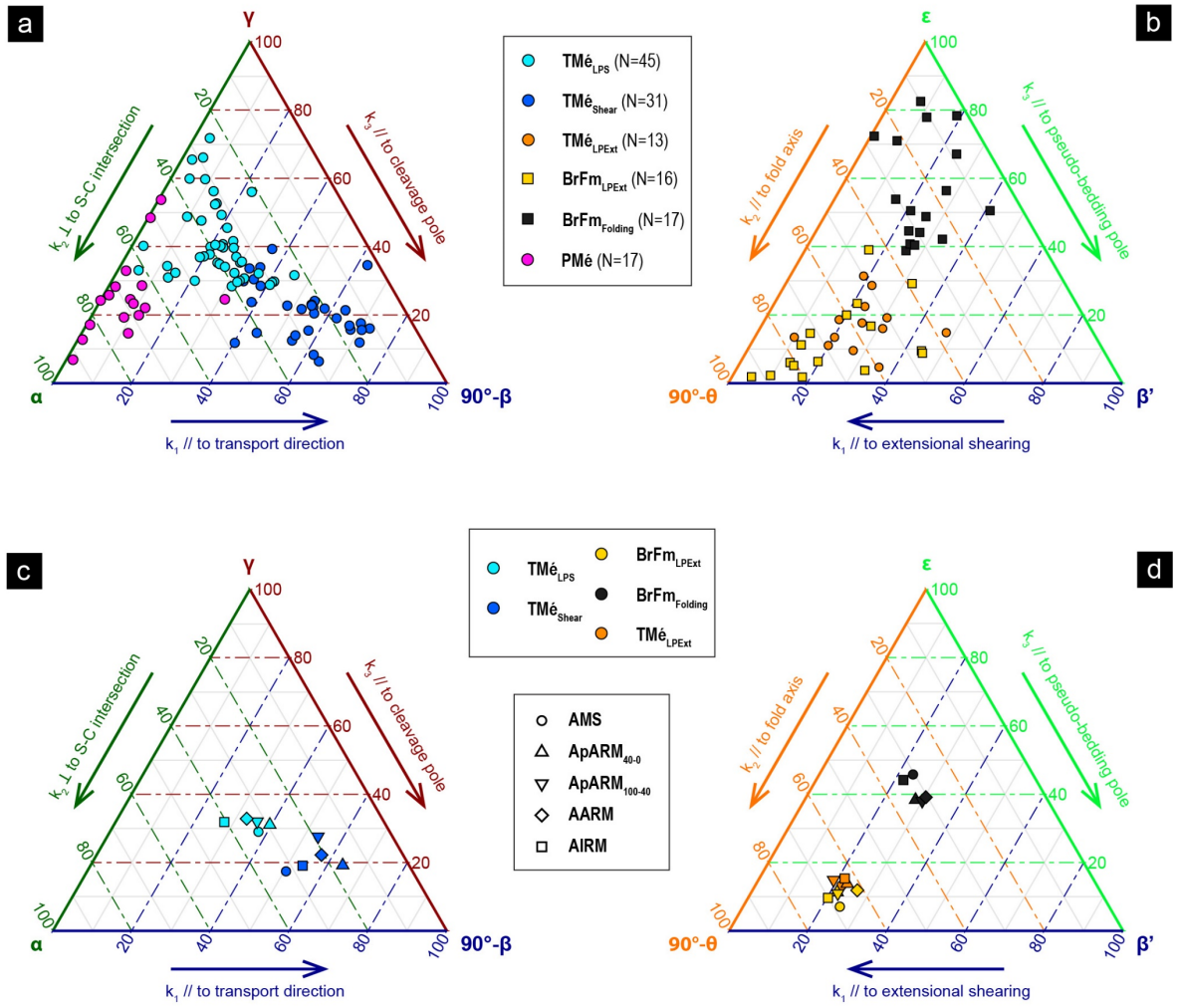

Figure 6.17. Ternary diagrams (see **Figure 3.3** for parameters details) relating structural and magnetic directional data. Anisotropy of magnetic susceptibility (AMS) (**a**) and mean anisotropy of magnetic remanence (ARM) (**c**) data from the tectonic mélanges; data from the broken formation: AMS (**b**) and ARM (**d**).

6.5 Concluding Remarks

The different types of chaotic rock unit (mélanges and broken formations), cropping out in different structural positions within the external Ligurian and Epiligurian units in the Northern Apennines (northwest Italy), represent the products of different interrelated and locally-superposed processes (sedimentary, tectonic, and polygenetic; see, Codegone et al., 2012; Festa et al., 2019), which accompanied the Late Cretaceous–early Miocene tectono-stratigraphic evolution of an exhumed Ligurian accretionary complex and the overlying wedge-top basin succession (Codegone et al., 2012). Through the analysis of the magnetic fabric of the different types of chaotic rock unit differing each other by diverse diagnostic block-in-matrix fabrics (Codegone et al., 2012; Festa et al., 2019), our findings document that a close relationship exists between mesoscale structural fabrics and the configurations and orientation of the principal axes of the magnetic susceptibility and remanence subfabrics. The broken formation shows a tectonic magnetic fabric with a prolate to oblate AMS ellipsoid for both para- and ferromagnetic components. The magnetic lineation (k_1; A_1; I_1) is consistent with the block-long axis and layer parallel extension directions, while the girdle-shaped distribution of intermediate and minimum axes is well-consistent with a heterogeneous deformation, as occurred at the toe of the accretionary wedge (coeval flattening, boudinage, and layer-parallel extension, see Festa et al., 2013). The tectonic mélange showed a magnetic fabric with neutral-to-oblate AMS and ARM ellipsoids. The magnetic lineation and the magnetic foliation are parallel to the direction of shear and the mélange foliation, respectively. Away from the main thrust surface, the occurrence of an intermediate/transitional magnetic fabric documents the partial preservation of the previous broken formation fabric. The sedimentary mélange showed a depositional magnetic fabric defining an oblate AMS ellipsoid with a magnetic lineation perpendicular to the direction of emplacement. Only within the sheared horizon at the base of the gravitational body, the magnetic fabric defines a neutral ellipsoid with magnetic lineation parallel to the clast-long axis and the direction of downslope emplacement. The polygenetic mélange showed a transitional magnetic fabric with a neutral AMS ellipsoid. The magnetic lineation and the magnetic foliation are oriented perpendicular to the shear direction and parallel to the scaly fabric, respectively, while the girdle-shaped distribution of k_2 and k_3 axes is well-consistent with a partial reworking and reorientation of grains due to the overprinting of tectonic processes onto sedimentary ones.

Our findings thus document the significance of the application of the magnetic fabric method (AMS, ApARM, AIRM) to the complex rock assemblages commonly characterizing subduction–accretionary complexes as a valuable tool in distinguishing different types of chaotic rock units (mélanges and broken formations). The comparison between field-observed meso-structural fabric and magnetic fabric on an exhumed subduction–accretion complex in the Northern Apennines allowed us to define and validate the diagnostic magnetic fabric features that are necessary to analytically distinguish the contribution of different mélange forming-processes (tectonic, sedimentary, and their mutual superposition) during its evolution. Importantly, since the studied Ligurian accretionary complex represents an ancient analogue for the shallow portion of present-day subduction complexes (e.g., Pini, 1999; Remitti et al., 2011; Codegone et al., 2012;

Festa et al., 2013, 2018), the diagnostic magnetic fabric configuration defined for each type of chaotic rock unit may be successfully applied in the investigation of deformation in modern subduction–accretionary complexes where direct field-observations are not possible. Therefore, our results may provide potential significant constraints to better understand the internal structural architecture of modern subduction–accretion complexes, and the role played by different (and locally superposed) processes during their tectono-stratigraphic evolution.

Chapter 7

SUMMARY & CONCLUDING REMARKS

The main purpose of this thesis was to investigate the magnetic signatures of fault rocks in convergent margins at shallow depth. Anisotropy of magnetic susceptibility and remanence, with emphasis on the separation of different subfabric, were used as primary sources of information to unravel different deformation stages, variations in stress regime and discriminate between localized and diffuse deformation. Magnetic mineralogy investigations were essential to verify changes in magnetic properties and their link to physical-chemical processes associated with faulting. In this final Chapter, similarities and differences between ancient and actual convergent margins are discussed, providing possible explanations for discrepancy in the magnetic signature among IODP data and the results of the studied exhumed analogues. The main findings are then summarized, with focus on the role of lithological variations/heterogeneities in controlling the sensitivity in the registration of the faulting processes by different magnetic minerals. Finally, future perspectives on the importance of the use of magnetic measurements and their integration with other discipline to enrich our knowledge and provide fundamental insight into the interpretation of the mechanisms involved in the evolution of shear zones in the seismogenic zone (both in modern and exhumed fault zones) are addressed.

7.1 Summary of main findings & comparison with modern equivalent

The detailed analysis of rock magnetic properties in three exhumed analogues of intraplate and convergent margin shear zones has provided interesting new findings to further progress the understanding of heterogeneities related to the faulting processes. Separation of composite fabrics using statistical treatments of directional data has proven to be a powerful tool to discern superposed magnetic subfabrics/fabric patterns at site level and evaluate the different contribution of diffused and localized deformation along convergent

margin shear zones. Discrimination of subfabrics also allows unveiling the presence of minor thrust planes or secondary zones of localized strain even where the field structures do not clearly show a change in the deformation regime. It is important to emphasize that detailed data analysis and comparison with structural data were crucial in quantifying the number of samples that recorded different deformation processes (e.g., pure or simple shear dominated regimes), leading to greater statistical significance of the observed fabrics.

Specific AMS fabrics and their distribution demonstrate a good correlation with the intensity of reworking related to non-coaxial deformation and the relative position in the complex internal architecture of the convergent margin shear zones (e.g., proximity to the major tectonic structures). Indeed, despite the different lithology involved, the paramagnetic subfabrics (HF-AMS_{para}) are nearly coaxial with the AMS, suggesting that the different AMS fabrics are closely related to the deformation of paramagnetic clay minerals of the matrix rather than mineralogical changes. The lithological changes play only a minor role on the occurrence of AMS shear-related fabrics, as they appear to control only the frequency of a particular magnetic fabric along the studied convergent margin shear zones in response to lithological-specific deformation mechanism (for further discussion on lithological influence see **Subchapter 7.2** below). Overall, a general common trend can be observed in term of magnetic fabric distribution and its progressive evolution. The main common observations consist in the recurrence of two main patterns showing specific geometric relationships with the structural elements (**Figure 7.1**), which could be associated with the degree of non-coaxial deformation and progressive localization of strain.

In the proximity of the main thrust faults and basal décollement, both clay-rich and carbonate-rich sediments revealed a dominantly oblate magnetic fabric that shows direct correlation with the development of a shear related fabric, suggesting high-degree of non-coaxial strain and shear localization recorded along the main faults. In fact, in the first few meters to tens of meters, the dominant magnetic fabric always shows a magnetic foliation consistent with the structural foliation (i.e., S-planes or mélange foliation) or C-planes and a magnetic lineation parallel to the shear/transport direction (shear fabrics in **Figure 7.1b, d-e**). In addition, k_1 can be parallel to the calculated slip vector or transport direction for dominant simple or pure shear component, respectively (Stage E_{pure} and Stage$E//_{pure}$ in **Figure 7.1d**). This fabric can also be ubiquitous in tectonic slices tens of meters thick, indicating the influence of diffuse high-degree of shear strain. The dominance of this shear pattern decreases with distance, but it can also occur several tens of meters away from the main thrust planes, suggesting the presence of local shear concentration within the tectonic slices or secondary/minor thrust planes.

The second recurrent pattern shows magnetic foliation consistent with the cleavage (S-planes), but the magnetic lineation is at the intersection between S and C planes (S-C intersection fabric in **Figure 7.1d-e** and $TMé_{LPS}$ in **Figure 7.1b**). The S-C intersection fabric is characterized by a less oblate to prolate fabric and a lower anisotropy degree. This fabric becomes dominant away from the thrust plane, revealing a lower degree of shear strain with dominant LPS or local contraction within a convergent margin shear zone.

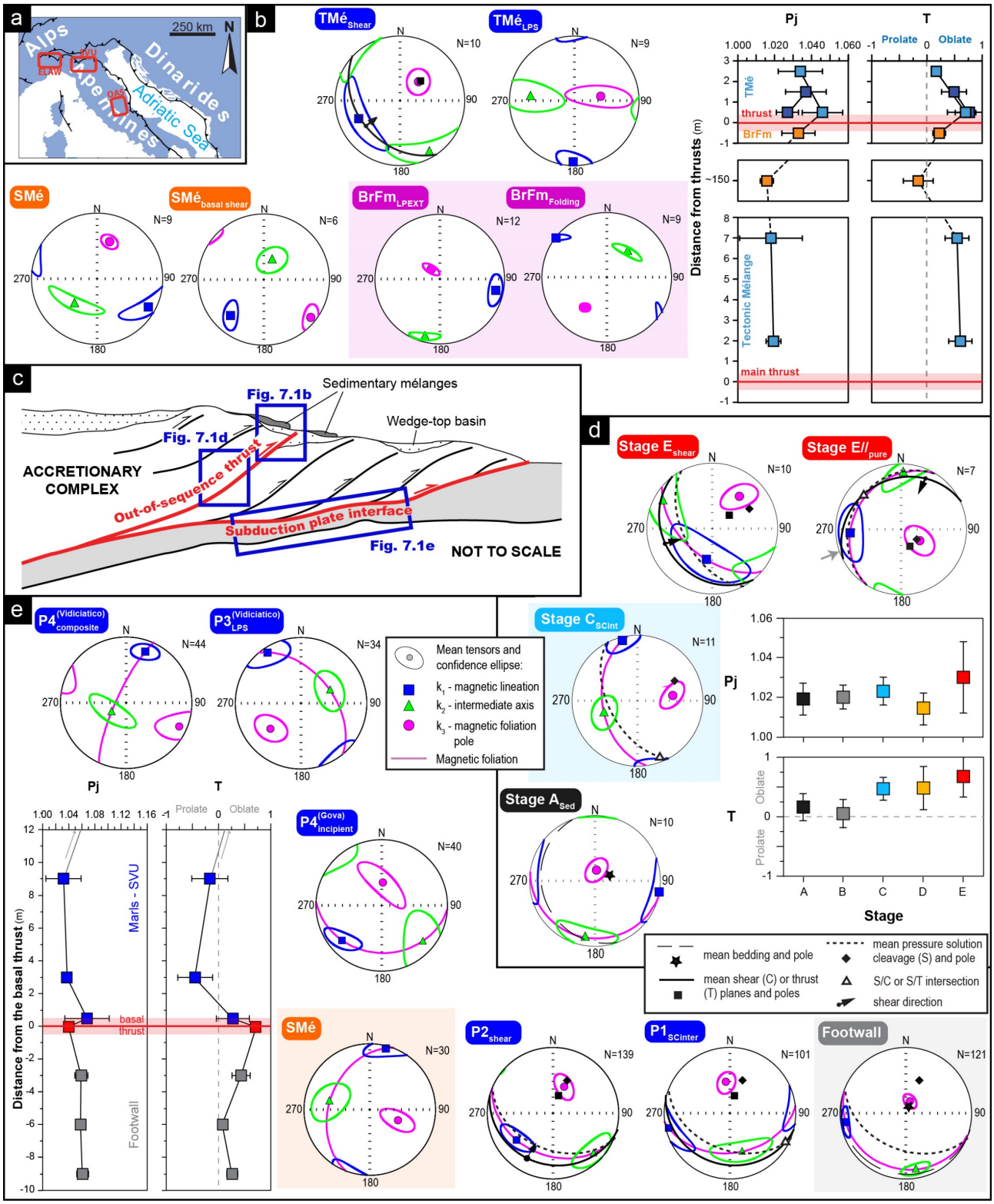

Figure 7.1. (**a**) Location of the case studies in the Northern Apennines, Italy. Summary of the main AMS findings and scalar parameters (Pj and T) variations with distance from the main thrust planes for each case study: (**b**) the ELAW (Chapter 6), (**d**) the OAS (Chapter 4), and (**e**) the SVU (Chapter 5). (**c**) Structural position of the studied convergent margin shear zones within an accretionary complex (modified from Robustelli Test et al., 2019).

In addition, composite/transitional fabrics and fabrics related to early deformation stages are locally preserved within intraplate shear zones and become significant at a greater distance from the thrust planes. The presence of subfabrics related to less intense non-coaxial deformation is also associated with a gradual

decrease in anisotropy degree and ellipsoid oblateness (**Figure 7.1**). The distance at which those fabric becomes significant is highly variable and depends on several factors such as structural position, lithology and pervasivity of tectonic structures.

Therefore, the presence of competing fabrics highlights heterogeneities in strain distribution within a convergent margin shear zone and could explain the high variability of magnetic fabrics, spanning from isotropic to directly related to the shearing or previous deformational fabrics, observed in modern convergent margin investigated during IODP and ODP Expeditions (**Figure 7.2**, **Figure *7.3***, **Figure *7.4***, and **Figure *7.5***).

The most recurrent fabric observed within and close to shear zones in modern context is equivalent to the S-C intersection fabric observed in the studied exhumed analogues, showing a slightly inclined magnetic foliation and a magnetic lineation dominantly clustered orthogonal to the shear direction (e.g., deformed zones Site 1178 and above the décollement Site 808 **Figure 7.2c**; Sites C0006 and C0007 **Figure 7.3**; Fault zone **Figure 7.4c**). Across the Ashizuri transect at Site 583 (**Figure 7.2d**), close to the frontal thrust, the k_1 clustering has been interpretated as indicator of paleocurrent direction (Taira & Niitsuma, 1986), but alternatively may represent evidence of incipient stages of LPS and possible initial shearing at the front of the accretionary prism, as supported by the prolate shape of the magnetic ellipsoid. The distribution of the S-C intersection fabric across thrust faults is highly variable. At the Kumano transect this fabric is largely distributed in accreted and basin sediments affected by a series of minor thrust faults (Sites C0001 Unit II, and C0006 and C0007 Unit III in **Figure 7.3**; Louis et al., 2012). At the Muroto transect at Site 1178, a S-C intersection fabric related to diffuse shear/faulting was detected within the accretionary prism in a ~100m thick deformed zone (Ujiee et al., 2005). In contrast, at the accretionary wedge of the Hikurangi margin an "S-C intersection-like" fabric, with magnetic foliation oblique to the bedding and k_1 orthogonal to the SW relative motion of the Pacific Plate east of New Zealand (Greve et al., 2020), is confined only to the Lower hangingwall and presumably to the lower subsidiary fault zone (**Figure 7.4a, c**).

Overall, a shear parallel magnetic lineation fabric is mostly not observed or not interpreted in actual convergent margins. The only case study in which this fabric is associated with shearing due to the underthrusting process is the Costa Rica subduction margin along the Middle Americas Trench. Here, at Site 1043, the occurrence of a magnetic lineation parallel to the convergence vector suggests localized deformation within the décollement zone and in the upper few meters of the underthrust hemipelagic sediment (**Figure 7.5b**; Housen & Kanamatsu, 2003). This difference suggest that the Costa Rica subduction margin has accommodated more ductile deformation than the Nankai and Japan plate boundary shear zone (Ujiie et al., 2003). In fact, the Costa Rica margin is also the only case where the degree of anisotropy and the shape parameter increase within the shear zone (Ujiie et al., 2003), displaying the same trend observed in the exhumed case studies (**Figure 7.1b, d-e**). In the others convergent margins, Pj increases only slightly approaching the major and minor thrust faults (Sites C0004, C0006 and C0007 **Figure 7.3**; **Figure 7.2b, c**; **Figure 7.4c**) In contrast, the shape parameter tends to became more prolate but never turn back to the oblate shape.

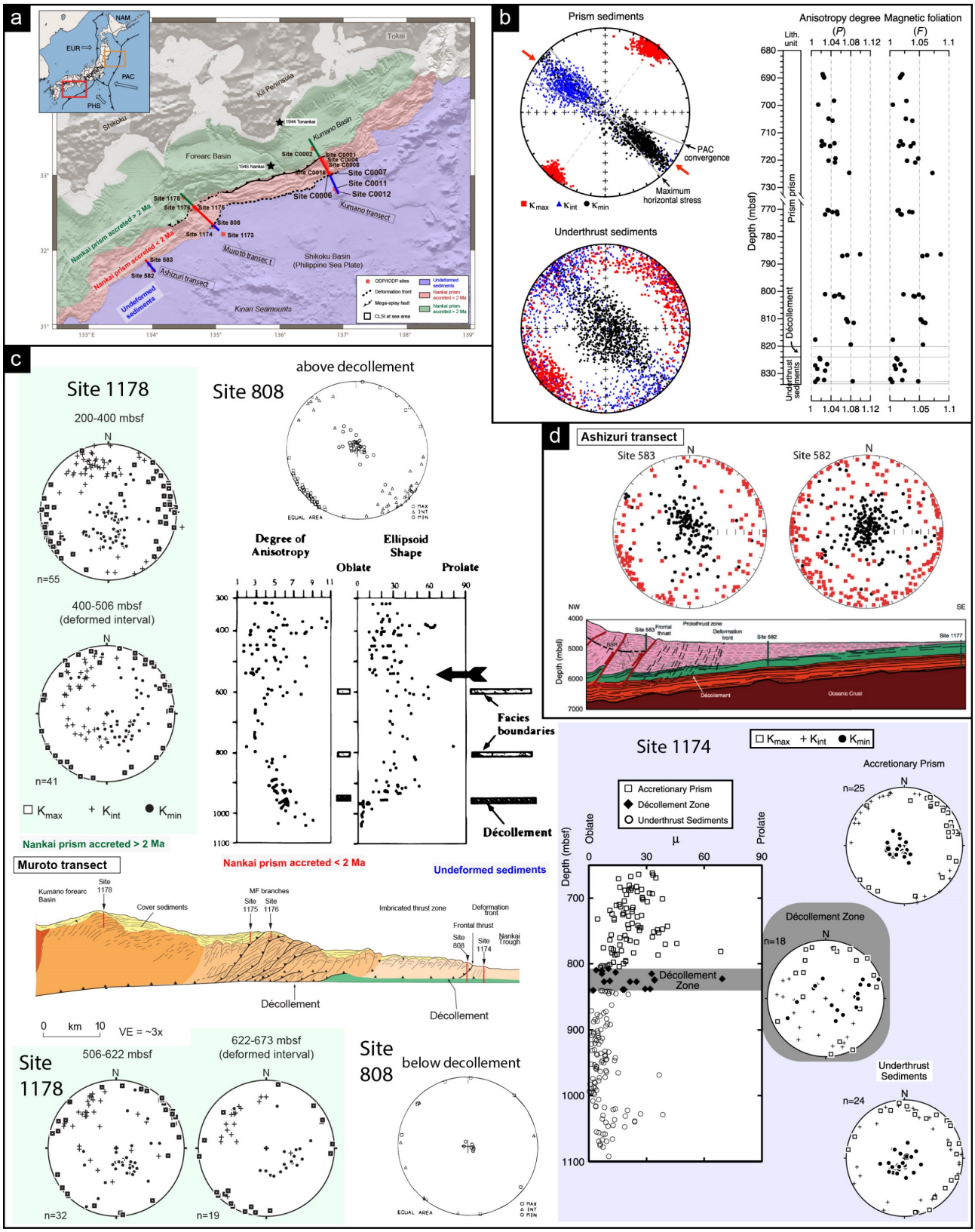

Figure 7.2. (**a**) Simplified map (at the top left) showing the location of the Japan Trench (orange square) and Nankai Trough (red square) with details of relative position of Sites drilled by IODP and ODP Expeditions across the Nankai Trough (modified from Cerchiari et al., 2018). (**b**) Magnetic fabric at the Japan Trench with down-core anisotropy degree (P) and magnetic foliation (F) (Yang et al., 2013; 2020). Main AMS results across (**c**) the Muroto transect (Byrne et al., 1993; Owens, 1993; Ujiie et al., 2003, 2005) and (**d**) the Ashizuri transect (Taira & Niitsuma, 1986; Parés, 2015) with relative cross sections reporting the structural position of the drilling Sites.

For example, at Site 808 the magnetic fabric tends to be more prolate with depth, where changes in shape parameter were associated to more penetrative strain than in the upper portion of the sediments that were relatively fissile (Byrne et al., 1993). However, a closer look might reveal a progressive increase in oblateness in the few tens of meters above the décollement (Site 808 **Figure 7.2c**), as observed in the exhumed analogues (**Figure 7.1b, d-e**). At site 1174, the overall fabric within the décollement zone is more prolate than in the other portions of the accretionary prism. Nevertheless, the magnetic fabric becomes progressively more oblate at the lower part of the accretionary wedge approaching the décollement zone and also at the upper and lower limits of the shear. These observations might support possible changes in ellipsoid shape due to the occurrence of composite fabrics related to the partial preservation of the previous sedimentary and/or deformation fabrics, with strain localization and consequent oblate fabric only close to the main fault planes separating the different tectonic domains. In addition, the absence or insufficient evidence of localized deformation can be related to the different sampling resolution in respect, which is significantly limited in the punctual observations obtained during scientific ocean drilling and does not allow the detection of subtle variation in the strain regime as in exhumed analogues.

The comparison between the magnetic fabric observed in the décollement zones of the Hikurangi margin and the Nankai accretionary prism with the specific fabric variations occurring in the studied exhumed analogues (this thesis) can help to discern the local presence of shear fabric even when the limited number of samples or the composite nature of the fabric did not allow the authors to draw significant conclusions. In fact, at the Hikurangi margin, the fabric observed close to the main brittle fault shows a magnetic lineation variable oriented from NE-SW to NW-SE displaying a double tendency to be parallel and orthogonal to the oblique motion of the Pacific Plate (**Figure 7.4c**). Thus, this fabric can also be interpreted in terms of a dominant shearing close to the main thrust faults, with fewer samples showing low non-coaxial strain reworking (i.e., S-C intersection fabric). In addition, this interpretation may strengthen the possible explanation of the fabric obtained in the lower subsidiary fault zone as S-C intersection fabric, despite the limited number of samples that does not allow to the authors to infer conclusions for this interval. In the Nankai Through offshore Muroto, the magnetic fabric found within the damage zone of Site 1174 has been related to a random orientation of particles due to the absence of transmitted shear within the brecciated fragments (**Figure 7.2c**; Ujiie et al., 2003). Alternatively, based on the observation across exhumed analogues, this fabric can be interpreted as a composite fabric. Indeed, the magnetic lineation shows a double tendency to be parallel or orthogonal to the shortening direction, which might reveal the superposition of preserved LPS fabric with shear related fabric. Similar considerations can be made for the deformed intervals at Site 1178, where the presence of few samples with sub-horizontal k_3 axes (**Figure 7.2e**) might reveal the preservation of previous stages of deformation, as occurs in the case of exhumed analogues within tectonic slices (e.g., $P3_{LPS}$ and $P4_{composite}$ in **Figure 7.1e**) or at greater distance from the basal décollement (e.g., $TMé_{LPS}$ in **Figure 7.1b**). Local preservation of the LPS is also observed across the Kumano transect in Units affected by the occurrence of megathrust faults or splay thrusts, where few samples show transitional fabric with k_3 rotating toward the shortening direction (Unit IV Site C0002, Site C0004, Unit III of Sites C0006 and C0007, and

Site 808 in **Figure 7.3**; Owens, 1993; Louis et al., 2012). The occurrence of composite and transitional fabrics is also coupled with decreased oblateness of the magnetic ellipsoids, supporting the interpretation of lower degree of non-coaxial strain and preservation of previous or different deformation stages in both exhumed and actual contexts.

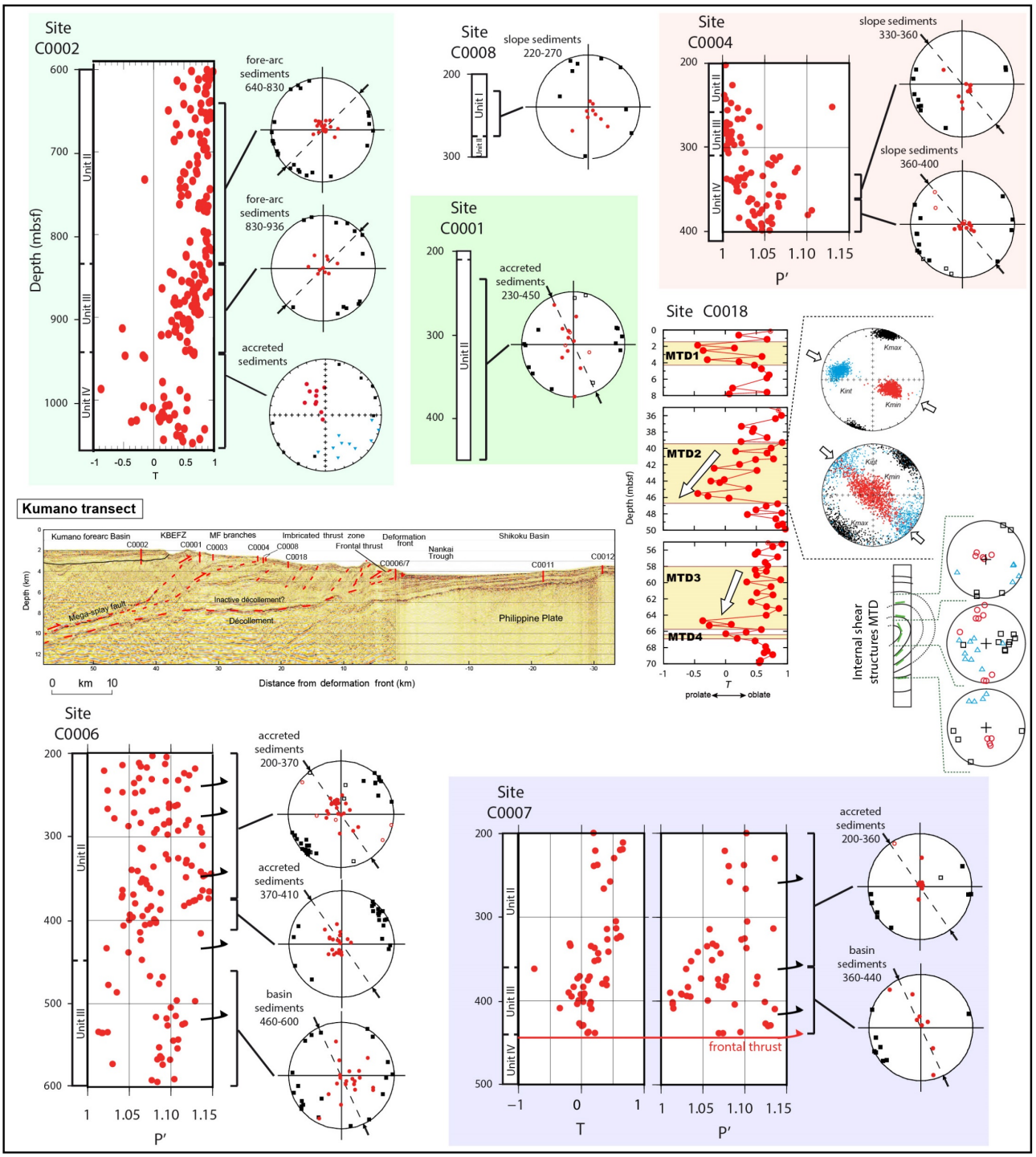

Figure 7.3. AMS results from IODP and ODP Expeditions across the Kumano transect, Nankai Trough (Louis et al., 2012; Kanamatsu et al., 2012, 2014; Kitamura et al., 2015). The transect location is shown in **Figure 7.2a.**

Transitional fabric is also observed in the prism sediments of the Japan trench and in the hangingwall of the Hikurangi margin and Nankai Trough (**Figure 7.2b-c**; **Figure 7.4a**). For example, at Site 1178, outside the

deformed zones, the magnetic fabric reflects the modification of the initial sedimentary fabric due to LPS (Ujiee et al., 2005 - **Figure 7.2c**). In contrast, in exhumed analogues, away from the thrust faults, the effect of LPS is not always preserved or recorded. In fact, if the initial fabric is significantly anisotropic, the superposition of subsequent deformation events may not necessarily modify the magnetic fabric. This is the case of broken formations observed at the ELAW (BrFm in **Figure 7.1b**), which reveals fabrics consistent with pre-faulting deformation, as the layer parallel extension occurred at the toe of the accretionary wedge, but no LPS. Another example is the sedimentary mélanges subsequently involved in the SVU shear zones, where a strong control of the initial bedding parallel foliation always emerges (**Figure 7.1e**). In the exhumed case studies, the sedimentary mélanges show magnetic lineation orthogonal to the transport or shear direction (SMé in **Figure 7.1b, e**), suggesting absent or only partial tectonic reworking. Results in the exhumed analogues are consistent with the magnetic fabric observed in the MTDs occurring at the top of the Nankai accretionary prism along the Kumano transect (Site C0018 **Figure 7.3**). In both cases the magnetic fabric becomes more prolate at the base of the MTDs.

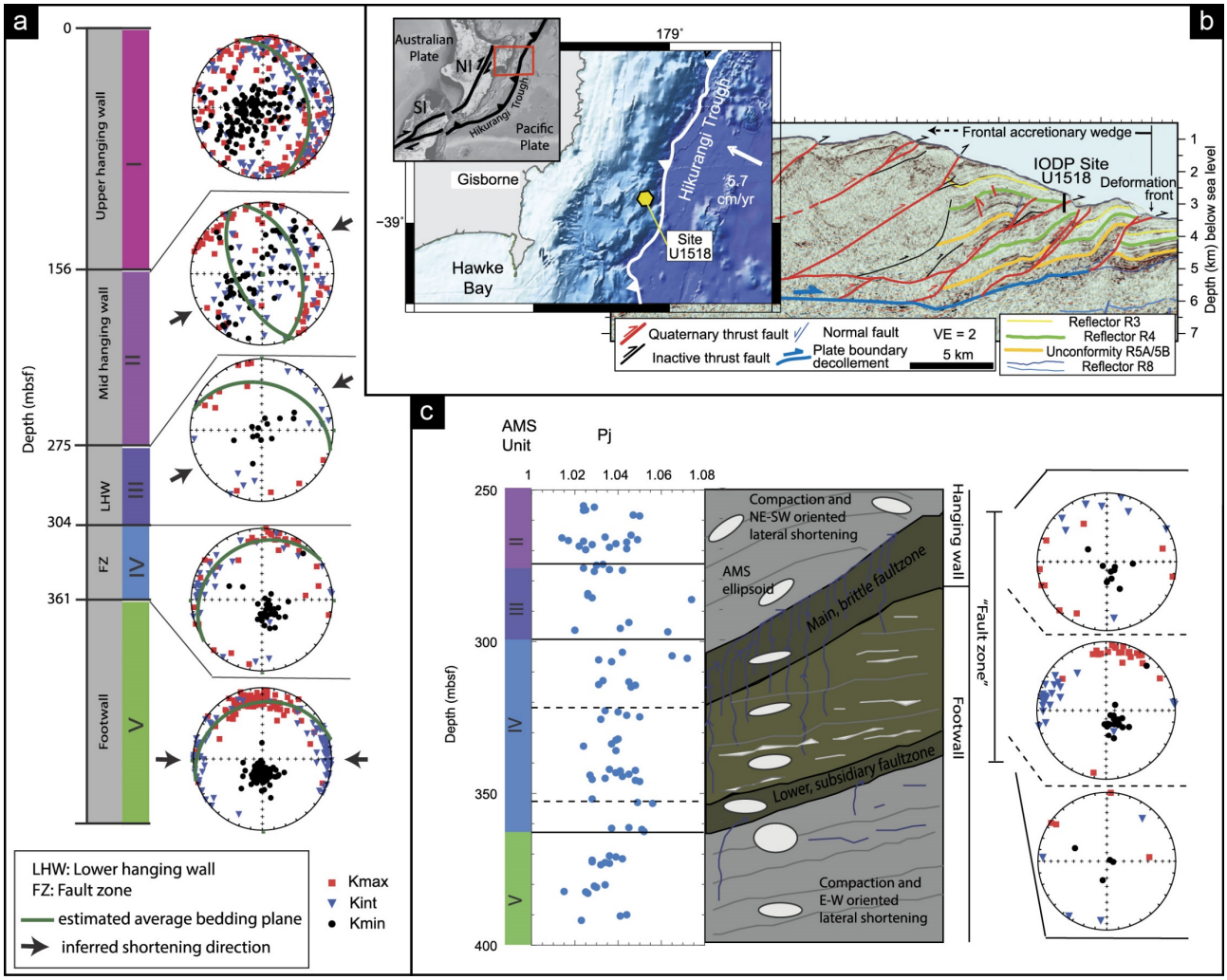

Figure 7.4. (**a**) Main magnetic fabric results observed across the frontal accretionary wedge of the Hikurangi subduction margin. (**b**) Location of the New Zealand plate boumdaty zone and position of Site U1518 within the frontal accretionary wedge. (**c**) Down-hole variations in anisotropy degree and magnetic fabric across the Pāpaku fault zone (Greve et al., 2020).

In addition, there is a second magnetic fabric in common, characterized by sub-horizontal k_3 and k_1 in the emplacement direction, which can be related to internal shear occurring during the emplacement of the MTDs (SMé$_{basal\ shear}$ in **Figure 7.1b** and Site C0018 **Figure 7.3**). Despite the occurrence of the same fabric and their association with shearing, their presence is located in different portions of the MTDs. At ELAW, the shear-related fabric is located at the base of the MTD, where the occurrence of a thin layer of sheared argillaceous breccia has been reported (Festa et al., 2015, 2016). In contrast, at Nankai, this fabric is located in the central portion of an MTD and related to shearing along internal folds while emplacing (Kanamatsu et al., 2014). This difference can indicate that may be located either at the base or within an MTD. Alternatively, the shear fabric of Site C0018 can be interpreted as a basal shear zone separating two overlaying MTDs.

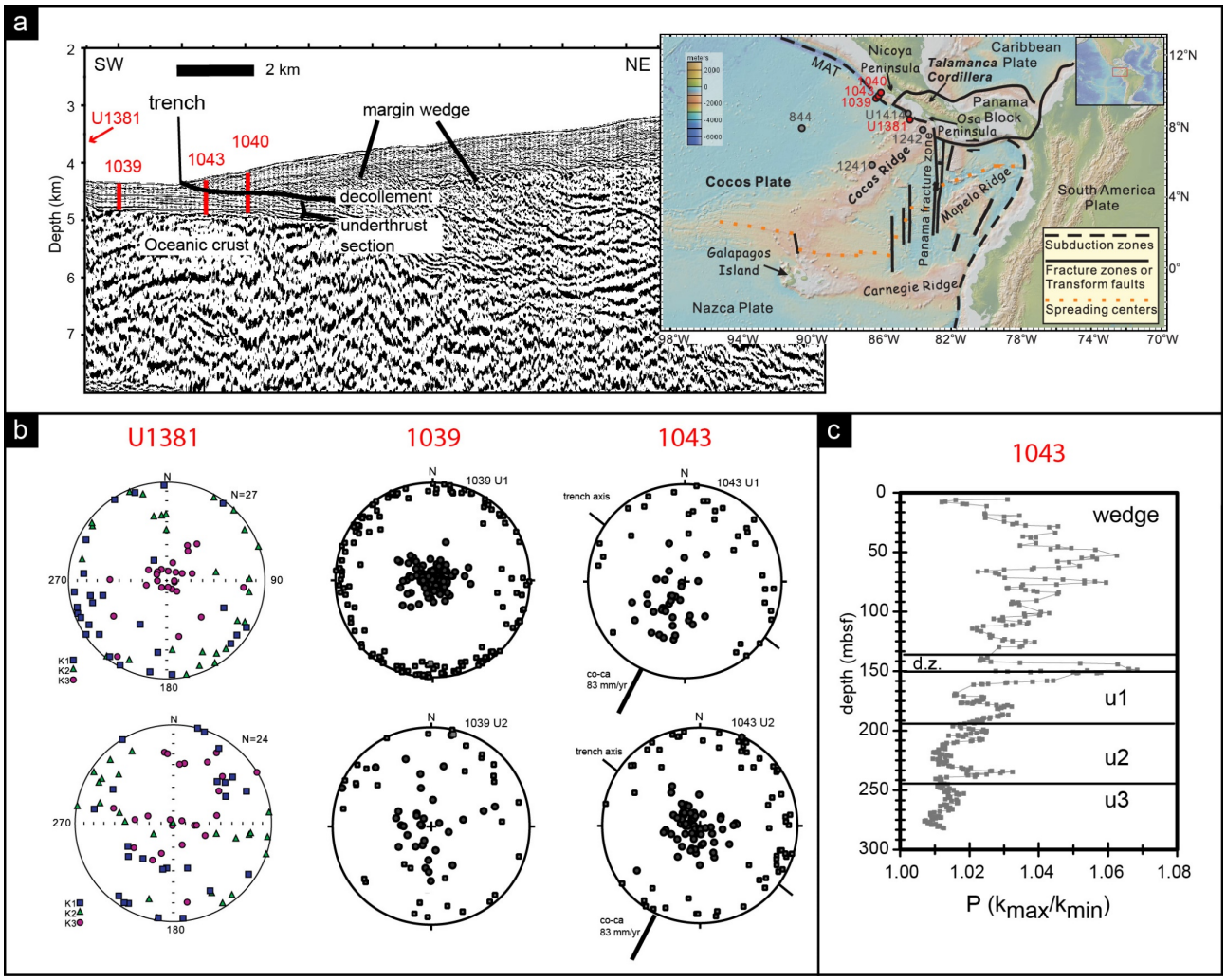

Figure 7.5. (**a**) Location of the IODP and ODP Sites along the Central America Trench and their positions across the Costa Rica subduction margin (Housen & Kanamatsu, 2003; Li et al., 2015). (**b**) Main AMS results in underthrust sediments at the front of the margin wedge (Housen & Kanamatsu, 2003; Li et al., 2015). (**c**) Down-core variation of anisotropy degree across the accretionry wedge, décollement zone (d.z.) and underthrust sediments at Site 1043 (Housen & Kanamatsu, 2003).

In the footwall of the studied exhumed convergent margin shear zones, the magnetic fabric shows subtle but significant variations among localities. The most common fabric reveals a sub-horizontal bedding parallel

magnetic foliation and a well-clustered magnetic lineation consistent with the B-S intersection (Stage A_{sed} **Figure 7.1d**; Footwall **Figure 7.1e**). This fabric is mostly associated to vertical loading/compaction with a minor component of LPS and is commonly observed in the footwall of megathrust or basal décollement shear zones in actual convergent margins (Below the décollement at Site 1174 **Figure 7.2c**; Underthrust sediments **Figure 7.2b**; **Figure 7.4a**). The different degree of k_1 clustering is associated with the intensity of the superposed LPS fabric. In fact, where sediments are completely undeformed and register only the vertical compaction prior to underthrusting, the k_1 axes are interspersed within the foliation plane (Site 808 **Figure 7.2c**; Site U1381 and 1039 **Figure 7.5b**). The gravitational loading dominated magnetic fabric can also be preserved in the less deformed portion of the shear zones, as occurs in the central portion of the Pāpaku fault zone (Hikurangi margin; **Figure 7.4c**; Greve et al., 2020). Overall, significant changes in the magnetic fabric below a thrust fault are associated with lower Pj and a reduced ellipsoid oblateness, suggesting the occurrence of weak décollement and strain decoupling (Housen et al., 1996; Yang et al., 2013; Greve et al., 2020).

The strong heterogeneities of the magnetic fabric occurring at convergent margin shear zones in both modern and exhumed contexts reflect the heterogeneous distribution of the strain, the progressive evolution of faulting processes, and the intensity of previous pre-shearing fabrics.

To better constrain these heterogeneities, a comparison with AMS results of laboratory experiments is needed. Laboratory models (Schöfisch et al., 2021, 2022) reveal the frequent presence of LPS fabrics associated with kinking and folding processes occurring away from the thrust surfaces and in thrust-affected areas under low-friction rate along the basal décollement (.**Figure 7.6a, c**). This context appears to produce mostly composite and transitional fabrics, typical of LPS superposed on the initial bedding-parallel magnetic fabric (e.g., $P3_{LPS}$ and $P4_{composite}$ in **Figure 7.1e**; prism sediments **Figure 7.2b**; middle hangingwall **Figure 7.4a**) without any significant evidence of non-coaxial strain and shearing. This model represents a less evolved stage than the studied exhumed analogues and most of the megathrust shear zones investigated by the IODP and ODP expeditions in actual convergent margins. In fact, laboratory models reveal a progressive decrease in both Pj and T in the magnetic fabric associated with the thrusting stage, while in the case studies in nature the AMS scalar parameters tend to increase. The S-C intersection and the shear-related fabrics occur only in the case of high-friction rate models and along thrust planes, supporting the interpretation of these fabrics in exhumed analogues as a consequence of localized deformation along the main thrust planes.

Therefore, results reported in this thesis correspond to precious evidence of localized deformation that are difficult to observe both in nature and in the laboratory, since they appear to be strictly related to the entity of basal-friction rate and the non-coaxial strain degree. Then, to define the presence of shear-related fabric and better understand the strain distribution along convergent margin shear zones, it is recommended to sample at high-resolution with increasing distance from the thrust plane, promoting the discrimination between localized and distributed deformation. In addition, the study of exhumed analogues provides an opportunity for 3D observation of the structures, allowing direct correlation between magnetic fabric and structural

elements, for example, using ternary diagrams, leading to a semi-quantitative interrelation with the prevailing deformation processes.

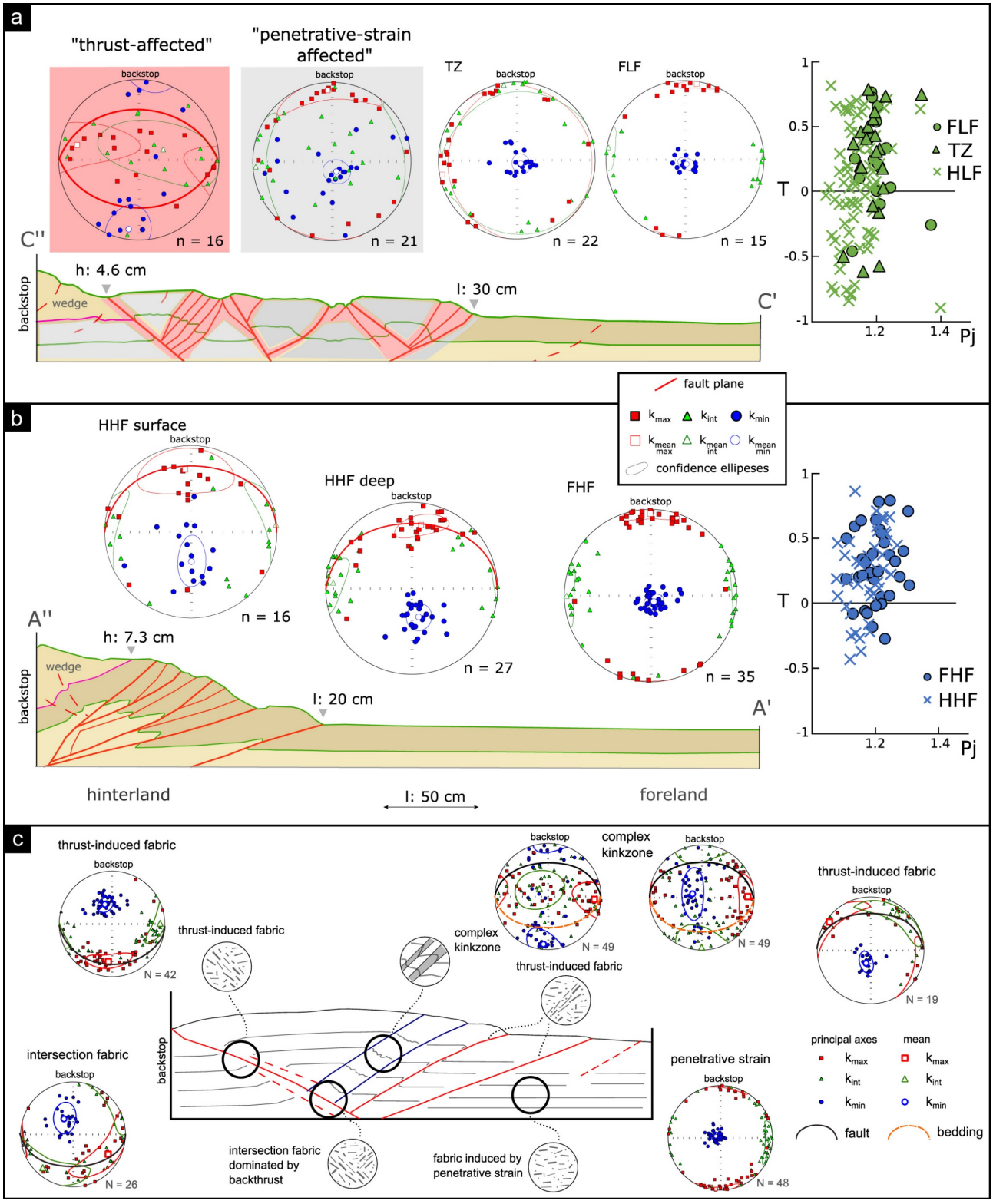

Figure 7.6. Distribution of magnetic fabric along different portions of an analogue model of fold-and-thrust belt above a (**a**) low-friction and (**b**) high-friction décollement (Schöfisch et al., 2021). The shortening direction is N-S oriented. Variation of Pj and T among fabrics are also reported. (**c**) Grain alignment and magnetic fabric in different areas of a thrust imbricate analogue model (Schöfisch et al., 2022).

7.2 Lithological control on magnetic fabric record of strain & outlook

Another important aspect dealt in this thesis is the extensive separation of subpopulation of magnetic grains and their correlation with the different processes/stages of the evolution of convergent margin shear zones. Despite the occurrence of similar AMS fabrics, significant differences were observed in the contribution of para- and ferro-magnetic subfabrics in the three study areas, suggesting the possible role of lithological variation in recording faulting processes. As mentioned previously, the occurrence of shear-related and S-C intersection fabric is not commonly observed in both modern and exhumed convergent margins. Therefore, the following discussion will focus on the nature of these fabrics in different sedimentary units involved in the studied convergent margin shear zones and the relative influence of para- and ferro-magnetic subfabrics.

Depending on the lithology, ferro- and para-magnetic grains show different sensitivity to respond to deformation. In general, in the studied lithologies (i.e., limestones, mudstones and claystone/shales), the paramagnetic subfabric is almost always coaxial with the AMS for both shear and S-C intersection fabrics (**Figure 7.7a**). To a first approximation, we can assume that the AMS provides a good proxy for the orientation of paramagnetic clay minerals in the studied samples, where the different magnetic fabric is mostly related to the intensity of deformation. However, even if bulk susceptibility shows values consistent with paramagnetic-dominated rocks, clay minerals do not necessarily represent the carriers of the AMS (Biedermann & Bilardello, 2021). It should be noted that this coherence may also reveal a similar reorientation of para- and ferro-magnetic subpopulations under non-coaxial strain, where subtle variations may indicate a different alignment between the para/diamagnetic matrix and ferromagnetic grains. In fact, carbonate-rich sediments (OAS fabrics in **Figure 7.7a**) reveal a slight variation in the orientation of the principal magnetic susceptibility axes between AMS and HF-AMS_{para}, suggesting that in these lithologies the paramagnetic subfabric and the AMS record similar processes, but that a contribution from the ferromagnetic subfabrics should be considered in the interpretation of the AMS. At the OAS, the paramagnetic subfabric is less aligned with the mesoscale structures than the AMS (see, Ternary diagrams in **Figure 4.13c**). In contrast, in clay-rich units the geometric relationships of AMS and paramagnetic fabric with structural elements are significantly similar (see also **Figure 5.25c** and **Figure 6.14c**). Thus, carbonate-rich, and clay-rich units differ slightly in the degree of alignment of the clay minerals with respect to non-coaxial strain, suggesting lithological control in the reorientation of the paramagnetic minerals.

In addition, most of the differences relate to the orientation of ferromagnetic subfabrics with respect to AMS and strain acting during the thrusting and faulting processes. In carbonate-rich rocks, ferromagnetic subfabrics show a slight spreading of intermediate and maximum axes in the foliation plane, but still consistent with the orientation of the AMS. A similar consideration can be made for the Tectonic mélanges observed at ELAW, which are clay-rich units. In the latter case, the ferromagnetic subfabrics are very well-grouped (ELAW fabrics in **Figure 7.7a**), suggesting a more efficient reorientation process that resulted in mostly coaxial para- (HF-AMS_{para}) and ferromagnetic minerals (both remanence-bearing and HF-AMS_{ferro}). In contrast, the clay-rich sediments of the SVU intraplate shear zone show an independent orientation of the

ferromagnetic subfabrics from AMS and paramagnetic matrix (SVU fabrics in **Figure 7.7a**), indicating the registration of different deformation stages or a different degree of alignment to the main mesoscopic structures. In fact, at the SVU, the shear-related fabric ($P2_{shear}$ in **Figure 7.7a**) shows interchanged maximum and intermediate axis between ferromagnetic subfabrics and both AMS and paramagnetic subfabric. Therefore, in the marly units involved in the SVU, the ferromagnetic subfabric might reveal previous or less deformed stages such as the S-C intersection fabric, while paramagnetic minerals show a more rapid reorientation consistent with shear localization.

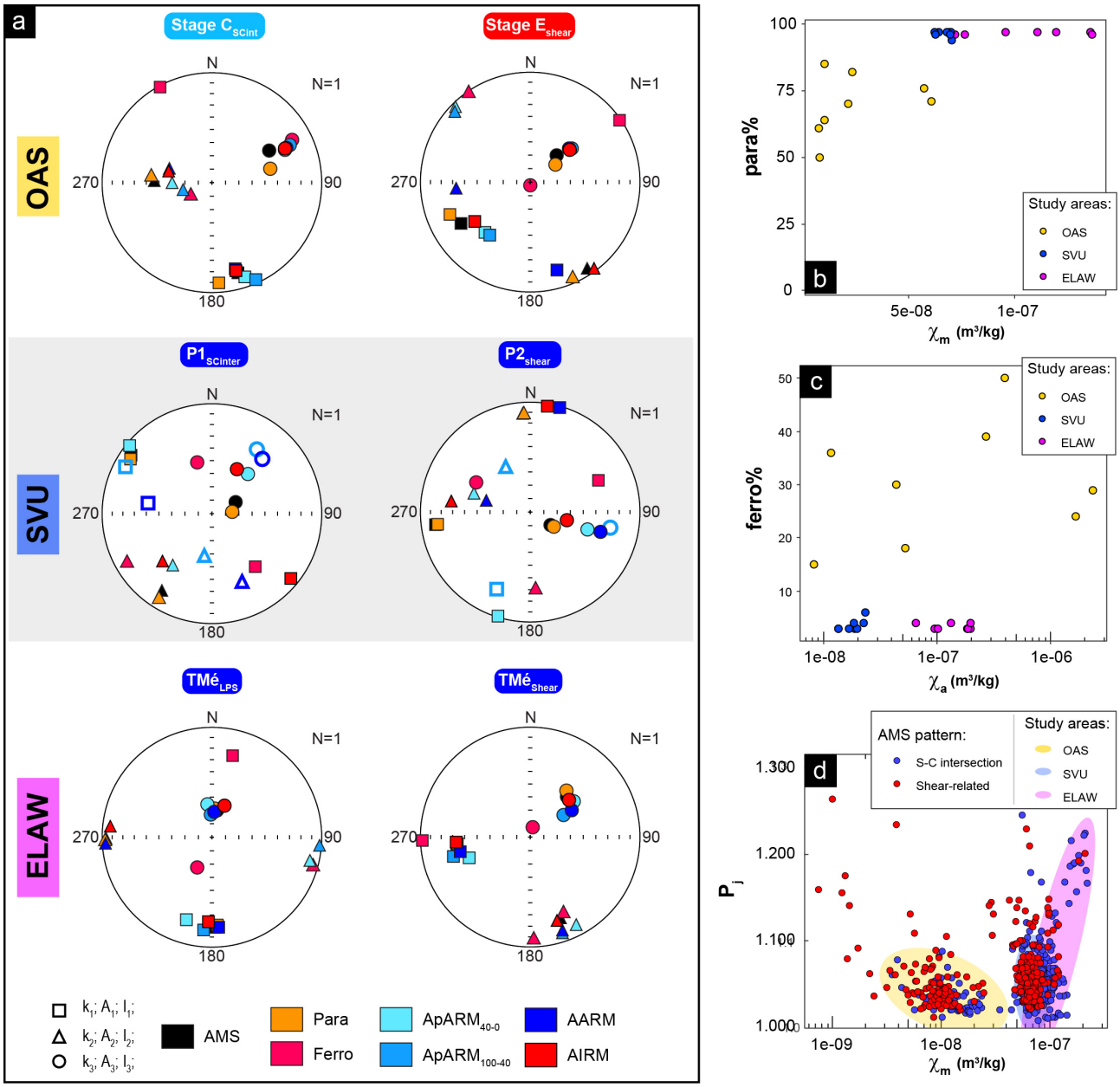

Figure 7.7. (**a**) Stereoplots (Lower hemisphere equal-area projections) of the principal directions of the LF-AMS, ARM experiments and the paramagnetic and ferromagnetic components of the high-field AMS for representative samples showing S-C intersection and shear-related fabric in the three different study areas. (**b**) Paramagnetic contribution (%) as a function of χ_m. (**c**) Percentage of ferromagnetic contribution versus susceptibility of ARM (χ_a). (**d**) Pj versus χ_m for samples displaying S-C intersection and shear-related fabrics. Data are clustered according to study areas.

Then, variations in ferromagnetic contents and different grain-sizes of the ferromagnetic minerals need to be investigated to unravel the processes that condition the ability of ferromagnetic minerals to record different deformation stages. Overall, the studied lithologies show a dominant paramagnetic component, about 97% in clay-rich sediments (SVU and ELAW in **Figure 7.7b**) and 70% in carbonate-rich units (OAS in **Figure 7.7b**). In carbonate-rich sediments, the contribution of ferromagnetic fraction to the total High-field AMS is significantly higher, on average around 30% (**Figure 7.7c**).

Variations in the ferromagnetic contribution are related here with different χ_m (**Figure 7.7b**), suggesting a strong control by the matrix over the bulk susceptibility and the percentage of ferromagnetic component to the total AMS. Indeed, the highest contribution of the ferromagnetic subfabric is observed in carbonate-rich sediments, where the lower χ_m values can be ascribed to a higher content in diamagnetic minerals (e.g., calcite) in the matrix. In contrast, in clay-rich units, the contribution of the ferromagnetic minerals is significantly low, regardless the different χ_m between lithologies (ELAW and SVU in **Figure 7.7b**). The inverse relationship between carbonate content and the higher contribution of the ferromagnetic fraction is also supported by the similar content in ferromagnetic minerals in the different clay- and carbonate-rich units (**Figure 7.7c**). Actually, the ferromagnetic percentage does not show a direct correlation with the χ_a nor with the different orientation of ferromagnetic minerals with respect to strain. The relative changes in χ_m and χ_a appear to be related to the different composition of the matrix (**Figure 7.8a**), where low χ_m values are strictly related to higher carbonate content. Furthermore, the different contribution and concentration of ferromagnetic grains in the same lithologies does not influence the occurrence of a magnetic lineation parallel or orthogonal to the shear direction. In fact, the occurrence of the two main patterns does not reveal a correlation with different χ_m (**Figure 7.7d**), supporting our interpretation in terms of higher deformation degree rather than different content in ferromagnetic minerals, opposed to what has been observed in other shear zones (e.g., Roman-Berdiel et al., 2019). Here, there is a correlation between lithology and the different anisotropy degree. In carbonate-rich sediments, the anisotropy degree is generally higher in the shear-related fabric, suggesting a stronger alignment of minerals than in the S-C intersection fabric (OAS in **Figure 7.7d**). In contrast, similar Pj was observed for both low and high non-coaxial strain patterns in clay-rich units (ELAW and SVU in **Figure 7.7d**). Therefore, no significant variations in ferromagnetic content are observed to explain the variable response of ferromagnetic minerals in the different studied lithologies. Another aspect that may influence the different subfabric orientations is the variation in ferromagnetic minerals assemblages and their relative grain-size. However, the studied lithologies show the presence of similar subpopulations of ferromagnetic grains. In fact, all the different units reveal similar M_{rs}/M_s and B_c values (**Figure 7.8b**) in the range of dominant low-coercivity minerals (e.g., magnetite). Only carbonate-rich sediments show a slightly higher content in high-coercivity minerals (**Figure 7.8c**), but not at levels sufficient to significantly induce different orientation of the ferromagnetic subfabrics.

These observations show a close relationship between lithologies and ferromagnetic subfabrics. However, considering the homogeneities in the subpopulation of ferromagnetic grains, their different response to deformation appears to be strongly governed by the rheological behaviour of the matrix.

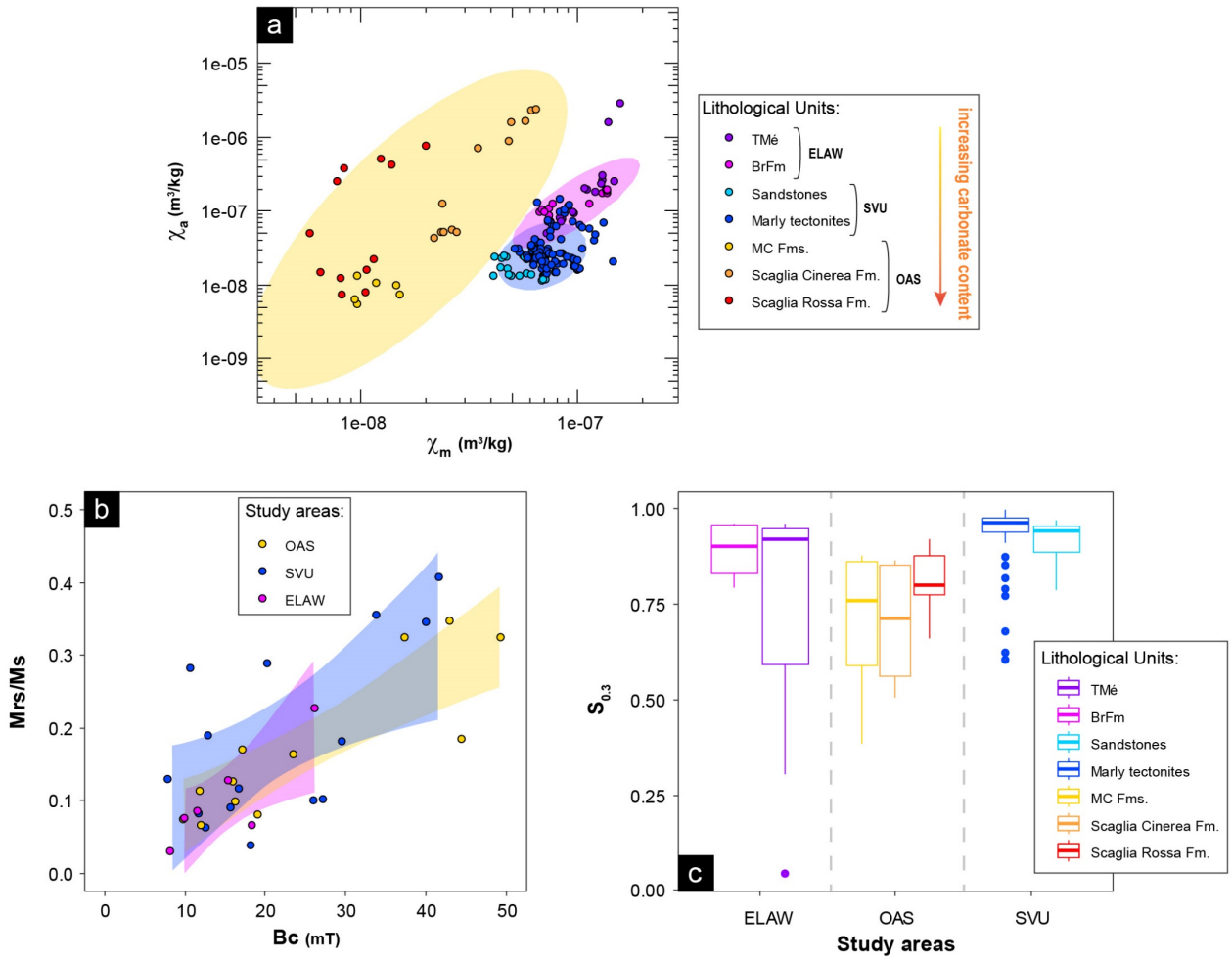

Figure 7.8. (**a**) Biplot of χ_a versus χ_m for different lithological units. Data are clustered according to study areas. (**b**) Squarness versus B_c plot (Tauxe et al., 2002) with areas of relative distribution for the different case studies. (**c**) Box-and-whisker plots of the $S_{0.3}$ ratio (Thompson & Oldfield, 1986) grouped for different lithological units.

Then, the variation in ferromagnetic subfabric orientation may be associated with the different deformation mechanism occurring in clay-rich and carbonate-rich sediments.

Carbonate-rich sediments undergo pressure-solution (e.g., stylolitization) (Leoni et al., 2007; Leah et al., 2020), which is a process of favourable alignment of both para- and ferro-magnetic minerals with respect to the strain axes (Borradaile & Jackson, 2010). Phyllosilicates and magnetite tend to concentrate in the dissolution zones, rotating accordingly to the deformation of adjacent calcite grains. In this way, the matrix behaviour strongly conditions the magnetic subfabrics (Borradaile & Tarling, 1981; Evans et al., 2003). In addition, new ferromagnetic minerals may grow in the tectonic solution structures, mimicking the progressive evolution of the strain. The latter process may explain the slightly minor alignment of paramagnetic minerals to the stylolite cleavage compared to the AMS. Moreover, ferromagnetic grains of different grain-size may have a different degree of freedom to rotate within the dissolution sites, justifying the slight spreading of different ferromagnetic subfabrics around the AMS and strain axes (**Figure 7.7a**). Thus, the orientation of para and ferro-magnetic minerals in carbonate-rich sediments is strongly influenced by matrix behaviour, with progressive registration of the strain depending on the extent of the dissolution

process and partial preservation of previous fabrics. This observation may also associate the different anisotropy degree observed in the shear-related fabric (**Figure 7.7d**), with a greater alignment of both para- and ferro-magnetic grains due to increased non-coaxial strain.

In contrast, clay-rich sediments deform by cataclasis, progressive rotation, micro-folding, intergranular slip and intragranular kinking of phyllosilicates (Mattei et al., 1995, 1997; Parés et al, 1999; Cifelli et al., 2004, 2005). The different orientation of para- and ferro-magnetic minerals must be related to the preferred orientation obtained by rotation of clastic grains, with some grains moving more efficiently than their neighbours, which depends strongly on the degree of deformation (Borradaile, 1988). The occurrence of these processes may explain the coaxiality between AMS and paramagnetic subfabrics in clay-rich lithological units. While the strong difference in orientation of ferromagnetic subfabrics between ELAW and SVU (**Figure 7.7a**), despite similar clay content, must be associated with other conditions that can influence the degree of reorientation of the ferromagnetic minerals. A possible explanation is the different lithification state prior to the deformation, which may significantly affect the deformation mechanisms. In fact, sediments in the SVU were mostly unlithified when thrusting occurred (Remitti et al., 2012). Under these conditions, deformation within the fault zone is accommodated by soft sediment particulate flow involving grain boundary sliding (Borradaile, 1981; Mittempergher et al., 2018). In contrast, the chaotic rock units (i.e., mélanges) involved in the ELAW have been previously deformed, which implies the formation of pre-thrusting fabrics (e.g., broken formation fabrics) associated with pore volume reduction and progressive lithification during deformation at the toe of the accretionary wedge before the transposition under thrusting-related tectonic shearing (Codegone et al., 2012; Festa et al., 2013). Therefore, the different lithification rate of sediments prior to involvement in a convergent margin shear zone is the most plausible mechanism that conditions the degree of freedom of ferromagnetic minerals to reorient within a clay-rich matrix during shearing.

These final considerations highlight the lithological control over heterogeneities in strain registration by the magnetic fabric. The rheological control of the matrix on the reorientation of the ferromagnetic minerals remains to be verified using multidisciplinary approaches that combine other physical properties such as porosity and shear strength prior and during deformation. The application of X-ray diffraction and geochemistry better characterization of the geochemical composition of the matrix and strengthen the links between lithology and strain records. Additional textural and morphological analysis at the microscale may also be useful in modelling the correlation with strain in the magnetic sub-fabrics related to the shear (both S-C intersection fabric and shear-related fabric) occurring in convergent margin shear zones. Combing multidisciplinary approaches with the separation of para- and ferro-magnetic subfabrics expands the possibility of using rock magnetic properties, especially magnetic fabric studies, to discern the different rheological response of the sediments involved in convergent margin shear zones and to better unravel their heterogeneous and complex evolution.

APPENDIX

I. Rock magnetic parameters

This appendix contains the selection of anisotropy and mineralogical parameters used in this thesis and their reference sources.

Anisotropy parameters

Parameter	*Equation*	*Reference*
$\mathbf{k_m}$	$k_m = (k_1 + k_2 + k_3)/3$	Nagata, 1961
Pj	$\mathrm{Pj} = \exp\sqrt{2\sum_{i=1}^{3}(\ln k_i - \ln k_m)^2}$	Jelinek, 1981
k'	$\mathrm{k'} = \sqrt{[(k_1 - k_m)^2 + (k_2 - k_m)^2 + (k_3 - k_m)^2]/3}$	Jelinek, 1984
T	$\mathrm{T} = 2\ln(k_2/k_3)/\ln(k_1/k_3) - 1$	Jelinek, 1981
U	$\mathrm{U} = (2k_2 - k_1 - k_3)/(k_1 - k_3)$	Jelinek, 1981
L	$\mathrm{L} = k_1/k_2$	Balsley & Buddington, 1960
F	$\mathrm{F} = k_2/k_3$	Stacey et al., 1960

Magnetic mineralogy parameters

$\chi_{fd\%}$	$\chi_{\mathrm{fd\%}} = [(\chi_{\mathrm{lf}} - \chi_{\mathrm{hf}})/(\chi_{\mathrm{lf}})] * 100$	Dearing et al., 1996
$\mathbf{V_a}$	$V_{\mathrm{a}} = [(k_{450} - k_i)/(k_i)] * 100$ where $k_i = (k_2 + k_4 + k_6 + k_8)/4$	Hrouda et al., 2006
$\mathbf{S_{0.3}}$	$\mathrm{S}_{0.3} = -IRM_{-300mT}/SIRM$	Thompson & Oldfield, 1986
$\mathbf{S_{0.1}}$	$\mathrm{S}_{0.1} = -IRM_{-100mT}/SIRM$	Thompson & Oldfield, 1986
$\boldsymbol{\delta}$	$\delta = (\mathrm{SIRM}_{80K} - \mathrm{SIRM}_{150K})/(\mathrm{SIRM}_{80K})$	Moskowitz et al., 1993
$\mathbf{R_{LT}}$	$R_{LT} = FC\ SIRM_{20K}/(\mathrm{ZFC\ SIRM}_{20K})$	Smirnov, 2009
G%	$\mathrm{G\%} = [(\mathrm{RTSIRM}_{150K} - \mathrm{RTSIRM}_{300K})/(\mathrm{RTSIRM}_{150K})] * 100$	Aubourg et al., 2021
$\mathbf{A_{50}}$	$\mathrm{A}_{50} = \frac{\chi_{50cool} - \chi_{50heat}}{\chi_{50heat}} \times 100$	Hrouda, 2003
$\boldsymbol{\delta_{\chi curve}\%}$	$\delta_{\chi\mathrm{curve}}\% = \frac{\int_{T_0}^{T_{max}} \lvert\chi_{cool}(T) - \chi_{heat}(T)\rvert\, dT}{\int_{T_0}^{T_{max}} \chi_{heat}(T) dT} \times 100$	Yang et al., 2016

II. Supplementary figures & tables

This appendix is divided according to chapters and includes:

1. *AMS and ARM experiments data at site and pattern level, respectively;*
2. *Pj and T variation among AMS and ARM experiments;*
3. *Additional magnetic mineralogy data from the SVU.*

Chapter 4 – The OAS thrust

Table 4.S 1. Summary of the anisotropy of magnetic susceptibility data at site level. Columns: Locality; Site; Stage = degree of deformation from sedimentary fabric (A) to latest tectonic event (F), (*) inverse fabric and (//) tectonic fabric parallel to the transport direction; n/N = number of specimens accepted/number of specimens measured; χ_m = mean mass magnetic susceptibility ($10^{-9}m^3kg^{-1}$) and its standard deviation; Pj = corrected anisotropy degree; T = shape parameter; D = declination (°), I = inclination (°) and 95% confidence angle (°) of the principal magnetic susceptibility axes k_1 and k_3, respectively.

Locality	Site	Stage	n/N	χ_m (± σ) (x 10^{-9} m^3Kg^{-1})		Pj	st. dev.	T	st. dev.	k_1				k_2				k_3			
										D	I	95% conf. angles		D	I	95% conf. angles		D	I	95% conf. angles	
Sassotetto	**SSR1**		16/20	11.16	5.19	1.040	0.021	0.785	0.340	295	32	52.1	18.3	171	43	52.1	15.4	47	31	21.1	11.6
	SSR1-SF1	**E**	10/16	12.71	5.76	1.030	0.018	0.671	0.346	191	50	56.7	22.9	299	15	56.8	18.6	40	36	26.8	12.9
	SSR1-SF2	**C**	6/16	8.56	2.86	1.061	0.019	0.386	0.356	304	29	18.6	8.8	176	48	18.2	12.0	51	28	13.3	8.6
Monastero	**MSC1**		19/20	39.65	21.54	1.021	0.006	0.613	0.175	342	5	35.1	13.5	246	50	35.7	15.4	76	39	18.6	12.1
	MSC1-SF1	**C**	8/19	17.20	4.45	1.021	0.004	0.903	0.157	161	2.3	77.5	12.0	255	58	77.5	10.4	70	32	14.4	8.9
	MSC1-SF2	**C**	11/19	55.98	11.19	1.023	0.007	0.465	0.185	346	6	19.2	13.2	250	45	21.9	15.4	82	45	20.2	10.7
	MSC2		19/19	24.69	2.66	1.017	0.007	0.648	0.273	133	13	59.4	13.0	226	13	59.3	22.0	1	71	22.2	13.8
	MSC2-SF1	**A**	10/19	24.12	1.91	1.019	0.008	0.158	0.230	100	1	31.8	12.9	190	14	32.0	15.0	8	77	17.0	11.4
	MSC2-SF2	**B**	9/19	25.32	3.39	1.020	0.006	0.052	0.240	169	22	28.5	14.2	259	1	32.4	28.2	351	68	32.5	14.2
Infernaccio	**ISC1**		19/21	22.07	7.02	1.032	0.051	0.856	0.398	212	50	75.1	24.4	332	23	75.1	22.8	76	32	30.1	24.6
	ISC1-SF1	**D**	14/19	18.63	2.86	1.014	0.008	0.479	0.365	183	35	53.3	21.6	308	39	53.6	29.5	68	31	33.8	14.9
	ISC1-SF2	**E**	5/19	31.71	6.10	1.117	0.017	0.657	0.127	297	59	17.9	7.7	177	17	24.1	7.5	79	25	18.7	7.6
Monte Boragine	**BSR2**	**F***	10/15	-2.03	0.98	1.076	0.048	-0.351	0.230	319	59	68.7	18.1	81	18	68.7	28.2	180	25	31.9	16.0
	BSR1	**F***	10/19	-3.33	1.81	1.027	0.031	-0.656	0.247	169	80	70.0	31.0	279	4	70.0	39.6	9	10	43.3	23.9
	BMC1	**E$^{//}$**	8/12	2.52	1.94	1.055	0.050	0.147	0.364	250	46	59.9	27.9	110	36	61.8	46.5	4	21	52.9	20.8
	BMC2		13/16	9.83	6.33	1.032	0.013	0.593	0.272	243	13	43.6	17.3	339	26	43.7	25.3	128	61	25.7	17.3
	BMC2-SF1	**E or E$^{//}$**	6/13	6.44	2.28	1.027	0.015	0.175	0.286	35	6	37.0	23.4	301	32	36.4	25.2	134	57	31.3	14.7
	BMC2-SF2	**D$^{//}$**	7/13	12.74	7.37	1.040	0.011	0.410	0.260	266	23	30.8	18.2	2	14	32.6	12.3	121	63	22.4	14.2
	BMC3		15/21	1.05	2.96	1.121	0.052	-0.037	0.220	201	21	44.2	24.5	109	4	59.4	42.9	9	69	59.4	23.6
	BMC3-SF1	**E or E$^{//}$**	8/15	3.34	1.96	1.035	0.036	-0.225	0.230	211	1	49.7	20.5	121	18	48.4	41.5	304	72	45.3	28.5
	BMC3-SF2	**D***	7/15	-1.56	1.00	1.080	0.072	0.071	0.175	197	29	34.2	19.9	290	5	54.7	31.8	29	61	54.6	15.2
Valle Scura	**VSR2**		19/21	7.23	1.88	1.022	0.013	0.010	0.348	207	25	32.2	17.8	298	1	35.3	31.2	31	65	35.3	16.6
	VSR2-SF1	**E$^{//}$**	14/19	7.12	1.80	1.027	0.013	-0.383	0.379	211	25	23.3	16.7	120	1	43.2	22.0	28	65	43.5	15.2
	VSR2-SF2	**F**	5/19	7.52	2.29	1.020	0.006	-0.134	0.252	132	4	23.0	12.1	224	31	19.6	7.5	35	59	22.7	15.6
	VSR1	**E$^{//}$**	23/24	9.29	2.17	1.039	0.020	0.091	0.249	230	28	24.3	18.0	324	7	26.1	21.6	67	61	24.3	18.0
	VMC1		18/21	8.56	3.56	1.015	0.010	0.529	0.220	263	21	68.5	14.8	164	24	68.5	31.9	29	57	33.5	18.7
	VMC1-SF1	**E$^{//}$**	10/18	8.16	2.22	1.020	0.010	-0.346	0.252	227	26	22.5	18.6	125	22	45.0	19.2	1	55	45.1	21.6
	VMC1-SF2	**F**	8/18	9.07	4.89	1.023	0.011	-0.361	0.182	303	5	28.3	9.6	208	47	46.2	26.4	38	42	46.0	10.3
	VCM2		19/21	12.25	2.37	1.024	0.013	0.406	0.250	234	21	49.0	15.8	142	6	49.1	22.1	37	68	22.7	15.8
	VMC2-SF1	**D$^{//}$**	9/19	12.25	2.37	1.032	0.012	-0.004	0.234	253	19	11.6	10.5	159	10	27.6	11.0	43	68	28.2	8.7
	VMC2-SF2	**E**	10/19	12.42	1.51	1.020	0.013	0.186	0.229	191	20	25.6	14.1	283	6	26.3	18.1	28	69	26.8	14.9
	VCM3		18/21	11.56	3.62	1.022	0.012	0.442	0.259	204	22	44.0	20.6	300	14	44.0	27.9	60	64	28.3	20.1
	VMC3-SF1	**D$^{//}$**	8/18	11.44	3.24	1.025	0.013	0.120	0.245	244	38	30.4	17.3	334	1	28.3	22.5	64	53	23.6	21.8
	VMC3-SF2	**E**	10/18	12.18	4.37	1.025	0.013	0.181	0.273	185	12	21.0	15.1	277	7	26.4	16.6	37	77	25.9	16.3

Table 4.S 2. ARM experiments for the different magnetic fabric stages detected in the study area. Structural position along the accretionary prism; Magnetic fabric pattern; Type of ARM experiment; n/N = number of specimens accepted/number of specimens measured; Mean remanent magnetization (RM) and its standard deviation [10^{-3} A/m]; AMS scalar parameters and their standard deviations: Pj = corrected anisotropy degree, T = shape parameter; D = declination (°), I = inclination (°) and 95% confidence angle (°) of the principal magnetic susceptibility axes k_1, k_2 and k_3, respectively.

Structural position	Pattern	ARM experiment	n/N	Mean RM & st. dev. ($\times 10^{-6}$ Am^2Kg^{-1})		Pj	st. dev.	T	st. dev.	k_1				k_2				k_3			
										D	I	95% conf. angles		D	I	95% conf. angles		D	I	95% conf. angles	
Frontal Thrut Ramp	*Stage A*	AMS	6/6	--	--	1.022	0.008	0.111	0.156	103	2	32.0	12.1	194	15	32.4	5.5	4	75	12.9	9.6
		$ApARM_{40-0}$	6/6	2.87	1.51	1.060	0.030	0.096	0.457	302	7	24.9	4.4	32	2	25.1	13.2	142	83	15.1	7.0
		$ApARM_{100-40}$	6/6	2.17	0.97	1.081	0.041	0.874	0.255	228	1	56.0	8.5	138	5	55.9	14.3	324	85	14.3	10.5
		AARM	5/6	5.12	2.49	1.058	0.042	0.670	0.234	155	1	57.9	13.2	65	0	57.7	16.0	329	89	21.3	8.8
		AIRM	6/6	10.35	2.94	1.115	0.053	0.662	0.570	308	4	17.7	4.8	39	9	17.5	12.9	194	80	13.2	5.9
	Stage C	AMS	6/6	--	--	1.026	0.008	0.494	0.127	343	4	13.0	10.1	249	39	14.5	12.3	78	51	17.0	3.2
		$ApARM_{40-0}$	6/6	83.16	35.85	1.209	0.059	0.361	0.220	340	5	13.8	8.2	245	46	19.3	13.2	75	43	20.3	3.7
		$ApARM_{100-40}$	6/6	42.24	19.23	1.226	0.078	0.311	0.204	342	3	11.9	6.4	248	50	23.0	7.8	75	40	24.7	2.4
		AARM	6/6	126.39	55.50	1.214	0.064	0.390	0.126	341	2	11.9	9.4	249	47	20.9	11.0	73	43	22.2	2.3
		AIRM	6/6	151.23	56.33	1.196	0.056	0.471	0.172	336	8	11.7	7.9	239	45	22.4	9.0	74	44	22.0	5.5
	Stage $E_{FRONTAL}$	AMS	6/6	--	--	1.044	0.020	0.717	0.391	207	45	59.9	13.4	300	3	60.0	6.0	33	45	13.6	5.8
		$ApARM_{40-0}$	6/6	25.45	15.57	1.143	0.090	0.756	0.328	226	49	25.0	9.4	130	6	25.0	8.4	35	41	12.1	3.8
		$ApARM_{100-40}$	6/6	6.24	3.61	1.179	0.122	0.785	0.231	224	46	29.8	7.3	132	2	9.8	8.2	39	44	9.0	6.4
		AARM	5/6	31.88	19.28	1.184	0.094	0.939	0.170	203	47	63.2	8.8	302	8	63.2	4.9	39	42	10.0	3.2
		AIRM	5/6	54.59	31.69	1.130	0.090	0.791	0.304	224	50	45.2	10.2	128	5	45.3	9.4	34	40	13.8	6.5
Oblique Thrust Ramp	*Stage* $E_{OBLIQUE}$	AMS	6/6	--	--	1.022	0.007	0.392	0.290	191	2	24.1	14.1	281	9	27.0	18.2	90	81	24.9	11.4
		$ApARM_{40-0}$	6/6	0.35	0.14	1.085	0.060	0.044	0.390	290	18	33.2	6.4	199	3	43.8	13.8	99	72	37.8	9.6
		$ApARM_{100-40}$	5/6	0.29	0.09	1.107	0.036	0.893	0.346	135	4	67.2	17.7	228	38	67.2	17.7	41	52	20.6	14.2
		AARM	6/6	0.70	0.23	1.095	0.065	0.293	0.545	142	0	31.8	9.8	232	37	32.3	8.5	52	53	13.0	10.4
		AIRM	6/6	2.27	0.75	1.148	0.136	0.254	0.578	245	31	39.6	14.5	148	12	39.9	7.6	40	56	16.8	10.2
	Stage $E//_{OBLIQUE}$	AMS	6/6	--	--	1.039	0.014	0.042	0.220	238	34	18.1	17.2	333	6	24.7	7.3	72	56	20.9	16.3
		$ApARM_{40-0}$	6/6	0.53	0.23	1.065	0.036	0.520	0.332	192	18	35.2	21.2	291	26	35.8	17.5	70	58	24.4	15.1
		$ApARM_{100-40}$	6/6	0.49	0.20	1.119	0.067	0.747	0.244	168	6	45.1	16.7	262	31	45.9	16.1	69	58	22.3	17.3
		AARM	6/6	1.08	0.44	1.081	0.040	0.562	0.374	195	16	27.8	19.6	294	29	27.2	22.0	80	56	23.3	19.2
		AIRM	5/6	2.70	0.85	1.095	0.035	0.255	0.437	178	6	33.6	14.5	271	27	32.1	22.8	77	63	32.0	15.0

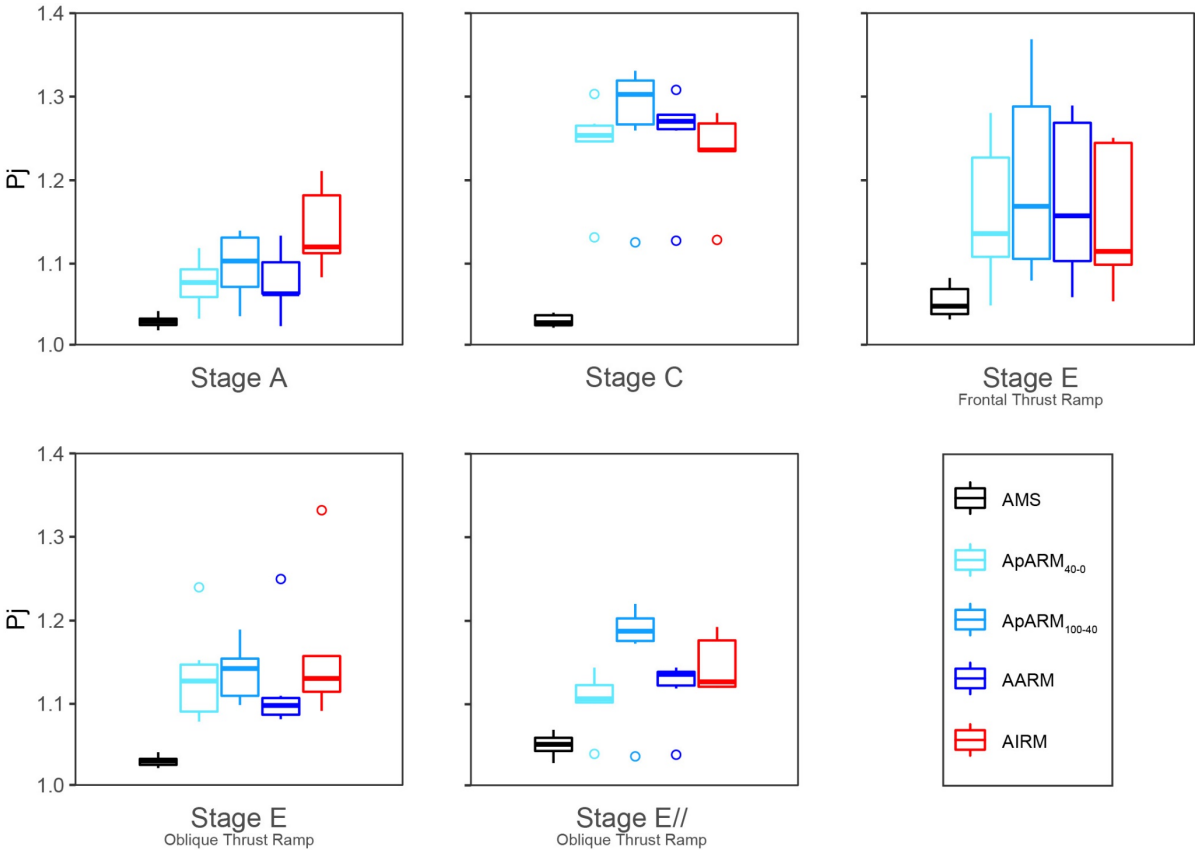

Figure 4.S 1. Box-and-whisker plots of the corrected anisotropy degree (Pj) of the AMS and ARM experiments divided by representative stages.

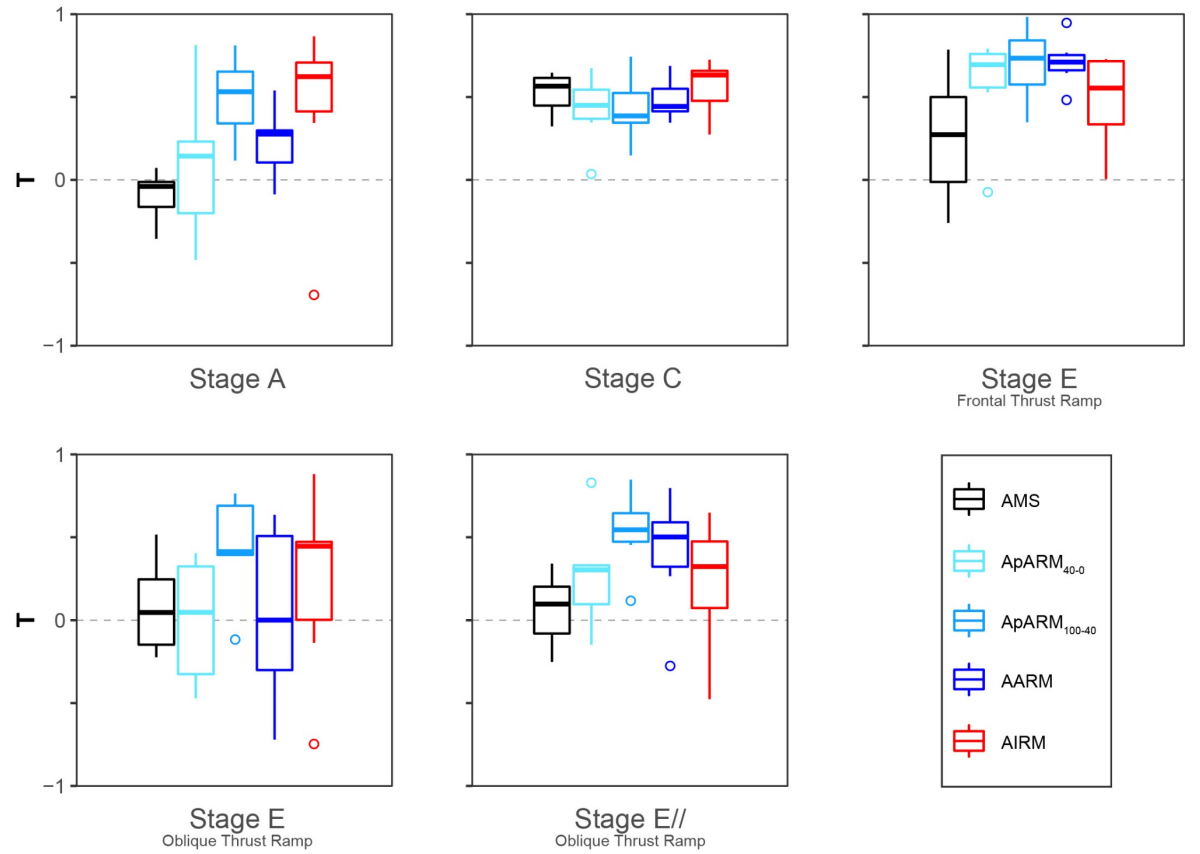

Figure 4.S 2. Box-and-whisker plots of the shape parameter (T) of the AMS and ARM experiments divided by representative stages.

Chapter 5 – The SVU

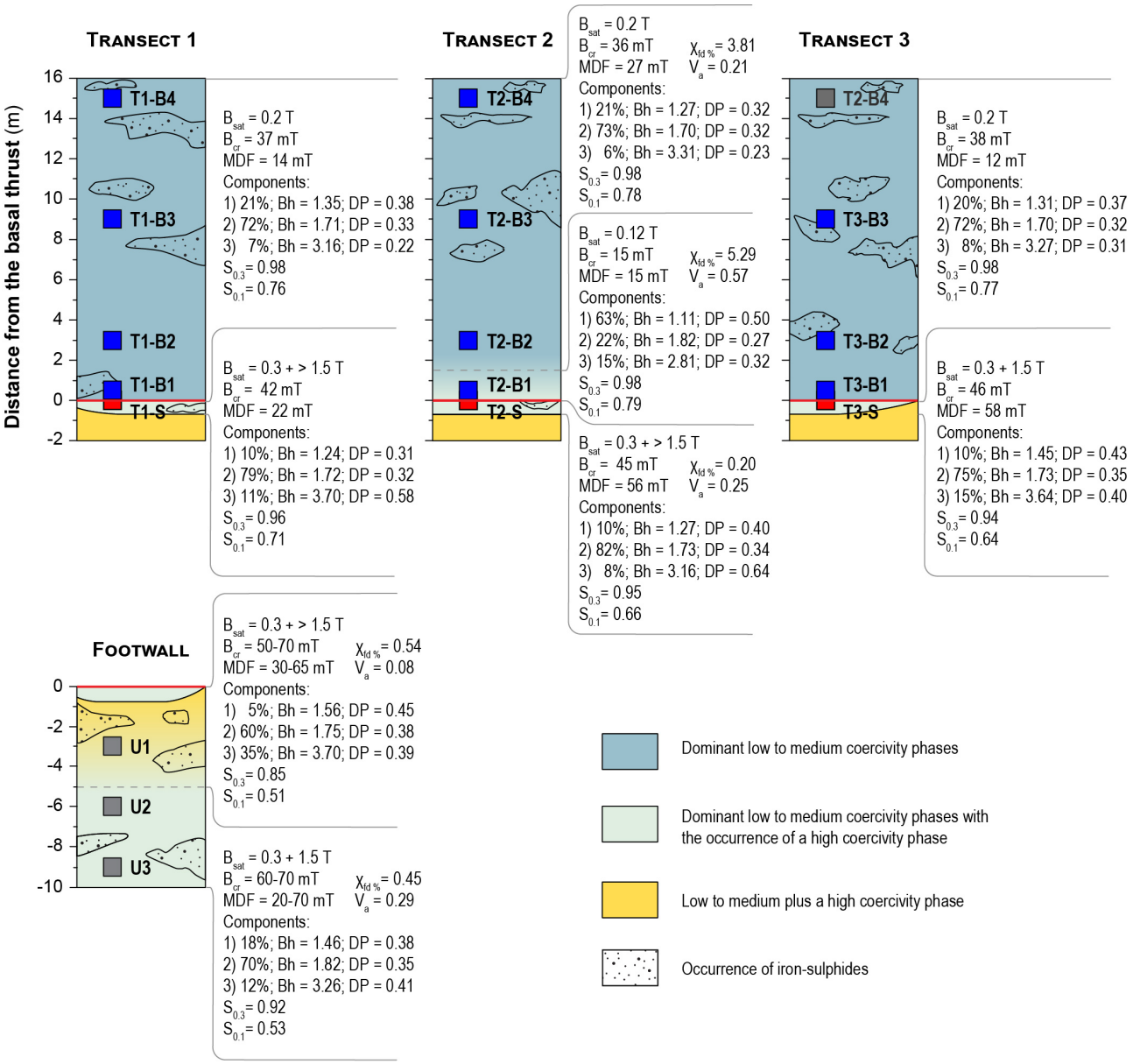

Figure 5.S 1. Magnetic mineral assemblages in the footwall and SVU transects at the Gova Tectonic window and distinctive parameters: B_{sat} = saturation field; B_{cr} = remanence coercive force; MDF = Median destructive field; $\chi_{fd\%}$ = frequency-dependent magnetic susceptibility (%); V_a field variation parameter; Relative abundance (%), mean remanence coercivity (Bh in log10 units) and dispersion parameter (DP) of the components of the IRMs acquisition curves deconvolution; S-ratios $S_{0.3}$= -$IRM_{-0.3T}$/IRM_{1T}; $S_{0.1}$= -$IRM_{-0.1T}$/IRM_{1T}. The local occurrence of iron-sulfides derives from the Lowrie experiments.

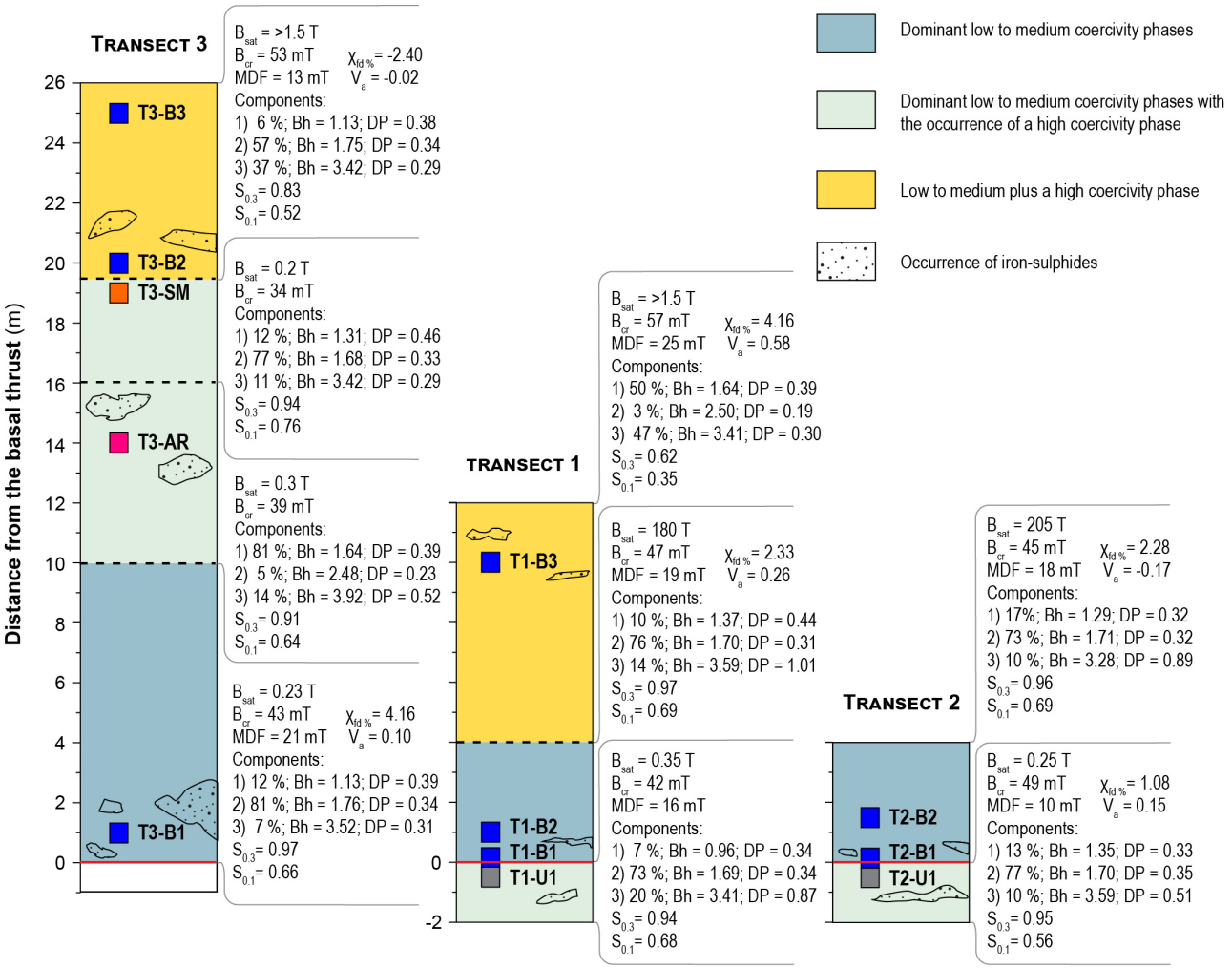

Figure 5.S 2. Magnetic mineral assemblages in the footwall and SVU transects at Vidiciatico and distinctive parameters: B_{sat}; B_{cr}; MDF; $\chi_{fd\%}$; V_a ;Bh; DP; $S_{0.3}$; Legend as in **Figure 5.S 1**.

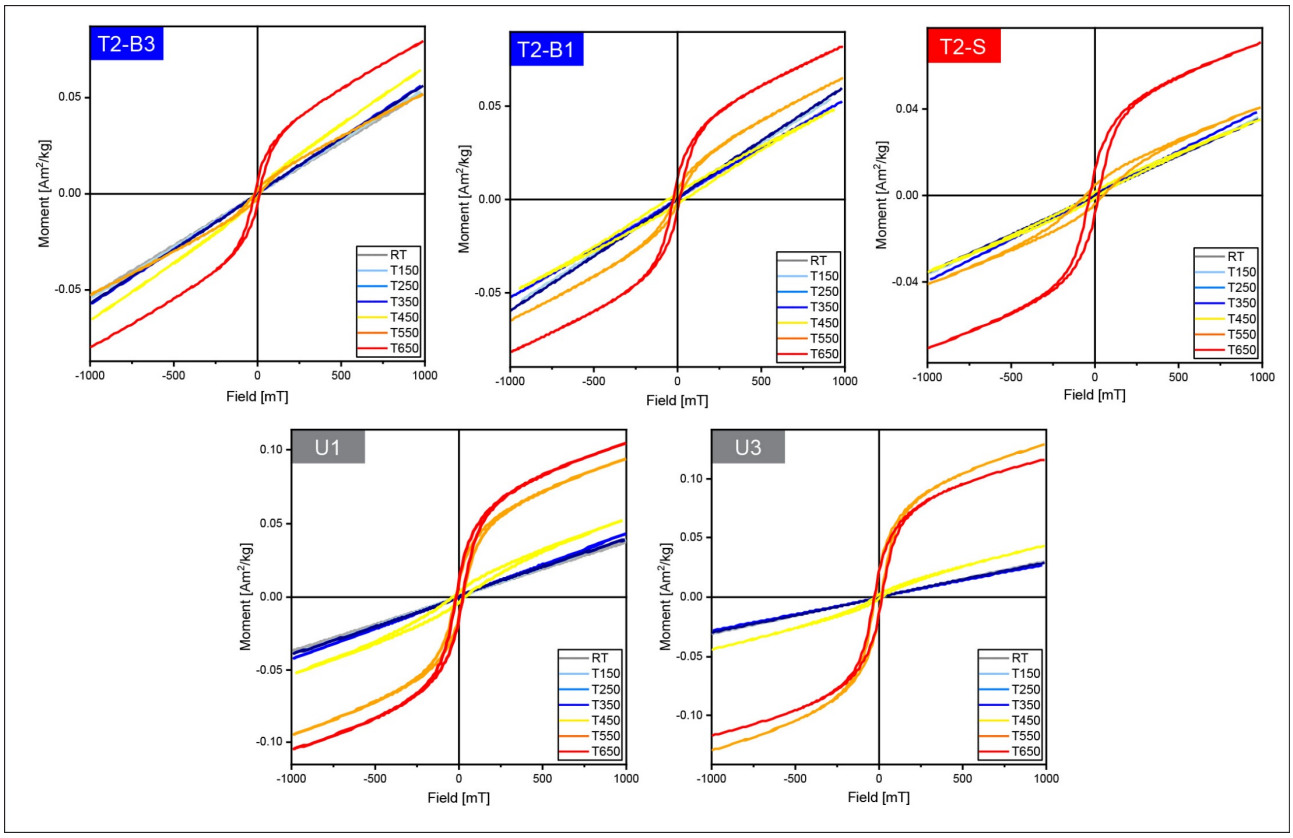

Figure 5.S 3. Representatives hysterisis loops after stepwise thermal treatment at progressive increase maximum temperature. Hysteresis loop corrected for the high-field slope are reported in **Figure 5.13**.

Table 5.S 1. AMS data at site level and relative detected subfabrics at the Gova Tectonic window. Site; Distance from the basal thrust; Magnetic fabric patterns detected through contouring and cluster analysis; n/N = number of specimens accepted/number of specimens measured; Type of specimens: Cores or cubes; χ_m = mean mass magnetic susceptibility [10^{-9} m^3kg^{-1}] and its standard deviation; AMS scalar parameters and their standard deviations: Pj = corrected anisotropy degree, T = shape parameter; D = declination (°), I = inclination (°) and 95% confidence angle (°) of the principal magnetic susceptibility axes k_1, k_2 and k_3, respectively.

Site	Distance	Pattern	n/N	Specimen type	χ_m & st. dev. (x 10^{-9} m^3Kg^{-1})		Pj	st. dev.	T	st. dev.	k_1				k_2				k_3			
											D	I	95% conf. angles		D	I	95% conf. angles		D	I	95% conf. angles	
U3	*-9*	U_{Main}	**55**/*56*	*Cores*	52.29	9.49	1.062	0.009	0.266	0.105	261	6	6.0	4.8	170	7	6.0	4.3	31	81	5.6	3.5
U2	*-6*	U_{Main}	**7**/*7*	*Cores*	66.76	0.62	1.058	0.001	0.086	0.067	280	5	1.9	1.3	190	9	2.8	1.4	39	80	3.1	1.3
U1			**59**/*60*		49.28	8.53	1.059	0.010	0.437	0.174	259	10	20.3	6.6	165	20	20.0	7.5	14	68	12.6	5.3
Sf1	*-3*	U_{Main}	44/59	*Cores*	45.25	4.53	1.065	0.010	0.425	0.149	267	12	13.4	4.1	174	18	13.4	5.4	29	69	5.8	3.9
Sf2		*U1-Sf2 (strike slip)*	15/59		61.10	6.16	1.057	0.006	0.485	0.216	64	0	13.7	4.7	154	37	14.6	5.5	333	53	12.6	3.0
T1-S	*0*	*S-T1*	**7**/*7*	*Cores*	61.17	0.92	1.056	0.004	0.733	0.043	249	31	7.5	2.9	148	19	7.9	4.0	31	53	5.6	4.2
T1-B1	*0.5*	*P2*	**14**/*15*	*Cubes*	62.51	7.79	1.057	0.015	0.296	0.479	235	37	13.3	8.0	132	18	15.7	12.5	21	48	15.2	7.8
T1-B2			**16**/*16*		55.46	4.94	1.052	0.014	0.166	0.248	241	22	12.5	7.3	140	26	20.9	9.8	6	55	19.6	7.3
Sf1	*3*	*P2*	11/16	*Cubes*	54.40	4.70	1.059	0.015	0.221	0.215	246	20	10.4	6.8	149	19	11.7	8.5	19	62	10.0	6.8
Sf2		*P4*	5/16		57.82	5.11	1.048	0.007	0.402	0.314	226	34	14.3	8.7	106	37	14.3	10.2	344	35	10.3	8.9
T1-B3	*9*	*P2*	**34**/*38*	*Cubes*	66.16	4.65	1.037	0.015	0.351	0.305	236	30	25.3	8.5	133	21	25.5	10.8	15	52	12.1	8.6
T1-B4			**29**/*32*		82.40	7.32	1.039	0.020	0.459	0.209	175	41	37.2	16.0	74	12	37.2	36.9	331	46	36.9	16.0
Sf1	*15*	*P1*	8/29	*Cubes*	82.71	6.15	1.045	0.016	0.593	0.131	108	14	20.2	7.3	214	49	22.3	11.3	8	38	17.2	4.9
Sf2		*P2*	9/29		78.86	9.69	1.057	0.019	0.673	0.229	224	31	36.3	11.9	123	18	36.3	10.2	7	53	15.0	4.6
Sf3		*P5*	12/29		84.86	5.21	1.064	0.020	0.848	0.194	176	39	32.0	9.9	52	36	31.6	7.2	296	32	14.0	7.6
T2-S	*0*	*S-T2&3*	**13**/*14*	*Cores*	46.67	10.17	1.028	0.008	0.324	0.415	264	13	13.1	3.8	151	60	13.0	9.7	1	27	9.8	4.0
T2-B1			**70**/*75*		63.79	5.57	1.044	0.024	0.585	0.378	93	8	36.8	12.1	189	36	36.6	15.0	352	53	15.1	13.0
Sf1	*0.5*	*P1*	44/75	*Cubes*	63.05	5.62	1.045	0.022	0.237	0.354	92	8	24.4	10.4	189	41	24.3	16.2	353	48	16.5	11.0
Sf2		*P2*	8/75		66.29	4.36	1.048	0.014	0.611	0.192	207	25	22.0	8.3	116	2	22.9	8.9	22	65	12.6	9.9
Sf3		*P3*	18/75		64.51	5.78	1.052	0.030	0.752	0.314	157	37	33.5	11.9	249	3	33.4	12.7	344	53	12.8	12.1
T2-B2			**17**/*21*		55.30	5.86	1.030	0.013	-0.114	0.453	228	36	33.0	17.0	123	19	35.3	21.9	11	48	27.2	17.0
Sf1	*3*	*P2*	9/17	*Cubes*	56.35	6.75	1.038	0.012	0.265	0.405	226	50	31.9	8.6	123	11	31.2	11.8	24	38	12.5	11.9
Sf2		*P4*	8/17		54.11	4.83	1.033	0.015	-0.580	0.529	227	18	23.8	4.4	125	32	52.1	13.7	341	53	51.3	5.9
T2-B3			**38**/*40*		64.39	5.04	1.046	0.030	0.586	0.231	251	27	25.3	12.6	154	14	25.6	11.4	39	59	12.7	12.4
Sf1	*9*	*P1*	6/38	*Cubes*	63.85	7.37	1.049	0.024	0.519	0.160	263	3	19.1	2.4	171	27	19.4	9.4	359	63	10.3	1.3
Sf2		*P2*	32/38		64.49	4.64	1.048	0.031	0.579	0.244	251	30	23.9	10.5	154	12	24.1	10.3	46	58	12.6	8.5
T2-B4			**37**/*39*		76.21	8.66	1.083	0.049	0.401	0.192	234	22	20.8	11.4	132	27	21.0	11.3	358	54	13.6	11.1
Sf1	*15*	*P1*	28/37	*Cubes*	76.65	8.38	1.082	0.042	0.381	0.190	236	17	21.1	8.3	135	32	19.7	8.5	350	53	12.2	8.1
Sf2		*P2*	9/37		74.85	9.88	1.098	0.064	0.472	0.186	228	32	16.1	12.5	130	14	16.9	11.6	19	55	17.2	4.1
T3-S	*0*	*S-T2&3*	**8**/*8*	*Cores*	61.09	1.82	1.039	0.002	0.725	0.088	261	10	21.9	4.7	162	39	22.0	4.5	3	49	5.7	5.2
T3-B1	*0.7*	*P2*	**13**/*13*	*Cubes*	57.97	8.04	1.067	0.034	0.291	0.315	212	44	16.5	4.4	110	12	18.0	11.8	9	43	14.0	4.1
T3-B2	*3*	*P4*	**17**/*18*	*Cubes*	63.02	4.03	1.036	0.005	-0.431	0.333	218	28	10.7	6.6	314	11	30.1	5.8	63	59	30.1	10.0
T3-B3			**25**/*29*		65.42	6.68	1.031	0.027	-0.150	0.345	248	8	15.6	9.9	153	34	30.0	15.5	349	55	30.1	9.7
Sf1	*9*	*P1*	15/25	*Cubes*	65.26	5.51	1.031	0.023	0.281	0.292	246	15	21.4	9.6	141	45	21.3	13.1	350	41	14.4	8.0
Sf2		*P4*	10/25		65.65	8.46	1.039	0.034	-0.219	0.336	245	3	12.5	6.6	155	3	20.8	8.3	16	86	18.9	6.6

Table 5.S 2. ARM experiments for the different AMS pattern detected in the Gova tectonic window area. Structural position in respect to the megathrust shear zone; Magnetic fabric pattern; Type of ARM experiment; n/N = number of specimens accepted/number of specimens measured; Mean remanent magnetization (RM) and its standard deviation [10^{-3} A/m]; AMS scalar parameters and their standard deviations: Pj = corrected anisotropy degree, T = shape parameter; D = declination (°), I = inclination (°) and 95% confidence angle (°) of the principal magnetic susceptibility axes k_1, k_2 and k_3, respectively.

Structural position	Pattern	ARM experiment	n/N	Mean RM & st. dev. ($\times 10^{-6}$ Am^2Kg^{-1})		Pj	st. dev.	T	st. dev.	k_1				k_2				k_3			
										D	I	95% conf. angles		D	I	95% conf. angles		D	I	95% conf. angles	
Footwall	*Main fabric (U_{Main})*	AMS	6/6	--	--	1.069	0.008	0.375	0.098	261	9	9.2	2.7	170	11	9.3	5.5	31	76	6.2	1.3
		$ApARM_{40-0}$	6/6	0.85	0.03	1.114	0.039	-0.073	0.323	264	13	14.4	6.6	172	9	13.8	10.0	49	75	11.1	6.2
		$ApARM_{100-40}$	5/6	1.00	0.02	1.090	0.034	-0.394	0.351	257	8	14.2	7.0	164	21	27.5	14.0	6	68	27.6	6.7
		AARM	6/6	1.88	0.05	1.098	0.041	0.114	0.508	264	6	22.1	6.8	354	3	22.9	8.8	114	83	11.3	6.7
		AIRM	6/6	3.56	0.73	1.087	0.022	0.144	0.309	264	14	16.7	9.8	173	3	17.0	10.1	69	76	13.9	3.8
	U1-Sf2 (Strike slip)	AMS	6/6	--	--	1.064	0.008	0.439	0.084	248	1	2.7	2.3	157	32	2.4	2.0	339	59	3.0	1.7
		$ApARM_{40-0}$	6/6	0.91	0.03	1.146	0.019	-0.149	0.281	232	10	8.0	4.6	137	27	10.7	5.9	341	61	9.2	4.6
		$ApARM_{100-40}$	6/6	1.01	0.02	1.119	0.017	-0.151	0.181	230	10	8.3	5.6	135	28	10.1	7.2	338	60	11.1	4.1
		AARM	6/6	1.95	0.05	1.124	0.023	-0.001	0.443	228	9	7.5	1.9	133	28	6.7	6.3	335	60	6.5	4.0
		AIRM	6/6	4.29	0.20	1.096	0.047	-0.135	0.295	229	13	5.9	4.5	134	20	11.2	3.7	349	66	11.1	3.9
Sheared Sandstones	*Transect 2-3 (S-T2&3)*	AMS	6/6	--	--	1.032	0.008	0.537	0.217	259	15	13.7	2.7	153	46	15.4	12.3	2	40	14.2	2.6
		$ApARM_{40-0}$	6/6	0.76	0.20	1.085	0.022	0.125	0.346	260	9	12.0	6.5	159	53	17.9	10.8	356	35	17.4	6.6
		$ApARM_{100-40}$	6/6	0.83	0.21	1.081	0.024	0.311	0.454	255	9	14.5	7.6	157	40	18.7	11.7	355	48	16.9	7.9
		AARM	6/6	1.63	0.41	1.082	0.023	0.116	0.400	262	5	9.5	4.4	166	47	10.7	8.6	356	42	9.9	4.4
		AIRM	5/6	5.23	1.44	1.063	0.015	0.268	0.279	265	14	35.0	2.7	160	45	36.7	16.1	8	42	21.4	2.9
	Transect 1 (S-T1)	AMS	5/5	--	--	1.057	0.005	0.753	0.035	247	31	7.1	2.6	146	18	6.0	3.3	31	53	5.0	3.5
		$ApARM_{40-0}$	5/5	0.94	0.03	1.089	0.025	0.648	0.259	138	10	33.5	12.2	237	40	32.8	7.4	36	48	14.7	7.8
		$ApARM_{100-40}$	5/5	1.01	0.04	1.081	0.022	0.657	0.349	253	33	61.3	4.2	150	18	61.3	10.4	36	51	11.4	3.8
		AARM	4/5	1.94	0.07	1.090	0.028	0.628	0.174	202	36	--	--	297	7	--	--	37	53	--	--
		AIRM	5/5	6.25	0.45	1.148	0.029	0.850	0.222	129	1	58.2	3.4	220	42	58.3	3.6	38	48	9.8	4.3
Civago marls Hanging wall (SVU)	*Pattern 1 (P1)*	AMS	6/6	--	--	1.027	0.016	0.233	0.233	251	14	26.2	8.1	147	45	29.0	14.8	353	42	21.1	4.1
		$ApARM_{40-0}$	6/6	2.65	1.80	1.037	0.016	-0.229	0.555	86	64	31.3	11.3	292	24	31.1	29.3	197	10	29.5	12.5
		$ApARM_{100-40}$	5/6	2.56	1.89	1.033	0.008	-0.118	0.450	28	80	24.8	17.6	272	5	46.9	16.4	181	9	45.4	16.5
		AARM	6/6	5.28	3.54	1.038	0.010	-0.102	0.503	65	71	22.4	15.8	293	13	31.0	17.0	200	14	28.4	15.3
		AIRM	6/6	10.60	3.41	1.040	0.034	0.232	0.467	236	23	49.5	12.3	128	36	50.3	20.7	351	45	28.6	8.9
	Pattern 2 (P2)	AMS	6/6	--	--	1.048	0.014	0.483	0.573	236	40	12.6	4.4	129	19	5.5	3.5	20	43	12.5	3.6
		$ApARM_{40-0}$	6/6	1.25	0.19	1.049	0.028	0.511	0.471	80	6	58.1	15.0	175	40	58.0	14.3	343	50	18.3	14.8
		$ApARM_{100-40}$	5/6	1.14	0.22	1.134	0.193	-0.543	0.164	56	46	28.4	9.5	244	43	70.2	9.0	151	4	70.1	19.2
		AARM	6/6	2.28	0.66	1.038	0.016	0.411	0.489	242	12	39.3	21.8	142	41	39.3	15.6	345	47	22.6	14.4
		AIRM	6/6	6.53	1.45	1.095	0.023	0.296	0.281	233	23	16.1	9.7	135	20	17.8	13.4	8	59	16.9	11.7
	Pattern 3 (P3)	AMS	6/6	--	--	1.035	0.011	0.637	0.294	167	36	31.5	8.3	258	1	31.0	6.5	348	54	10.8	6.9
		$ApARM_{40-0}$	6/6	1.09	0.10	1.052	0.029	-0.018	0.453	136	23	38.6	14.9	19	47	40.8	25.4	243	34	31.4	18.3
		$ApARM_{100-40}$	6/6	1.12	0.09	1.070	0.023	0.536	0.343	151	4	42.4	7.5	53	66	42.8	10.9	243	24	15.6	9.3
		AARM	6/6	2.20	0.18	1.051	0.022	-0.403	0.155	329	4	29.7	12.1	77	76	39.5	25.1	238	14	39.6	21.0
		AIRM	5/6	4.39	0.51	1.058	0.014	-0.436	0.386	147	3	24.4	10.3	297	86	33.4	22.0	57	2	32.9	13.8
	Pattern 4 (P4)	AMS	7/7	--	--	1.032	0.012	-0.374	0.284	231	30	18.0	9.8	339	28	13.2	8.8	103	47	18.9	10.7
		$ApARM_{40-0}$	5/7	1.93	2.20	1.043	0.023	0.498	0.429	5	51	56.2	12.3	116	16	57.2	24.6	217	35	33.0	8.8
		$ApARM_{100-40}$	7/7	1.72	1.64	1.056	0.026	0.306	0.406	14	50	39.8	15.2	124	16	40.7	26.7	226	36	28.7	15.1
		AARM	5/7	2.20	0.44	1.060	0.022	0.472	0.557	6	37	51.3	23.2	121	29	51.5	23.2	238	40	24.7	11.4
		AIRM	7/7	5.81	4.07	1.039	0.036	-0.457	0.340	321	18	34.2	20.1	231	1	70.0	27.0	139	72	70.1	17.0
	Pattern 5 (P5)	AMS	6/6	--	--	1.055	0.010	0.792	0.256	176	34	27.5	11.4	57	36	27.7	7.1	295	36	13.6	10.4
		$ApARM_{40-0}$	6/6	4.31	0.37	1.039	0.013	-0.011	0.373	110	86	30.8	3.3	325	3	40.6	22.0	234	2	38.5	12.2
		$ApARM_{100-40}$	6/6	4.03	0.49	1.034	0.010	-0.050	0.634	110	68	36.6	9.8	321	19	45.3	27.9	228	11	42.0	15.0
		AARM	6/6	8.48	0.91	1.041	0.019	-0.113	0.425	110	73	34.0	8.6	315	16	53.8	26.6	223	7	52.8	8.2
		AIRM	6/6	18.31	4.95	1.053	0.029	0.565	0.352	149	62	61.4	26.8	23	17	61.0	32.8	286	21	41.8	19.4

Table 5.S 3. AMS results and relative distinguished subfabric from Vidiciatico. Legend as in **Table 5.S 1**.

Site	Distance	Pattern	n/N	Specimen type	χ_m & st. dev. ($\times 10^{-9}$ m^3Kg^{-1})		Pj	st. dev.	T	st. dev.	k_1				k_2				k_3			
											D	I	95% conf. angles		D	I	95% conf. angles		D	I	95% conf. angles	
T1-U1			**17**/17		61.67	9.58	1.043	0.017	0.487	0.131	331	10	15.4	8.9	239	12	25.8	12.4	100	74	25.8	8.0
Sf1	*-0.2*	*U-Sf1*	7/17	*Cores*	67.22	5.25	1.043	0.007	0.751	0.054	287	31	22.7	7.1	192	8	22.5	3.0	89	57	9.0	2.3
Sf2		*U-Sf2*	10/17		57.79	10.19	1.050	0.019	0.393	0.147	332	6	9.7	7.8	62	0	20.5	7.7	153	84	20.9	8.0
T1-B1			**29**/31		69.07	5.10	1.037	0.016	0.640	0.328	289	14	46.2	13.8	198	3	46.3	12.1	95	76	14.5	11.9
Sf1	*0.15*	*P1*	19/31	*Cubes*	69.43	5.89	1.039	0.015	0.432	0.205	313	11	20.3	9.5	221	12	20.4	12.7	86	74	13.2	9.3
Sf2		*P2*	10/31		68.27	2.77	1.039	0.016	0.182	0.463	251	9	27.0	8.4	343	10	23.5	14.3	117	77	20.3	12.1
T1-B2	*1*	*P1*	**27**/31	*Cubes*	103.90	12.52	1.031	0.018	0.642	0.328	336	5	20.0	12.8	244	28	20.1	11.8	75	62	14.6	9.5
T1-B3			**34**/40		65.49	8.91	1.024	0.011	-0.168	0.397	328	7	22.1	18.6	63	32	44.0	20.9	227	57	43.8	18.4
Sf1	*10*	*P1*	12/40	*Cubes*	64.69	9.55	1.030	0.011	0.065	0.387	167	0	20.5	15.8	257	14	23.1	17.3	76	76	22.3	13.8
Sf2		*P3*	22/40		64.54	6.45	1.030	0.012	0.308	0.391	321	8	18.4	12.8	60	49	20.7	16.9	224	40	21.0	13.7
T2-U1	*-0.2*	*U-Sf2*	**20**/20	*Cores*	88.94	16.44	1.104	0.015	0.227	0.199	332	24	7.4	4.8	235	16	21.0	6.3	114	61	20.7	5.2
T2-B1	*0.15*	*P1*	**31**/31	*Cubes*	88.56	5.90	1.135	0.012	0.610	0.086	302	32	14.6	5.8	34	3	15.2	4.8	128	58	7.9	4.8
T2-B2			**26**/29		92.84	17.70	1.037	0.015	0.897	0.229	330	13	65.0	5.3	236	17	65.0	10.5	97	68	11.2	5.7
Sf1	*1.5*	*P1*	21/29	*Cubes*	92.07	17.18	1.037	0.011	0.737	0.216	340	11	33.4	6.0	246	21	33.3	7.4	95	67	8.6	5.1
Sf2		*P2*	5/29		96.07	21.59	1.042	0.025	0.439	0.278	255	14	22.6	11.5	347	9	22.6	8.2	108	74	13.7	3.5
T3-B1			**31**/31		75.91	7.95	1.043	0.016	0.249	0.425	330	26	21.1	9.7	227	24	21.0	19.1	100	54	19.4	10.2
Sf1	*1*	*P1*	26/31	*Cubes*	76.53	8.36	1.044	0.016	0.152	0.406	334	25	17.6	9.1	229	28	17.9	13.0	99	51	14.1	9.5
Sf2		*P2*	5/31		72.65	4.55	1.045	0.015	0.377	0.405	284	27	17.7	11.8	15	1	29.7	14.7	107	63	29.9	10.9
T3-B2			**39**/42		85.32	18.20	1.066	0.038	0.732	0.442	346	16	37.9	12.4	248	29	37.7	12.3	101	57	16.8	9.4
Sf1	*20*	*P1*	21/42	*Cubes*	89.04	21.34	1.085	0.023	0.582	0.309	340	18	18.9	8.5	242	24	19.1	8.4	104	59	11.3	6.7
Sf2		*P2*	9/42		88.63	13.21	1.096	0.034	0.879	0.173	241	30	39.6	13.7	341	16	39.7	13.2	95	55	16.6	9.3
Sf3		*P4*	9/42		65.67	24.16	1.024	0.008	-0.238	0.326	35	25	18.4	9.9	233	64	17.0	11.3	128	7	16.5	14.8
T3-B3	*25*	*P4*	**32**/33	*Cubes*	76.61	4.00	1.037	0.017	-0.258	0.401	16	19	11.4	9.2	238	66	32.5	8.6	111	15	32.2	10.2
T3-AR			**35**/37		138.19	46.63	1.075	0.073	0.638	0.259	348	22	37.3	13.7	251	16	38.1	21.4	129	62	23.5	13.8
Sf1	*14*	*P1-AR*	15/37	*Cubes*	170.53	35.40	1.108	0.068	0.814	0.294	345	23	46.4	11.8	247	17	46.6	16.5	124	61	18.1	11.9
Sf2		*P2-AR*	8/37		123.49	50.67	1.083	0.064	0.568	0.443	31	3	21.0	11.9	301	15	23.7	15.1	132	75	20.0	9.8
Sf3-Boudins		*P3-AR*	12/37	*Cores*	107.57	29.78	1.028	0.009	0.779	0.148	348	21	32.5	15.9	101	46	31.0	19.5	242	37	24.5	13.8
T3-SM	*19*	*SM*	**31**/31	*Cubes*	105.88	7.37	1.052	0.017	0.290	0.306	15	4	22.5	11.7	281	38	27.8	18.2	110	51	25.3	10.7

Table 5.S 4. ARM experiments for the AMS pattern detected in the Vidiciatico sector. Legend as in **Table 5.S 2**

Structural position	Pattern	ARM experiment	n/N	Mean RM & st. dev. ($\times 10^{-6}$ Am^2Kg^{-1})		Pj	st. dev.	T	st. dev.	k_1				k_2				k_3			
										D	I	95% conf. angles		D	I	95% conf. angles		D	I	95% conf. angles	
Footwall	*U1-Sf1*	AMS	**6**/*6*	--	--	1.045	0.006	0.725	0.058	294	28	12.8	7.1	198	12	12.8	2.5	86	59	7.4	2.3
		$ApARM_{40\text{-}0}$	**6**/*6*	0.49	0.02	1.071	0.072	-0.154	0.451	241	55	36.1	11.5	151	0	43.4	22.3	61	35	38.1	9.9
		$ApARM_{100\text{-}40}$	**5**/*6*	0.54	0.03	1.076	0.045	-0.760	0.339	228	52	22.3	9.8	88	31	63.8	19.2	345	20	63.7	11.6
		AARM	**5**/*6*	1.08	0.03	1.071	0.027	-0.158	0.281	214	62	23.8	10.4	14	27	27.7	22.8	108	8	27.4	8.8
		AIRM	**6**/*6*	2.31	0.21	1.121	0.036	-0.511	0.233	214	30	14.9	9.5	118	10	46.7	7.0	11	58	46.5	14.5
	U1-Sf2	AMS	**6**/*6*	--	--	1.050	0.018	0.491	0.071	330	12	12.8	7.7	238	8	20.6	9.1	116	76	19.3	8.4
		$ApARM_{40\text{-}0}$	**5**/*6*	0.51	0.04	1.048	0.028	-0.625	0.217	262	41	34.7	6.7	158	16	45.7	15.4	52	45	46.3	17.0
		$ApARM_{100\text{-}40}$	**6**/*6*	0.92	0.87	1.049	0.049	0.139	0.366	168	3	27.2	20.1	261	40	37.4	22.4	74	50	36.1	16.9
		AARM	**6**/*6*	1.01	0.08	1.084	0.026	-0.908	0.382	274	50	22.2	7.4	103	40	71.6	21.1	10	5	71.6	8.8
		AIRM	**5**/*6*	2.84	0.68	1.069	0.016	-0.248	0.466	189	38	23.0	19.4	23	51	37.8	20.0	285	7	39.0	19.1
	T2-U1	AMS	**6**/*6*	--	--	1.109	0.014	0.297	0.153	330	24	5.0	3.7	232	17	17.0	3.8	110	60	17.3	4.0
		$ApARM_{40\text{-}0}$	**6**/*6*	0.88	0.21	1.089	0.025	-0.539	0.422	335	27	14.3	6.1	240	9	46.0	11.1	134	62	46.1	9.9
		$ApARM_{100\text{-}40}$	**6**/*6*	0.74	0.14	1.086	0.035	-0.353	0.360	350	23	7.0	4.6	245	30	42.3	2.2	111	50	42.8	6.5
		AARM	**6**/*6*	1.66	0.32	1.084	0.023	-0.038	0.205	349	25	20.9	8.2	242	32	26.3	20.1	109	47	25.9	8.0
		AIRM	***5***/*6*	3.36	0.95	1.135	0.102	0.752	0.443	346	2	56.2	6.0	255	8	56.0	12.2	91	82	14.6	12.1
Hanging wall (SVU - Transcet 1)	*Pattern 1 (P1)*	AMS	**6**/*6*	--	--	1.030	0.015	0.340	0.423	327	3	15.9	5.3	235	22	23.0	15.1	65	68	22.5	5.2
		$ApARM_{40\text{-}0}$	**6**/*6*	1.07	0.55	1.033	0.013	0.368	0.431	237	50	63.3	20.6	145	2	63.5	29.0	54	40	34.7	17.2
		$ApARM_{100\text{-}40}$	**5**/*6*	1.21	0.89	1.036	0.016	0.710	0.372	246	64	75.6	21.1	136	10	75.6	16.0	42	24	25.9	9.3
		AARM	**6**/*6*	2.27	1.43	1.047	0.022	-0.390	0.364	227	62	30.1	9.0	342	13	56.5	19.7	77	25	55.3	9.2
		AIRM	**6**/*6*	6.31	6.17	1.053	0.033	0.314	0.243	291	14	37.4	10.8	195	20	37.5	26.2	53	66	26.7	11.7
	Pattern 2 (P2)	AMS	**6**/*6*	--	--	1.043	0.011	-0.025	0.442	255	7	16.0	3.1	346	7	13.9	4.7	122	80	9.8	4.3
		$ApARM_{40\text{-}0}$	**6**/*6*	2.13	0.40	1.053	0.010	-0.474	0.166	239	23	19.6	16.4	11	58	61.7	11.2	139	22	61.6	18.2
		$ApARM_{100\text{-}40}$	**6**/*6*	1.90	0.42	1.054	0.016	-0.530	0.311	245	33	18.0	9.7	51	56	58.9	9.7	151	6	59.1	11.5
		AARM	**5**/*6*	4.10	0.86	1.054	0.013	-0.380	0.279	247	29	16.7	10.2	25	54	49.4	9.7	145	20	49.5	15.0
		AIRM	**6**/*6*	5.21	1.00	1.040	0.017	0.632	0.276	226	11	73.4	8.4	324	39	73.4	21.8	123	49	22.1	13.0
	Pattern 3 (P3)	AMS	**6**/*6*	--	--	1.034	0.010	0.345	0.301	321	6	14.2	7.8	57	46	9.5	6.8	225	43	14.6	8.0
		$ApARM_{40\text{-}0}$	**6**/*6*	1.03	0.11	1.053	0.015	-0.426	0.339	76	79	17.0	15.6	195	6	34.8	16.1	286	10	35.3	14.7
		$ApARM_{100\text{-}40}$	**5**/*6*	0.92	0.07	1.045	0.019	-0.198	0.254	97	70	29.8	12.4	187	0	42.9	22.6	277	20	40.6	8.9
		AARM	**6**/*6*	1.97	0.18	1.054	0.016	-0.452	0.310	100	72	16.9	10.3	210	6	39.6	15.4	302	17	39.7	11.3
		AIRM	**5**/*6*	3.08	0.15	1.042	0.032	-0.641	0.407	25	17	42.2	30.4	118	10	69.9	25.9	238	70	69.2	31.5
Hanging wall (SVU - Transcet 2)	*T2-B1*	AMS	**6**/*6*	--	--	1.134	0.006	0.550	0.041	300	32	8.4	3.0	32	4	8.5	2.8	128	58	4.1	3.6
		$ApARM_{40\text{-}0}$	**6**/*6*	1.03	0.11	1.035	0.018	0.532	0.225	276	14	46.3	11.8	13	25	46.3	9.6	160	61	13.3	8.0
		$ApARM_{100\text{-}40}$	**6**/*6*	0.92	0.07	1.087	0.025	0.525	0.154	290	35	25.3	6.8	30	14	25.3	4.2	138	51	7.1	4.1
		AARM	**6**/*6*	1.97	0.18	1.086	0.014	0.556	0.183	299	36	28.4	5.5	39	13	28.5	8.6	146	51	9.5	5.2
		AIRM	**5**/*6*	3.08	0.15	1.088	0.045	-0.253	0.459	280	27	30.2	4.2	26	27	31.8	18.9	152	50	28.6	10.0
	Pattern 1 (P1)	AMS	**6**/*6*	--	--	1.044	0.011	0.780	0.112	347	8	29.1	5.6	253	25	29.0	2.4	94	63	6.0	2.4
		$ApARM_{40\text{-}0}$	**5**/*6*	2.16	0.86	1.044	0.014	-0.971	0.412	168	87	10.8	7.4	5	3	88.3	9.6	275	1	88.3	4.1
		$ApARM_{100\text{-}40}$	**6**/*6*	2.02	0.80	1.034	0.016	-0.119	0.363	297	82	36.9	22.5	11	2	36.3	35.0	101	8	40.6	12.7
		AARM	**6**/*6*	4.23	1.69	1.037	0.014	-0.363	0.333	105	89	22.9	11.9	359	0	54.3	12.2	269	1	55.0	6.1
		AIRM	**5**/*6*	5.06	1.90	1.028	0.011	-0.128	0.434	174	42	38.1	17.5	27	43	51.2	24.6	280	17	47.7	21.2
	Pattern 2 (P2)	AMS	**5**/*5*	--	--	1.042	0.025	0.439	0.278	255	14	22.6	11.5	347	9	22.6	8.2	108	74	13.7	3.5
		$ApARM_{40\text{-}0}$	**5**/*5*	2.13	0.40	1.059	0.012	0.153	0.309	357	67	35.3	15.0	211	19	34.7	9.2	117	12	17.8	10.6
		$ApARM_{100\text{-}40}$	**5**/*5*	1.90	0.42	1.051	0.014	-0.042	0.493	336	73	26.7	20.8	213	9	27.5	18.5	121	14	27.7	5.1
		AARM	**5**/*5*	3.60	1.44	1.049	0.016	0.331	0.367	337	73	38.4	23.3	218	8	38.4	21.5	126	15	23.6	21.6
		AIRM	**4**/*5*	4.50	1.94	1.037	0.011	-0.736	0.116	10	12	--	--	110	37	--	--	265	51	--	--
Hanging wall (SVU - Transcet 3)	*Pattern 1 (P1)*	AMS	**6**/*6*	--	--	1.066	0.034	0.436	0.421	327	23	9.2	2.0	227	22	9.9	5.7	98	57	7.0	1.5
		$ApARM_{40\text{-}0}$	**6**/*6*	0.92	0.22	1.040	0.022	-0.066	0.401	348	9	19.0	16.8	234	69	44.0	17.9	81	19	44.3	16.5
		$ApARM_{100\text{-}40}$	**5**/*6*	0.86	0.20	1.049	0.021	0.348	0.246	285	56	40.0	18.5	194	0	41.7	8.7	104	34	19.8	17.3
		AARM	**5**/*6*	1.82	0.42	1.052	0.042	0.437	0.241	330	39	53.6	12.4	202	37	55.8	11.4	87	30	31.4	11.6
		AIRM	**5**/*6*	6.48	6.68	1.110	0.180	-0.035	0.539	277	72	51.1	16.0	171	5	49.2	17.4	80	18	29.9	21.2
	Pattern 2 (P2)	AMS	**6**/*6*	--	--	1.064	0.040	0.698	0.414	267	36	27.1	6.4	359	4	27.0	14.2	94	54	15.3	8.6
		$ApARM_{40\text{-}0}$	**5**/*6*	0.82	0.17	1.061	0.042	0.376	0.548	259	43	44.4	14.6	358	10	44.3	25.9	98	45	30.6	11.2
		$ApARM_{100\text{-}40}$	**5**/*6*	0.99	0.43	1.070	0.044	0.458	0.493	263	44	44.5	16.9	358	5	44.0	31.4	94	45	33.7	12.7
		AARM	**6**/*6*	1.70	0.26	1.058	0.044	0.676	0.336	235	38	64.6	16.0	346	24	64.4	15.5	100	42	26.4	9.0
		AIRM	**5**/*6*	3.68	1.30	1.096	0.028	0.268	0.350	291	32	34.9	4.4	196	9	35.0	20.2	92	57	21.8	6.0
	Pattern 4 (P4)	AMS	**6**/*6*	--	--	1.030	0.010	0.003	0.556	18	19	9.8	4.9	245	64	19.5	3.4	114	18	19.1	9.5
		$ApARM_{40\text{-}0}$	**6**/*6*	0.69	0.08	1.051	0.021	-0.263	0.343	27	22	29.1	8.6	173	65	36.9	20.7	291	13	32.9	7.8
		$ApARM_{100\text{-}40}$	**6**/*6*	0.63	0.08	1.055	0.025	0.304	0.468	22	19	29.9	12.2	202	71	32.3	23.0	112	0	30.0	10.6
		AARM	**6**/*6*	1.34	0.16	1.051	0.021	0.007	0.377	21	23	24.7	10.4	202	67	32.3	18.8	111	0	31.7	9.1
		AIRM	**5**/*6*	2.45	0.58	1.056	0.035	-0.347	0.564	21	2	21.0	12.8	135	85	54.3	17.6	291	5	54.2	7.9

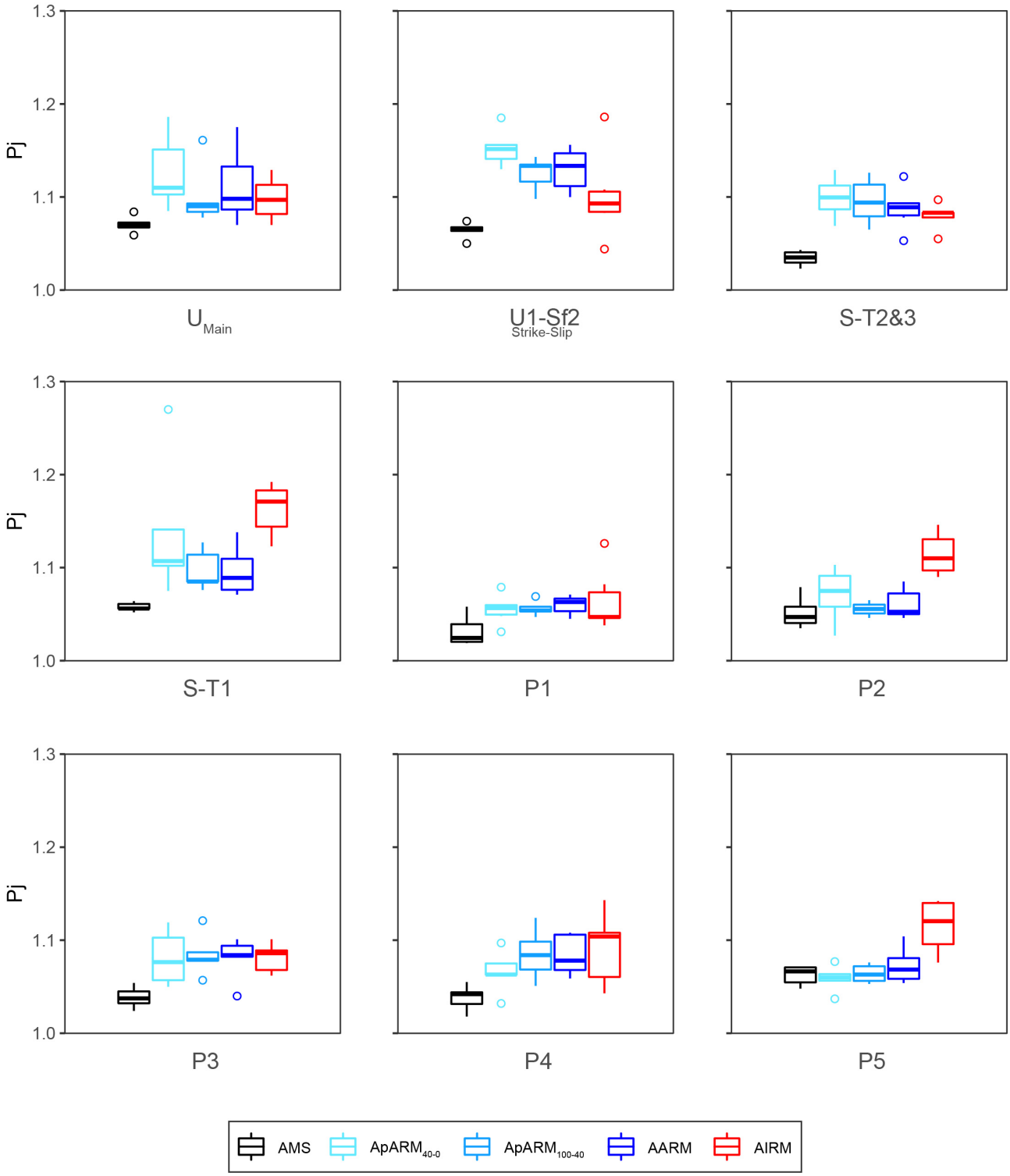

Figure 5.S 4. Box-and-whisker plots of the corrected anisotropy degree (Pj) of the AMS and ARM experiments divided by representative patterns from Gova Tectonic window.

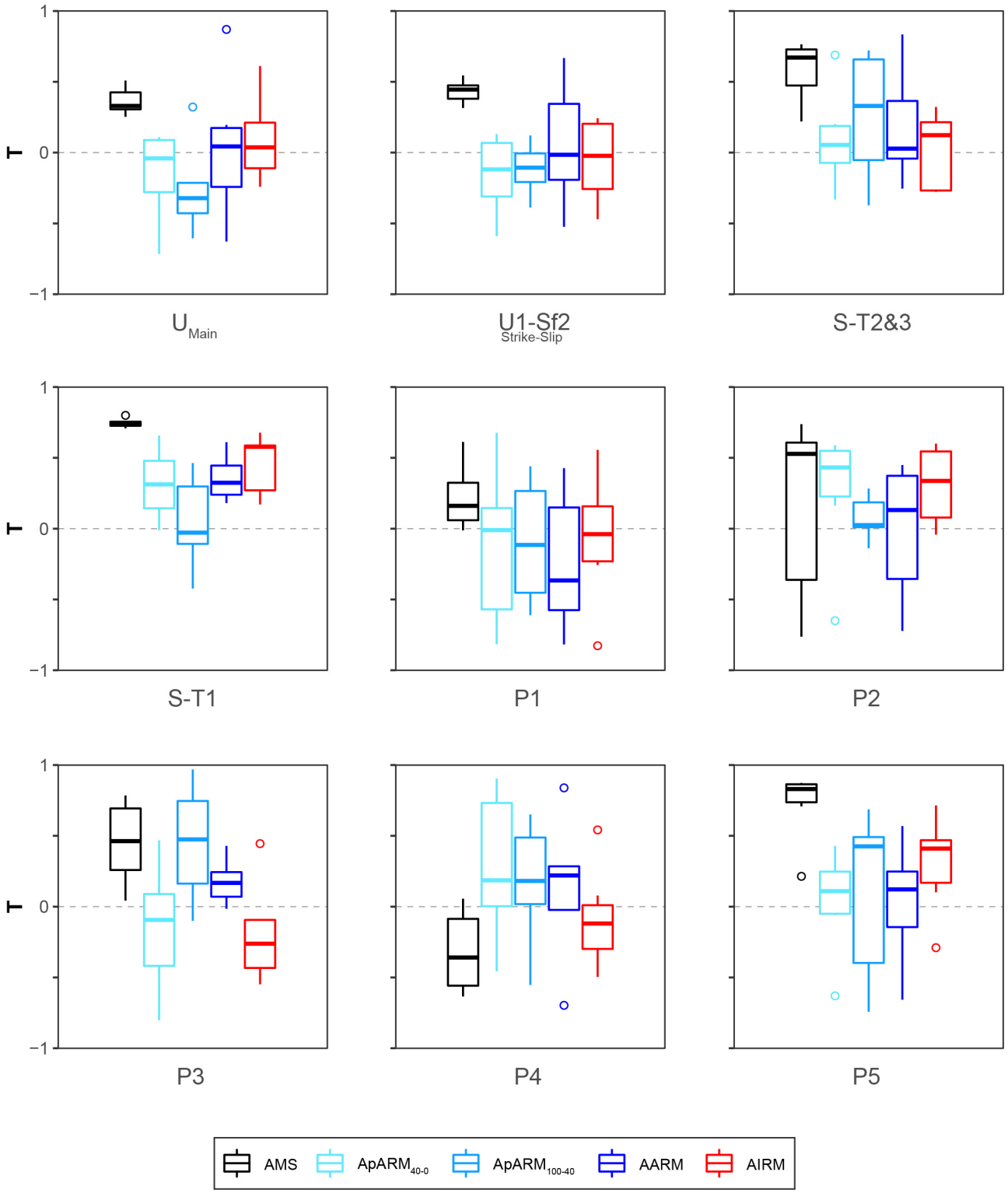

Figure 5.S 5. Box-and-whisker plots of the shape parameter (T) of the AMS and ARM experiments divided by representative patterns from Gova Tectonic window.

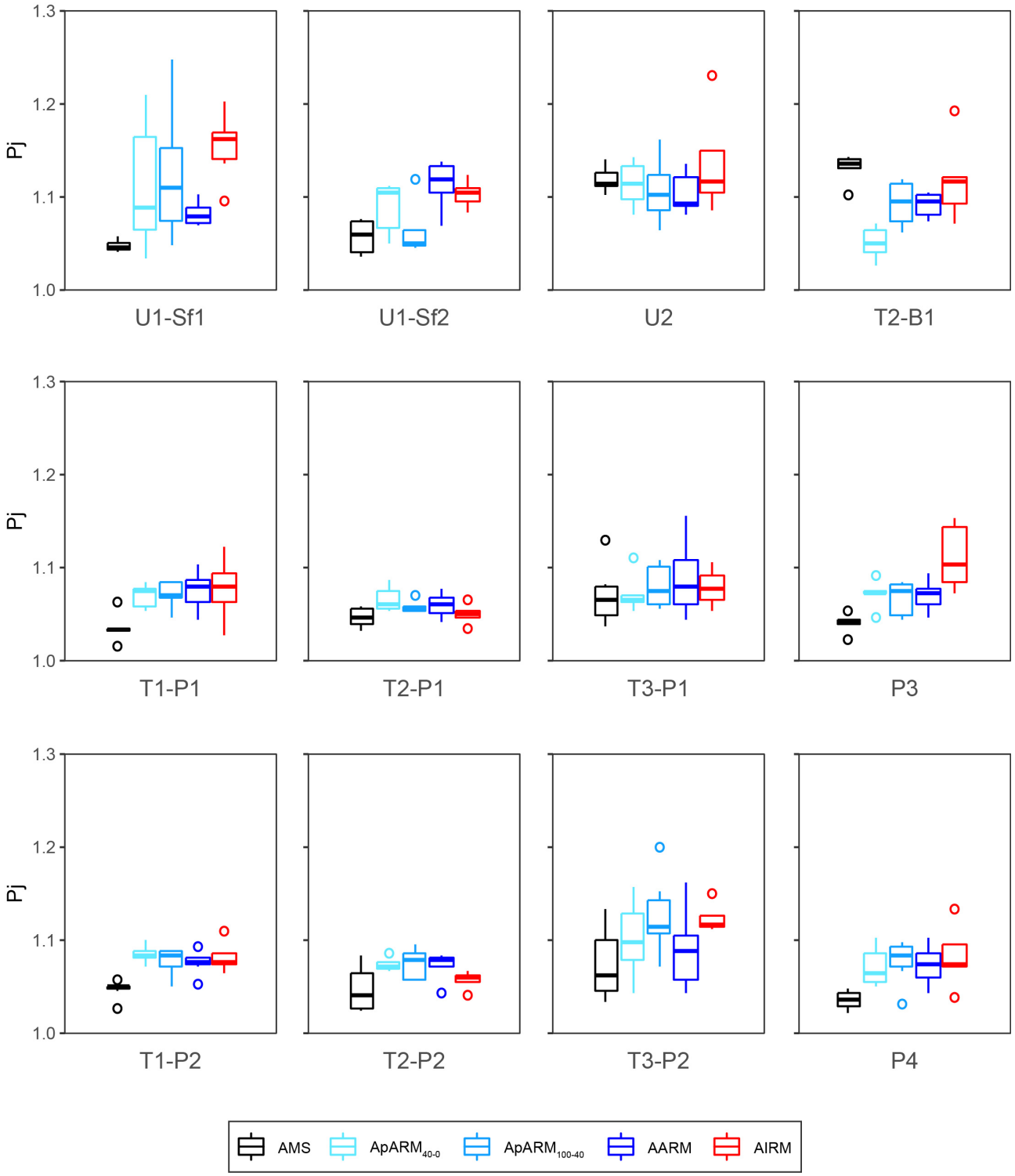

Figure 5.S 6. Box-and-whisker plots of the corrected anisotropy degree (Pj) of the AMS and ARM experiments divided by representative patterns from Vidiciatico sector.

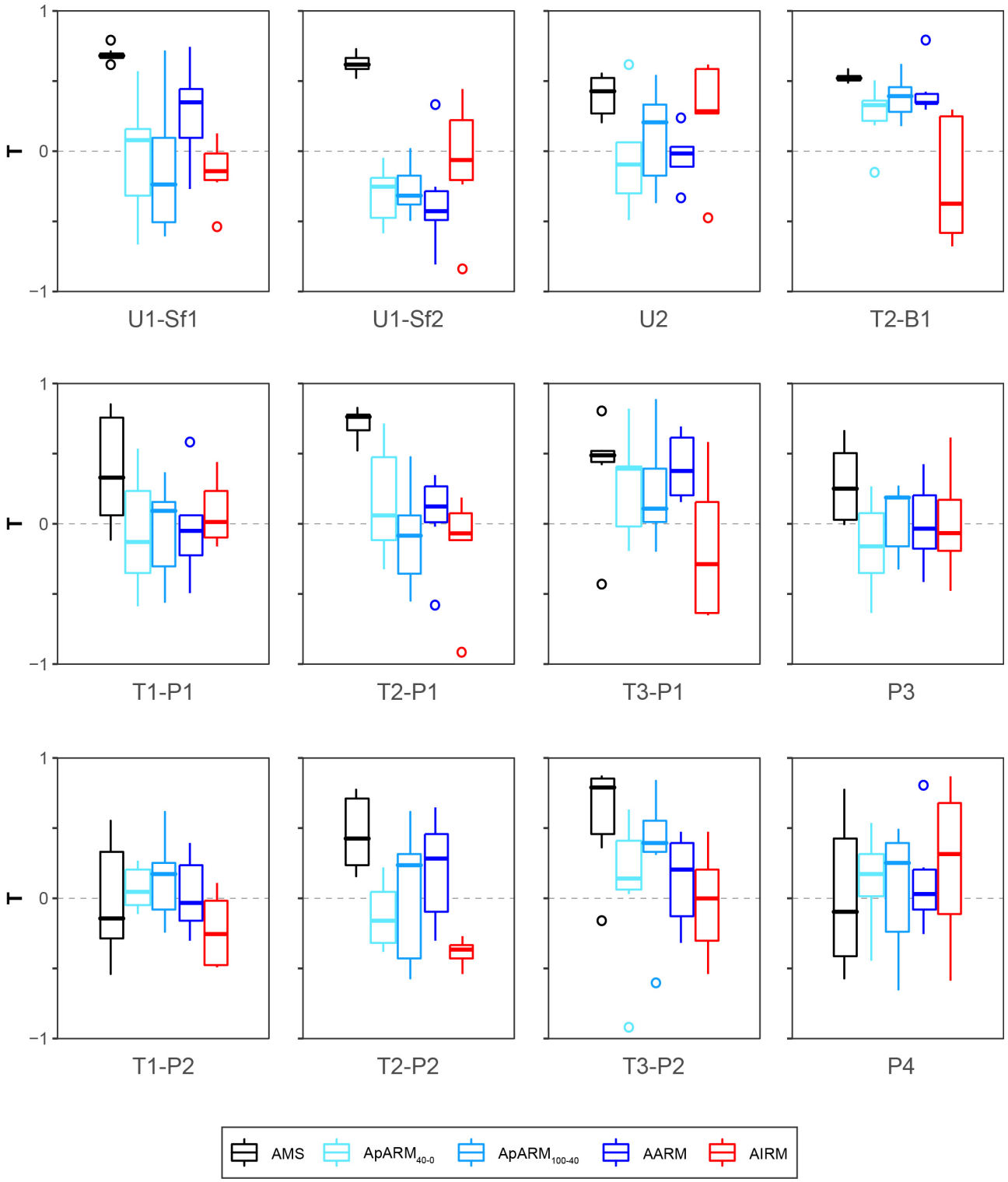

Figure 5.S 7. Box-and-whisker plots of the shape parameter (T) of the AMS and ARM experiments divided by representative patterns from Vidiciatico sector.

Chapter 6 – The ELAW

Table 6.S 1. Magnetic susceptibility and AMS data from broken formation (BrFm), tectonic (TMé), sedimentary (SMé), and polygenetic (PMé) mélanges and relative subfabrics (Sf1, Sf 2, Sf3) (modified from Robustelli Test et al., 2019). n/N = number of specimens used for calculation/number of measured specimens; K_m = mean susceptibility; L = magnetic lineation; F = magnetic foliation; Pj = corrected anisotropy degree; T = shape parameter; ± σ = standard deviation of each parameter; magnetic lineation: D, I = declination and inclination of the principal susceptibility axes (k_1, k_2, k_3) with relative angles of the 95% confidence ellipse.

Site	n/N	K_m (± σ) (μSI)	L (± σ)	F (± σ)	Pj (± σ)	T (± σ)	k_1				k_2				k_3			
							D	I	95% conf. angles		D	I	95% conf. angles		D	I	95% conf. angles	
BrFm1	7/7	**64.2** (± 3.6)	**1.011** (± 0.003)	**1.001** (± 0.003)	**1.013** (± 0.004)	**-0.820** (± 0.269)	113	26	12.0	4.8	243	53	71.1	4.8	10	25	71.0	10.7
Sf 1	(4+4)/7	**64.7** (± 3.3)	**1.007** (± 0.002)	**1.005** (± 0.003)	**1.012** (± 0.001)	**-0.216** (± 0.351)	105	26	--	--	202	14	--	--	318	60	--	--
Sf 2	(3+3)/7	**63.5** (± 4.6)	**1.011** (± 0.002)	**1.007** (± 0.001)	**1.018** (± 0.003)	**-0.186** (± 0.038)	117	24	--	--	297	66	--	--	27	1	--	--
BrFm2	21/*21*	**65.3** (± 24.2)	**1.013** (± 0.004)	**1.020** (± 0.006)	**1.033** (± 0.009)	**0.223** (± 0.113)	112	13	18.6	8.0	20	11	33.3	13.7	250	73	32.3	11.4
Sf1	12/21	**76.5** (± 24.0)	**1.009** (± 0.003)	**1.035** (± 0.004)	**1.046** (± 0.005)	**0.601** (± 0.098)	102	12	15.9	11.1	194	9	15.6	5.8	321	75	12.2	4.7
Sf2	9/21	**50.3** (± 15.3)	**1.006** (± 0.003)	**1.029** (± 0.006)	**1.038** (± 0.008)	**0.644** (± 0.123)	307	1	19.7	3.4	38	49	19.5	5.3	216	41	6.6	5.3
TMé1	18/20	**106.0** (± 12.4)	**1.005** (± 0.002)	**1.011** (± 0.002)	**1.016** (± 0.003)	**0.351** (± 0.173)	261	59	16.6	4.9	159	9	25.8	18.2	63	30	25.7	4.5
Sf 1	9/20	**110.0** (± 16.5)	**1.004** (± 0.002)	**1.015** (± 0.003)	**1.020** (± 0.003)	**0.597** (± 0.199)	254	56	22.1	4.5	52	5	23.4	7.3	86	33	12.4	4.6
Sf 2	9/20	**102.0** (± 6.36)	**1.003** (± 0.001)	**1.014** (± 0.001)	**1.018** (± 0.001)	**0.664** (± 0.152)	258	62	14.0	3.0	136	16	13.6	6.1	40	23	6.2	4.1
TMé2	41/42	**92.8** (± 20.8)	**1.001** (± 0.002)	**1.007** (± 0.004)	**1.009** (± 0.004)	**0.746** (± 0.217)	189	7	62.3	18.9	86	76	42.9	31.3	281	9	24.4	19.1
Sf 1	5/42	**78.0** (± 19.1)	**1.003** (± 0.001)	**1.007** (± 0.004)	**1.010** (± 0.005)	**0.414** (± 0.165)	108	7	20.8	17.2	339	78	32.2	14.0	199	9	31.7	19.5
Sf 2	24/42	**90.0** (± 20.4)	**1.004** (± 0.002)	**1.007** (± 0.004)	**1.011** (± 0.004)	**0.282** (± 0.245)	9	4	16.3	13.3	130	83	27.4	14.7	279	6	27.1	14.1
Sf 3	12/42	**105.0** (± 17.4)	**1.003** (± 0.001)	**1.01** (± 0.003)	**1.013** (± 0.004)	**0.557** (± 0.165)	173	62	18.4	12.8	25	24	22.1	15.2	289	13	20.1	12.2
TMé3	20/*20*	**55.4** (± 17.7)	**1.005** (± 0.004)	**1.029** (± 0.009)	**1.037** (± 0.011)	**0.709** (± 0.144)	196	24	45.1	17.0	295	20	45.0	23.7	60	58	25.1	16.8
(0-1m) Sf1	10/20	**57.3** (± 21.9)	**1.006** (± 0.005)	**1.036** (± 0.010)	**1.046** (± 0.011)	**0.700** (± 0.186)	246	32	47.1	13.7	150	9	46.9	14.9	46	56	16.8	14.2
(2-3 m) Sf2	9/20	**53.3** (± 12.6)	**1.014** (± 0.003)	**1.019** (± 0.009)	**1.034** (± 0.012)	**0.170** (± 0.084)	181	7	19.8	12.5	276	33	45.3	16.6	80	56	44.7	12.7
TMé4	19/*20*	**67.2** (± 29.4)	**1.009** (± 0.006	**1.019** (± 0.010)	**1.029** (± 0.010)	**0.347** (± 0.294)	152	10	30.7	16.4	243	7	32.3	23.4	7	78	26.3	15.4
Sf1	6/19	**49.9** (± 29.0)	**1.003** (± 0.007	**1.021** (± 0.010)	**1.027** (± 0.006)	**0.768** (± 0.396)	162	4	51.2	20.8	255	43	51.4	13.4	68	47	25.8	16.6
Sf2	13/19	**75.1** (± 27.0)	**1.009** (± 0.005)	**1.027** (± 0.010)	**1.037** (± 0.011)	**0.492** (± 0.224)	141	13	22.2	12.7	51	0	21.6	14.9	319	77	15.2	13.5
SMé1	17/24	**180.0** (± 30.5)	**1.013** (± 0.007)	**1.015** (± 0.011)	**1.028** (± 0.015)	**0.059** (± 0.233)	229	40	25.8	13.8	124	26	74.6	27.5	6	41	39.6	14.0
Sf 1	9/24	**170.0** (± 32.5)	**1.007** (± 0.006)	**1.034** (± 0.008)	**1.044** (± 0.009)	**0.639** (± 0.244)	119	12	36.3	10.2	222	47	36.4	8.3	19	40	10.6	8.5
Sf 2	6/24	**197.0** (± 22.4)	**1.020** (± 0.004)	**1.035** (± 0.015)	**1.057** (± 0.018)	**0.264** (± 0.160)	223	26	20.9	8.4	23	63	20.7	14.9	129	8	15.7	9.6
PMé1	17/18	**95.7** (± 19.2)	**1.01** (± 0.004)	**1.009** (± 0.006)	**1.019** (± 0.006)	**-0.077** (± 0.340)	326	12	10.3	6.1	225	40	21.6	7.5	69	48	21.8	8.8

Table 6.S 2. ARM experiments for the different AMS pattern detected in the study area. Type of chaotic rock units; Magnetic fabric pattern; Type of ARM experiment; n/N = number of specimens accepted/number of specimens measured; Mean remanent magnetization (RM) and its standard deviation [10^{-3} A/m]; AMS scalar parameters and their standard deviations: Pj = corrected anisotropy degree, T = shape parameter; D = declination (°), I = inclination (°) and 95% confidence angle (°) of the principal magnetic susceptibility axes k_1, k_2 and k_3, respectively.

Chaotic Units	Pattern	ARM experiment	n/N	Mean RM & st. dev. ($\times 10^{-6}$ Am^2Kg^{-1})		Pj	st. dev.	T	st. dev.	k_1				k_2				k_3			
										D	I	95% conf. angles		D	I	95% conf. angles		D	I	95% conf. angles	
Broken Formation	*BrFm LPExt*	AMS	6/6	--	--	1.046	0.004	0.576	0.089	98	13	19.5	7.0	191	12	18.4	4.8	323	72	10.6	3.0
		$ApARM_{40-0}$	6/6	8.12	1.46	1.153	0.024	0.211	0.182	102	10	14.0	6.1	194	15	13.1	5.9	338	72	9.2	4.0
		$ApARM_{100-40}$	6/6	5.48	1.21	1.150	0.030	0.407	0.186	101	11	16.2	7.1	194	16	15.3	4.3	337	70	9.1	3.9
		AARM	6/6	14.20	2.10	1.144	0.013	0.155	0.206	98	9	13.0	7.2	191	15	12.5	7.9	339	72	10.5	4.4
		AIRM	6/6	38.70	2.59	1.194	0.051	0.599	0.143	102	12	19.9	8.5	195	13	19.3	5.5	331	73	10.6	4.3
	BrFm Folding	AMS	6/6	--	--	1.037	0.007	0.635	0.118	308	4	4.4	2.7	43	46	5.3	2.5	214	43	6.1	2.9
		$ApARM_{40-0}$	6/6	4.93	0.88	1.117	0.027	0.280	0.106	315	10	6.2	3.2	53	40	6.2	3.3	213	48	4.2	2.5
		$ApARM_{100-40}$	6/6	3.76	1.30	1.109	0.029	0.387	0.105	319	12	12.2	5.1	59	40	15.0	2.5	215	47	10.0	4.2
		AARM	6/6	8.28	1.06	1.119	0.024	0.267	0.188	318	13	9.0	3.9	60	42	10.0	4.0	214	45	6.5	2.6
		AIRM	6/6	16.31	6.73	1.168	0.018	0.578	0.258	304	3	23.8	5.4	37	42	23.6	5.2	211	48	7.7	3.9
Tectonic Mélanges	*TMé LPExt*	AMS	6/6	--	--	1.041	0.010	0.456	0.262	139	6	14.9	5.9	230	5	14.9	4.4	359	83	6.2	4.3
		$ApARM_{40-0}$	6/6	42.05	47.82	1.133	0.074	0.504	0.348	140	4	25.2	7.0	231	3	26.2	6.1	4	85	10.6	6.4
		$ApARM_{100-40}$	6/6	30.38	37.97	1.180	0.096	0.492	0.295	129	5	12.0	7.1	220	4	14.9	9.4	348	84	14.3	4.0
		AARM	6/6	73.51	87.03	1.151	0.070	0.452	0.329	140	5	13.4	7.0	231	4	13.8	6.7	355	84	9.7	3.6
		AIRM	6/6	117.30	111.96	1.161	0.045	0.322	0.301	134	2	11.8	5.6	224	4	13.1	6.3	14	85	9.2	5.8
	TMé LPS	AMS	6/6	--	--	1.055	0.007	0.595	0.194	266	32	15.5	5.8	167	14	15.3	11.9	57	54	17.4	8.1
		$ApARM_{40-0}$	6/6	3.42	0.70	1.155	0.038	0.230	0.343	246	35	14.7	11.5	155	2	16.4	3.0	62	55	15.5	11.5
		$ApARM_{100-40}$	6/6	2.57	0.61	1.131	0.036	0.506	0.213	249	25	16.3	12.7	157	3	17.9	2.8	61	65	14.7	8.1
		AARM	6/6	6.08	1.33	1.156	0.041	0.467	0.289	251	31	14.7	14.4	159	3	16.5	4.1	64	58	15.2	7.7
		AIRM	6/6	15.92	2.97	1.295	0.053	0.487	0.181	260	32	14.0	10.5	164	10	16.4	8.1	59	56	14.6	7.8
	TMé Shear	AMS	6/6	--	--	1.044	0.013	0.260	0.081	190	13	11.7	7.5	285	19	28.9	11.7	69	67	29.1	6.5
		$ApARM_{40-0}$	6/6	6.32	3.24	1.110	0.036	0.128	0.174	194	13	12.3	5.8	287	14	32.7	10.9	63	71	32.6	6.0
		$ApARM_{100-40}$	6/6	4.39	1.84	1.102	0.049	0.182	0.165	191	10	10.0	3.0	285	17	22.5	5.0	72	70	22.9	7.8
		AARM	6/6	10.83	5.07	1.113	0.040	0.106	0.164	188	9	13.1	4.7	280	15	26.9	3.9	68	73	26.2	4.4
		AIRM	6/6	27.51	12.07	1.160	0.078	0.306	0.155	177	10	30.3	14.2	269	11	38.2	4.1	46	75	28.4	14.8

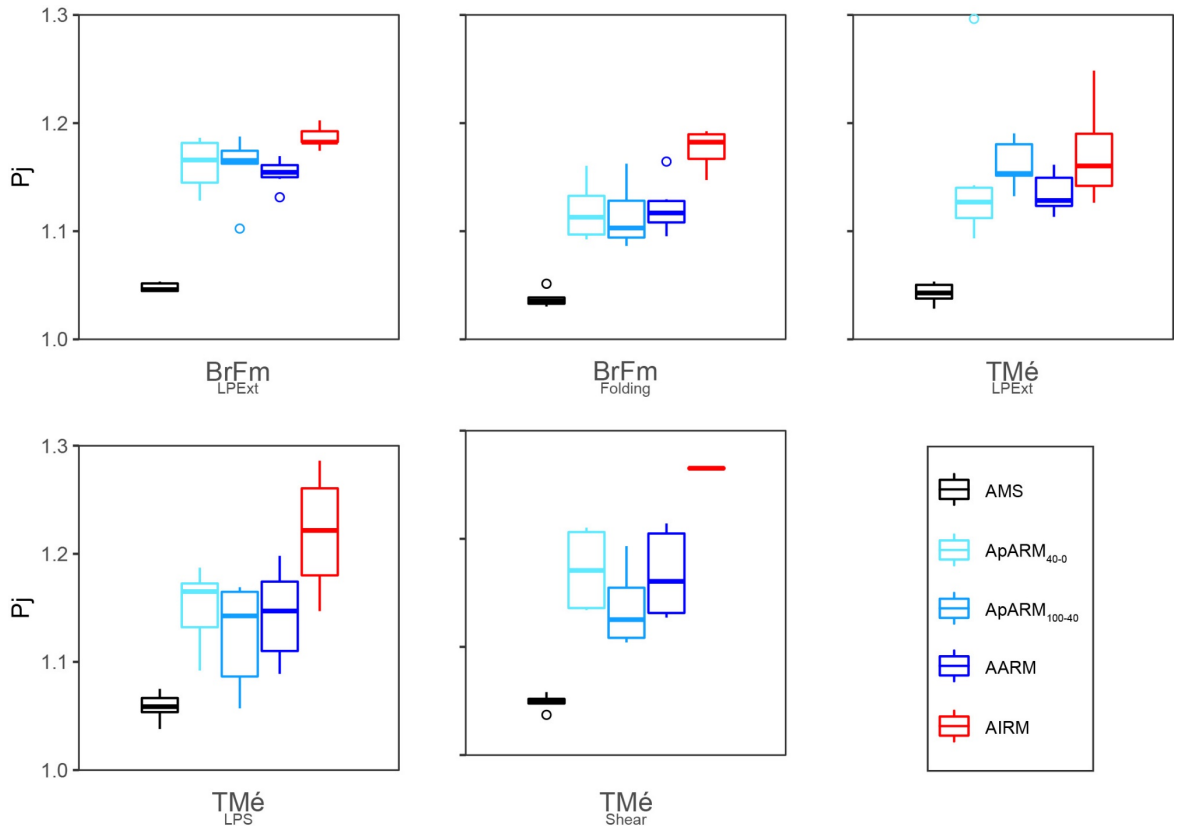

Figure 6.S 1. Box-and-whisker plots of the corrected anisotropy degree (Pj) of the AMS and ARM experiments divided by representative patterns.

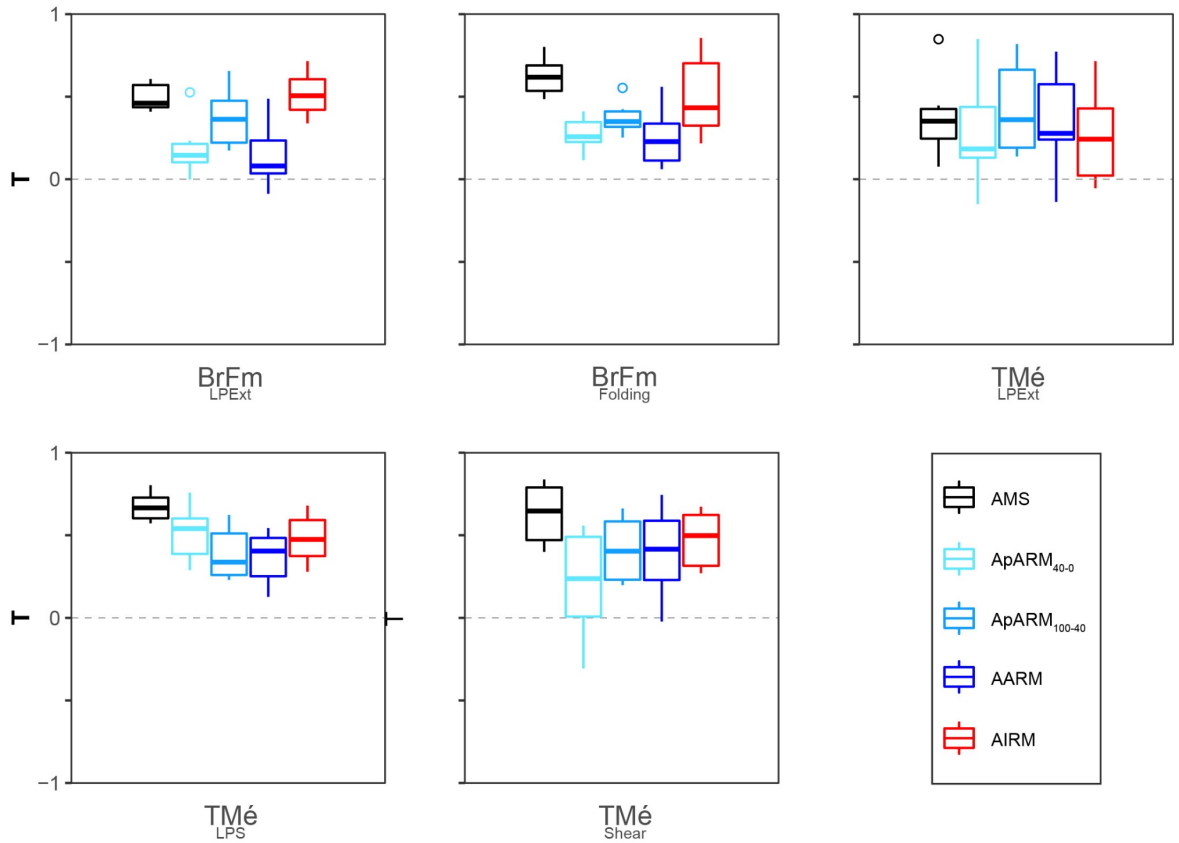

Figure 6.S 2. Box-and-whisker plots of the shape parameter (T) of the AMS and ARM experiments divided by representative patterns.

ACKNOWLEDGMENTS

This project was funded by MIUR ex-60% attributed to E. Zanella and PhD grants-Budget 10% attributed to C. Robustelli Test. Part of the field work was funded by MIUR ex-60% attributed to S. Satolli and A. Festa.

I am very grateful to Elena Zanella for strongly supporting me, but especially for involving me in several projects that allowed me to explore other scientific aspects, certainly contributing to the improvement of this project but more importantly my scientific growth during the transition to a more independent geoscientist.

I thank Andrea Festa for his constructive and insightful discussions on the geological and structural aspects of this thesis that greatly improved the research project.

I would like to thank all the scientists working at the CIMaN-ALP Laboratory, especially Luca Lanci, Matteo Maron and Zeudia Pastore, for the time spent together in the Laboratory having interesting scientific discussions.

Special thanks go to Sara Satolli for her positivity, the interesting scientific discussion that led to the publication of a significant part of this project, and especially for all the valuable advice that will surely be useful in the near future.

I am very thankful to Andrea Biedermann for arranging my stay at the LNM, sharing with me her deep knowledge about magnetic fabric during passionate discussions on various aspects of my research and future perspectives.

I gratefully acknowledge the ETH Zurich Institut für Geophysik for their support during my stay at the Laboratory for Natural Magnetism (LNM) while performing measurements with the Torque magnetometer.

Part of this work was performed as a Visiting Fellow at the Institute for Rock Magnetism (IRM) at the University of Minnesota. The IRM is a US National Multi-user Facility supported through the Instrumentation and Facilities program of the National Science Foundation, Earth Sciences Division, and by funding from the University of Minnesota. I would like to thank Dario Bilardello for performing the measurements on my behalf and for the great support in the interpretation of results. Max Brown, Joshua Feinberg, Bruce Moskowitz and Peat Solheid are thanked for helpful discussions and advice.

E. Ferrara is acknowledged for his technical support during the hysteresis measurements at the Istituto Nazionale di Ricerca Metrologica (INRiM), Torino (Italy).

I would also like to thank all the scientists I met at conferences, with a special note to Eric Ferré and Martin Chadima, for their criticisms and fruitful discussions that certainly improved the perspectives of my projects.

REFERENCES

Agrò, A., Zanella, E., Le Pennec, J.-L., & Temel, A. (2015). Magnetic fabric of ignimbrites: a case study from the Central Anatolian Volcanic Province. *Geological Society, London, Special Publications*, *396*(1), 159–175. https://doi.org/10.1144/SP396.9

Alberti, M., Decandia, F. A., & Tavarnelli, E. (1996). Modes of propagation of the compressional deformation in the Umbria-Marche Apennines. *Memorie Della Società Geologica Italiana*, *51*, 71–82.

Aldega, L., Botti, F., & Corrado, S. (2007). Clay mineral assemblages and vitrinite reflectance in the Laga Basin (Central Apennines, Italy): what do they record? *Clays and Clay Minerals*, *55*(5), 504–518. https://doi.org/10.1346/CCMN.2007.0550505

Almqvist, B. S. G., & Koyi, H. (2018). Bulk strain in orogenic wedges based on insights from magnetic fabrics in sandbox models. *Geology*, *46*(6), 483–486. https://doi.org/10.1130/G39998.1

Almqvist, B. S. G., Hirt, A. M., Schmidt, V., & Dietrich, D. (2009). Magnetic fabrics of the Morcles Nappe complex. *Tectonophysics*, *466*(1–2), 89–100. https://doi.org/10.1016/j.tecto.2008.07.014

Almqvist, B. S. G., Bender, H., Bergman, A., & Ring, U. (2020). Magnetic properties of pseudotachylytes from western Jämtland, central Swedish Caledonides. *Solid Earth*, *11*(3), 807–828. https://doi.org/10.5194/se-11-807-2020

Araki, E., Saffer, D. M., Kopf, A. J., Wallace, L. M., Kimura, T., Machida, Y., et al. (2017). Recurring and triggered slow-slip events near the trench at the Nankai Trough subduction megathrust. *Science*, *356*(6343), 1157–1160. https://doi.org/10.1126/science.aan3120

Aranguren, A., Cuevas, J., & Tubía, J. M. (1996). Composite magnetic fabrics from S-C mylonites. *Journal of Structural Geology*, *18*(7), 863–869. https://doi.org/10.1016/0191-8141(96)00013-2

Arthur, M. A., & Fischer, A. G. (1977). Upper Cretaceous–Paleocene magnetic stratigraphy at Gubbio, Italy I. Lithostratigraphy and sedimentology. *Geological Society of America Bulletin*, *88*(3), 367. https://doi.org/10.1130/0016-7606(1977)88<367:UCMSAG>2.0.CO;2

Aubourg, C., & Robion, P. (2002). Composite ferromagnetic fabrics (magnetite, greigite) measured * by AMS and partial AARM in weakly strained sandstones from western Makran, Iran. *Geophysical Journal International*, *151*(3), 729–737. https://doi.org/10.1046/j.1365-246X.2002.01800.x

Aubourg, Charles, Rochette, P., & Bergmüller, F. (1995). Composite magnetic fabric in weakly deformed black shales. *Physics of the Earth and Planetary Interiors*, *87*(3–4), 267–278. https://doi.org/10.1016/0031-9201(94)02962-B

Aubourg, Charles, Rochette, P., Stéphan, J.-F., Popoff, M., & Chabert-Pelline, C. (1999). The magnetic fabric of weakly deformed Late Jurassic shales from the southern subalpines chains (French Alps): evidence for SW-directed tectonic transport direction. *Tectonophysics*, *307*(1–2), 15–31. https://doi.org/10.1016/S0040-1951(99)00116-X

Aubourg, Charles, Smith, B., Eshraghi, A., Lacombe, O., Authemayou, C., Amrouch, K., et al. (2010). New magnetic fabric data and their comparison with palaeostress markers in the Western Fars Arc (Zagros, Iran): tectonic implications. *Geological Society, London, Special Publications*, *330*(1), 97–120. https://doi.org/10.1144/SP330.6

Aubourg, Charles, Kars, M., Pozzi, J.-P., Mazurek, M., & Grauby, O. (2021). A Magnetic Geothermometer in Moderately Buried Shales. *Minerals*, *11*(9), 957. https://doi.org/10.3390/min11090957

Averbuch, O., Frizon de Lamotte, D., & Kissel, C. (1992). Magnetic fabric as a structural indicator of the deformation path within a fold-thrust structure: a test case from the Corbières (NE Pyrenees, France). *Journal of Structural Geology*, *14*(4), 461–474. https://doi.org/10.1016/0191-8141(92)90106-7

Balestro, G., Festa, A., Dilek, Y., & Tartarotti, P. (2015). Pre-Alpine extensional tectonics of a peridotitelocalized oceanic core complex in the Late Jurassic, high-pressure Monviso ophiolite (Western Alps). *Episodes*, *38*(4), 266–282. https://doi.org/10.18814/epiiugs/2015/v38i4/82421

Balsley, J. R., & Buddington, A. F. (1960). Magnetic susceptibility anisotropy and fabric of some Adirondack granites and orthogneisses. *American Journal of Science*, *258A*, 6–20.

Barbero, E., Festa, A., Fioraso, G., & Catanzariti, R. (2017). Geology of the Curone and Staffora Valleys (NW Italy): field constraints for the Late Cretaceous – Pliocene tectono-stratigraphic evolution of Northern Apennines. *Journal of Maps*, *13*(2), 879–891. https://doi.org/10.1080/17445647.2017.1398114

Barbero, E., Festa, A., Saccani, E., Catanzariti, R., & D'Onofrio, R. (2020). Redefinition of the Ligurian Units at the Alps–Apennines junction (NW Italy) and their role in the evolution of the Ligurian accretionary wedge: constraints from mélanges and broken formations.

Journal of the Geological Society, *177*(3), 562–574. https://doi.org/10.1144/jgs2019-022

Benn, K. (1994). Overprinting of magnetic fabrics in granites by small strains: numerical modelling. *Tectonophysics*, *233*(3–4), 153–162. https://doi.org/10.1016/0040-1951(94)90238-0

Bergmüller, F., Bärlocher, C., Geyer, B., Grieder, M., Heller, F., & Zweifel, F. (1994). A torque magnetometer for measurements of the high-field anisotropy of rocks and crystals. *Measurement Science and Technology*, *5*, 1466–1470.

Bettelli, G., & Panini, F. (1987). I Mélanges Dell'Appennino Settentrionale Dal T. Tresinaro al T. Sillaro. *Memorie Della Società Geologica Italiana*, *39*, 187–214.

Bettelli, G., Bonazzi, U., Fazzini, P., Gasperi, G., Gelmini, R., & Panini, F. (1989). Nota illustrativa alla Carta geologica dell'Appennino modenese e delle aree limitrofe. *Memorie Della Società Geologica Italiana*, *39*, 487–498.

Bettelli, G., Bonazzi, U., Fazzini, P., & Panini, F. (1989). Schema introduttivo alla geologia delle Epiliguridi dell'Appennino modenese e delle aree limitrofe. *Memorie Della Società Geologica Italiana*, *39*, 215–244.

Bettelli, Giuseppe, & Vannucchi, P. (2003). Structural style of the offscraped Ligurian oceanic sequences of the Northern Apennines: new hypothesis concerning the development of mélange block-in-matrix fabric. *Journal of Structural Geology*, *25*(3), 371–388. https://doi.org/10.1016/S0191-8141(02)00026-3

Biedermann, A., & Bilardello, D. (2021). Practical Magnetism VII: Avoiding common misconceptions in magnetic fabric interpretation. *The IRM Quarterly University of Minnesota*, *31*(3).

Biedermann, A. R. (2020). Current challenges and future developments in magnetic fabric research. *Tectonophysics*, *795*, 228632. https://doi.org/10.1016/j.tecto.2020.228632

Biedermann, A. R., Bilardello, D., Jackson, M., Tauxe, L., & Feinberg, J. M. (2019). Grain-size-dependent remanence anisotropy and its implications for paleodirections and paleointensities – Proposing a new approach to anisotropy corrections. *Earth and Planetary Science Letters*, *512*, 111–123. https://doi.org/10.1016/j.epsl.2019.01.051

Biedermann, A. R., Jackson, M., Stillinger, M. D., Bilardello, D., & Feinberg, J. M. (2020). Anisotropy of Full and Partial Anhysteretic Remanence Across Different Rock Types: 1—Are Partial Anhysteretic Remanence Anisotropy Tensors Additive? *Tectonics*, *39*(2). https://doi.org/10.1029/2018TC005284

Biedermann, A. R., Jackson, M., Bilardello, D., & Feinberg, J. M. (2020). Anisotropy of Full and Partial Anhysteretic Remanence Across Different Rock Types: 2—Coercivity Dependence of Remanence Anisotropy. *Tectonics*, *39*(2). https://doi.org/10.1029/2018TC005285

Bilardello, D., & Jackson, M. J. (2014). A comparative study of magnetic anisotropy measurement techniques in relation to rock-magnetic properties. *Tectonophysics*, *629*, 39–54. https://doi.org/10.1016/j.tecto.2014.01.026

Bloemendal, J., King, J. W., Hall, F. R., & Doh, S.-J. (1992). Rock magnetism of Late Neogene and Pleistocene deep-sea sediments: Relationship to sediment source, diagenetic processes, and sediment lithology. *Journal of Geophysical Research*, *97*(B4), 4361. https://doi.org/10.1029/91JB03068

Boccaletti, M., & Coli, M. (1982). Carta strutturale dell'Appennino settentrionale. In *Progetto Finalizzato Geodinamica, Sottoprogetto 5* (Vol. 429). S.El.Ca. Scale 1:250,000 3 Sheets; CNR: Firenze, Italy.

Boccaletti, M., Coli, M., Decandia, F. A., Giannini, E., & Lazzarotto, A. (1980). Evoluzione dell'Appennino settentrionale secondo un nuovo modello strutturale. *Memorie Della Società Geologica Italiana*, *21*, 359–373.

Boccaletti, M., Calamita, F., & Viandante, M. G. (2005). 2005. La Neo-Catena litosferica appenninica nata a partire dal Pliocene inferiore come espressione della convergenza Africa- Europa. 124, 87–105. *Bollettino Della Società Geologica Italiana*, *124*, 87–105.

Borradaile, G., & Brown, H. (1987). The Shebandowan group: "Timiskaming-like" Archean rocks in northwestern Ontario. *Canadian Journal of Earth Sciences*, *24*(1), 185–188. https://doi.org/10.1139/e87-016

Borradaile, G.J., & Alford, C. (1988). Experimental shear zones and magnetic fabrics. *Journal of Structural Geology*, *10*(8), 895–904. https://doi.org/10.1016/0191-8141(88)90102-2

Borradaile, G.J., & Henry, B. (1997). Tectonic applications of magnetic susceptibility and its anisotropy. *Earth-Science Reviews*, *42*(1–2), 49–93. https://doi.org/10.1016/S0012-8252(96)00044-X

Borradaile, G.J., & Puumala, M. A. (1989). Synthetic magnetic fabrics in a plasticene medium. *Tectonophysics*, *164*(1), 73–78. https://doi.org/10.1016/0040-1951(89)90235-7

Borradaile, G.J., Tella, S., & McArthur, J. (1989). Magnetic fabric as a kinematic indicator of faults: a test case. *Ann. Tectonicae*, *3*, 3–11.

Borradaile, Graham. (1987). Anisotropy of magnetic susceptibility: rock composition versus strain. *Tectonophysics*, *138*(2–4), 327–329. https://doi.org/10.1016/0040-1951(87)90051-5

Borradaile, Graham. (2003). *Statistics of Earth Science Data*. Berlin, Heidelberg: Springer Berlin Heidelberg. https://doi.org/10.1007/978-3-662-05223-5

Borradaile, Graham, & Alford, C. (1987). Relationship between magnetic susceptibility and strain in laboratory experiments. *Tectonophysics*, *133*(1–2), 121–135. https://doi.org/10.1016/0040-1951(87)90285-X

Borradaile, Graham J. (1991). Correlation of strain with anisotropy of magnetic susceptibility (AMS). *Pure and Applied Geophysics PAGEOPH*, *135*(1), 15–29. https://doi.org/10.1007/BF00877006

Borradaile, Graham J. (2001). Magnetic fabrics and petrofabrics: their orientation distributions and anisotropies. *Journal of Structural Geology*, *23*(10), 1581–1596. https://doi.org/10.1016/S0191-8141(01)00019-0

Borradaile, Graham J., & Hamilton, T. (2004). Magnetic fabrics may proxy as neotectonic stress trajectories, Polis rift, Cyprus. *Tectonics*, *23*(1). https://doi.org/10.1029/2002TC001434

Borradaile, Graham J., & Jackson, M. (2004). Anisotropy of magnetic susceptibility (AMS): magnetic petrofabrics of deformed rocks. *Geological Society, London, Special Publications*, *238*(1), 299–360. https://doi.org/10.1144/GSL.SP.2004.238.01.18

Borradaile, Graham J., & Jackson, M. (2010). Structural geology, petrofabrics and magnetic fabrics (AMS, AARM, AIRM). *Journal of Structural Geology*, *32*(10), 1519–1551. https://doi.org/10.1016/j.jsg.2009.09.006

Borradaile, Graham J., & Tarling, D. H. (1981). The influence of deformation mechanisms on magnetic fabrics in weakly deformed rocks. *Tectonophysics*, *77*(1–2), 151–168. https://doi.org/10.1016/0040-1951(81)90165-7

Borradaile, Graham John. (1981). Particulate flow of rock and the formation of cleavage. *Tectonophysics*, *72*(3–4), 305–321. https://doi.org/10.1016/0040-1951(81)90243-2

Borradaile, Graham John. (1988). Magnetic susceptibility, petrofabrics and strain. *Tectonophysics*, *156*(1–2), 1–20. https://doi.org/10.1016/0040-1951(88)90279-X

Braun, D., Weinberger, R., Eyal, Y., Feinstein, S., Harlavan, Y., & Levi, T. (2015). Distinctive diamagnetic fabrics in dolostones evolved at fault cores, the Dead Sea Transform. *Journal of Structural Geology*, *77*, 11–26. https://doi.org/10.1016/j.jsg.2015.05.007

Bullock, R. J., De Paola, N., Holdsworth, R. E., & Trabucho-Alexandre, J. (2014). Lithological controls on the deformation mechanisms operating within carbonate-hosted faults during the seismic cycle. *Journal of Structural Geology*, *58*, 22–42. https://doi.org/10.1016/j.jsg.2013.10.008

Butler, R. W. H., Tavarnelli, E., & Grasso, M. (2006). Structural inheritance in mountain belts: An Alpine–Apennine perspective. *Journal of Structural Geology*, *28*(11), 1893–1908. https://doi.org/10.1016/j.jsg.2006.09.006

Byrne, T., Brückmann, W., Owens, W. H., Lallemant, S., & Maltman, A. J. (1993). Structural Synthesis: Correlation of Structural Fabrics, Velocity Anisotropy, and Magnetic Susceptibility Data. In I. A. Hill, A. Taira, J. V. Firth, & et al. (Eds.), *Proceedings of the Ocean Drilling Program, 131 Scientific Results* (Vol. 131). Ocean Drilling Program. https://doi.org/10.2973/odp.proc.sr.131.1993

Calamita, F., Deiana, G., Invernizzi, C., & Mastrovincenzo, S. (1987). Analisi strutturale della «Linea Amona-Anzio» Auct. tra Cittareale e Micigliano (Rieti). *Bollettino Della Società Geologica Italiana*, *106*, 365–375.

Calamita, F., Decandia, F. A., Deiana, G., & Fiori, A. P. (1991). Deformation of SC tectonites in the Scaglia Cinera Formation in the Spoleto area (Southeast Umbria). *Bollettino Della Società Geologica Italiana*, *110*, 661–665.

Calamita, F., Coltorti, M., Piccinini, D., Pierantoni, P. P., Pizzi, A., Ripepe, M., et al. (2000). Quaternary faults and seismicity in the Umbro-Marchean Apennines (Central Italy): evidence from the 1997 Colfiorito earthquake. *Journal of Geodynamics*, *29*(3–5), 245–264. https://doi.org/10.1016/S0264-3707(99)00054-X

Calamita, F., Satolli, S., & Turtù, A. (2012). Analysis of thrust shear zones in curve-shaped belts: Deformation mode and timing of the Olevano-Antrodoco-Sibillini thrust (Central/Northern Apennines of Italy). *Journal of Structural Geology*, *44*, 179–187. https://doi.org/10.1016/j.jsg.2012.07.007

Calamita, Fernando. (1991). Extensional mesostructures in thrust shear zones examples from the Umbro-Marchean Apennines. *Bollettino Della Società Geologica Italiana*, *110*, 649–660.

Camerlenghi, A., & Pini, G. A. (2009). Mud volcanoes, olistostromes and Argille scagliose in the Mediterranean region. *Sedimentology*, *56*(1), 319–365. https://doi.org/10.1111/j.1365-3091.2008.01016.x

Cañón-Tapia, E., & Pinkerton, H. (2000). The anisotropy of magnetic susceptibility of lava flows: an experimental approach. *Journal of Volcanology and Geothermal Research*, *98*(1–4), 219–233. https://doi.org/10.1016/S0377-0273(99)00155-9

Caricchi, C., Cifelli, F., Kissel, C., Sagnotti, L., & Mattei, M. (2016). Distinct magnetic fabric in weakly deformed sediments from extensional basins and fold-and-thrust structures in the Northern Apennine orogenic belt (Italy). *Tectonics*, *35*(2), 238–256. https://doi.org/10.1002/2015TC003940

Carlini, M., Artoni, A., Aldega, L., Balestrieri, M. L., Corrado, S., Vescovi, P., et al. (2013). Exhumation and reshaping of far-travelled/allochthonous tectonic units in mountain belts. New insights for the relationships between shortening and coeval extension in the western Northern Apennines (Italy). *Tectonophysics*, *608*, 267–287. https://doi.org/10.1016/j.tecto.2013.09.029

Carter-Stiglitz, B., Moskowitz, B., & Jackson, M. (2004). More on the low-temperature magnetism of stable single domain magnetite: Reversibility and non-stoichiometry: Reversibility and non-stoichiometry of magnetite. *Geophysical Research Letters*, *31*(6), n/a-n/a. https://doi.org/10.1029/2003GL019155

Casas-Sainz, A. M., Román-Berdiel, T., Oliva-Urcia, B., García-Lasanta, C., Villalaín, J. J., Aldega, L., et al. (2017). Multidisciplinary approach to constrain kinematics of fault zones at shallow depths: a case study from the Cameros–Demanda thrust (North Spain). *International Journal of Earth Sciences*, *106*(3), 1023–1055. https://doi.org/10.1007/s00531-016-1349-5

Casas-Sainz, A. M., Gil-Imaz, A., Simón, J. L., Izquierdo-Llavall, E., Aldega, L., Román-Berdiel, T., et al. (2018). Strain indicators and magnetic fabric in intraplate fault zones: Case study of Daroca thrust, Iberian Chain, Spain. *Tectonophysics*, *730*, 29–47. https://doi.org/10.1016/j.tecto.2018.02.013

Castellarin, A. (1994). Strutturazione eo-mesoalpina dell'Appennino Settentrionale attorno al nodo ligure. In R. Capozzi & A. Castellarin (Eds.), *tudi preliminari all'acquisizione dati del profilo CROP 1–1A La Spezia–Alpi orientali* (Studi Geol. Camerti, Vol. 1992/2, pp. 99–108). Università degli Studi di Camerino: Camerino, Italy.

Castellarin, A., Colacicchi, R., Praturlon, A., & Cantelli, C. (1982). The Jurassic-lower Pliocene history of the Ancona-Anzio Line (Central Italy). *Memorie Della Società Geologica Italiana*, *24*, 325–336.

Centamore, E., & Micarelli, A. (1991). L'ambiente fisico delle Marche. Geologia, Geomorfologia, Idrogeologia.

Cerchiari, A., Fukuchi, R., Gao, B., Hsiung, K.-H., Jaeger, D., Kaneki, S., et al. (2018). IODP workshop: Core-Log Seismic Investigation at Sea – Integrating legacy data to address outstanding research questions in the Nankai Trough Seismogenic Zone Experiment. *Scientific Drilling*, *24*, 93–107. https://doi.org/10.5194/sd-24-93-2018

Cerchiari, A., Remitti, F., Mittempergher, S., Festa, A., Lugli, F., & Cipriani, A. (2020). Cyclical variations of fluid sources and stress state in a shallow megathrust-zone mélange. *Journal of the Geological Society*, *177*(3), 647–659. https://doi.org/10.1144/jgs2019-072

CerrinaFeroni, A., Ottria, G., & Ellero, A. (2004). The northern Apennine, Italy: Geological structure and transpressive evolution. In U. Crescenti, S. D'offizi, S. Merlino, & L. Sacchi (Eds.), *Geology of Italy* (Geological Society of Italy, pp. 15–32). Florence, Italy.

Chadima, M., & Jelínek, V. (2008). Anisoft 4.2.–Anisotropy data browser. In *Proceedings paleo, rock and environmental magnetism, 11th Castle Meeting, Contribution to Geophysics and Geodesy* (p. 41).

Chadima, Martin, Pruner, P., Šlechta, S., Grygar, T., & Hirt, A. M. (2006). Magnetic fabric variations in Mesozoic black shales, Northern Siberia, Russia: Possible paleomagnetic implications. *Tectonophysics*, *418*(1–2), 145–162. https://doi.org/10.1016/j.tecto.2005.12.018

Chang, L., Winklhofer, M., Roberts, A. P., Heslop, D., Florindo, F., Dekkers, M. J., et al. (2013). Low-temperature magnetic properties of pelagic carbonates: Oxidation of biogenic magnetite and identification of magnetosome chains. *Journal of Geophysical Research: Solid Earth*, *118*(12), 6049–6065. https://doi.org/10.1002/2013JB010381

Chang, L., Heslop, D., Roberts, A. P., Rey, D., & Mohamed, K. J. (2016). Discrimination of biogenic and detrital magnetite through a double Verwey transition temperature. *Journal of Geophysical Research: Solid Earth*, *121*(1), 3–14. https://doi.org/10.1002/2015JB012485

Chester, F. M., Rowe, C., Ujiie, K., Kirkpatrick, J., Regalla, C., Remitti, F., et al. (2013). Structure and Composition of the Plate-Boundary Slip Zone for the 2011 Tohoku-Oki Earthquake. *Science*, *342*(6163), 1208–1211. https://doi.org/10.1126/science.1243719

Chou, Y., Aubourg, C., Yeh, E., Song, S., Lin, Y., Humbert, F., et al. (2020). The Magnetic Fabric of Gouge Mimics the Coseismic Focal Mechanism of the Chi-Chi Earthquake (1999, Mw 7.6). *Geophysical Research Letters*, *47*(22). https://doi.org/10.1029/2020GL090111

Chou, Y.-M., Song, S.-R., Aubourg, C., Lee, T.-Q., Boullier, A.-M., Song, Y.-F., et al. (2012). An earthquake slip zone is a magnetic recorder. *Geology*, *40*(6), 551–554. https://doi.org/10.1130/G32864.1

Chou, Yu-Min, Song, S.-R., Aubourg, C., Song, Y.-F., Boullier, A.-M., Lee, T.-Q., et al. (2012). Pyrite alteration and neoformed magnetic minerals in the fault zone of the Chi-Chi earthquake (M_w 7.6, 1999): Evidence for frictional heating and co-seismic fluids. *Geochemistry, Geophysics, Geosystems*, *13*(8), n/a-n/a. https://doi.org/10.1029/2012GC004120

Chou, Yu-Min, Song, S.-R., Aubourg, C., Lee, T.-Q., Song, Y.-F., & Yeh, E.-C. (2014). Quantitative modeling of the newly formed magnetic minerals in the fault gouge of 1999 Chi-Chi earthquake (M_w 7.6), Taiwan. *Journal of Geophysical Research: Solid Earth*, *119*(9), 6771–6781. https://doi.org/10.1002/2014JB011098

Ciarapica, G., & Passeri, L. (2002). The Paleogeographic Duplicity of the Apennines. *Bollettino Della Società Geologica Italiana*, *1*, 67–75.

Cifelli, F., Mattei, M., Hirt, A. M., & Günther, A. (2004). The origin of tectonic fabrics in "undeformed" clays: The early stages of deformation in extensional sedimentary basins. *Geophysical Research Letters*, *31*(9), n/a-n/a. https://doi.org/10.1029/2004GL019609

Cifelli, F, Mattei, M., Chadima, M., Hirt, A., & Hansen, A. (2005). The origin of tectonic lineation in extensional basins: Combined neutron texture and magnetic analyses on "undeformed" clays. *Earth and Planetary Science Letters*, *235*(1–2), 62–78. https://doi.org/10.1016/j.epsl.2005.02.042

Cifelli, F., Mattei, M., Chadima, M., Lenser, S., & Hirt, A. M. (2009). The magnetic fabric in "undeformed clays": AMS and neutron texture analyses from the Rif Chain (Morocco). *Tectonophysics*, *466*(1–2), 79–88. https://doi.org/10.1016/j.tecto.2008.08.008

Cifelli, Francesca, Ballato, P., Alimohammadian, H., Sabouri, J., & Mattei, M. (2015). Tectonic magnetic lineation and oroclinal bending of the Alborz range: Implications on the Iran-Southern Caspian geodynamics: oroclinal bending of the Alborz Range. *Tectonics*, *34*(1), 116–132. https://doi.org/10.1002/2014TC003626

Cipollari, P., & Cosentino, D. (1995). Miocene unconformities in the Central Apennines: geodynamic significance and sedimentary basin evolution. *Tectonophysics*, *252*(1–4), 375–389. https://doi.org/10.1016/0040-1951(95)00088-7

Clendenen, W. S., Kligfield, R., Hirt, A. M., & Lowrie, W. (1988). Strain studies of cleavage development in the Chelmsford Formation, Sudbury Basin, Ontario. *Tectonophysics*, *145*(3–4), 191–211. https://doi.org/10.1016/0040-1951(88)90195-3

Codegone, G., Festa, A., Dilek, Y., & Pini, G. A. (2012). Small-scale polygenetic mélanges in the Ligurian accretionary complex, Northern Apennines, Italy, and the role of shale diapirism in superposed mélange evolution in orogenic belts. *Tectonophysics*, *568–569*, 170–184. https://doi.org/10.1016/j.tecto.2012.02.003

Collot, J.-Y., Ribodetti, A., Agudelo, W., & Sage, F. (2011). The South Ecuador subduction channel: Evidence for a dynamic mega-shear zone from 2D fine-scale seismic reflection imaging and implications for material transfer. *Journal of Geophysical Research: Solid Earth*, *116*(B11), n/a-n/a. https://doi.org/10.1029/2011JB008429

Constable, C., & Tauxe, L. (1990). The bootstrap for magnetic susceptibility tensors. *Journal of Geophysical Research*, *95*(B6), 8383. https://doi.org/10.1029/JB095iB06p08383

Cornamusini, G. C., Conti, P. C., & Bambini, A. M. B. (2018). The Late Oligocene to Early Miocene foredeep basin system evolution of the Northern Apennines (Emilia-Tuscany, Italy): review and new litho-biostratigraphic data. *Italian Journal of Geosciences*, *137*(3), 396–419. https://doi.org/10.3301/IJG.2018.06

Cowan, D. S. (1985). Structural styles in Mesozoic and Cenozoic mélanges in the western Cordillera of North America. *Geological Society of America Bulletin*, *96*, 451–462.

Cronin, M., Tauxe, L., Constable, C., Selkin, P., & Pick, T. (2001). Noise in the quiet zone. *Earth and Planetary Science Letters*, *190*(1–2), 13–30. https://doi.org/10.1016/S0012-821X(01)00354-5

Day, R., Fuller, M., & Schmidt, V. A. (1977). Hysteresis properties of titanomagnetites: Grain-size and compositional dependence. *Physics of the Earth and Planetary Interiors*, *13*(4), 260–267. https://doi.org/10.1016/0031-9201(77)90108-X

Dearing, J. A., Dann, R. J. L., Hay, K., Lees, J. A., Loveland, P. J., Maher, B. A., & O'Grady, K. (1996). Frequency-dependent susceptibility measurements of environmental materials. *Geophysical Journal International*, *124*(1), 228–240. https://doi.org/10.1111/j.1365-246X.1996.tb06366.x

Dekkers, M. J. (1989). Magnetic Properties of Natural Goethite-Ii. Trm Behaviour During Thermal and Alternating Field Demagnetization and Low-Temperature Treatment. *Geophysical Journal International*, *97*(2), 341–355. https://doi.org/10.1111/j.1365-246X.1989.tb00505.x

Dekkers, M. J., Mattéi, J.-L., Fillion, G., & Rochette, P. (1989). Grain-size dependence of the magnetic behavior of pyrrhotite during its low-temperature transition at 34 K. *Geophysical Research Letters*, *16*(8), 855–858. https://doi.org/10.1029/GL016i008p00855

Dellisanti, F., Pini, G. A., & Baudin, F. (2010). Use of T_{max} as a thermal maturity indicator in orogenic successions and comparison with clay mineral evolution. *Clay Minerals*, *45*(1), 115–130. https://doi.org/10.1180/claymin.2010.045.1.115

Dewey, J. F., Helman, M. L., Knott, S. D., Turco, E., & Hutton, D. H. W. (1989). Kinematics of the western Mediterranean. *Geological Society, London, Special Publications*, *45*(1), 265–283. https://doi.org/10.1144/GSL.SP.1989.045.01.15

Di Domenica, A., Turtù, A., Satolli, S., & Calamita, F. (2012). Relationships between thrusts and normal faults in curved belts: New insight in the inversion tectonics of the Central-Northern Apennines (Italy). *Journal of Structural Geology*, *42*, 104–117. https://doi.org/10.1016/j.jsg.2012.06.008

Dielforder, A., Vollstaedt, H., Vennemann, T., Berger, A., & Herwegh, M. (2015). Linking megathrust earthquakes to brittle deformation in a fossil accretionary complex.

Nature Communications, *6*(1), 7504. https://doi.org/10.1038/ncomms8504

Dragert, H., Wang, K., & James, T. S. (2001). A Silent Slip Event on the Deeper Cascadia Subduction Interface. *Science*, *292*(5521), 1525–1528. https://doi.org/10.1126/science.1060152

Dunlop, D. J. (2002a). Theory and application of the Day plot (M_{rs} / M_s versus H_{cr} / H_c) 1. Theoretical curves and tests using titanomagnetite data. *Journal of Geophysical Research*, *107*(B3), 2056. https://doi.org/10.1029/2001JB000486

Dunlop, D. J. (2002b). Theory and application of the Day plot (M_{rs} / M_s versus H_{cr} / H_c) 2. Application to data for rocks, sediments, and soils. *Journal of Geophysical Research*, *107*(B3), 2057. https://doi.org/10.1029/2001JB000487

Ejembi, J. I., Ferré, E. C., Satolli, S., & Friedman, S. A. (2020). Post-Depositional Fluid Flow in Jurassic Sandstones of the Uncompahgre Uplift: Insights From Magnetic Fabrics. *Frontiers in Earth Science*, *8*, 601415. https://doi.org/10.3389/feart.2020.601415

Elter, P., Grasso, M., Parotto, M., & Vezzani, L. (2003). Structural setting of the Apennine-Maghrebian thrust belt. *Episodes*, *26*(3), 205–211. https://doi.org/10.18814/epiiugs/2003/v26i3/009

Evans, M. A., Lewchuk, M. T., & Elmore, R. D. (2003). Strain partitioning of deformation mechanisms in limestones: examining the relationship of strain and anisotropy of magnetic susceptibility (AMS). *Journal of Structural Geology*, *25*(9), 1525–1549. https://doi.org/10.1016/S0191-8141(02)00186-4

Fabian, K. (2003). Some additional parameters to estimate domain state from isothermal magnetization measurements. *Earth and Planetary Science Letters*, *213*(3–4), 337–345. https://doi.org/10.1016/S0012-821X(03)00329-7

Fagereng, Å., Savage, H. M., Morgan, J. K., Wang, M., Meneghini, F., Barnes, P. M., et al. (2019). Mixed deformation styles observed on a shallow subduction thrust, Hikurangi margin, New Zealand. *Geology*, *47*(9), 872–876. https://doi.org/10.1130/G46367.1

Fagereng, Åke, & Sibson, R. H. (2010). Mélange rheology and seismic style. *Geology*, *38*(8), 751–754. https://doi.org/10.1130/G30868.1

Fagereng, Åke, Remitti, F., & Sibson, R. H. (2011). Incrementally developed slickenfibers — Geological record of repeating low stress-drop seismic events? *Tectonophysics*, *510*(3–4), 381–386. https://doi.org/10.1016/j.tecto.2011.08.015

Fagereng, Åke, Hillary, G. W. B., & Diener, J. F. A. (2014). Brittle-viscous deformation, slow slip, and tremor. *Geophysical Research Letters*, *41*(12), 4159–4167. https://doi.org/10.1002/2014GL060433

Famin, V., Raimbourg, H., Andreani, M., & Boullier, A.-M. (2021). Deformation-enhanced diagenesis and bacterial proliferation in the Nankai accretionary prism. *Solid Earth*, *12*(9), 2067–2085. https://doi.org/10.5194/se-12-2067-2021

Ferré, E. C. (2002). Theoretical models of intermediate and inverse AMS fabrics. *Geophysical Research Letters*, *29*(7), 1127. https://doi.org/10.1029/2001GL014367

Ferré, E. C., Martín-Hernández, F., Teyssier, C., & Jackson, M. (2004). Paramagnetic and ferromagnetic anisotropy of magnetic susceptibility in migmatites: measurements in high and low fields and kinematic implications. *Geophysical Journal International*, *157*(3), 1119–1129. https://doi.org/10.1111/j.1365-246X.2004.02294.x

Ferré, E. C., Gébelin, A., Till, J. L., Sassier, C., & Burmeister, K. C. (2014). Deformation and magnetic fabrics in ductile shear zones: A review. *Tectonophysics*, *629*, 179–188. https://doi.org/10.1016/j.tecto.2014.04.008

Festa, A., Dilek, Y., Pini, G. A., Codegone, G., & Ogata, K. (2012). Mechanisms and processes of stratal disruption and mixing in the development of mélanges and broken formations: Redefining and classifying mélanges. *Tectonophysics*, *568–569*, 7–24. https://doi.org/10.1016/j.tecto.2012.05.021

Festa, A., Dilek, Y., Codegone, G., Cavagna, S., & Pini, G. A. (2013). Structural anatomy of the Ligurian accretionary wedge (Monferrato, NW Italy), and evolution of superposed melanges. *Geological Society of America Bulletin*, *125*(9–10), 1580–1598. https://doi.org/10.1130/B30847.1

Festa, Andrea, & Codegone, G. (2013). Geological map of the External Ligurian Units in western Monferrato (Tertiary Piedmont Basin, NW Italy). *Journal of Maps*, *9*(1), 84–97. https://doi.org/10.1080/17445647.2012.757711

Festa, Andrea, Pini, G. A., Dilek, Y., Codegone, G., Vezzani, L., Ghisetti, F., et al. (2010). Peri-Adriatic mélanges and their evolution in the Tethyan realm. *International Geology Review*, *52*(4–6), 369–403. https://doi.org/10.1080/00206810902949886

Festa, Andrea, Fioraso, G., Bissacca, E., & Petrizzo, M. R. (2015). Geology of the Villalvernia – Varzi Line Between Scrivia and Curone valleys (NW Italy). *Journal of Maps*, *11*(1), 39–55. https://doi.org/10.1080/17445647.2014.959569

Festa, Andrea, Ogata, K., Pini, G. A., Dilek, Y., & Codegone, G. (2015). Late Oligocene–early Miocene olistostromes (sedimentary mélanges) as tectono-stratigraphic constraints to the geodynamic evolution of the exhumed Ligurian accretionary complex (Northern Apennines, NW

Italy). *International Geology Review*, *57*(5–8), 540–562. https://doi.org/10.1080/00206814.2014.931260

Festa, Andrea, Ogata, K., Pini, G. A., Dilek, Y., & Alonso, J. L. (2016). Origin and significance of olistostromes in the evolution of orogenic belts: A global synthesis. *Gondwana Research*, *39*, 180–203. https://doi.org/10.1016/j.gr.2016.08.002

Festa, Andrea, Pini, G. A., Ogata, K., & Dilek, Y. (2019). Diagnostic features and field-criteria in recognition of tectonic, sedimentary and diapiric mélanges in orogenic belts and exhumed subduction-accretion complexes. *Gondwana Research*, *74*, 7–30. https://doi.org/10.1016/j.gr.2019.01.003

Festa, Andrea, Cavagna, S., Barbero, E., Catanzariti, R., & Pini, G. A. (2020). Mid-Eocene giant slope failure (sedimentary mélanges) in the Ligurian accretionary wedge (NW Italy) and relationships with tectonics, global climate change and the dissociation of gas hydrates. *Journal of the Geological Society*, *177*(3), 575–586. https://doi.org/10.1144/jgs2019-020

Festa, Andrea, Balestro, G., Borghi, A., De Caroli, S., & Succo, A. (2020). The role of structural inheritance in continental break-up and exhumation of Alpine Tethyan mantle (Canavese Zone, Western Alps). *Geoscience Frontiers*, *11*(1), 167–188. https://doi.org/10.1016/j.gsf.2018.11.007

Festa, Andrea, Barbero, E., Remitti, F., Ogata, K., & Pini, G. A. (2022). Mélanges and chaotic rock units: Implications for exhumed subduction complexes and orogenic belts. *Geosystems and Geoenvironment*, *1*(2), 100030. https://doi.org/10.1016/j.geogeo.2022.100030

Fuller, M. D. (1960). Anisotropy of Susceptibility and the Natural Remanent Magnetization of Some Welsh Slates. *Nature*, *186*(4727), 791–792. https://doi.org/10.1038/186791a0

Fuller, M. D. (1963). Magnetic anisotropy and paleomagnetism. *Journal of Geophysical Research*, *68*(1), 293–309. https://doi.org/10.1029/JZ068i001p00293

García-Lasanta, C., Oliva-Urcia, B., Casas-Sainz, A. M., Román-Berdiel, T., Izquierdo-Llavall, E., Soto, R., et al. (2018). Inversion tectonics and magnetic fabrics in Mesozoic basins of the Western Tethys: A review. *Tectonophysics*, *745*, 1–23. https://doi.org/10.1016/j.tecto.2018.08.005

Ghisetti, F. (1987). Mechanisms of thrust faulting in the gran sasso chain, central apennines, italy. *Journal of Structural Geology*, *9*(8), 955–967. https://doi.org/10.1016/0191-8141(87)90004-6

Ghisetti, F., & Vezzani, L. (1997). Interfering paths of deformation and development of arcs in the fold-and-thrust belt of the central Apennines (Italy). *Tectonics*, *16*(3), 523–536. https://doi.org/10.1029/97TC00117

Goldstein, A. G. (1980). Magnetic susceptibility anisotropy of mylonites from the Lake Char mylonite zone, southeastern New England. *Tectonophysics*, *66*(1–3), 197–211. https://doi.org/10.1016/0040-1951(80)90046-3

Graham, J. W. (1954). Magnetic susceptibility anisotropy, an unexploited petrofabric element., *65*, 1257–1258.

Graham, J. W. (1966). Significance of Magnetic Anisotropy in Appalachian Sedimentary Rocks. In J. S. Steinhart & T. J. Smith (Eds.), *The Earth beneath the continents, Geophysical Monograph Series* (Vol. 10, pp. 627–648). American Geophysical Union (AGU). https://doi.org/10.1029/GM010p0627

Greve, A., Kars, M., Zerbst, L., Stipp, M., & Hashimoto, Y. (2020). Strain partitioning across a subduction thrust fault near the deformation front of the Hikurangi subduction margin, New Zealand: A magnetic fabric study on IODP Expedition 375 Site U1518. *Earth and Planetary Science Letters*, *542*, 116322. https://doi.org/10.1016/j.epsl.2020.116322

Greve, A., Kars, M., & Dekkers, M. J. (2021). Fluid Accumulation, Migration and Anaerobic Oxidation of Methane Along a Major Splay Fault at the Hikurangi Subduction Margin (New Zealand): A Magnetic Approach. *Journal of Geophysical Research: Solid Earth*, *126*(2). https://doi.org/10.1029/2020JB020671

Hamilton, N. E., & Ferry, M. (2018). ggtern: Ternary Diagrams Using ggplot2. *Journal of Statistical Software*, *87*(Code Snippet 3). https://doi.org/10.18637/jss.v087.c03

Heslop, D., Dekkers, M. J., Kruiver, P. P., & Van Oorschot, I. H. M. (2002). Analysis of isothermal remanent magnetization acquisition curves using the expectation-maximization algorithm. *Geophysical Journal International*, *148*(1), 58–64. https://doi.org/10.1046/j.0956-540x.2001.01558.x

Hext, G. R. (1963). The Estimation of Second-Order Tensors, with Related Tests and Designs. *Biometrika*, *50*(3/4), 353. https://doi.org/10.2307/2333905

Hirt, A. M. (2007). Magnetic remanence, anisotropy. In D. Gubbins & E. Herrero-Bervera (Eds.), *Encyclopedia of Geomagnetism and Paleomagnetism* (pp. 535–540). Dordrecht: Springer Netherlands. https://doi.org/10.1007/978-1-4020-4423-6_186

Hirt, A. M., Lowrie, W., Clendenen, W. S., & Kligfield, R. (1988). The correlation of magnetic anisotropy with strain in the Chelmsford Formation of the Sudbury Basin, Ontario. *Tectonophysics*, *145*(3–4), 177–189. https://doi.org/10.1016/0040-1951(88)90194-1

Hirt, A. M., Banin, A., & Gehring, A. U. (1993). Thermal generation of ferromagnetic minerals from iron-enriched smectites. *Geophysical Journal International*, *115*(3), 1161–1168. https://doi.org/10.1111/j.1365-246X.1993.tb01518.x

Hirt, A. M., Lowrie, W., Lüneburg, C., Lebit, H., & Engelder, T. (2004). Magnetic and mineral fabric development in the Ordovician Martinsburg Formation in the Central Appalachian Fold and Thrust Belt, Pennsylvania. *Geological Society, London, Special Publications*, *238*(1), 109–126. https://doi.org/10.1144/GSL.SP.2004.238.01.09

Hounslow, M. W. (1985). Magnetic fabric arising from paramagnetic phyllosilicate minerals in mudrocks. *Journal of the Geological Society*, *142*(6), 995–1006. https://doi.org/10.1144/gsjgs.142.6.0995

Housen, B. A., & Kanamatsu, T. (2003). Magnetic fabrics from the Costa Rica margin: sediment deformation during the initial dewatering and underplating process. *Earth and Planetary Science Letters*, *206*(1–2), 215–228. https://doi.org/10.1016/S0012-821X(02)01076-2

Housen, B. A., & Moskowitz, B. M. (2006). Depth distribution of magnetofossils in near-surface sediments from the Blake/Bahama Outer Ridge, western North Atlantic Ocean, determined by low-temperature magnetism. *Journal of Geophysical Research*, *111*(G1), G01005. https://doi.org/10.1029/2005JG000068

Housen, B. A., Richter, C., & van der Pluijm, B. A. (1993). Composite magnetic anisotropy fabrics: experiments, numerical models and implications for the quantification of rock fabrics. *Tectonophysics*, *220*(1–4), 1–12. https://doi.org/10.1016/0040-1951(93)90219-A

Housen, B. A., Van Der Pluijm, B. A., & Essene, E. J. (1995). Plastic behavior of magnetite and high strains obtained from magnetic fabrics in the Parry Sound shear zone, Ontario Grenville Province. *Journal of Structural Geology*, *17*(2), 265–278. https://doi.org/10.1016/0191-8141(94)E0045-Z

Housen, B. A., Tobin, H. J., Labaume, P., Leitch, E. C., Maltman, A. J., & Ocean Drilling Program Leg 156 Shipboard Science Party. (1996). Strain decoupling across the decollement of the Barbados accretionary prism. *Geology*, *24*(2), 127–130. https://doi.org/10.1130/0091-7613(1996)024<0127:SDATDO>2.3.CO;2

Hrouda, F. (1976). The origin of cleavage in the light of magnetic anisotropy investigations. *Physics of the Earth and Planetary Interiors*, *13*(2), 132–142. https://doi.org/10.1016/0031-9201(76)90078-9

Hrouda, F. (1979). The Strain Interpretation of Magnetic Anisotropy in Rocks of the Nízký Jeseník Mountains (Czechoslovakia). *Sbor. Geol. Věd*, *UG 16*, 27–62.

Hrouda, F., & Jelínek, V. (1990). Resolution of ferrimagnetic and paramagnetic anisotropies in rocks, using combined low-field and high-field measurements. *Geophysical Journal International*, *103*(1), 75–84. https://doi.org/10.1111/j.1365-246X.1990.tb01753.x

Hrouda, FrantiŠek. (1987). Mathematical model relationship between the paramagnetic anisotropy and strain in slates. *Tectonophysics*, *142*(2–4), 323–327. https://doi.org/10.1016/0040-1951(87)90131-4

Hrouda, František. (1993). Theoretical models of magnetic anisotropy to strain relationship revisited. *Physics of the Earth and Planetary Interiors*, *77*(3–4), 237–249. https://doi.org/10.1016/0031-9201(93)90101-E

Hrouda, František. (1994). A technique for the measurement of thermal changes of magnetic susceptibility of weakly magnetic rocks by the CS-2 apparatus and KLY-2 Kappabridge. *Geophysical Journal International*, *118*(3), 604–612. https://doi.org/10.1111/j.1365-246X.1994.tb03987.x

Hrouda, František. (2002). Low-field variation of magnetic susceptibility and its effect on the anisotropy of magnetic susceptibility of rocks. *Geophysical Journal International*, *150*(3), 715–723. https://doi.org/10.1046/j.1365-246X.2002.01731.x

Hrouda, František. (2003). Indices for Numerical Characterization of the Alteration Processes of Magnetic Minerals Taking Place During Investigation of Temperature Variation of Magnetic Susceptibility. *Studia Geophysica et Geodaetica*, *47*(4), 847–861. https://doi.org/10.1023/A:1026398920172

Hrouda, František, & Chadima, M. (2020). Examples of tectonic overprints of magnetic fabrics in rocks of the Bohemian Massif and Western Carpathians. *International Journal of Earth Sciences*, *109*(4), 1321–1336. https://doi.org/10.1007/s00531-019-01786-8

Hrouda, František, & Ježek, J. (1999). Theoretical models for the relationship between magnetic anisotropy and strain: effect of triaxial magnetic grains. *Tectonophysics*, *301*(3–4), 183–190. https://doi.org/10.1016/S0040-1951(98)00267-4

Hrouda, František, Jelínek, V., & Zapletal, K. (1997). Refined technique for susceptibility resolution into ferromagnetic and paramagnetic components based on susceptibility temperature-variation measurement. *Geophysical Journal International*, *129*(3), 715–719. https://doi.org/10.1111/j.1365-246X.1997.tb04506.x

Hrouda, František, Chlupáčová, M., & Mrázová, Š. (2006). Low-field variation of magnetic susceptibility as a tool for magnetic mineralogy of rocks. *Physics of the Earth and Planetary Interiors*, *154*(3–4), 323–336. https://doi.org/10.1016/j.pepi.2005.09.013

Hrouda, František, Krejčí, O., Potfaj, M., & Stráník, Z. (2009). Magnetic fabric and weak deformation in sandstones of accretionary prisms of the Flysch and Klippen Belts of the Western Carpathians: Mostly offscraping indicated. *Tectonophysics*, *479*(3–4), 254–270. https://doi.org/10.1016/j.tecto.2009.08.016

Hrouda, František, Gilder, S., Wack, M., & Ježek, J. (2018). Diverse response of paramagnetic and ferromagnetic minerals to deformation from Intra-Carpathian Palaeogene sedimentary rocks: Comparison of magnetic susceptibility and magnetic remanence anisotropies. *Journal of Structural Geology*, *113*, 217–224. https://doi.org/10.1016/j.jsg.2018.06.001

Hsü, K. J. (1968). Principles of Mélanges and Their Bearing on the Franciscan-Knoxville Paradox. *Geological Society of America Bulletin*, *79*(8), 1063. https://doi.org/10.1130/0016-7606(1968)79[1063:POMATB]2.0.CO;2

Humbert, F., Louis, L., & Robion, P. (2014). Method for estimating ductile horizontal strain from magnetic fabrics in poorly consolidated clay-rich sediments. *Tectonophysics*, *629*, 335–352. https://doi.org/10.1016/j.tecto.2014.07.003

Hyndman, R. D., Yamano, M., & Oleskevich, D. A. (1997). The seismogenic zone of subduction thrust faults. *The Island Arc*, *6*(3), 244–260. https://doi.org/10.1111/j.1440-1738.1997.tb00175.x

Ide, S., Beroza, G. C., Shelly, D. R., & Uchide, T. (2007). A scaling law for slow earthquakes. *Nature*, *447*(7140), 76–79. https://doi.org/10.1038/nature05780

ISPRA. (2007). Carta Geologica d'Italia 1:50.000 - Catalogo delle Formazioni. Periodici Tecnici 7.

Issachar, R., Levi, T., Marco, S., & Weinberger, R. (2015). Anisotropy of magnetic susceptibility in diamagnetic limestones reveals deflection of the strain field near the Dead Sea Fault, northern Israel. *Tectonophysics*, *656*, 175–189. https://doi.org/10.1016/j.tecto.2015.06.021

Izquierdo-Llavall, E., Casas-Sainz, A. M., & Oliva-Urcia, B. (2013). Heterogeneous deformation recorded by magnetic fabrics in the Pyrenean Axial Zone. *Journal of Structural Geology*, *57*, 97–113. https://doi.org/10.1016/j.jsg.2013.10.005

Jackson, M. (1991). Anisotropy of magnetic remanence: A brief review of mineralogical sources, physical origins, and geological applications, and comparison with susceptibility anisotropy. *Pure and Applied Geophysics PAGEOPH*, *136*(1), 1–28. https://doi.org/10.1007/BF00878885

Jackson, M., & Solheid, P. (2010). On the quantitative analysis and evaluation of magnetic hysteresis data: HYSTERESIS LOOP EVALUATION AND ANALYSIS. *Geochemistry, Geophysics, Geosystems*, *11*(4), n/a-n/a. https://doi.org/10.1029/2009GC002932

Jackson, M., Gruber, W., Marvin, J., & Banerjee, S. K. (1988). Partial anhysteretic remanence and its anisotropy: Applications and grainsize-dependence. *Geophysical Research Letters*, *15*(5), 440–443. https://doi.org/10.1029/GL015i005p00440

Jackson, M., Sprowl, D., & Ellwood, B. (1989). Anisotropies of partial anhysteretic remanence and susceptibility in compacted black shales: Grainsize- and composition-dependent magnetic fabric. *Geophysical Research Letters*, *16*(9), 1063–1066. https://doi.org/10.1029/GL016i009p01063

Jackson, M., Borradaile, G., Hudleston, P., & Banerjee, S. (1993). Experimental deformation of synthetic magnetite-bearing calcite sandstones: Effects on remanence, bulk magnetic properties, and magnetic anisotropy. *Journal of Geophysical Research: Solid Earth*, *98*(B1), 383–401. https://doi.org/10.1029/92JB01028

Jackson, M., Moskowitz, B., Rosenbaum, J., & Kissel, C. (1998). Field-dependence of AC susceptibility in titanomagnetites. *Earth and Planetary Science Letters*, *157*(3–4), 129–139. https://doi.org/10.1016/S0012-821X(98)00032-6

Jackson, M. J., & Moskowitz, B. (2021). On the distribution of Verwey transition temperatures in natural magnetites. *Geophysical Journal International*, *224*(2), 1314–1325. https://doi.org/10.1093/gji/ggaa516

Jelinek, V. (1981). Characterization of the magnetic fabric of rocks. *Tectonophysics*, *79*(3–4), T63–T67. https://doi.org/10.1016/0040-1951(81)90110-4

Jelinek, V. (1984). On a mixed quadratic invariant of the magnetic susceptibility tensor. *Journal of Geophysics - Zeitschrift Fur Geophysik*, *56(1)*, 58–60.

Jelínek, V. (1996). Theory and measurements of the anisotropy of isothermal remanent magnetization of rocks. *Travaux Géophysiques*, *37*, 124–134.

Ježek, J., & Hrouda, F. (2000). The relationship between the Lisle orientation tensor and the susceptibility tensor. *Physics and Chemistry of the Earth, Part A: Solid Earth and Geodesy*, *25*(5), 469–474. https://doi.org/10.1016/S1464-1895(00)00072-7

Ježek, J., & Hrouda, F. (2002). A technique for numerical modeling of magnetic anisotropy to strain relationship. *Physics and Chemistry of the Earth, Parts A/B/C*, *27*(25–31), 1247–1252. https://doi.org/10.1016/S1474-7065(02)00118-3

Kanamatsu, T., Parés, J. M., & Kitamura, Y. (2012). Pliocene shortening direction in Nankai Trough off Kumano, southwest Japan, Sites IODP C0001 and C0002, Expedition 315: Anisotropy of magnetic susceptibility analysis for paleostress. *Geochemistry, Geophysics, Geosystems*, *13*(1), n/a-n/a. https://doi.org/10.1029/2011GC003782

Kanamatsu, T., Kawamura, K., Strasser, M., Novak, B., & Kitamura, Y. (2014). Flow dynamics of Nankai Trough submarine landslide inferred from internal deformation using magnetic fabric. *Geochemistry, Geophysics, Geosystems*, *15*(10), 4079–4092. https://doi.org/10.1002/2014GC005409

Kimura, G., & Mukai, A. (1991). Underplated units in an accretionary complex: Melange of the Shimanto Belt of eastern Shikoku, southwest Japan. *Tectonics*, *10*(1), 31–50. https://doi.org/10.1029/90TC00799

Kimura, G., Yamaguchi, A., Hojo, M., Kitamura, Y., Kameda, J., Ujiie, K., et al. (2012). Tectonic mélange as fault rock of subduction plate boundary. *Tectonophysics*, *568–569*, 25–38. https://doi.org/10.1016/j.tecto.2011.08.025

King, J. W., & Channell, J. E. T. (1991). Sedimentary magnetism, environmental magnetism, and magnetostratigraphy. *Reviews of Geophysics*, *29*(S1), 358–370. https://doi.org/10.1002/rog.1991.29.s1.358

Kirkpatrick, J. D., Rowe, C. D., Ujiie, K., Moore, J. C., Regalla, C., Remitti, F., et al. (2015). Structure and lithology of the Japan Trench subduction plate boundary fault. *Tectonics*, *34*(1), 53–69. https://doi.org/10.1002/2014TC003695

Kissel, C., Barrier, E., Laj, C., & Lee, T.-Q. (1986). Magnetic fabric in "undeformed" marine clays from compressional zones. *Tectonics*, *5*(5), 769–781. https://doi.org/10.1029/TC005i005p00769

Kitamura, Y., & Kimura, G. (2012). Dynamic role of tectonic mélange during interseismic process of plate boundary mega earthquakes. *Tectonophysics*, *568–569*, 39–52. https://doi.org/10.1016/j.tecto.2011.07.008

Kitamura, Y., Sato, K., Ikesawa, E., Ikehara-Ohmori, K., Kimura, G., Kondo, H., et al. (2005). Mélange and its seismogenic roof décollement: A plate boundary fault rock in the subduction zone-An example from the Shimanto Belt, Japan. *Tectonics*, *24*(5), n/a-n/a. https://doi.org/10.1029/2004TC001635

Kitamura, Y., Kanamatsu, T., & Zhao, X. (2010a). Structural evolution in accretionary prism toe revealed by magnetic fabric analysis from IODP NanTroSEIZE Expedition 316. *Earth and Planetary Science Letters*, *292*(1–2), 221–230. https://doi.org/10.1016/j.epsl.2010.01.040

Kitamura, Y., Kanamatsu, T., & Zhao, X. (2010b). Structural evolution in accretionary prism toe revealed by magnetic fabric analysis from IODP NanTroSEIZE Expedition 316. *Earth and Planetary Science Letters*, *292*(1–2), 221–230. https://doi.org/10.1016/j.epsl.2010.01.040

Kitamura, Y., Zhao, X., & Kanamatsu, T. (2015). Data report: anisotropy of magnetic susceptibility measurement on samples from Sites C0004, C0006, C0007, and C0008, IODP Expedition 3161. In *Proceedings of the Integrated Ocean Drilling Program, Volume 314/315/316*. Integrated Ocean Drilling Program. https://doi.org/10.2204/iodp.proc.314315316.222.2015

Kligfield, R., Lowrie, W., Hirt, A., & Siddans, A. W. B. (1983). Effect of progressive deformation on remanent magnetization of permian redbeds from the alpes maritimes (France). *Tectonophysics*, *98*(1–2), 59–85. https://doi.org/10.1016/0040-1951(83)90211-1

Kligfield, Roy, Lowrie, W., & Dalziel, I. W. D. (1977). Magnetic susceptibility anisotropy as a strain indicator in the sudbury basin, Ontario. *Tectonophysics*, *40*(3–4), 287–308. https://doi.org/10.1016/0040-1951(77)90070-1

Kligfield, Roy, Owens, W. H., & Lowrie, W. (1981). Magnetic susceptibility anisotropy, strain, and progressive deformation in Permian sediments from the Maritime Alps (France). *Earth and Planetary Science Letters*, *55*(1), 181–189. https://doi.org/10.1016/0012-821X(81)90097-2

Kligfield, Roy, Lowrie, W., & Pfiffner, O. A. (1982). Magnetic properties of deformed oolitic limestones from the Swiss Alps: the correlation of magnetic anisotropy and strain [Text/html,application/pdf,text/html]. https://doi.org/10.5169/SEALS-165221

Kneen, S. J. (1976). The relationship between the magnetic and strain fabrics of some haematite-bearing Welsh slates. *Earth and Planetary Science Letters*, *31*(3), 413–416. https://doi.org/10.1016/0012-821X(76)90123-0

Koopman, A. (1983). Detachment tectonics in the Central Apennines, Italy. *Geol. Utraiect.*, *30*, 1–55.

Kruiver, P. P., Dekkers, M. J., & Heslop, D. (2001). Quantification of magnetic coercivity components by the analysis of acquisition curves of isothermal remanent magnetisation. *Earth and Planetary Science Letters*, *189*(3–4), 269–276. https://doi.org/10.1016/S0012-821X(01)00367-3

Kuranaga, M., Kawamura, K., & Kanamatsu, T. (2020). The progressive development of microfabrics from initial deposition to slump deformation: an example from a modern sedimenary mélange on the Nankai Prism. *Journal of the Geological Society*, *177*(3), 619–628. https://doi.org/10.1144/jgs2018-218

Kusbach, V. K., Machek, M., Roxerová, Z., Racek, M., & Silva, P. F. (2019). Localization effect on AMS fabric revealed by microstructural evidence across small-scale shear zone in marble. *Scientific Reports*, *9*(1), 17483. https://doi.org/10.1038/s41598-019-53794-y

Kusky, T. M., & Bradley, D. C. (1999). Kinematic analysis of mélange fabrics: examples and applications from the McHugh Complex, Kenai Peninsula, Alaska. *Journal of Structural Geology*, *21*(12), 1773–1796. https://doi.org/10.1016/S0191-8141(99)00105-4

Larrasoaña, J.C., Pueyo-Morer, E. L., Millán-Garrido, H., Parés, J. M., & Del Valle, J. (1997). Deformation mechanisms deduced from AMS data in the Jaca-Pamplona basin (southern Pyrenees). *Physics and Chemistry of the Earth*, *22*(1–2), 147–152. https://doi.org/10.1016/S0079-1946(97)00093-1

Larrasoaña, Juan C., Pueyo, E. L., & Parés, J. M. (2004). An integrated AMS, structural, palaeo- and rock-magnetic study of Eocene marine marls from the Jaca-Pamplona basin (Pyrenees, N Spain); new insights into the timing of magnetic fabric acquisition in weakly deformed mudrocks. *Geological Society, London, Special Publications*, *238*(1), 127–143. https://doi.org/10.1144/GSL.SP.2004.238.01.10

Lavecchia, G. (1985). Il sovrascorrimento dei Monti Sibillini: analisi cinematica e strutturale. *Bollettino Della Società Geologica Italiana*, *104*, 161–194.

Leah, H., Fagereng, Å., Meneghini, F., Morgan, J. K., Savage, H. M., Wang, M., et al. (2020). Mixed Brittle and Viscous Strain Localization in Pelagic Sediments Seaward of the Hikurangi Margin, New Zealand. *Tectonics*, *39*(8). https://doi.org/10.1029/2019TC005965

Leoni, L., Vannucchi, P., Principi, G., & Catani, F. (2007). Deformation pattern in the underthrust carbonate-rich sequence of the Sibillini Thrust (central Italy): insights for shear zone evolution in modern subduction complexes. *Geodinamica Acta*, *20*(1–2), 53–69. https://doi.org/10.3166/ga.20.53-69

Levi, T., Weinberger, R., & Marco, S. (2014). Magnetic fabrics induced by dynamic faulting reveal damage zone sizes in soft rocks, Dead Sea basin. *Geophysical Journal International*, *199*(2), 1214–1229. https://doi.org/10.1093/gji/ggu300

Levi, Tsafrir, & Weinberger, R. (2011). Magnetic fabrics of diamagnetic rocks and the strain field associated with the Dead Sea Fault, northern Israel. *Journal of Structural Geology*, *33*(4), 566–578. https://doi.org/10.1016/j.jsg.2011.02.001

Li, Y., Zhao, X., Jovane, L., Petronotis, K. E., Gong, Z., & Xie, S. (2015). Paleomagnetic constraints on the tectonic evolution of the Costa Rican subduction zone: New results from sedimentary successions of IODP drill sites from the Cocos Ridge. *Geochemistry, Geophysics, Geosystems*, *16*(12), 4479–4493. https://doi.org/10.1002/2015GC006058

Liu, P., Hirt, A. M., Schüler, D., Uebe, R., Zhu, P., Liu, T., & Zhang, H. (2019). Numerical unmixing of weakly and strongly magnetic minerals: examples with synthetic mixtures of magnetite and hematite. *Geophysical Journal International*, *217*(1), 280–287. https://doi.org/10.1093/gji/ggz022

Liu, Q., Yu, Y., Torrent, J., Roberts, A. P., Pan, Y., & Zhu, R. (2006). Characteristic low-temperature magnetic properties of aluminous goethite [α -(Fe, Al)OOH] explained. *Journal of Geophysical Research: Solid Earth*, *111*(B12), n/a-n/a. https://doi.org/10.1029/2006JB004560

Louis, L., Humbert, F., Robion, P., Henry, P., Knuth, M., & Likos, W. (2012). Data report: joint analysis of acoustic and magnetic susceptibility anisotropies in the Nankai accretionary prism. In M. Kinoshita, H. Tobin, J. Ashi, G. Kimura, S. Lallemant, E. J. Screaton, et al. (Eds.), *Proc. IODP, 314/315/316.* Integrated Ocean Drilling Program. https://doi.org/10.2204/iodp.proc.314315316.2009

Lowe, D. R. (1982). Sediment Gravity Flows: II Depositional Models with Special Reference to the Deposits of High-Density Turbidity Currents. *SEPM Journal of Sedimentary Research*, *52*, 279–297. https://doi.org/10.1306/212F7F31-2B24-11D7-8648000102C1865D

Lowrie, W. (1990). Identification of ferromagnetic minerals in a rock by coercivity and unblocking temperature properties. *Geophysical Research Letters*, *17*(2), 159–162. https://doi.org/10.1029/GL017i002p00159

Lucente, C. C., & Pini, G. A. (2008). Basin-wide mass-wasting complexes as markers of the Oligo-Miocene foredeep-accretionary wedge evolution in the Northern Apennines, Italy. *Basin Research*, *20*(1), 49–71. https://doi.org/10.1111/j.1365-2117.2007.00344.x

Lüneburg, C. M., Lampert, S. A., Lebit, H. D., Hirt, A. M., Casey, M., & Lowrie, W. (1999). Magnetic anisotropy, rock fabrics and finite strain in deformed sediments of SW Sardinia (Italy). *Tectonophysics*, *307*(1–2), 51–74. https://doi.org/10.1016/S0040-1951(99)00118-3

Maher, B. A. (1988). Magnetic properties of some synthetic sub-micron magnetites. *Geophysical Journal International*, *94*(1), 83–96. https://doi.org/10.1111/j.1365-246X.1988.tb03429.x

Marcén, M., Casas-Sainz, A. M., Román-Berdiel, T., Oliva-Urcia, B., Soto, R., & Aldega, L. (2018). Kinematics and strain distribution in an orogen-scale shear zone: Insights from structural analyses and magnetic fabrics in the Gavarnie thrust, Pyrenees. *Journal of Structural Geology*, *117*, 105–123. https://doi.org/10.1016/j.jsg.2018.09.008

Marroni, M., Molli, G., Montanini, A., & Tribuzio, R. (1998). The association of continental crust rocks with ophiolites in the Northern Apennines (Italy): implications for the continent-ocean transition in the Western Tethys. *Tectonophysics*, *292*(1–2), 43–66. https://doi.org/10.1016/S0040-1951(98)00060-2

Marroni, Michele, Meneghini, F., & Pandolfi, L. (2010). Anatomy of the Ligure-Piemontese subduction system: evidence from Late Cretaceous–middle Eocene convergent margin deposits in the Northern Apennines, Italy. *International Geology Review*, *52*(10–12), 1160–1192. https://doi.org/10.1080/00206810903545493

Martín-Hernández, F., & Ferré, E. C. (2007). Separation of paramagnetic and ferrimagnetic anisotropies: A review. *Journal of Geophysical Research*, *112*(B3), B03105. https://doi.org/10.1029/2006JB004340

Martín-Hernández, F., & Hirt, A. M. (2004). A method for the separation of paramagnetic, ferrimagnetic and haematite magnetic subfabrics using high-field torque magnetometry. *Geophysical Journal International*,

157(1), 117–127. https://doi.org/10.1111/j.1365-246X.2004.02225.x

Martín-Hernández, F., & Hirt, A. M. (2001). Separation of ferrimagnetic and paramagnetic anisotropies using a high-field torsion magnetometer. *Tectonophysics*, *337*(3–4), 209–221. https://doi.org/10.1016/S0040-1951(01)00116-0

Mattei, M., Funiciello, R., & Kissel, C. (1995). Paleomagnetic and structural evidence for Neogene block rotations in the Central Apennines, Italy. *Journal of Geophysical Research: Solid Earth*, *100*(B9), 17863–17883. https://doi.org/10.1029/95JB00864

Mattei, M., Sagnotti, L., Faccenna, C., & Funiciello, R. (1997). Magnetic fabric of weakly deformed clay-rich sediments in the Italian peninsula: Relationship with compressional and extensional tectonics. *Tectonophysics*, *271*(1–2), 107–122. https://doi.org/10.1016/S0040-1951(96)00244-2

Mattei, M., D'Agostino, N., Zananiri, I., Kondopoulou, D., Pavlides, S., & Spatharas, V. (2004). Tectonic evolution of fault-bounded continental blocks: Comparison of paleomagnetic and GPS data in the Corinth and Megara basins (Greece). *Journal of Geophysical Research: Solid Earth*, *109*(B2). https://doi.org/10.1029/2003JB002506

Maxbauer, D. P., Feinberg, J. M., & Fox, D. L. (2016a). Magnetic mineral assemblages in soils and paleosols as the basis for paleoprecipitation proxies: A review of magnetic methods and challenges. *Earth-Science Reviews*, *155*, 28–48. https://doi.org/10.1016/j.earscirev.2016.01.014

Maxbauer, D. P., Feinberg, J. M., & Fox, D. L. (2016b). MAX UnMix: A web application for unmixing magnetic coercivity distributions. *Computers & Geosciences*, *95*, 140–145. https://doi.org/10.1016/j.cageo.2016.07.009

Meneghini, F., Marroni, M., & Pandolfi, L. (2007). Fluid flow during accretion in sediment-dominated margins: Evidence of a high-permeability fossil fault zone from the Internal Ligurian accretionary units of the Northern Apennines, Italy. *Journal of Structural Geology*, *29*(3), 515–529. https://doi.org/10.1016/j.jsg.2006.10.003

Meneghini, F., Pandolfi, L., & Marroni, M. (2020). Recycling of heterogeneous material in the subduction factory: evidence from the sedimentary mélange of the Internal Ligurian Units, Italy. *Journal of the Geological Society*, *177*(3), 587–599. https://doi.org/10.1144/jgs2019-081

Middleton, G. V., & Hampton, M. A. (1973). Part I. Sediment Gravity Flows: Mechanics of Flow and Deposition. In G. V. Middleton & A. H. Bouma (Eds.), *Turbidites and Deep-Water Sedimentation: Lecture Notes for a Short Course* (pp. 1–88). Pacific Section: Tulsa, OK, USA: Society of Economic Paleontologists and Mineralogists.

Mishima, T., Hirono, T., Nakamura, N., Tanikawa, W., Soh, W., & Song, S.-R. (2009). Changes to magnetic minerals caused by frictional heating during the 1999 Taiwan Chi-Chi earthquake. *Earth, Planets and Space*, *61*(6), 797–801. https://doi.org/10.1186/BF03353185

Mittempergher, S., Cerchiari, A., Remitti, F., & Festa, A. (2018). From soft sediment deformation to fluid assisted faulting in the shallow part of a subduction megathrust analogue: the Sestola Vidiciatico tectonic Unit (Northern Apennines, Italy). *Geological Magazine*, *155*(2), 438–450. https://doi.org/10.1017/S0016756817000668

Moore, J. C., & Saffer, D. (2001). Updip limit of the seismogenic zone beneath the accretionary prism of southwest Japan: An effect of diagenetic to low-grade metamorphic processes and increasing effective stress. *Geology*, *29*(2), 183. https://doi.org/10.1130/0091-7613(2001)029<0183:ULOTSZ>2.0.CO;2

Moore, J. C., Rowe, C. D., & Meneghini, F. (2007). How can Accretionary Prisms Elucidate Seismogenesis in Subduction Zones? *New York*, 28.

Morin, F. J. (1950). Magnetic Susceptibility of α Fe 2 O 3 and α Fe 2 O 3 with Added Titanium. *Physical Review*, *78*(6), 819–820. https://doi.org/10.1103/PhysRev.78.819.2

Moskowitz, B. M., Frankel, R. B., & Bazylinski, D. A. (1993). Rock magnetic criteria for the detection of biogenic magnetite. *Earth and Planetary Science Letters*, *120*(3–4), 283–300. https://doi.org/10.1016/0012-821X(93)90245-5

Mulder, T., & Alexander, J. (2001). The physical character of subaqueous sedimentary density flows and their deposits. *Sedimentology*, *48*(2), 269–299. https://doi.org/10.1046/j.1365-3091.2001.00360.x

Mullender, T. A. T., Velzen, A. J., & Dekkers, M. J. (1993). Continuous drift correction and separate identification of ferrimagnetic and paramagnetic contributions in thermomagnetic runs. *Geophysical Journal International*, *114*(3), 663–672. https://doi.org/10.1111/j.1365-246X.1993.tb06995.x

Mutti, E., Papani, L., Di Biase, D., Davoli, G., Mora, S., Segadelli, S., & Tinterri, R. (1995). Il Bacino Terziario Epimesoalpino e Le Sue Implicazioni Sui Rapporti Tra Alpi Ed Appennino. *Memorie Di Scienze Geologiche Di Padova*, *47*, 217–244.

Muxworthy, A. R., & McClelland, E. (2000). Review of the low-temperature magnetic properties of magnetite from a rock magnetic perspective. *Geophysical Journal International*, *140*(1), 101–114. https://doi.org/10.1046/j.1365-246x.2000.00999.x

Nagata, T. (1961). Rock magnetism. *Maruzen, Tokyo*, 390.

Nakamura, N., & Borradaile, G. J. (2001). Strain, anisotropy of anhysteretic remanence, and anisotropy of magnetic

susceptibility in a slaty tuff. *Physics of the Earth and Planetary Interiors*, *125*(1–4), 85–93. https://doi.org/10.1016/S0031-9201(01)00214-X

Naylor, M. A., Mandl, G., & Supesteijn, C. H. K. (1986). Fault geometries in basement-induced wrench faulting under different initial stress states. *Journal of Structural Geology*, *8*(7), 737–752. https://doi.org/10.1016/0191-8141(86)90022-2

Obara, K. (2002). Nonvolcanic Deep Tremor Associated with Subduction in Southwest Japan. *Science*, *296*(5573), 1679–1681. https://doi.org/10.1126/science.1070378

Obara, K., & Kato, A. (2016). Connecting slow earthquakes to huge earthquakes. *Science*, *353*(6296), 253–257. https://doi.org/10.1126/science.aaf1512

Ogata, K., Tinterri, R., Pini, G. A., & Mutti, E. (2012). The Specchio Unit (Northern Apennines, Italy): An Ancient Mass Transport Complex Originated from Near-Coastal Areas in an Intra-Slope Setting. In Y. Yamada, K. Kawamura, K. Ikehara, Y. Ogawa, R. Urgeles, D. Mosher, et al. (Eds.), *Submarine Mass Movements and Their Consequences* (Springer, pp. 595–605). Dordrecht, The Netherlands.

Ogata, K., Mountjoy, J. J., Pini, G. A., Festa, A., & Tinterri, R. (2014). Shear zone liquefaction in mass transport deposit emplacement: A multi-scale integration of seismic reflection and outcrop data. *Marine Geology*, *356*, 50–64. https://doi.org/10.1016/j.margeo.2014.05.001

Ogawa, Y. (2019). Conceptual consideration and outcrop interpretation on early stage deformation of sand and mud in accretionary prisms for chaotic deposit formation. *Gondwana Research*, *74*, 31–50. https://doi.org/10.1016/j.gr.2019.03.007

Okada, Y., Kasahara, K., Hori, S., Obara, K., Sekiguchi, S., Fujiwara, H., & Yamamoto, A. (2004). Recent progress of seismic observation networks in Japan —Hi-net, F-net, K-NET and KiK-net—. *Earth, Planets and Space*, *56*(8), xv–xxviii. https://doi.org/10.1186/BF03353076

Oleskevich, D. A., Hyndman, R. D., & Wang, K. (1999). The updip and downdip limits to great subduction earthquakes: Thermal and structural models of Cascadia, south Alaska, SW Japan, and Chile. *Journal of Geophysical Research: Solid Earth*, *104*(B7), 14965–14991. https://doi.org/10.1029/1999JB900060

Oliva-Urcia, B., Larrasoaña, J. C., Pueyo, E. L., Gil, A., Mata, P., Parés, J. M., et al. (2009). Disentangling magnetic subfabrics and their link to deformation processes in cleaved sedimentary rocks from the Internal Sierras (west central Pyrenees, Spain). *Journal of Structural Geology*, *31*(2), 163–176. https://doi.org/10.1016/j.jsg.2008.11.002

Oliva-Urcia, Belén, Román-Berdiel, T., Casas, A. M., Bógalo, M. F., Osácar, M. C., & García-Lasanta, C. (2013). Transition from extensional to compressional magnetic fabrics in the Cretaceous Cabuérniga basin (North Spain). *Journal of Structural Geology*, *46*, 220–234. https://doi.org/10.1016/j.jsg.2012.09.001

Owens, W. H. (1993). Magnetic fabric studies of samples from Hole 808C, Nankai Trough. *Proceedings of the Ocean Drilling Program, Scientific Results*, *131*, 301–310.

Özdemir, Ö., & Dunlop, D. J. (2014). Hysteresis and coercivity of hematite. *Journal of Geophysical Research: Solid Earth*, *119*(4), 2582–2594. https://doi.org/10.1002/2013JB010739

Özdemir, Ö., Dunlop, D. J., & Berquó, T. S. (2008). Morin transition in hematite: Size dependence and thermal hysteresis: MORIN TRANSITION IN HEMATITE. *Geochemistry, Geophysics, Geosystems*, *9*(10), n/a-n/a. https://doi.org/10.1029/2008GC002110

Pace, P., Calamita, F., & Tavarnelli, E. (2015). Brittle-ductile shear zones along inversion-related frontal and oblique thrust ramps: Insights from the Central-Northern Apennines curved thrust system (Italy). In S. Mukherjee & K. F. Mulchrone (Eds.), *Ductile Shear Zones* (pp. 111–127). Chichester, UK: John Wiley & Sons, Ltd. https://doi.org/10.1002/9781118844953.ch8

Pan, Y., Zhu, R., Banerjee, S. K., Gill, J., & Williams, Q. (2000). Rock magnetic properties related to thermal treatment of siderite: Behavior and interpretation. *Journal of Geophysical Research: Solid Earth*, *105*(B1), 783–794. https://doi.org/10.1029/1999JB900358

Panini, F., Fioroni, C., Fregni, P., & Bonacci, M. (2002). Le Rocce Caotiche Dell'Oltrepo Pavese: Note Illustrative Della Carta Geologica Dell'Appennino Vogherese Tra Borgo Priolo e Ruino. *Atti Ticinensi Di Scienze Della Terra*, *43*, 83–109.

Panini, Filippo, Fioroni, C., & Fregni, P. (2013). Le Brecce Argillose Di Musigliano (Appennino Vogherese–Tortonese): Dati Stratigrafici Preliminari. *Rendiconti Online Della Società Geologica Italiana*, *26*, 21–31.

Parés, J M. (2015). Sixty years of anisotropy of magnetic susceptibility in deformed sedimentary rocks. *Frontiers in Earth Science*, *3*. https://doi.org/10.3389/feart.2015.00004

Parés, J M, & van der Pluijm, B. A. (2004). Correlating magnetic fabrics with finite strain: Comparing results from mudrocks in the Variscan and Appalachian Orogens. *Geologica Acta*, 9.

Parés, Josep M., & van der Pluijm, B. A. (2002). Evaluating magnetic lineations (AMS) in deformed rocks. *Tectonophysics*, *350*(4), 283–298. https://doi.org/10.1016/S0040-1951(02)00119-1

Parés, Josep M, & van der Pluijm, B. A. (2003). Magnetic fabrics and strain in pencil structures of the Knobs Formation, Valley and Ridge Province, US Appalachians.

Journal of Structural Geology, *25*(9), 1349–1358. https://doi.org/10.1016/S0191-8141(02)00197-9

Parés, Josep M., van der Pluijm, B. A., & Dinarès-Turell, J. (1999). Evolution of magnetic fabrics during incipient deformation of mudrocks (Pyrenees, northern Spain). *Tectonophysics*, *307*(1–2), 1–14. https://doi.org/10.1016/S0040-1951(99)00115-8

Passchier, C. W., & Trouw, R. A. J. (2005). *Microtectonics* (2nd, rev.enl. ed ed.). Berlin; New York: Springer.

Paterson, G. A., Zhao, X., Jackson, M., & Heslop, D. (2018). Measuring, Processing, and Analyzing Hysteresis Data. *Geochemistry, Geophysics, Geosystems*, *19*(7), 1925–1945. https://doi.org/10.1029/2018GC007620

Peng, Z., & Gomberg, J. (2010). An integrated perspective of the continuum between earthquakes and slow-slip phenomena. *Nature Geoscience*, *3*(9), 599–607. https://doi.org/10.1038/ngeo940

Pierantoni, P. P. (1996). Faglie trascorrenti sin-thrusting come ripartizione della deformazione: L'esempio della Faglia Sabina (Appennino Centrale). *Studi Geologici Camerti*, *14*, 279–289.

Pini, G. A., Lucente, C., Cowan, D. S., De Libero, C. M., Dellisanti, F., Landuzzi, A., et al. (2004). The Role of Olistostromes and Argille Scagliose in the Structural Evolution of the Nothern Apennines. In L. Guerrieri, I. Rischia, & L. Serva (Eds.), *Field Trip Guidebooks, Proceedings of the 32nd IGC, Florence, Italy, 20–28 August 2004; Memorie Descrittive della Carta Geologica d'Italia 63* (Vol. B13, pp. 1–40). Roma, Italy.

Pini, G. A., Ogata, K., Camerlenghi, A., Festa, A., Lucente, C., & Codegone, G. (2012). Sedimentary mélanges and Fossil Mass-Transport Complexes: A Key for Better Understanding Submarine Mass Movements? In Y. Yamada, K. Kawamura, K. Ikehara, Y. Ogawa, R. Urgeles, D. Mosher, et al. (Eds.), *Submarine Mass Movements and Their Consequences* (Springer, pp. 585–594). Dordrecht, The Netherlands.

Pini, Gian Andrea. (1999). *Tectonosomes and olistostromes in the argille scagliose of the northern Apennines, Italy*. Boulder, Colo: Geological Society of America Special Paper 335.

Plesi, G. (2002). Note illustrative della Carta Geologica d'Italia alla scala 1:50.000, Foglio 235 "Pievepelago". *Servizio Geologico d'Italia-Regione Emilia Romagna. S.EL.CA.*

Plesi, G., Daniele, G., Botti, F., & Palandri, S. (2002). Carta strutturale dell'alto Appennino tosco-emiliano (scala 1:100000) fra il Passo della Cisa e il Corno alle Scale. In Atti del terzo seminario sulla cartografia geologica, Bologna 2002. SELCA Firenze.

Pokorný, J., Pokorný, P., Suza, P., & Hrouda, F. (2011). A Multi-Function Kappabridge for High Precision Measurement of the AMS and the Variations of Magnetic Susceptibility with Field, Temperature and Frequency. In E. Petrovský, D. Ivers, T. Harinarayana, & E. Herrero-Bervera (Eds.), *The Earth's Magnetic Interior* (pp. 293–301). Dordrecht: Springer Netherlands. https://doi.org/10.1007/978-94-007-0323-0_20

Potter, D. K., & Stephenson, A. (1988). Single-domain particles in rocks and magnetic fabric analysis. *Geophysical Research Letters*, *15*(10), 1097–1100. https://doi.org/10.1029/GL015i010p01097

Pueyo Anchuela, Ó., Pocoví Juan, A., & Gil Imaz, A. (2010). Tectonic imprint in magnetic fabrics in foreland basins: A case study from the Ebro Basin, N Spain. *Tectonophysics*, *492*(1–4), 150–163. https://doi.org/10.1016/j.tecto.2010.06.016

Pueyo Anchuela, Ó., Gil Imaz, A., & Pocoví Juan, A. (2012). Factors affecting the record of strain fabrics at the anisotropy of magnetic susceptibility: West-Central South-Pyrenean cleavage domain (Southern Pyrenees; NE Spain). *Tectonophysics*, *554–557*, 1–17. https://doi.org/10.1016/j.tecto.2012.05.028

R Development Core Team. (2014). R: A language and environment for statistical computing. R Foundation for statistical computing. Retrieved from https://www.r-project.org/

Rathore, Jaswant Singh, & Henry, B. (1982). Comparison of strain and magnetic fabrics in Dalradian rocks from the southwest Highlands of Scotland. *Journal of Structural Geology*, *4*(3), 373–384. https://doi.org/10.1016/0191-8141(82)90020-7

Rathore, J.S. (1979). Magnetic susceptibility anisotropy in the Cambrian slate belt of North Wales and correlation with strain. *Tectonophysics*, *53*(1–2), 83–97. https://doi.org/10.1016/0040-1951(79)90355-X

Rathore, J.S., & Becke, M. (1980). Magnetic fabric analyses in the Gail Galley (Carinthia, Austria) for the determination of the sense of movements along this region of the Periadriatic Line. *Tectonophysics*, *69*(3–4), 349–368. https://doi.org/10.1016/0040-1951(80)90216-4

Remitti, F., Vannucchi, P., Bettelli, G., Fantoni, L., Panini, F., & Vescovi, P. (2011). Tectonic and sedimentary evolution of the frontal part of an ancient subduction complex at the transition from accretion to erosion: The case of the Ligurian wedge of the northern Apennines, Italy. *Geological Society of America Bulletin*, *123*(1–2), 51–70. https://doi.org/10.1130/B30065.1

Remitti, F., Balestrieri, M. L., Vannucchi, P., & Bettelli, G. (2013). Early exhumation of underthrust units near the toe of an ancient erosive subduction zone: A case study from the Northern Apennines of Italy. *Geological Society of America Bulletin*, *125*(11–12), 1820–1832. https://doi.org/10.1130/B30862.1

Remitti, Francesca, Bettelli, G., & Vannucchi, P. (2007). Internal structure and tectonic evolution of an underthrust tectonic mélange: the Sestola-Vidiciatico tectonic unit of the Northern Apennines, Italy. *Geodinamica Acta*, *20*(1–2), 37–51. https://doi.org/10.3166/ga.20.37-51

Remitti, Francesca, Bettelli, G., Panini, F., Carlini, M., & Vannucchi, P. (2012). Deformation, fluid flow, and mass transfer in the forearc of convergent margins: A two-day field trip in an ancient and exhumed erosive convergent margin in the Northern Apennines. In *Deformation, Fluid Flow, and Mass Transfer in the Forearc of Convergent Margins: Field Guides to the Northern Apennines in Emilia and in the Apuan Alps (Italy)* (pp. 1–33). Geological Society of America. https://doi.org/10.1130/2012.0028(01)

Reutter, K. J., Heinitz, I., & Ensslin, R. (1991). Structural and geothermal evolution of the Modino-Cervarola Unit. *Mem. Descr. Carta Geol. Ital.*, *46*, 257–266.

Rice, J. R., & Cocco, M. (2007). Seismic fault rheology and earthquake dynamics. In *Tectonic Faults: Agents of Change on a Dynamic Earth* (pp. 99–137). The MIT Press. Retrieved from https://doi.org/10.7551/mitpress/6703.003.0007

Roberts, A. P., Cui, Y., & Verosub, K. L. (1995). Wasp-waisted hysteresis loops: Mineral magnetic characteristics and discrimination of components in mixed magnetic systems. *Journal of Geophysical Research: Solid Earth*, *100*(B9), 17909–17924. https://doi.org/10.1029/95JB00672

Robustelli Test, C., & Zanella, E. (2021). Rock Magnetic Signature of Heterogeneities Across an Intraplate Basal Contact: An Example From the Northern Apennines. *Geochemistry, Geophysics, Geosystems*, *22*(12). https://doi.org/10.1029/2021GC010004

Robustelli Test, C., Festa, A., Zanella, E., Codegone, G., & Scaramuzzo, E. (2019). Distinguishing the Mélange-Forming Processes in Subduction-Accretion Complexes: Constraints from the Anisotropy of Magnetic Susceptibility (AMS). *Geosciences*, *9*(9), 381. https://doi.org/10.3390/geosciences9090381

Rochette, P., & Vialon, P. (1984). Development of planar and linear fabrics in Dauphinois shales and slates (French Alps) studied by magnetic anisotropy and its mineralogical control. *Journal of Structural Geology*, *6*(1–2), 33–38. https://doi.org/10.1016/0191-8141(84)90081-6

Rochette, P., Jackson, M., & Aubourg, C. (1992). Rock magnetism and the interpretation of anisotropy of magnetic susceptibility. *Reviews of Geophysics*, *30*(3), 209. https://doi.org/10.1029/92RG00733

Rochette, Pierre. (1987). Magnetic susceptibility of the rock matrix related to magnetic fabric studies. *Journal of Structural Geology*, *9*(8), 1015–1020. https://doi.org/10.1016/0191-8141(87)90009-5

Rochette, Pierre. (1988). Inverse magnetic fabric in carbonate-bearing rocks. *Earth and Planetary Science Letters*, *90*(2), 229–237. https://doi.org/10.1016/0012-821X(88)90103-3

Rochette, Pierre, Fillion, G., Mattéi, J.-L., & Dekkers, M. J. (1990). Magnetic transition at 30–34 Kelvin in pyrrhotite: insight into a widespread occurrence of this mineral in rocks. *Earth and Planetary Science Letters*, *98*(3–4), 319–328. https://doi.org/10.1016/0012-821X(90)90034-U

Rochette, Pierre, Aubourg, C., & Perrin, M. (1999). Is this magnetic fabric normal? A review and case studies in volcanic formations. *Tectonophysics*, *307*(1–2), 219–234. https://doi.org/10.1016/S0040-1951(99)00127-4

Román-Berdiel, T., Casas-Sainz, A. M., Oliva-Urcia, B., Calvín, P., & Villalaín, J. J. (2019). On the influence of magnetic mineralogy in the tectonic interpretation of anisotropy of magnetic susceptibility in cataclastic fault zones. *Geophysical Journal International*, *216*(2), 1043–1061. https://doi.org/10.1093/gji/ggy481

Rusciadelli, G., Viandante, M. G., Calamita, F., & Cook, A. C. (2005). Burial-exhumation history of the central Apennines (Italy), from the foreland to the chain building: thermochronological and geological data. *Terra Nova*, *17*(6), 560–572. https://doi.org/10.1111/j.1365-3121.2005.00649.x

Saffer, D. M., & Tobin, H. J. (2011). Hydrogeology and Mechanics of Subduction Zone Forearcs: Fluid Flow and Pore Pressure. *Annual Review of Earth and Planetary Sciences*, *39*(1), 157–186. https://doi.org/10.1146/annurev-earth-040610-133408

Saffer, D. M., & Wallace, L. M. (2015). The frictional, hydrologic, metamorphic and thermal habitat of shallow slow earthquakes. *Nature Geoscience*, *8*(8), 594–600. https://doi.org/10.1038/ngeo2490

Sagiya, T. (2004). A decade of GEONET: 1994–2003 —The continuous GPS observation in Japan and its impact on earthquake studies—. *Earth, Planets and Space*, *56*(8), xxix–xli. https://doi.org/10.1186/BF03353077

Sagnotti, L. (2011). Magnetic Anisotropy. In H. K. Gupta (Ed.), *Encyclopedia of Solid Earth Geophysics* (Springer, pp. 717–729). Dordrecht, The Netherlands.

Sagnotti, Leonardo, & Speranza, F. (1993). Magnetic fabric analysis of the Plio-Pleistocene clayey units of the Sant'Arcangelo basin, southern Italy. *Physics of the Earth and Planetary Interiors*, *77*(3–4), 165–176. https://doi.org/10.1016/0031-9201(93)90096-R

Sagnotti, Leonardo, Faccenna, C., Funiciello, R., & Mattei, M. (1994). Magnetic fabric and structural setting of Plio-Pleistocene clayey units in an extensional regime: the Tyrrhenian margin of central Italy. *Journal of Structural Geology*, *16*(9), 1243–1257. https://doi.org/10.1016/0191-8141(94)90067-1

Sagnotti, Leonardo, Speranza, F., Winkler, A., Mattei, M., & Funiciello, R. (1998). Magnetic fabric of clay sediments from the external northern Apennines (Italy). *Physics of the Earth and Planetary Interiors*, *105*(1–2), 73–93. https://doi.org/10.1016/S0031-9201(97)00071-X

Sagnotti, Leonardo, Winkler, A., Montone, P., Di Bella, L., Florindo, F., Mariucci, M. T., et al. (1999). Magnetic anisotropy of Plio–Pleistocene sediments from the Adriatic margin of the northern Apennines (Italy): implications for the time–space evolution of the stress field. *Tectonophysics*, *311*(1–4), 139–153. https://doi.org/10.1016/S0040-1951(99)00159-6

Satolli, S., Robustelli Test, C., Staneczek, D., Zanella, E., Calamita, F., & Tema, E. (2020). Magnetic fabric in carbonatic rocks from thrust shear zones: A study from the Northern Apennines (Italy). *Tectonophysics*, *791*, 228573. https://doi.org/10.1016/j.tecto.2020.228573

Schöfisch, T., Koyi, H., & Almqvist, B. (2022). Magnetic Fabric Signature Within a Thrust Imbricate; an Analog Modeling Approach. *Tectonics*, *41*(7). https://doi.org/10.1029/2021TC007054

Schöfisch, Thorben, Koyi, H., & Almqvist, B. (2021). Influence of décollement friction on anisotropy of magnetic susceptibility in a fold-and-thrust belt model. *Journal of Structural Geology*, *144*, 104274. https://doi.org/10.1016/j.jsg.2020.104274

Scholz, C. H. (2019). *The Mechanics of Earthquakes and Faulting* (3rd ed.). Cambridge University Press. https://doi.org/10.1017/9781316681473

Schwehr, K., & Tauxe, L. (2003). Characterization of soft-sediment deformation: Detection of cryptoslumps using magnetic methods. *Geology*, *31*(3), 203. https://doi.org/10.1130/0091-7613(2003)031<0203:COSSDD>2.0.CO;2

Sibson, R. H. (2013). Stress switching in subduction forearcs: Implications for overpressure containment and strength cycling on megathrusts. *Tectonophysics*, *600*, 142–152. https://doi.org/10.1016/j.tecto.2013.02.035

Smirnov, A. V. (2009). Grain size dependence of low-temperature remanent magnetization in natural and synthetic magnetite: Experimental study. *Earth, Planets and Space*, *61*(1), 119–124. https://doi.org/10.1186/BF03352891

Stacey, F. D., Joplin, G., & Lindsay, J. (1960). Magnetic anisotropy and fabric of some foliated rocks from S.E. Australia. *Geofisica Pura e Applicata*, *47*(1), 30–40. https://doi.org/10.1007/BF01992481

Taira, A., & Niitsuma, N. (1986). Turbidite sedimentation in the Nankai Trough as interpreted from magnetic fabric, grain size, and detrital modal analyses. In H. Kagami, D. E. Karig, W. T. Coulbourn, & et al. (Eds.), *Initial Reports of the Deep Sea Drilling Project, 87* (Vol. 87). U.S. Government Printing Office. https://doi.org/10.2973/dsdp.proc.87.1986

Tanikawa, W., Mishima, T., Hirono, T., Soh, W., & Song, S.-R. (2008). High magnetic susceptibility produced by thermal decomposition of core samples from the Chelungpu fault in Taiwan. *Earth and Planetary Science Letters*, *272*(1–2), 372–381. https://doi.org/10.1016/j.epsl.2008.05.002

Tarling, D. H., & Hrouda, F. (1993). *The magnetic anisotropy of rocks*. Chapman & Hall.

Tauxe, L., Mullender, T. A. T., & Pick, T. (1996). Potbellies, wasp-waists, and superparamagnetism in magnetic hysteresis. *Journal of Geophysical Research: Solid Earth*, *101*(B1), 571–583. https://doi.org/10.1029/95JB03041

Tauxe, Lisa, Bertram, H. N., & Seberino, C. (2002). Physical interpretation of hysteresis loops: Micromagnetic modeling of fine particle magnetite. *Geochemistry, Geophysics, Geosystems*, *3*(10), 1–22. https://doi.org/10.1029/2001GC000241

Tavarnelli, E. (1997). Structural evolution of a foreland fold-and-thrust belt: the Umbria-Marche Apennines, Italy. *Journal of Structural Geology*, *19*(3–4), 523–534. https://doi.org/10.1016/S0191-8141(96)00093-4

Tavarnelli, E. (1999). Normal faults in thrust sheets: pre-orogenic extension, post-orogenic extension, or both? *Journal of Structural Geology*, *21*(8–9), 1011–1018. https://doi.org/10.1016/S0191-8141(99)00034-6

Tavarnelli, E., Butler, R. W. H., Decandia, F. A., Calamita, F., Grasso, M., Alvarez, W., & Renda, P. (2004). Implications of fault reactivation and structural inheritance in the Cenozoic tectonic evolution of Italy. In U. Crescenti, S. D'offizi, S. Merlino, & S. Sacchi (Eds.), *The Geology of Italy* (Vol. Speciale, pp. 209–222). Società Geologica Italiana.

Thompson, R., & Oldfield, F. (1986). *Environmental Magnetism*. Dordrecht: Springer Netherlands. https://doi.org/10.1007/978-94-011-8036-8

Till, J. L., Jackson, M. J., & Moskowitz, B. M. (2010). Remanence stability and magnetic fabric development in synthetic shear zones deformed at 500°C. *Geochemistry, Geophysics, Geosystems*, *11*(12), n/a-n/a. https://doi.org/10.1029/2010GC003320

Till, J. L., Moskowitz, B. M., & Jackson, M. J. (2012). High-temperature magnetic fabric development from plastically deformed magnetite in experimental shear zones: Magnetic fabric from magnetite deformation. *Geophysical Journal International*, *189*(1), 229–239. https://doi.org/10.1111/j.1365-246X.2011.05338.x

Tokiwa, T., & Yamamoto, Y. (2012). Relationship between magnetic fabrics and shear directions in mélange within the Miyama Formation, Shimanto accretionary complex,

Japan. *Tectonophysics*, *568–569*, 53–64. https://doi.org/10.1016/j.tecto.2011.11.001

Turtù, A., Satolli, S., Maniscalco, R., Calamita, F., & Speranza, F. (2013). Understanding progressive-arc- and strike-slip-related rotations in curve-shaped orogenic belts: The case of the Olevano-Antrodoco-Sibillini thrust (Northern Apennines, Italy). *Journal of Geophysical Research: Solid Earth*, *118*(2), 459–473. https://doi.org/10.1002/jgrb.50096

Ujiie, K., Hisamitsu, T., & Soh, W. (2000). Magnetic and structural fabrics of the melange in the Shimanto accretionary complex, Okinawa Island: Implication for strain history during decollement-related deformation. *Journal of Geophysical Research: Solid Earth*, *105*(B11), 25729–25741. https://doi.org/10.1029/2000JB900251

Ujiie, K., Hisamitsu, T., & Taira, A. (2003). Deformation and fluid pressure variation during initiation and evolution of the plate boundary décollement zone in the Nankai accretionary prism. *Journal of Geophysical Research*, *108*(B8), 2398. https://doi.org/10.1029/2002JB002314

Ujiie, K., Hisamitsu, T., Maltman, A. J., Morgan, J. K., Sánchez-Gómez, M., & Tobin, H. J. (2005). Deformation Structures and Magnetic Fabrics at Site 1178: Implication for Deformation History Recorded in Accreted Sediments at an Evolved Portion of the Nankai Accretionary Prism. In H. Mikada, G. F. Moore, A. Taira, K. Becker, J. C. Moore, & A. Klaus (Eds.), *Proceedings of the Ocean Drilling Program, 190/196 Scientific Results* (Vol. 190/196). Ocean Drilling Program. https://doi.org/10.2973/odp.proc.sr.190196.2005

Urrutia-Fucugauchi, J. (2007). Magnetic Susceptibility, Anisotropy, Effects Of Heating. In D. Gubbins & E. Herrero-Bervera (Eds.), *Encyclopedia of Geomagnetism and Paleomagnetism* (pp. 560–564). Dordrecht: Springer Netherlands. https://doi.org/10.1007/978-1-4020-4423-6_186

Vannucchi, P., & Bettelli, G. (2002). Mechanisms of subduction accretion as implied from the broken formations in the Apennines, Italy. *Geology*, *30*(9), 835. https://doi.org/10.1130/0091-7613(2002)030<0835:MOSAAI>2.0.CO;2

Vannucchi, P., Remitti, F., & Bettelli, G. (2008). Geological record of fluid flow and seismogenesis along an erosive subducting plate boundary. *Nature*, *451*(7179), 699–703. https://doi.org/10.1038/nature06486

Vannucchi, P., Remitti, F., Bettelli, G., Boschi, C., & Dallai, L. (2010). Fluid history related to the early Eocene-middle Miocene convergent system of the Northern Apennines (Italy): Constraints from structural and isotopic studies. *Journal of Geophysical Research*, *115*(B5), B05405. https://doi.org/10.1029/2009JB006590

Vannucchi, P., Remitti, F., & Bettelli, G. (2012). Lateral variability of the erosive plate boundary in the Northern Apennines, Italy. *Italian Journal of Geosciences*, *131*(2), 215–227.

Vannucchi, Paola. (2012). Geothermal and rheological regime in the Po plain sector of Adria (Northern Italy). *Italian Journal of Geosciences*, (Vol. 131, N. 2), 215–227. https://doi.org/10.3301/IJG.2012.11

Velzen, A. J., & Zijderveld, J. D. A. (1992). A method to study alterations of magnetic minerals during thermal demagnetization applied to a fine-grained marine marl (Trubi formation, Sicily). *Geophysical Journal International*, *110*(1), 79–90. https://doi.org/10.1111/j.1365-246X.1992.tb00715.x

van Velzen, A. J., & Zijderveld, J. D. A. (1992). A method to study alterations of magnetic minerals during thermal demagnetization applied to a fine-grained marine marl (Trubi formation, Sicily). *Geophysical Journal International*, *110*(1), 79–90. https://doi.org/10.1111/j.1365-246X.1992.tb00715.x

Verwey, E. J. W. (1939). Electronic Conduction of Magnetite (Fe3O4) and its Transition Point at Low Temperatures. *Nature*, *144*(3642), 327–328. https://doi.org/10.1038/144327b0

Vollmer, F. W. (2015). Orient 3: A new integrated software program for orientation data analysis, kinematic analysis, spherical projections, and Schmidt plots. *Geological Society of America Abstracts with Programs*, *47*(7), 49.

Weaver, R., Roberts, A. P., & Barker, A. J. (2002). A late diagenetic (syn-folding) magnetization carried by pyrrhotite: implications for paleomagnetic studies from magnetic iron sulphide-bearing sediments. *Earth and Planetary Science Letters*, *200*(3–4), 371–386. https://doi.org/10.1016/S0012-821X(02)00652-0

Weil, A. B., & Yonkee, A. (2009). Anisotropy of magnetic susceptibility in weakly deformed red beds from the Wyoming salient, Sevier thrust belt: Relations to layer-parallel shortening and orogenic curvature. *Lithosphere*, *1*(4), 235–256. https://doi.org/10.1130/L42.1

Weil, Arlo Brandon, & Yonkee, W. A. (2012). Layer-parallel shortening across the Sevier fold-thrust belt and Laramide foreland of Wyoming: spatial and temporal evolution of a complex geodynamic system. *Earth and Planetary Science Letters*, *357–358*, 405–420. https://doi.org/10.1016/j.epsl.2012.09.021

Wood, D. S., Oertel, G., Singh, J., Bennett, H. F., & Tarling, D. H. (1976). Strain and Anisotropy in Rocks [and Discussion]. *Philosophical Transactions of the Royal Society of London*, *A. 283*, 27–42.

Worm, H.-U., Clark, D., & Dekkers, M. J. (1993). Magnetic Susceptibility of Pyrrhotite: Grain Size, Field and Frequency Dependence. *Geophysical Journal International*, *114*(1), 127–137. https://doi.org/10.1111/j.1365-246X.1993.tb01472.x

Xypolias, P. (2010). Vorticity analysis in shear zones: A review of methods and applications. *Journal of Structural Geology*, *32*(12), 2072–2092. https://doi.org/10.1016/j.jsg.2010.08.009

Yamaji, A., & Sato, K. (2011). Clustering of fracture orientations using a mixed Bingham distribution and its application to paleostress analysis from dike or vein orientations. *Journal of Structural Geology*, *33*(7), 1148–1157. https://doi.org/10.1016/j.jsg.2011.05.006

Yamamoto, Y. (2006). Systematic variation of shear-induced physical properties and fabrics in the Miura–Boso accretionary prism: The earliest processes during off-scraping. *Earth and Planetary Science Letters*, *244*(1–2), 270–284. https://doi.org/10.1016/j.epsl.2006.01.049

Yamamoto, Yuzuru, Tonogai, K., & Anma, R. (2012). Fabric-based criteria to distinguish tectonic from sedimentary mélanges in the Shimanto accretionary complex, Yakushima Island, SW Japan. *Tectonophysics*, *568–569*, 65–73. https://doi.org/10.1016/j.tecto.2011.10.018

Yang, T., Chen, J., Wang, H., & Jin, H. (2012). Rock magnetic properties of fault rocks from the rupture of the 2008 Wenchuan earthquake, China and their implications: Preliminary results from the Zhaojiagou outcrop, Beichuan County (Sichuan). *Tectonophysics*, *530–531*, 331–341. https://doi.org/10.1016/j.tecto.2012.01.019

Yang, T., Chen, J., Yang, X., Wang, H., & Jin, H. (2013). Differences in magnetic properties of fragments and matrix of breccias from the rupture of the 2008 Wenchuan earthquake, China: Relationship to faulting. *Tectonophysics*, *601*, 112–124. https://doi.org/10.1016/j.tecto.2013.05.002

Yang, T., Mishima, T., Ujiie, K., Chester, F. M., Mori, J. J., Eguchi, N., & Toczko, S. (2013). Strain decoupling across the décollement in the region of large slip during the 2011 Tohoku-Oki earthquake from anisotropy of magnetic susceptibility. *Earth and Planetary Science Letters*, *381*, 31–38. https://doi.org/10.1016/j.epsl.2013.08.045

Yang, T., Yang, X., Duan, Q., Chen, J., & Dekkers, M. J. (2016). Rock magnetic expression of fluid infiltration in the Yingxiu-Beichuan fault (Longmen Shan thrust belt, China). *Geochemistry, Geophysics, Geosystems*, *17*(3), 1065–1085. https://doi.org/10.1002/2015GC006095

Yang, T., Dekkers, M. J., & Zhang, B. (2016). Seismic heating signatures in the Japan Trench subduction plate-boundary fault zone: evidence from a preliminary rock magnetic 'geothermometer.' *Geophysical Journal International*, *205*(1), 319–331. https://doi.org/10.1093/gji/ggw013

Yang, T., Dekkers, M. J., & Chen, J. (2018). Thermal Alteration of Pyrite to Pyrrhotite During Earthquakes: New Evidence of Seismic Slip in the Rock Record. *Journal of Geophysical Research: Solid Earth*, *123*(2), 1116–1131. https://doi.org/10.1002/2017JB014973

Yang, T., Chou, Y., Ferré, E. C., Dekkers, M. J., Chen, J., Yeh, E., & Tanikawa, W. (2020). Faulting Processes Unveiled by Magnetic Properties of Fault Rocks. *Reviews of Geophysics*, *58*(4). https://doi.org/10.1029/2019RG000690

Yu, Y., Dunlop, D. J., & Özdemir, Ö. (2002). Partial anhysteretic remanent magnetization in magnetite 1. Additivity. *Journal of Geophysical Research: Solid Earth*, *107*(B10), EPM 7-1-EPM 7-9. https://doi.org/10.1029/2001JB001249